1 IXS: INELASTIC SCATTERING BEAMLINE

1.1 Executive Summary

We present in this chapter a preliminary design of the Inelastic X-ray Scattering (IXS) beamline for NSLS-II. The scientific objective of the beamline is focused on very high-resolution (1 meV ~ 0.1 meV) IXS experiments as outlined in the NSLS-II Conceptual Design Report delivered in December 2006. The NSLS-II User Workshop in July 2007 provides further inputs from the user community on the scientific drivers for this beamline. The beamline as designed includes two endstations, one with 1meV and the other with 0.1meV energy resolution, both of which take full advantage of the high brightness and flux of the NSLS-II source at ~10 keV. To achieve the 0.1meV resolution goal for NSLS-II, the current design employs a newly proposed scheme based on highly asymmetrically cut Si crystal optics operating at exact back-scattering. This novel approach, albeit yet to be demonstrated in a working device for which active R&D are required, provides a unique opportunity for NSLS-II to build a fundamentally new instrument with unprecedented performance for inelastic x-ray scattering experiments that are not yet feasible on any existing instruments to date.

The scope of the present document includes the scientific objective, the radiation source, the overall beamline layout, rationales for beamline optics, the power management and the expected performance. Some design details will be presented, including the beamline vacuum system, data acquisition and motion control, and beamline components that are likely to remain the same regardless the details of the endstation design. Details on the Personnel Safety System, the Equipment Protection System, as well as additional requirements on the conventional facilities and accelerator systems will also be discussed.

Several possible configurations of the 1meV endstation will be outlined. One will be based on the same scheme as that for the 0.1meV endstation, but optimized to operate at 1meV energy resolution. This would be a logical choice as demonstrating the scheme for achieving the 0.1meV energy resolution works for 1 meV is a milestone of its own. Others are based on existing experience in building IXS beamlines that offer 1meV energy resolution at ESRF, SPring-8 and APS using Si crystal optics operating at higher photon energies. The intension here is to use crystals of lower symmetry such as quartz or sapphire which offer many possible choices of refraction with intrinsic width of the order of 1 meV at energies ~10 keV. There are concerns regarding the quality of these crystals for use as high-resolution x-ray optics. There are however substantial efforts now in making better crystals at several groups around the world. We will monitor the progress of those efforts and make a decision on the configuration of the 1meV endstation at some point in future.

The total estimated cost of the beamline based on the details of the current design stands at $9.915M, which includes the enclosures, beam transport, utilities, white beam components, high heatload optics, beam conditioning optics, Personnel Safety System, Equipment Protection System, beamline controls, and project management. The cost for the 0.1meV endstation is also included.

Finally, we would like to emphasize that the present design is still at a very preliminary stage. The final design of the beamline as well as the endstations will largely depend on the final technical details for achieving the 0.1meV energy resolution, where an active R&D program will be required and pursued. The design process will further involve consultations with the user community through workshops and with the Beamline Advisory Team (BAT) in the coming years, whereby the scientific focus of the beamline and endstations and hence their design will be further refined.

1.2 Scientific Objective

Inelastic X-ray Scattering is a momentum-resolved technique for studying dynamics and excitations in condensed matter systems. The scientific objective of the present IXS beamline is focused on very high-resolution (1 meV ~ 0.1 meV) IXS experiments for studying low-energy dynamics of a variety of systems. The NSLS-II User Workshop in July 2007 (see the breakout session on inelastic x-ray scattering at the following link: http://www.bnl.gov/nsls2/workshops/UserWorkshop_BOS2.asp) further identifies a few key scientific drivers for this beamline. They are grouped into several classes of experiments according to the required energy resolution:

- 0.1meV resolution experiments
  Examples include visco-elastic crossover behaviors of disordered systems and fluids, and new low-energy modes in complex fluids and confined systems that would require the 0.1meV resolution to be resolved. Another important area of research is in the collective dynamics of lipid membranes and other biological systems, where correlated molecular motions and density fluctuations on the meV energy scale play a significant role in determining their physical properties. The 0.1meV resolution would also be potentially useful for mapping the superconducting band gap with phonons.
- 1meV resolution experiments
  Examples include relaxation processes in disordered systems such as glasses, fluids, polymers, etc. The higher available flux promised by NSLS-II compared to existing instruments will be highly valuable for studying phonons in single crystals, surfaces, thin films, small samples down to micrometer sizes, systems under extreme pressure, phonons in excited states (pump probe), and exotic excitations in strongly correlated systems.

It is clearly recognized by the community that the 0.1meV endstation should be designed to bridge, at least partially, the dynamic gap between existing high- and low-frequency probes, which would enable new science to be done. The most exciting scientific problems requiring this energy resolution are envisaged to come from disordered systems in the forward scattering direction, where very high momentum resolution (<0.1 nm^{-1}) would also be required. For the 1meV resolution experiments, the higher available flux promised by NSLS-II should allow studies ranging from phonons in small single crystals, surfaces, thin films, to exotic excitations in strongly correlated materials, where the range of momentum transfer should cover typical Brillouin zone sizes. To take full advantage of the superior performance at ~10 keV of the NSLS-II source, the requirements and specifications for the beamline and endstations include:

- The primary beam energy is chosen at 9.1 keV near the peak of the tuning curve of a U19 undulator and also to match the proposed scheme for achieving the 0.1meV energy resolution. This energy should however be tunable over 7 ~ 12 keV to retain certain flexibility in case a different choice of refraction may be required.
- Due to the different experimental requirements for 0.1meV and 1meV resolution, there should be two endstations, one optimized for the 0.1meV, and the other for the 1meV experiments.
- The energy scan range should be on the order of 100 meV for the 0.1meV endstation, and up to about 1 eV for the 1meV endstation.
- Momentum resolution should be better than 0.1 nm^{-1} at low momentum transfer. This corresponds to an angular acceptance of less than 10 mrad for the analyzer at 9.1 keV.
- For the 1meV endstation, the momentum scan range should be up to 80 nm^{-1} in order to cover typical Brillouin zone sizes of small single crystals. This translates to a scattering angle of 120 deg at 9.1 keV.
- Beam spot size should be ≤ 5 μm (V) × 10 μm (H). This would enable studies of very small samples and samples under extreme pressure generated using diamond anvil cells.

1.3 Insertion Device

Inelastic x-ray scattering is a photon-hungry experiment. The figure-of merit for a radiation source for an IXS beamline is therefore the flux (photons per second per meV) that it delivers to the sample. The brightness or the ultimate beam spot size on the sample becomes secondary in this case, so long as it suffices to achieve the required energy resolution and be compatible with the required sample environments such as for extreme pressure. Of the devices considered in the baseline of NSLS-II, a 3m-long U19 undulator offers the best performance over 7 ~ 12 keV. Key parameters of the U19 undulator are summarized in Table 1.1.

Table 1.1. Basic parameters of a U19 undulator.

IVU specs	U19
Device type	CPMU / in vacuum
Peak field	1.14 T
Lowest 3rd harmonic energy for 3.0 GeV beam	4.4 keV
Highest harmonic to be used	7
Maximum K value – corresponding to the lowest third harmonic energy	2.03
Overall length of magnet array	3 m
Period	19 mm
Minimum magnet gap	5 mm

For further improvements that could lead to a significant increase of the incident flux, one of the options being considered is placing multiple undulators in a single long straight section. Possible choices include two 3m-long U19 or three 2m-long U14 undulators. A five-fold increase of flux is expected, for example, by using three 2m-long superconducting undulators (SCU) U14 instead of a single 3m U19 device (Figure 1.1). This assumes the ability to refocus the beam between such devices, which requires careful studies of the accelerator systems during the design phase. If the issue of refocusing can be resolved, it is obvious that the IXS beamline could make a perfect case for yet an even longer straight section for more devices.

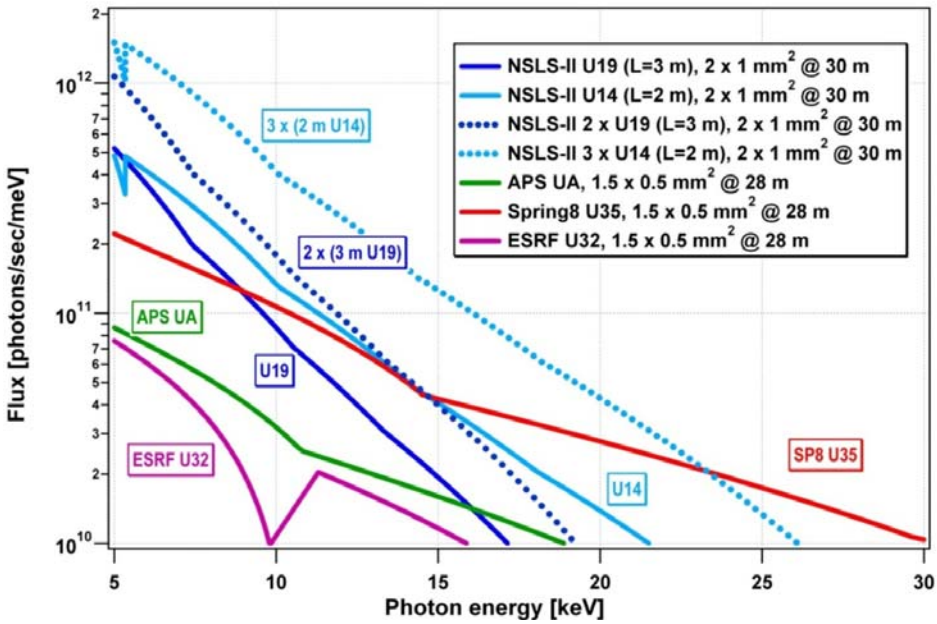

Figure 1.1. Flux comparison of various devices at NSLS-II and elsewhere, as measured in ph/s/meV. The light blue dotted curve shows the increase associated with placing three 2 m-long U14 undulators in a single straight at NSLS-II. The solid blue curve is for one 3 m-long U19 undulator.

Another option being considered is to optimize the undulator parameters to maximize the peak flux at the primary energy of the beamline. Figure 1.2 shows a comparison between a U17 and a U19 undulator of the same length. With a similar strength of the magnetic field, the U17 is expected to deliver a factor of 2 more flux at around 9 keV compared to the U19. Potentially, this type of optimization can be done for each individual beamline. There is therefore some cost implication for the additional design effort. However, the impact on the accelerator systems would be minimal.

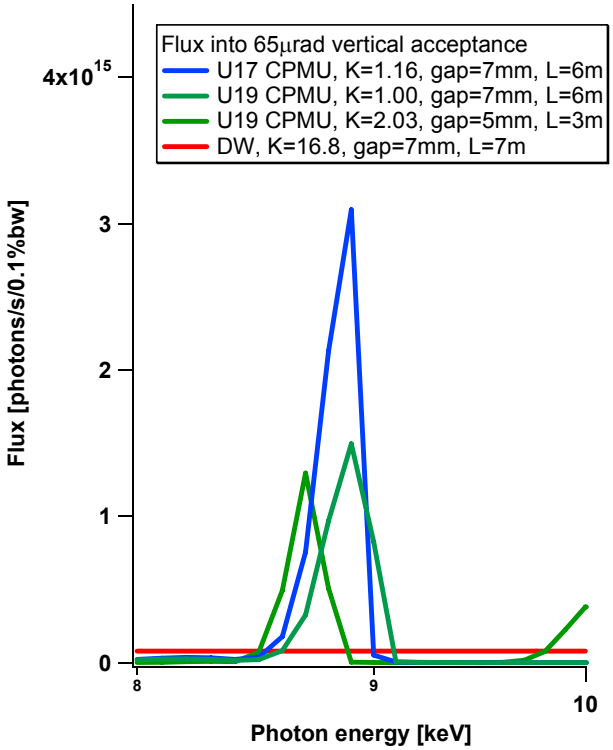

Figure 1.2. Flux comparison of various devices at NSLS-II. Here a U17 with a similar strength of magnetic field is expected to deliver a factor of 2 more flux than a U19 at ~9 keV.

In order to provide the possibility of accommodating two 3m U19 or three 2m U14 undulators, the longer 9.3m high-β straight section of the current storage ring design will be needed. Even for a single U19 undulator, there are other benefits associated with a high-β straight section for the beamline, due to the differences in the beam size and divergence between the low-β and the high-β straight section. As shown in Table 1.2, the horizontal beam size increases by about a factor of 3, whereas the angular divergence decreases by about a factor of 3.5, on moving from a low-β to a high-β straight section. This leads to a corresponding increase of horizontal source size and decrease of horizontal divergence by about a factor of 3 (Table 1.3). Consequently, the horizontal photon beam size reduces by more than a factor of 2 as a result of the reduced beam divergence as it travels downstream of the beamline. The heatload delivered onto the first optics within the central cone of the photon beam reduces also by a factor of 3 (Table 1.4). It should be noted that the flux within the central cone remains essentially the same between the low-β and the high-β straight section. Therefore, the use of a high-β straight section allows a smaller horizontal aperture with no cost to the flux. The heatload on the first optics is reduced to a manageable level, even for two U19 undulators. The smaller horizontal beam size also allows the use of shorter mirrors for the horizontal plane.

Note that a U20 is currently in the baseline device. Calculations show that there are minimal differences between the U19 and U20 in terms of their performance. The discussions in the subsequent sections will still assume the U19 device for convenience.

Table 1.2 Beam parameters assuming eight damping wigglers with 0.55nm-rad horizontal emittance.

Parameters		Low β	High β	Units	Ref.
Emittance	ε_x (horizontal) ε_y (vertical)	0.55 0.008		nm · rad	2,3
Beta function	β_x (horizontal) β_y (vertical)	1.5 0.8	18 3.1	m	3
Energy spread		0.0005 - 0.001		-	3
Beam size (sigma)	σ_x (horizontal) σ_y (vertical)	28.7 2.5	99.5 5.0	μm	Calc.
Angular divergence (sigma)	σ'_x (horizontal) σ'_y (vertical)	19.2 3.2	5.5 1.6	μrad	Calc.

Table 1.3 Source parameters of a U19 operating at several conditions in a low-β and a high-β straight section.

K	N	E, keV	Source size (σ), μm				Angular Divergence (σ), μrad			
			Low-β		High-β		Low-β		High-β	
			H	V	H	V	H	V	H	V
2.03	1	1.47	29.3	6.2	99.7	7.5	22.5	12.3	13.1	12
1.713	5	9.1	28.8	3.4	99.5	5.5	19.8	5.7	7.3	5.0
0.981	3	9.1	28.8	3.4	99.5	5.5	19.8	5.7	7.3	5.0

Table 1.4 Power from a U19 undulator in a low-β and high-β straight section delivered to the first optics at 30 m from the source through an angular aperture defined by 4σ (H) x 4σ (V) of the source divergence.

Distance, m	K (N)	Low-β			High-β		
		Ang. Aperture (HxV), μrad²	Beam Size, (HxV), mm²	Power, W	Ang. Aperture (HxV), μrad²	Beam Size, (HxV), mm²	Power, W
30	1.713 (5)	79.2 x 22.8	2.4 x 0.7	118	29.2 x 20.0	1.0 x 0.6	38
30	0.981 (3)			65			21

1.4 Sector Layout

The Inelastic X-ray Scattering beamline will occupy only the insertion device port of a sector with a long high-β straight section. Nevertheless, the required floor space to accommodate the 1meV endstation may be extended to the floor space of the adjacent beamline on the bending magnet port, which should be given due consideration regarding whether and how the bending magnet port will be used in future.

1.4.1 Front-End Layout

The current generic layout of the front-end for a long, high-β straight section is shown in Figure 1.3. As shown, this front-end layout is compatible with the current design of the IXS beamline. However, the design can be further optimized and coordinated with components planned for the first optical enclosure (FOE) of the beamline, which may provide some cost savings and allow for more efficient use of floor space in the experimental hall. For example, the space between the fast gate valve (FGV) and the second x-ray beam position monitor (XBPM-2) can be used to accommodate the X-Y slit that defines the x-ray beam for the first optical component of the beamline (i.e., the first crystal of the high heatload double crystal monochromator). Other components that should be included in the front-end include (removable) filters and screen monitors at a few locations, for diagnostics during commissioning.

A U19 undulator is expected to generate a total power of 11.2 kW and a peak power density of 77.86 $kW/mrad^2$. If two of this device are used, the total power and the power density will be doubled. The front-end must be designed to handle these power loads.

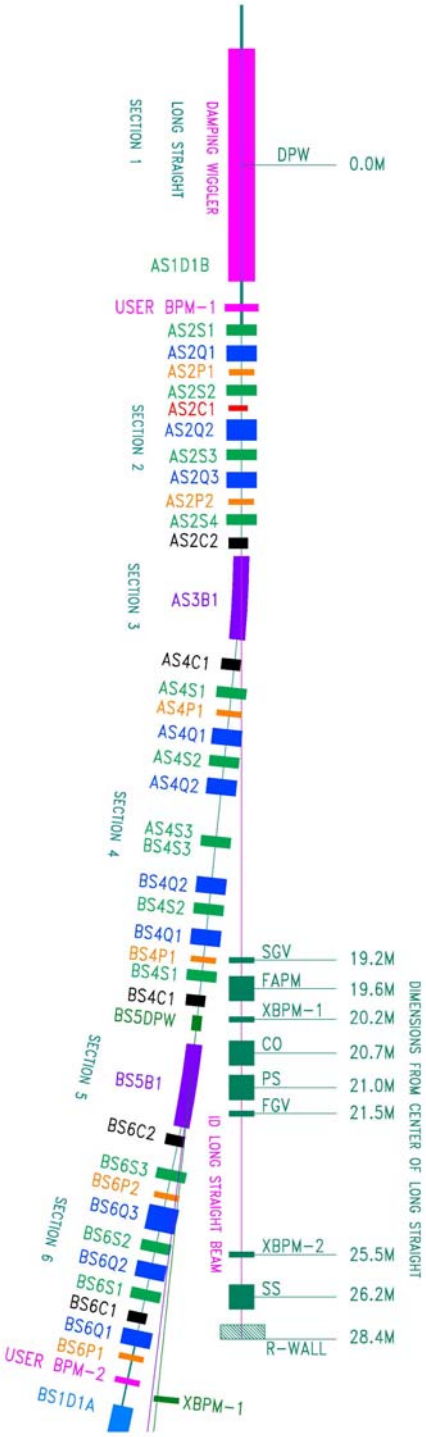

Figure 1.3 Generic layout of the front end for a long, high-β straight section. Components as shown include a slow gate valve (SGV), a fixed aperture mask (FAPM), two x-ray beam position monitors (XBPM), a lead collimator (CO), a photon shutter (PS), a fast gate valve (FGV), and a safety shutter (SS). Positions shown in meters are distance from the center of the straight section.

1.4.2 Beamline Layout

A CAD drawing of the beamline and endstations showing the general layout of the beamline is given in Figure 1.4. Functionally, there are four major optical components before each endstation. These include the high heatload double crystal monochromator (DCM), a vertical collimating/focusing mirror (VCM), a high-resolution monochromator (HRM), and a set of KB focusing mirrors. For the 0.1meV endstation, the HRM will be an inline monochromator based on the CDDW scheme [Ref]. For the 1meV endstation, the optical scheme depends on the approach we will use and will be described in more detail later. All these optical and other beamline components are housed in three enclosures. The first one (the first optical enclosure: FOE) is for the white beam components including the high heatload DCM, and the other two are for each of the two endstations. The VCM is placed in the FOE for convenience. The HRM for each endstation is considered as an integrated part of the endstation, and is therefore housed with the endstation in the same enclosure.

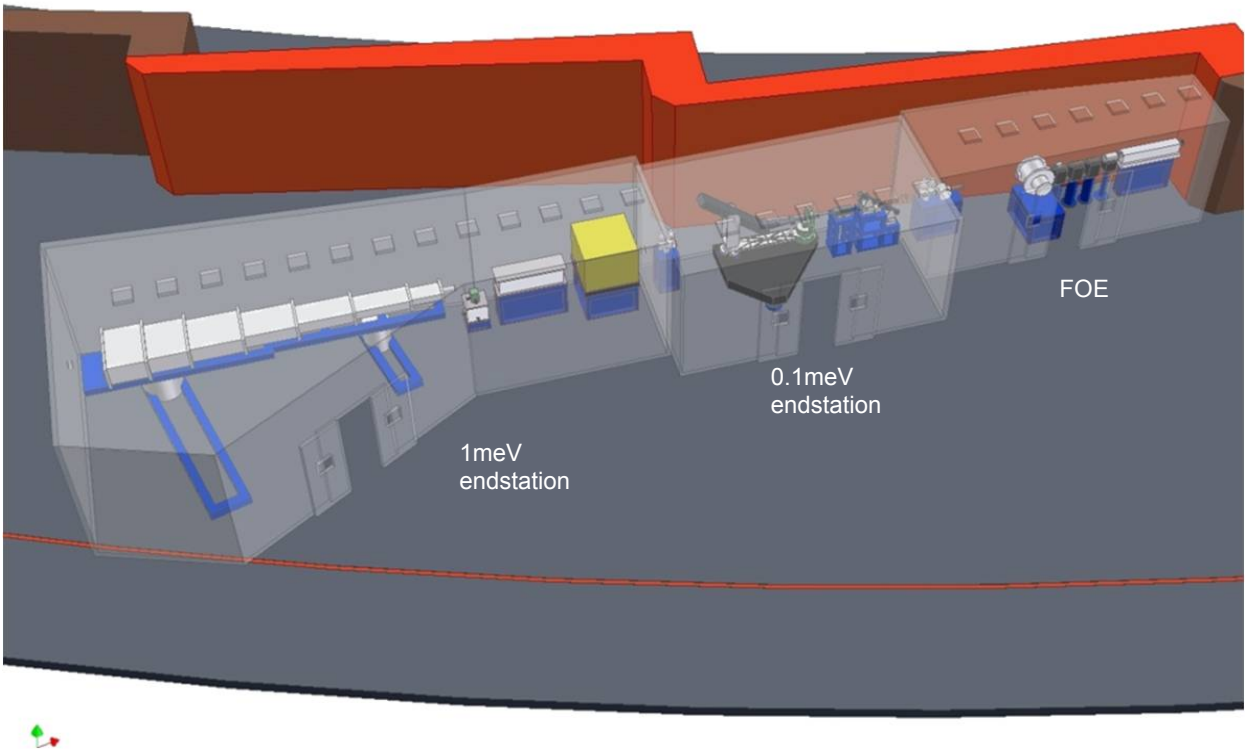

Figure 1.4. Schematic layout of the Inelastic X-ray Scattering (IXS) beamline, showing (right to left) the first optical enclosure (FOE), the 0.1meV endstation, and the 1meV endstation.

1.4.2.1 Survey and Alignment Plans

All beamline components will be surveyed and aligned in place by NSLS-II staff. To facilitate ease of alignment, all components will be fiducialized to external reference points on their table during assembly. All components are designed with a liberal tolerance allowance greater than 0.5 mm. Where necessary, laser trackers will be used which provide alignment precision to ~ 50 microns.

1.4.2.2 Utility Layouts

We will need power panels for single phase 100V and 200V rated to 100Amp each, and 3 phase 200V to 300Amp, distributed to the hutches and control areas. For each hutch, there should be de-ionized and chilled

water, compressed air, N2 and He gas distribution system. For the FOE LN2 outlet is required for the cryogenic cooling system of the DCM. The two experimental hutches will require temperature control to ±0.1 K.)

1.4.2.4 Beamline Vacuum System

The beamline vacuum will be separated from the front-end by a Be window. All beamline components will be designed to ultrahigh vacuum (UHV) standards. The beamline will be operated in most part in high vacuum level. Turbo pumps backed up by oil-free roughing pumps will be used for the pumping stations. High vacuum will be maintained by ion pumps where necessary (for concerns of vibration, for example). A rough vacuum pumping system is planned for each of the endstations for use in pumping sample chambers, flight paths, etc.

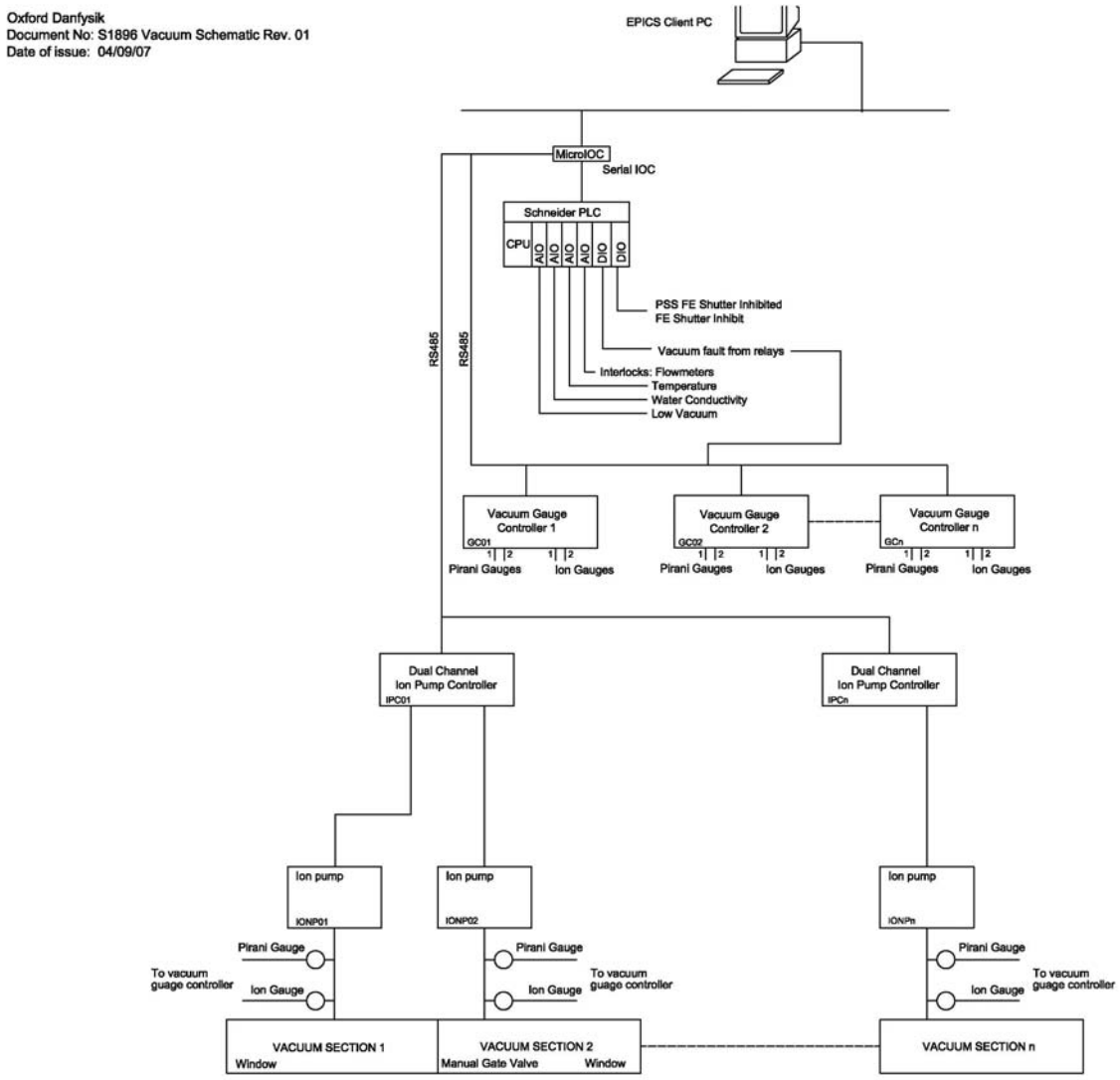

Figure 1.5. Vacuum schematic for the inelastic x-ray scattering beamline.

Figure 1.5 provides a schematic of the vacuum system for the IXS beamline. Vacuum gauge controllers are used to monitoring vacuum level measured by Pirani and ion gauges mounted on different beamline components.

Ion pump controllers provide power to each of the ion pumps used on the beamline. High-voltage splitter units are used, where necessary, to power more than one pump per output channel.

1.4.2.5 Data Acquisition System and Motion Control

The contents of the signal schematics are shown in Table 1.5. The 8-axis motion control boxes having RS232, USB, and Ethernet interfaces are customized to suit the beamline motorized axis. They also have built-in micro IOCs. Separate micro IOCs control the vacuum pump controllers, vacuum gauge controllers, DPT controllers, current amplifiers, and CCD cameras.

The EPS PLC has analog input and digital input and output, and is linked to solenoid valve actuators, fluorescent screen actuators limits, thermocouples, water flow meters, vacuum interlocks, vacuum gauge controllers, cooling water flow meters in the heat exchangers, thermocouples in the heat exchangers, and water conductivity probes.

The PSS shutter is controlled from the PSS and sends and receives status signals to and from the EPS PLC.

The micro IOC controlling the vacuum system uses RS485 protocol for communication with the pump and gauge controllers. Vacuum gauge controllers are integrated with the EPS system to monitor vacuum level in different sections of the beamline.

Piezo actuators and a bimorph mirror will need vacuum interlocks linked to the vacuum gauge controllers. The cryocooler is connected via Ethernet to a dedicated IOC, which is linked to the PSS. The Y-Z profile monitor is connected to a 32-channel electrometer.

Table 1.5. Controls schematics for the IXS beamline.

Beamline Component	No. of units	Number of Elements per Unit											
		Controlled by 8 axis Motion Control units					Controlled by EPS PLC			Controlled by micro IOC			PC
		Stepper/ Pico Motor	Server Motor	Limit/ datum switch	Encoder	Ref point	Flow meter	Thermo-couple	Solenoid valve actuator.	CCD camera	DP control unit	Current amplifier	
Beamline control system	1												1
Fixed mask	1						1	1					
Blade BPM	1	2		4			1					1	
CVD Diamond	1						1	1					
Bremsstrahlung collimator	1						1	1					
White Beam Slit (H **or** V)	2	1		2	1								
Gate Valve	16			2					1				
VFM/VCM	2	5		10	5	5					1		
HFM (bimorph)	1	5		10	5	5							
Bimorph PSU	1												
Beam shutter	3			4				1	1				
Fluorescent screen (water cooled)	1			2			1		1	1			
Fluorescent screen	5			2					1				
DCM	1	5	1	8	7	6	1	3			1		
Cryocooler	1												1
White beam / bremsstrahlung stop	1						1	1					
QBPM	5	1		2								1	
Y-Z profile monitor	1								1				
Monochromatic slits	10	2		4	2	2							

1.4.3 Beamline Components

Table 1.C.1 (see Appendix C) lists the position and size of different beamline components of the current design. Space between the main components will be filled with vacuum bellows and pipes of suitable length. The table also lists different sections of the beamline vacuum system. Positions of the beamline components are specified with respect to the center of the low-β straight section, which was used in the initial stage of the design study. It assumes the distance from the source to the external surface of the shield wall to be at 26.7m, and the distance to the end of the beamline at 66.8m.

The decision to use a high-β straight section will change the shield wall position to 28.6m, and therefore all components listed in Table 1.C.1 will need to be shifted downstream by 1.9m.

Important dimensional constraints for the high-β straight section are as follows:

- Distance from the source to the external surface of the shield wall: 28.6 m
- Maximum source to end of the beamline distance: 60.8 m

Several important considerations have been taken into account in the suggested layout of the main beamline components, which include:

- Share as many common endstation components as possible, to reduce the total cost of the project and complexity of the design.
- Reduce to a minimum the number of optical elements (crystals, mirrors, windows, etc.) put into the beam, to maximize the flux.
- Use most of the available fan of the x-ray beam, to keep the lengths of the optical elements within reasonable limits.
- Create an infrastructure and basis for further R&D that will follow the preliminary design.
- Provide enough flexibility for further beamline design based on the outcome of anticipated extensive R&D.
- For costs to be estimated realistically, include in the early design not just the main components, but all components that are not likely to be affected by further design changes.
- Fit the beamline components into the available floor space and identify any changes to the position of the walls needed to accommodate the equipment.

1.4.3.1 White Beam Slits

The white beam slits, currently planned as part of the FOE components, define the X-ray beam from the undulator source to the first optics of the beamline. If the X-Y slits are to be implemented in the front-end, this white beam slits may no longer be required.

Figure 1.6 shows the position of the white beam slits upstream of the high heatload monochromator. The slits consist of 2 L-shaped absorbers arranged in series along the beam (the downstream one being rotated by 180°) to define the aperture. Each absorber therefore defines two edges of the beam. Each absorber is moved laterally and vertically by external translation stages. There are edge-welded bellows before, between and after the two absorbers, which allow the movement of the slits relative to the beam. The slit mechanism is mounted on a synthetic granite-filled mild steel frame for stability and vibration rejection.

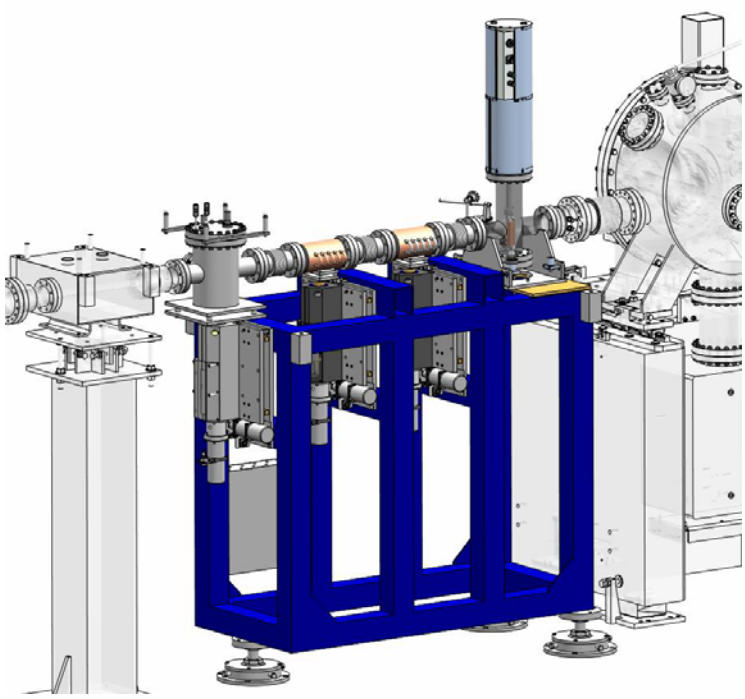

Figure 1.6. White beam slits assembly.

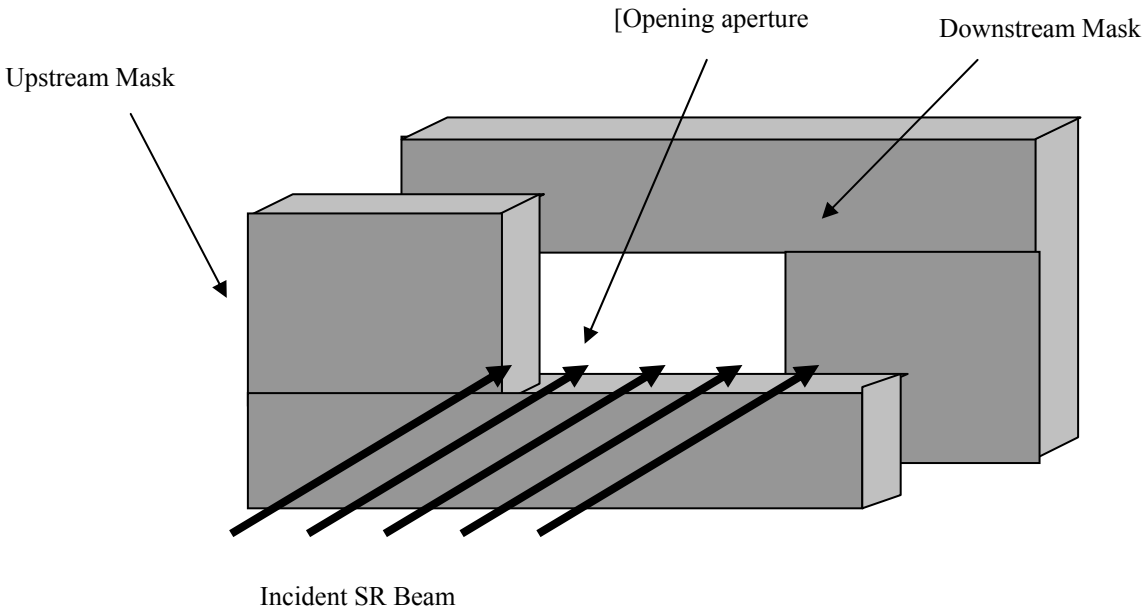

Figure 1.7. White beam slits schematic.

1.4.3.2 Bremsstrahlung Collimator and Beam Stops

The Bremsstrahlung collimators are typically made of 300 mm of lead and their dimensions are calculated from the ray tracing. We will use one of the collimators immediately after the CVD Diamond window/filter.

The Bremsstrahlung collimator is located immediately downstream the fixed mask defining the beam.

A Bremsstrahlung stop is also anticipated after the DCM. Depending on the detailed design it will be made of lead (out of vacuum) or Tungsten (in vacuum).

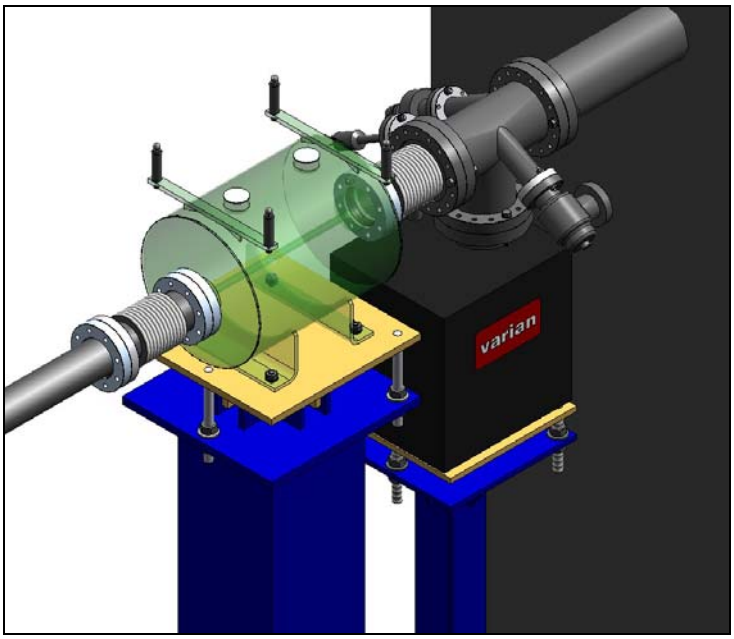

Figure 1.8. Pb collimating assembly.

1.4.3.3 High-Heatload Monochromator

A cryo-cooled Si(111) DCM with no sagittal focusing on the second crystal should provide energy resolution of ~10^{-4}, fixed exit beam height and operate across the requested energy range from 7 keV to 12 keV. Expected performance parameters of the DCM and some useful information are given in Table 1.6. We also assume 25 mm vertical offset between the incoming and outgoing beams and that beam 'walk' alone the second crystal as the energy changes will be taken by longitudinal translation of the crystal.

The results in show that

- The energy resolution is expected to be from $1.77 \cdot 10^{-4}$ to $2.45 \cdot 10^{-4}$.
- The Bragg angles are from 9.5° to 16.4°. The Bragg angle calculation assumes the lattice constant of Si(111) of 5.4309 Å.
- Perpendicular translation of the 2nd crystal over the energy range is about 0.3 mm.
- Longitudinal translation of the 2nd crystal over the energy range is approximately 32 mm.

- The footprint of the beam at the crystals of the Si(111) monochromator at all energies is less than 3.0 mm x 5.5 mm assuming 4σ (H) x 6σ (V) opening of the beam. Vertical size of the beam at the DCM position is about 1.0 mm.
- The lengths of monochromator crystals should be less than 177 mm to avoid shadowing.

The design of the DCM should meet stability requirements and be able to withstand high heat loads as discussed earlier.

It might be possible to use a water cooled DCM but more R&D is needed to prove this is a feasible. We therefore have provided a typical specification for a water cooled monochromator. The BNL water cooled system will most likely use much smaller vertical beam offset, of about 25 mm, than in the example and long second crystal to eliminate longitudinal translation and improve stability. The second crystal will be translated vertically to keep fixed offset of the beam.

The power density could however be very high, particularly when two U19 undulators will be used simultaneously in-line and at the same undulator gap as we have discussed earlier. We therefore believe that most likely a cryogenically cooled system will be needed. We therefore provide an appropriate functional specification for such a system which is being built for ASP SAXS beamline. The DCM is designed to operate at energies of 5-20 keV, has a fixed offset of 25 mm and uses a set of Si(111) crystals. The DCM is designed to achieve angular beam stability of 200 μrad that should be adequate for the current application. As the technology continuously improves using a cryogenically cooled monochromator instead of water cooled one does not create any unnecessary risk for the project.

Modifications to the standard design that should be considered include reducing the beam offset and using long high quality second crystal instead of longitudinal translation to improve stability.

Table 1.6. Performance parameters of the Si(111) DCM.

Parameters	Energy, keV		
	7	**9.1**	12
Wavelength, Å	1.7712	1.3625	1.0332
Bragg angle θ_B, deg	16.4058	12.5482	9.483
Reflectivity (double reflection)	0.85	0.91	0.94
Energy resolution			
Rocking (Darwin) width[1], μrad	39.1586	29.6027	22.2161
Bandpass due to source size	9.2×10^{-7}	1.2×10^{-6}	1.6×10^{-6}
Bandpass due to accepted angular divergence	1.2×10^{-4}	1.5×10^{-4}	2.1×10^{-4}
Resolution of the DCM	1.77×10^{-4}	2.04×10^{-4}	2.45×10^{-4}
Resolving power[2]	5649	4904	4079
Crystal size and position			
Vertical offset between incoming and outgoing beams, *D*, mm		25	
Perpendicular offset between 1st and 2nd crystals[3], mm	13.0	12.8	12.7
Longitudinal offset between the crystals[4], mm	44.3	57.5	75.9
Maximum beam footprint[5]			
transverse to the beam, mm	3.0		
along the beam, mm			6.2
Maximum length of crystals at no beam shadowing[6], mm	177		

Notes: 1) Intrinsic resolution of Si(111) is $\left(\frac{\delta\lambda}{\lambda}\right)_{cryst.}$ = 1.33 · 10^{-4} [30]. The rocking (Darwin) width is $\Omega = \frac{\delta\lambda}{\lambda}\tan\theta_B$.

2) The resolution is determined by the width of the rocking curve of the crystal, beam opening angle and size of the source

$$\frac{\Delta E}{E} = \sqrt{(\Delta\theta^2_{source} + \Delta\theta^2_{slit})\cot^2\theta_B + \left(\frac{\delta\lambda}{\lambda}\right)^2_{cryst.}},$$

$$\Delta\theta_{source} = \sigma_y / p \text{ and } \Delta\theta_{slit} = \min(\sigma_y^{'}, s_v)/p,$$

where σ_y is the vertical source size (FWHM), $\sigma_y^{'}$ is the vertical divergence of the beam (6 σ), s_v is the opening of the monochromator vertical entrance slit and *p* is a distance from the source.

Resolving power of the monochromator is reverse to the total band pass, i.e. it is $\frac{E}{\Delta E}$.

3) The distance, X, measured perpendicular to the optical surfaces of the crystals: $X = \frac{D}{2\sin\theta_B}$, where D is the constant vertical offset between incoming and outgoing beams.

4) The distance, Y, measured along the surface of the crystals: $Y = \frac{D}{2\cos\theta}$, where D is the constant vertical offset between incoming and outgoing beams. The longitudinal offset shows beam walk parallel to the surface of the crystals as the Bragg angle changes. To maintain the constant beam offset, D, the X and Y should satisfy the condition $\frac{1}{X^2} + \frac{1}{Y^2} = \frac{4}{D^2}$.

5) The beam footprint depends on the rms size and divergence of the incoming beam, DCM distance from the source and the Bragg angle so that

$$F = \sqrt{\sigma^2_{x,y} + (\sigma^{'}_{x,y}\cdot p)^2};\ F_x = F;\ F_y = F/\sin\theta,$$

where $\sigma_{x,y}$ and $\sigma^{'}_{x,y}$ are the size and divergence of the source, correspondingly, p is the distance from the source and θ is the Bragg angle.

6) To avoid shadowing of the beam at high Bragg angles, the lengths of the crystals should match the vertical beam offset.

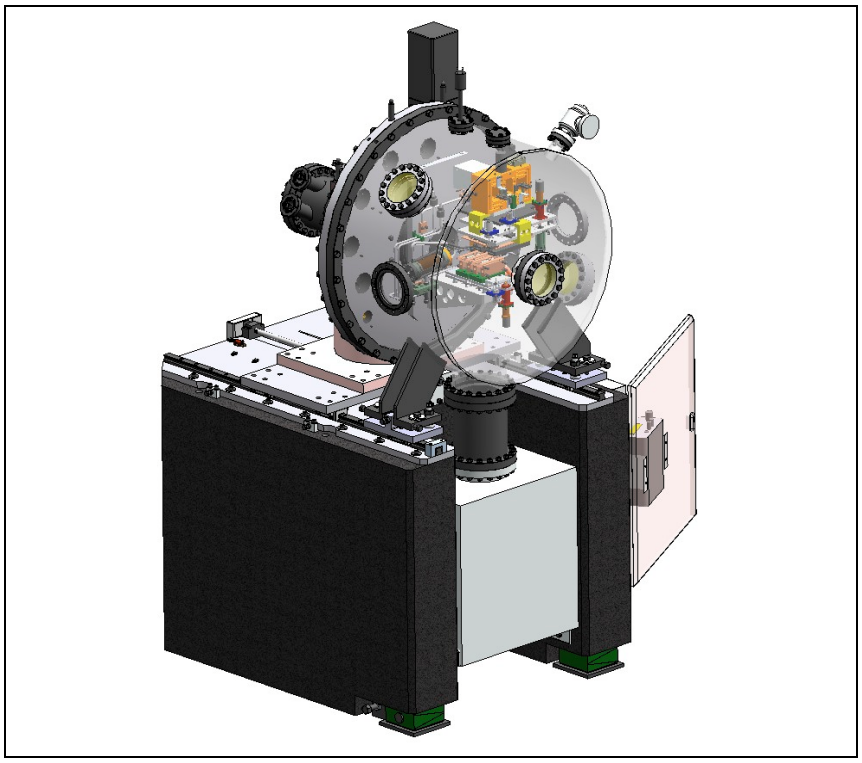

Figure 1.9. Isometric view of the Si(111) DCM.

1.4.3.4 White Beam Shutter

Special requirement for the beam shutters and their integration with the Personnel Protection System will be discussed with the vendor before the detailed design starts.

1.4.3.5 Collimating and Focusing Mirrors

As it has been discussed earlier, the beam line is expected to have few mirrors for collimating and focusing the beam in horizontal and vertical planes. Preliminary analysis shows that full energy range of 7 -12 keV can be covered without changing the angle of incidence while providing good transmission of the x-ray beam over the whole range.

Increase of the angle of incidence is favorable for reducing the cut-off energy, lengths of the mirrors and improving harmonic rejection, but the reflectivity of the mirrors decreases. We have considered using bare Si, Silica (SiO_2, less expensive option and good alternative to Si for using with monochromatic beams) and Pt, Pd and Rh coatings and concluded that Rh and bare Si or Silica are most suitable for the energy range. Pd is very similar to Rh but the latter has slightly better reflectivity. Reflectivity of Pt shows few absorption edges and it is more suitable for higher energies.

Most mirror suppliers will guarantee densities of Rh in the coatings to be better than 90% of the bulk material which is 12.41 g/cm^3 [28]. We therefore assume in this analysis the density of Rh of 11.17 g/cm^3 for calculating reflectivity of the mirror stripes. The densities are usually lower, about 85% of the bulk, for bimorph mirrors. The lower density means slightly lower reflectivity and lower cut-off energies at similar angles of incidence. The data in Figure 1.10 show that replacing Silica with Silicon as a mirror substrate increases the cut-off energy by approximately 300 eV. As the density of Rhodium decreases from 90% to 85%, the cut-off energy decreases by about 550 eV.

The density of Si, 2.33 g/cm^3 [28], is slightly higher than the density of Silica, 2.2 g/cm^3 [29]. Usually Silica is used as a substrate for making mirrors to focus monochromatic beam and silicon is used to make mirrors operating in a white beam.

Figure 1.10 shows variation of the critical angle of the mirrors versus energy for Si, Silica, Rh (and Pt). The critical angles were calculated as $\alpha_c = \sqrt{2\delta}$, where δ is a real part of the refractive index of material. Incidence angle of the mirrors should ensure that the low energy beam is not contaminated by the beam of higher energy. Also it is not desirable to make mirrors much longer than 1 m. But the reflectivity of the mirrors decreases as the angle of incidence increases. Therefore the incidence angle should be optimized taking into account these factors and ease of use.

Useful energy range is defined from 7 keV to 12 keV [2] and from the point of view of ease of use changing the mirror stripe in this region should be avoided. In that case the mirrors could be set at an incidence angle of approximately 4.5 mrad to achieve about 87-89.5% reflectivity using Rh stripe. Higher reflectivity can be obtained using Si or Silica stripe. Reflectivity of Silica, for example, at 3 mrad incidence at 7 – 9.5 keV is about 95 - 96.5%. But to cover the whole energy range of 7 – 12 keV the incidence angle should be much smaller, 2.5 mrad.

We therefore suggest operating in one of the three regimes:

- Use Rh stripe and incidence angle of 4.5 mrad.
- Use Rh stripe and incidence angle of 4.5 mrad at energies from 9.5 to 12 keV and Silica stripe and incidence angle of 3.0 mrad at energies from 7 to 9.5 keV.
- Use Use Rh stripe and incidence angle of 4.5 mrad for HCM and HFM and Silica stripe and incidence angle of 3.0 mrad for VCM and VFM.

The last option is probably a good compromise between reflectivity and ease of use. Figure 1.11 shows calculated reflectivity of bare Silica and Rh stripes.

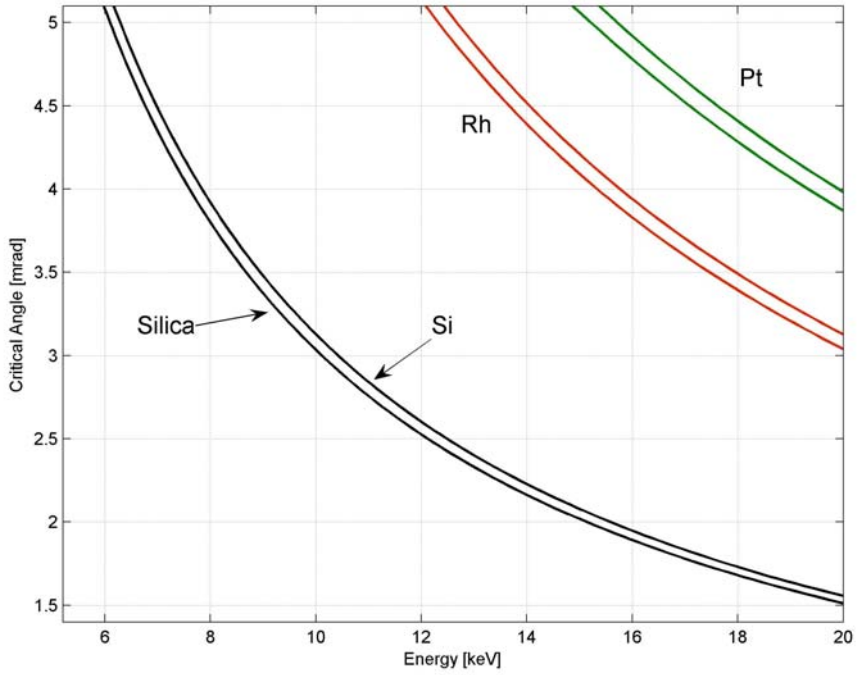

Figure 1.10 Variation of the critical thickness versus energy for bare Silica, Silicon, Rhodium and Platinum. The double lines for Rh and Pt correspond to different densities of the materials: 85% density of the bulk for the lower line and 90% for the upper line.

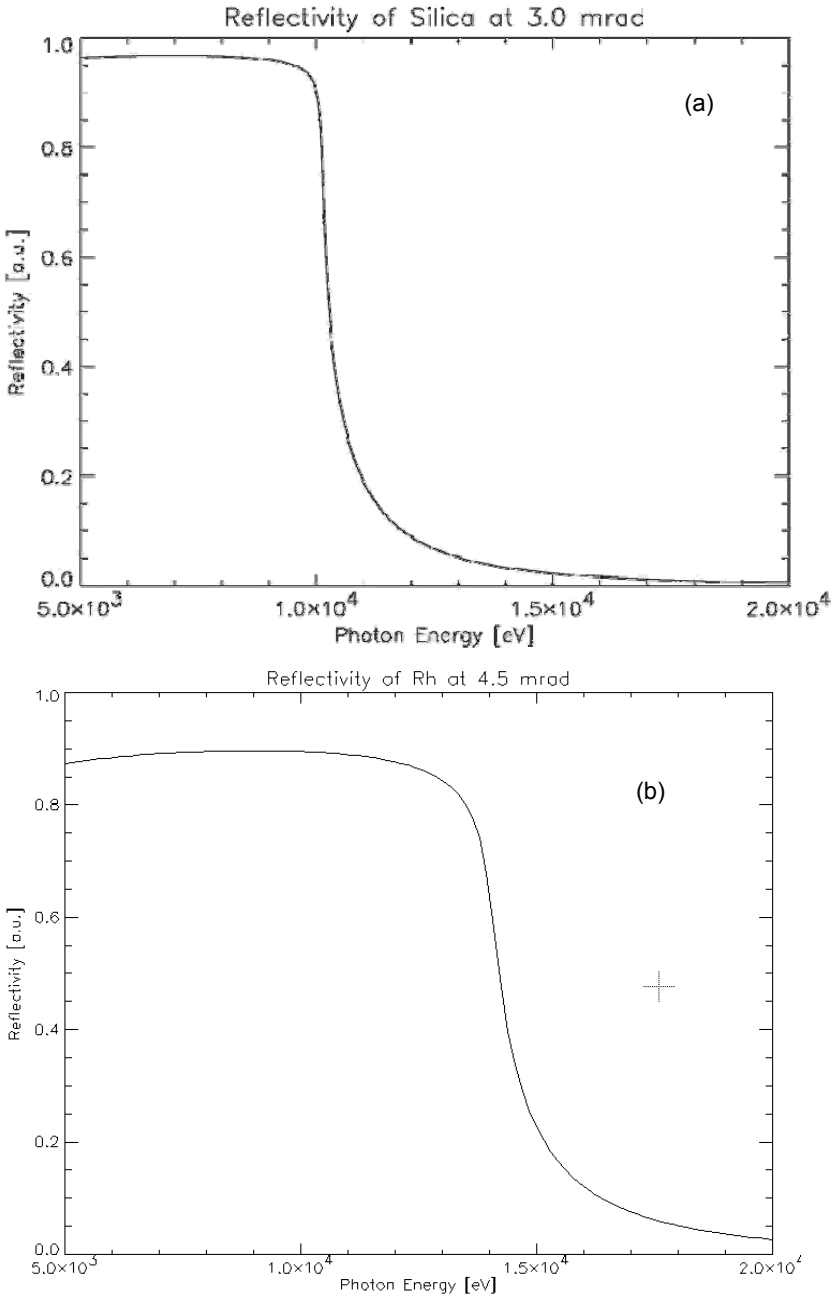

Figure 1.11 Reflectivity of Silica at 3.0 mrad (a) and Rhodium at 4.5 mrad (b)

We assume the HFM and VFM will be bent to a cylindrical shape. The lengths of the mirrors can then be calculated using the expressions given by Peatman [19]:

$$L = P\sin\left(\frac{\alpha}{2}\right)\left(\frac{1}{\sin(\theta_i + \frac{\alpha}{2})} + \frac{1}{\sin(\theta_i - \frac{\alpha}{2})}\right)$$

$$L \approx \frac{2P\sin\left(\frac{\alpha}{2}\right)}{\sin\theta_i}$$

where L is the length of the footprint of the beam on a mirror, P is a source-to-mirror distance, α is the vertical divergence of the beam and θ_i is the grazing angle of incidence of the mirror.

Estimated radii of the mirrors and some other useful characteristics are shown in Table 1.7 for the worse case in terms of beam angular divergence which is at low beta straight and ε_x =0.9 nm-rad. The VCM should have angular acceptance of 10 mrad (H) x 5 mrad (V). We have therefore increased the incidence angle to 5 mrad for that mirror to reduce its length. The cut-off energy of Rhodium at this angle will be 12.6 keV and reflectivity up to 88%. The length of the mirror depends on the amount of space required for the sample area. More accurate values of the parameters will be given after completing ray tracing analysis.

The lengths of the mirrors, particularly of the HCM and HFM ones, will decrease dramatically if the source parameters change. At ε_x =0.55 nm-rad in low beta straight the length will be 670 mm and in a high beta straight it will further decrease to 288 mm at ε_x =0.9 nm-rad and to 247 mm at ε_x =0.55 nm-rad.

Table 1.7 Parameters of the mirrors. Incident beam has angular divergence of 100 μrad (H) x 22.8 μrad (V). The *p* and *q* are source-to-mirror and mirror-to-image distances.

Mirror	Optical distance from source, m	Inci-dence angle, mrad	Coating	Beam Footprint, mm		Bent radius, m	*P*, m	*Q*, m
				Horizontal	Vertical			
VCM	31.88	2.5	Silica	3.2	291	25220	31.88	∞
VFM	39.15	2.5	Silica	3.8	291	336	- ∞	0.42
VCM[1]	40.33	5	Rh	7.6	1014	338	0.76	∞
VFM	74.46	2.5	Silica	3.8	291	516	- ∞	0.645
HFM	38.05	4.5	Rh	846	0.9	650	38.05	1.52
HCM	38.05	4.5	Rh	846	0.9	16911	38.05	∞
HFM	73.36	4.5	Rh	846	0.9	776	- ∞	1.745

Notes: 1) Footprint of the beam at VCM corresponds to angular acceptance of 10 mrad (H) and 5 mrad (V). To increase angular acceptance the VCM has Rh coating and higher angle of incidence.

The KB mirror system will include a bimorph horizontally focusing mirror and a conventional vertically focusing mirror equipped with a cylindrical bender. The bimorph mirror allows changing focus between the sample positions at the first and second endstations and reduces slope errors.

One vertically collimating (VCM) and one vertically focusing mirror will be used in monochromatic beam only. The VCM mirror systems will have capability of removing the optics from the beam delivered to the second, low-resolution, endstation using a backscattering monochromator.

The quality of the optical surface that can be achieved is being continuously improved by mirror manufacturers. We expect this trend will make it possible to purchase much better mirrors in few years time compared to those currently available on the market.

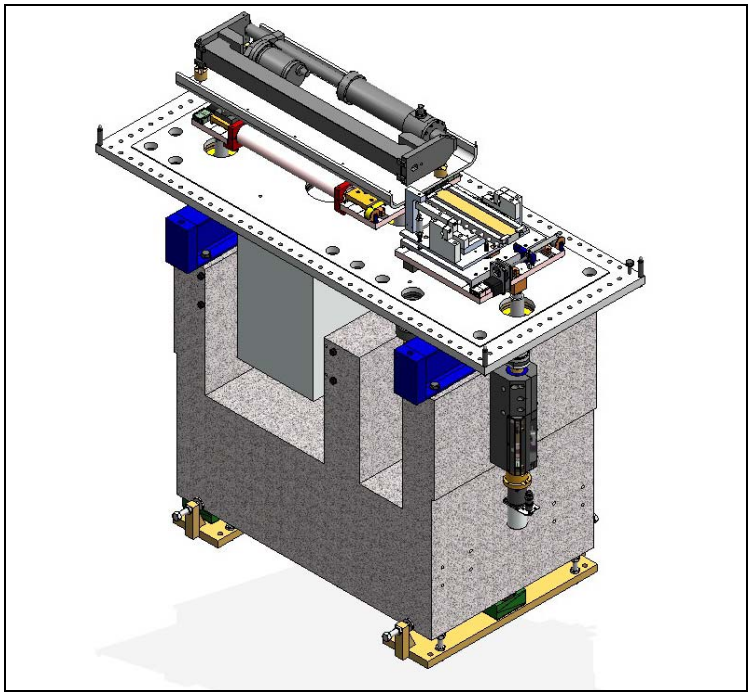

Figure 1.10. KB mirror assembly.

1.4.3.6 Monochromatic Shutter

Special requirement for the beam shutters and their integration with the Personnel Protection System will be discussed with the vendor before the detailed design starts.

1.4.3.7 Vacuum windows

Table 1.6 SiN 200nm window.

Supplier	SPI supplies
Outside frame dimensions	7.5mm x 7.5mm
Window size	1.5 mm x 1.5 mm
Membrane thickness	200 nm
Frame thickness	200 µm
Quantity	Pack of 50

1.4.4 Instruments

1.4.4.1 Endstation 1

End station 1 will have energy resolution of 0.1 meV at 9.1 keV [1]. The resolution will be achieved using novel design of high-resolution monochromator and analyzer optics exploiting an effect of angular dispersion in asymmetric Bragg diffraction predicted by dynamic theory of x-ray diffraction.

Design of the monochromator and analyzer is still subject to a debate. Significant design work and testing is required before the final working configuration becomes available. As it stays now a monochromator using this scheme consists of few Silicon crystals: a collimator, one or two dispersing elements and a wavelength selector. An inline configuration of the monochromator is preferable and the collimator and the wavelength selector could be just different sides of the same crystal, see Figure 11.5.4 in section 11.5.2.3.2 of reference [1]. To achieve a 0.1 meV energy band pass a very large asymmetry angle, of about 89.5^{o}, is required for the dispersing crystals.

The monochromator and the analyser will have an angular acceptance of 0.2-0.3 mrad in the horizontal scattering plane and 0.1 mrad in the vertical plane.

The spot size on the sample should not exceed 20-30 μm (H) x 10 μm (V). This requires a (micro) focused beam on the sample that can be achieved using a standard focusing system. The mirror to sample distance is likely to be of about 100 mm. The minimum distance is to provide some space for the sample environment.
An angular dispersive analyser similar to the monochromator will reflect the beam back to the detector. The backscattering analyser is chosen to reduce the total length of the beam line. An acceptance angle of Y^2 with Y~ 5 to 10 mrad is required. Therefore some collimating optics is needed in front of the analyser. As the asymmetry angle is large an angular acceptance of 2 to 3 mrad in the vertical plane translates into about 2 m long dispersive element length [1].

There will be a Kirkpatrick-Baez (KB) mirror system [2] with graded multilayer mirrors. This is preferred to a parabolic, or curved graded multilayer mirrors or tapered glass capillaries discussed in section 11.5.2.3 of reference [1]. The mirrors will be put after the sample but before the analyser. X-rays leaving the mirror system should match the angular acceptance of the analyser given above. Also the vertical beam size should not exceed 0.5 to 1.0 mm to restrict the length of the analyser crystals.

The spectrometer will be utilising 9.1 keV x-rays and providing an energy resolution of 0.1 meV and a momentum transfer resolution of about 0.1 – 0.4 nm^{-1}.
The energy of the photons selected by the spectrometer will be tuned by varying the temperature of the crystals. Temperature of individual segments of the segmented analyser (consisting of 8 to 10 segments 20-25 cm long) should be homogeneous to 0.5 mK corresponding to 0.01 meV energy shift [1].

1.4.4.2 Endstation 2

The vendor has considered several options for separating the beam used by the endstations. As there is significant uncertainty in the specification of the low-resolution endstation, they started by summarizing designs of the existing beamlines built at ESRF (ID28, ID16) [10,11], SPring-8 (BL35XU, BL11XU) [12-14], and ASP (3 IDC-C, IXS-CDT) [15,16] facilities. In every case there are some collimating optics in front of a high-resolution monochromator (HRM), particularly in a vertical plane. A logical conclusion is that, irrespective of the chosen monochromating scheme based on one of the known configurations of achieving high (meV) energy resolution [17-20], there will be some need for collimating the beam passing after the high

heat load monochromator and before a HRM. Therefore, we can try to use most of the optics from Endstation I at the Endstation II. That should be cost effective and allow saving some space at the second endstation.

It would be ideal to separate the beam going to Endstation II after the DCM, VCM, and HRM of Endstation I. It is unlikely, however, that the HFM can also be used as a HCM for the second endstation, as it needs to be curved to a certain radius during manufacturing. Hence the options are:

1. Design a HRM that will be flexible enough for using at both endstations. This is a risky approach, as it is unclear at present how the monochromator for Endstation II should look and if it is feasible to combine both monochromators into a single unit. To be on a safe side and keep all options open, we should assume that a completely different HRM will be designed for Endstation II. We can safely assume, however, that the HRM at Endstation I could be made capable of passing the beam straight through.
2. The HFM vessel could be used to accommodate a second mirror, the HCM, for collimating the beam at Endstation II. This option looks attractive, but some information on the design of the prospective sample area at Endstation II is needed to ensure there are no serious restrictions for pursuing this approach. It will be necessary to make specially designed gate valves with built-in windows to separate vacuum sections of the beamline so the beam is not attenuated by numerous vacuum windows before reaching the second endstation.
3. Insert a HCM for Endstation II after the high-heatload monochromator. An advantage is that a shorter HCM is needed, but it is difficult to find extra ~1.5 m space within the constraints on the position of the hatch walls. If the HCM is used for Endstation I, the HFM should have a similar length. The disadvantage of using an intermediate mirror is that about 10% of flux will be lost due to reflectivity and slope errors.
4. One option is to offset the beam horizontally using two silicon crystals, but this possibility was eliminated because of spare restrictions.
5. Offset the beam vertically using an additional vertical mirror.
6. Replace a CVD diamond window/filter with a Laue monochromator to create large angular offset between the beam paths to the endstations.

Whichever option, 2, 3 or 5, is selected, provision should be made to allow the second beam to reach Endstation II. The further upstream the mirror is, the more difficult it is to separate the beams. It might be necessary to provide translations or larger apertures to different components until the beams become sufficiently well separated. The vendor suggests implementing option 2 by putting two mirrors facing each other into a single vessel. In that case, the beam path to the second endstation becomes separated by distance x incidence angle x 4 horizontally at the HFM position and by distance x incidence angle x 2 vertically at the VFM position.

To provide enough flexibility for future developments the beamline components should be suitable for operating at energies of 7 – 12 keV. For this energy range, the most suitable mirror coating is probably Rhodium and an optimum incidence angle for the mirrors is 4.5 mrad. At low energies silicon is preferable, but a smaller (about 2.5 mrad) incidence angle is required to cover the entire energy range, and at 2.5 mrad the mirrors become too long; a good compromise is to operate at 3.0 – 3.1 mrad incidence. We would recommend using a bare silicon stripe at energies below approximately 9.0 – 9.5 keV to get about 5% higher reflectivity. As an option, the silicon stripe can be used for shorter, VCM and VFM mirrors. The diagonal offset of the beam at 4.5 mrad (assuming a Rh-coated mirror) will be approximately 20 mm per 1 m distance.

We do not know yet which configuration will be chosen for Endstation II. The options being considered include new asymmetric optics similar to Endstation I or a conventional single-bounce backscattering monochromator and a backscattering analyzer utilizing sapphire or quartz. The disadvantage of the former (or the one suggested by Baron [19]) is due to flux losses at crystals used simultaneously in Bragg reflection and transmission. The latter option appears to offer more diversity for the beamline, and there is a good chance that sufficient progress will be made over the next few years in growing high quality crystals of quartz and/or

sapphire. It sounds reasonable to use scattering in the horizontal plane as suggested in reference [1]. A proposed layout for Endstation II is listed in Table 1.C.1, but it must be noted that the layout may be subject to a major revision if the endstation is to be built on different principles.

Therefore the design of Endstation II may be similar to the recently built beamline BL35XU [13]. The points for consideration and approval include the following:

- Possible use of a pair of Si(111) crystals to shift the backscattered beam vertically by a convenient amount to separate the scattered and incident beams which are otherwise nearly parallel due to backscattering at an angle close to 90^o
- Possible need for vertical scattering analyzer
- More floor space is desirable

1.5 Additional Requirements Imposed on the Conventional Facilities

Temperature Stability

Stability requirements are determined by temperature stability and vibration (natural and self-inflicting), and were extensively discussed at the recent NSLS-II Stability Workshop in April 2007.

The beam stability requirements for different components are based on achieving less than 10% variation of the beam size. According to Shvyd'ko [22], 0.1 meV energy resolution requires <1K temperature stability inside the station. To keep broadening of the reflected beam lower than 10%, temperature variations along the dispersing elements should be within 2 mK [22].

Typical temperature variations measured at ESRF are about 0.5^o [24]. Therefore, 1K temperature stability can be achieved. For demanding beamlines, new high-flow air conditioning units (air renewal rate 20 cycles/hour) are used. Vibrations from air flow are reduced using porous ducts [23]. At the ID22 beamline at ESRF, temperature variations are $< 0.1^o$ over 24 hours [24].

Construction/conventional design measures that reduce thermal effects include choosing low-expansion materials, cooling local heat sources, thermally insulating vessels, moving all control electronics outside the hutches [24], using thermally insulated sand-filled stands, and striving for high thermal inertia [24].

1.6 Additional Requirements Imposed on the Accelerator Systems

Beam Stability

As stated above, stability requirements are determined by temperature stability and vibration (natural and self-inflicting). In terms of beam stability, the requirements for different components are based on achieving less than 10% variation of the beam size.

In addition to the temperature control measures discussed above, Shvyd'ko reports [22] that 0.1 meV energy resolution requires 0.25 μrad incident beam direction stability in the vertical plane and 0.25 μrad relative angular stability of the monochromator and analyzer single-crystal components. A similar requirement for beam stability better than 0.01 meV that would require stability of the incident beam direction (beam angle) better than 0.250 μrad is given in report [23] and its most recent updates [2]. Horizontal angle stability should be 10% of the opening angle. Horizontal and vertical position stability should be 10% of the beam size. It has been pointed out that angular vibration drifts are much worse than linear [24]. This is particularly true for long beamlines like IXS.

References [to be completed]

1-A Appendix A: Ray Tracing Using XOP and Shadow

The vendor conducted ray tracing of the beamline at 9.1 keV using the XOP and Shadow packages to analyze a combined effect of surface distortion of the first crystal of the DCM on beam size and flux at the first sample position. The assumed positions of the optical elements, DCM, VCM, HFM, and VFM, are as given in Table 1.C.1 (Appendix C). The results of the FEA analyses for several of the most important cases are given in Table 1.A.1 below and in Figures 1.A.1 and 1.A.2. Cases 2 and 4 are highlighted in the table, as the beamline is most likely to be used in a high-beta regime.

Table 1.A.1 Results of ray tracing analysis at different heat loads at first crystal of the high-heatload monochromator at 9.1 keV.

Case No.	Model (1xU19, 2xU19)	Spot size at no crystal distortion, μm	Flux at no crystal distortion, ph/s	Spot size, μm	Flux, ph/s
1	Low beta, 0.55 nm-rad, K=0.981, 1xU19, Power = 22 W	2.0 x 1.8	1.50×10^{13}	2.1 x 2.1	1.49×10^{13}
2	High beta, 0.55 nm-rad, K=0.981, 1xU19, Power= 7 W	7.0 x 1.8	1.49×10^{13}	7.0 x 2.0	1.49×10^{13}
2a	As above, but water cooled Si crystal	7.0 x 1.8	1.49×10^{13}	16 x 7.4	1.51×10^{13}
3	Low beta, 0.55 nm-rad, K=1.714, 1xU19, Power = 71 W	2.0 x 1.9	2.88×10^{13}	2.3 x 4.2	2.81×10^{13}
3a	As case 3, but base temperature is 105K to get the hot spot of the crystal at 125 K			2.1 x 0.5	2.92×10^{13}
3b	As case 3, but 2xU19, 115 W	2.0 x 2.0	5.80×10^{13}	2.9 x 5.9	5.14×10^{13}
4	High beta, 0.55 nm-rad, K=1.714, 1xU19, Power = 22 W	7.1 x 1.9	2.81×10^{13}	7.0 x 3.4	2.79×10^{13}
5	Low beta, 0.9 nm-rad, K=1.714, 2xU19, 148 W.	2.6 x 2.0	5.82×10^{13}	3.3 x 5.7	4.68×10^{13}

Corresponding heat loads are given in Table 3.4. Flux at the sample position was calculated over a 20 μm x 20 μm aperture. Mirrors were assumed to be elliptically bent, to show better spot size. The number of rays was converted into flux using the expression

$$\text{Flux[ph/s]} = \frac{\text{N}_\text{T}}{\text{N}_\text{i}} \frac{\Delta E\ [eV]}{E\ [\text{keV}]} I_0\ [\text{ph/s}],$$

where NT is the number of rays transmitted through the optical system, Ni is the number of incoming rays corresponding to the incident flux I0, $\Delta E=3eV$ is the bandwidth over which the ray tracing was performed, and E is the energy of photons in the middle of the bandwidth. The incident flux was calculated using the XUS program from the XOP package.

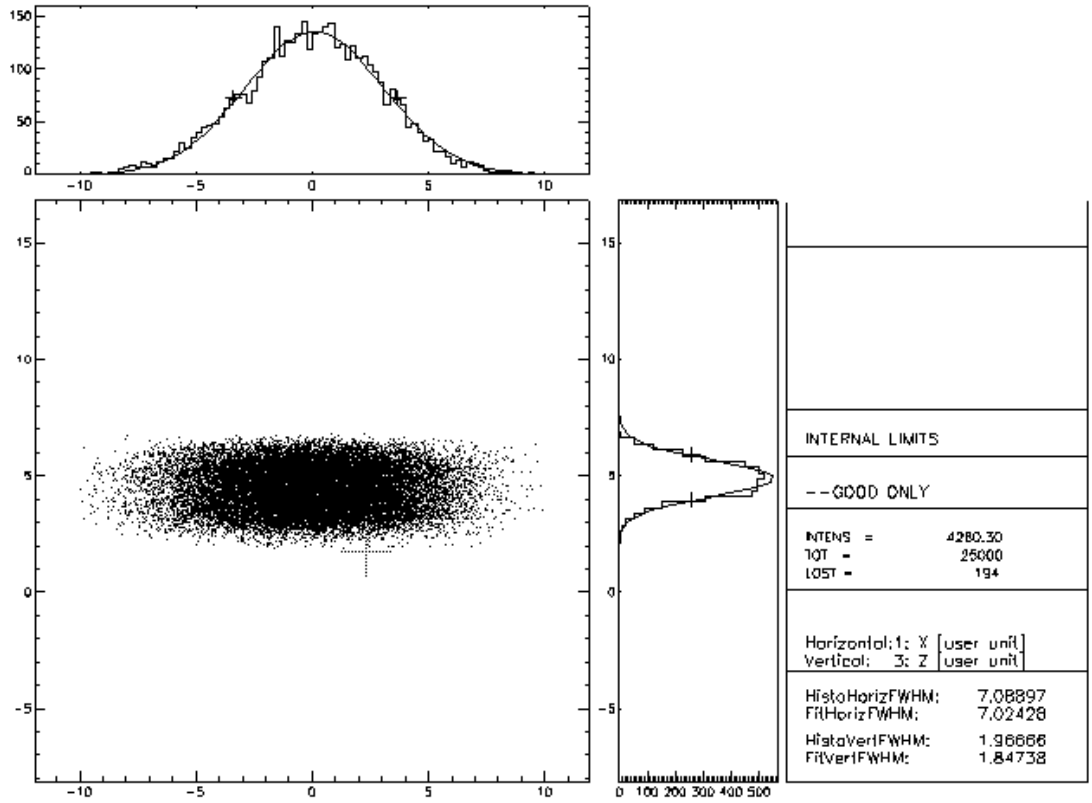

Figure B1. Beam spot at the sample for Case 2 in Table B1. Surface errors due to heating and cooling of the DCM crystal were included in the calculations.

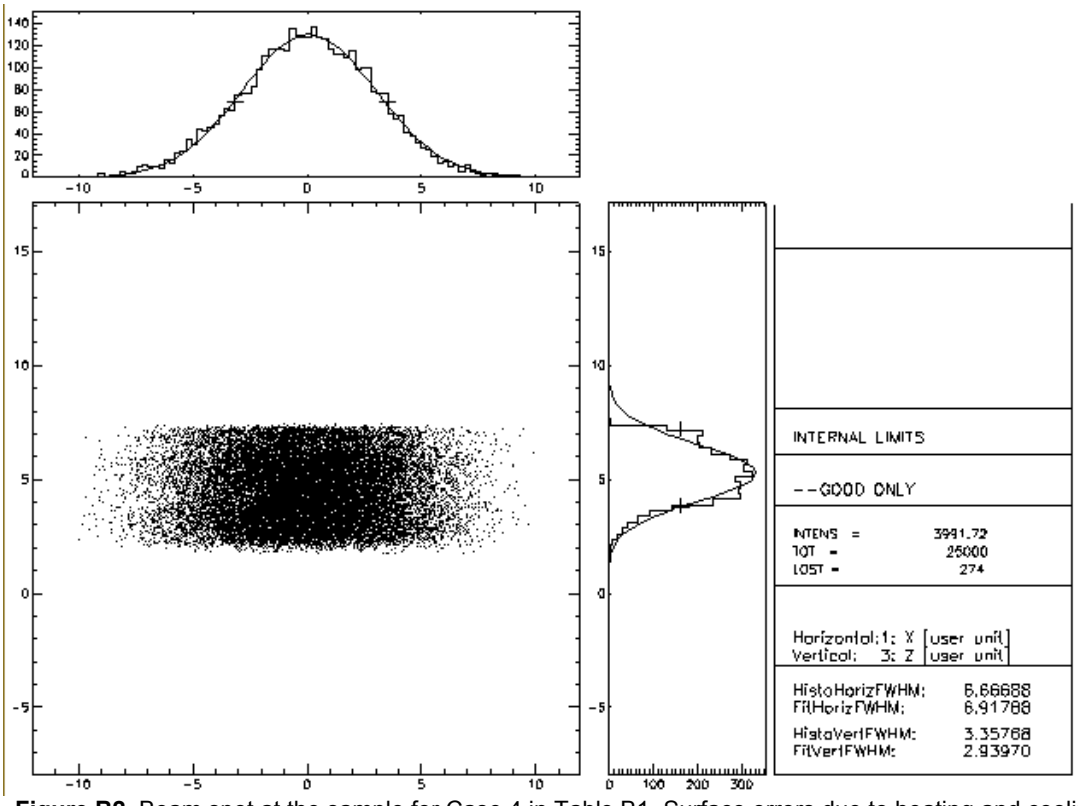

Figure B2. Beam spot at the sample for Case 4 in Table B1. Surface errors due to heating and cooling of the DCM crystal were included in the calculation.

Figure B3 shows a simulation for the same heat load as in Case 2 but for a water-cooled Si crystal. The data show significant broadening of the beam. There would be noticeable loss of flux if it were calculated over a smaller aperture than the 20 μm x 20 μm chosen here.

Results show that in the high-beta regime, the spot at the sample is sufficiently small and of a regular shape even at K=1.714 (Case 4), whereas the flux is nearly doubled compared to the case of K=0.981 (Case 2). The expected resolution of the beamline without the high-resolution optics is shown in Figure B4.

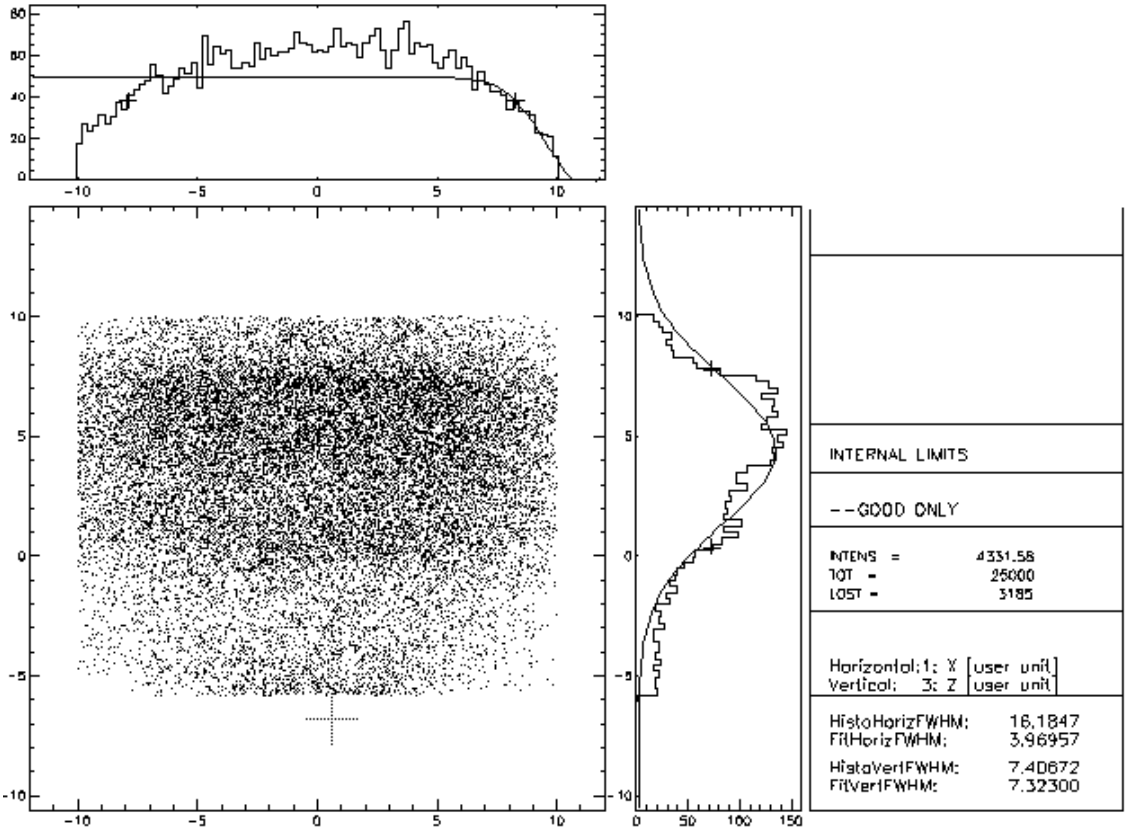

Figure B3. Beam spot at the sample for Case 2a in Table B1. Surface errors due to heating and cooling of the DCM crystal are included in the calculations. The crystal was water cooled.

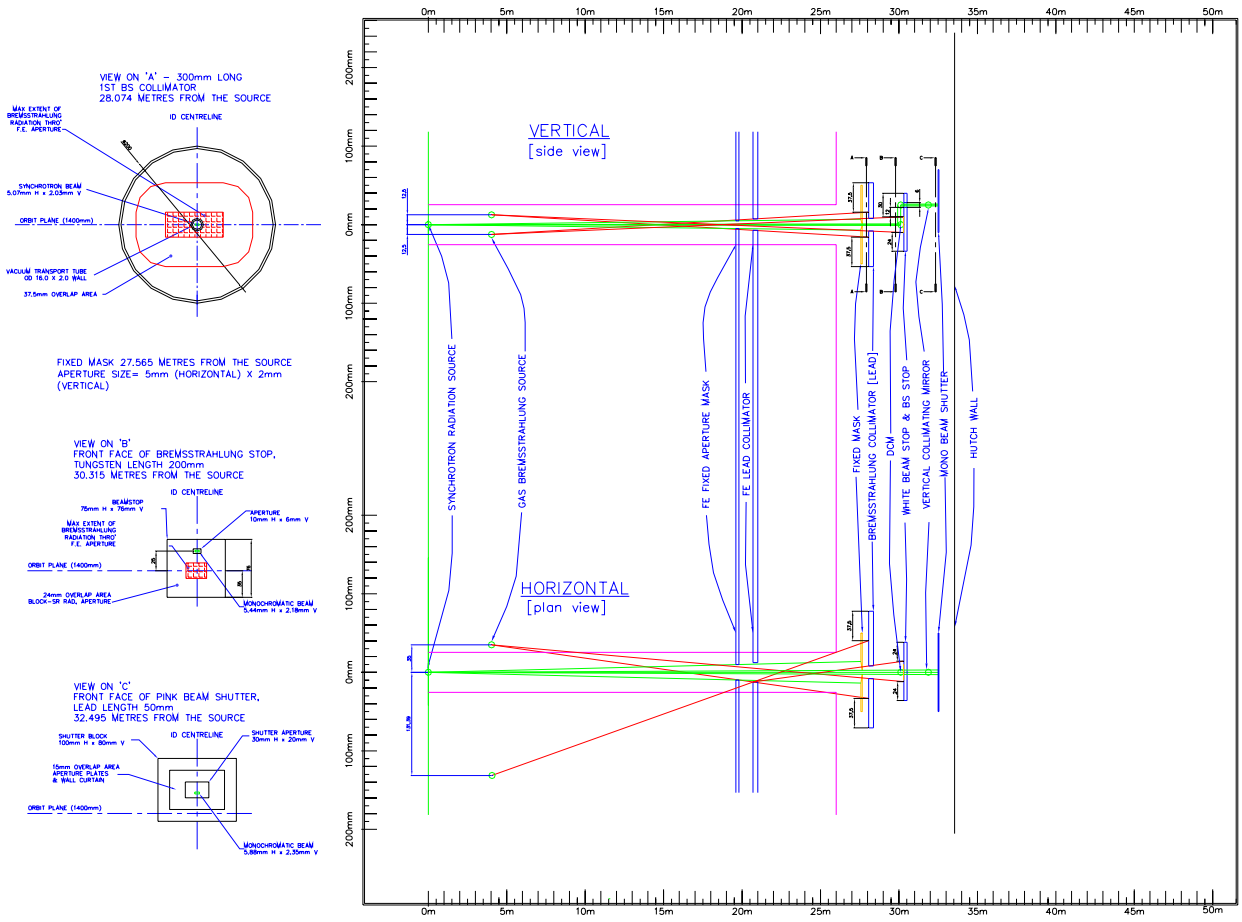

Figure B.4 Bremsstrahlung ray trace diagram for the inelastic x-ray scattering beamline.

1-B Appendix B: Beamline Layout Drawings

This is a possible layout of the IXS beamline showing a two-endstation and back-scattering monochromator configuration.

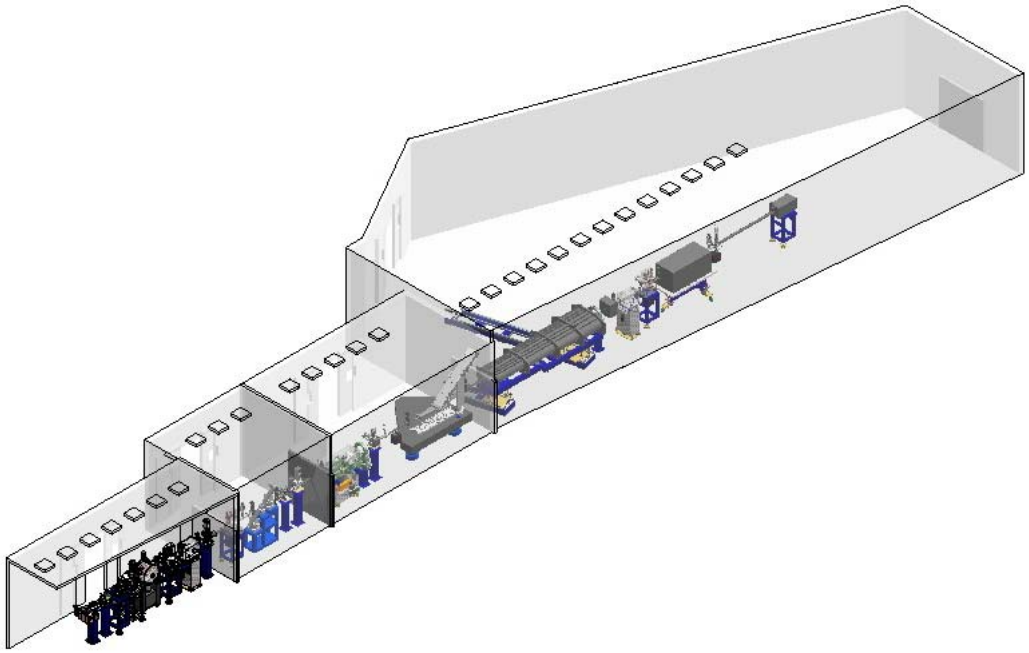

Figure B1. General view of the NSRS-2 IXS beamline and two endstations (Backscattering HRM).

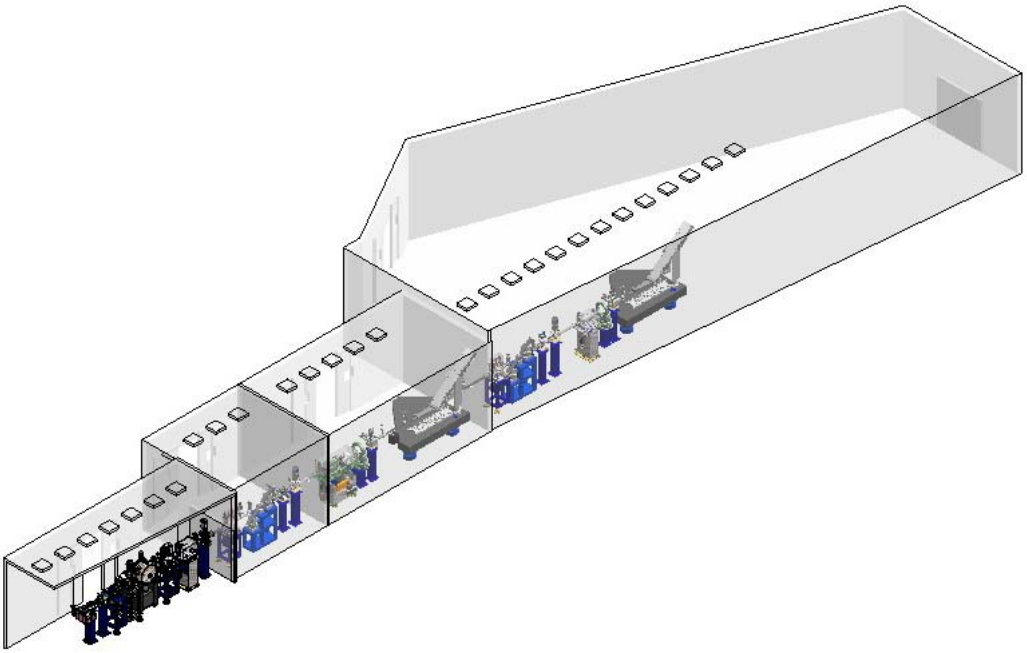

Figure B2. General view of the NSRS-2 IXS beamline and two endstations (In-line HRM) with an in-line, high-resolution monochromator.

1-C Appendix C: List of Key Beamline Components

Table 1.C.1. Proposed beamline layout based on the July 17, 2007 facility numbers.

Beamline Component	Starting position, mm	Length, mm	Vacuum section[1]	Center of Optical Element
Beamline isolation gate valve	26900	70	0/1	
Bellow	26970	175	1	
Pumping Tee	27145	420	1	
Cooled fixed mask	**27565**	**229**	1	**27680**
Bellow	27794	175	1	
CVD Diamond Window	27969	105	1/2	
Bremsstrahlung collimator	28074	388	2	
Bellow	28462	137	2	
Blade BPM	28599	319	2	
Bellow	28918	137	2	
White beam slits	**29055**	**229**	2	**29170**
Cooled Fluorescent screen	29284	211	2	
Bellow	29495	137	2	
Gate valve	29632	70	2/3	
DCM White beam / Bremsstrahlung stop	**29702**	**821**	3	**30113**
Gate valve	30523	70	3/4	
Bellow	30593	137	4	
Quadrant BPM	30730	35	4	
Monochromatic slits Fluorescent screen	30765	553	4	
Bellow	31318	137	4	
Gate valve	31455	70	4/5	
VCM	**31525**	**700**	5	**31875**
Gate valve	32225	70	5/6	
Bellow	32295	200	6	
Monochromatic beam shutter	32495	320	6	
Pipe Hutch Wall at 33.55 m	32815	600 340	6	
ENDSTATION 1				
Bellow	33415	200	6	
Monochromatic slits Fluorescent screen	33615	553	6	
Y-Z profile monitor	34168	406	6	
Bellow	34574	200	6	
Gate valve	34774	70	6/7	
High-resolution monochromator	**34844**	**1031**	7	**35360**
Gate valve	35875	70	7/8	
Bellow	35945	200	8	

Beamline Component	Starting position, mm	Length, mm	Vacuum section[1]	Center of Optical Element
Fluorescent screen	36145	300	8	
Bellow	36445	200	8	
Quadrant BPM	36645	35	8	
Monochromatic beam shutter	36680	320	8	
Pipe Hutch Wall at 37.3 m	37000	680 340	8	
Bellow	37680	200	8	
Gate valve	37880	70		
HFM	**37950**	**900**	8	**38400**
VFM	**38850**	**600**	8	**39150**
Be (150 μm) or SiN window	39450	20	8/9	
Sample position 1 (low vacuum)			9	**39570**
Be (150 μm) or SiN window	39670	20	9/10	
Monochromatic slits	39690	340	10	
Quadrant BPM	40030	35	10	
Bellow	40065	200	10	
Gate valve	40265	70	10/11	
Segmented high-resolution analyser (reflecting back at a different height) Gate valve Bellow/pipe SiN window (200 nm) Strip detector	40335 (finishes at 42835)	2500 70 300 20 600	11	**44238**
Gate valve	42835	70	11/12	
Bellow	43035	200	12	
Pipe Hutch Wall (separating Endstation II) at 46.05 m	43235	17647	12	
ENDSTATION 2 (Backscattering Monochromator option)				
Bellow	60882	200	12	
Gate valve	61082	70	12/14	
Backscattering monochromator	**61152**	**1000**	14	**61652**
Gate Valve	61082	70	14/13	
Bellow	60882	200	13	
Pipe	58932	1950	13	
Bellow	58732	200	13	
Double sided Fluorescent screen	58521	211	13	
Y-Z profile monitor	58115	406	13	
Si table	54415	3700	13	
Gate valve	54345	70	13/15	
Bellow	54145	200	15	
Monochromatic slits Fluorescent screen	53592	553	15	

Beamline Component	Starting position, mm	Length, mm	Vacuum section[1]	Center of Optical Element
Quadrant BPM	53557	35	15	
Bellow	53357	200	15	
VFM	52757	600	15	**53057**[1]
Monochromatic Slits	52692	65	15	
SiN window (200 nm)	52622	70	15	
Sample position 2 (low vacuum) Detector		446 400	16	**52451**[2]
SiN window (200 nm)	52106	70	17	

Notes: 1) Optical distance is 70.247 m from the source.
2) Optical distance is 70.853 m from the source.

2 HXN: NANOPROBE BEAMLINE

2.1 Executive Summary

The proposed beamline design follows many of the ideas presented in the December 2006 NSLS-II CDR with additional operation modes. Determining an optics plan for this beamline is complicated by the fact that the required final optics for achieving 1nm focal spots do not yet exist. The uncertainty associated with the optics requires that the beamline be designed with sufficient flexibility to provide the necessary contingency to accommodate an eventual optics solution. The challenge is to provide this flexibly without paying an excessive cost premium or the need to rebuild/replace components—allowing on-budget and on-time completion of the beamline. The design detailed here incorporates this flexibly and controls risk by utilizing well-understood front end and FOE optics components to deliver the x-ray beams generally required for illuminating any successful nano-focusing optics.

The plan is based on two focal points: one at 41 m and the other at 76 m, both supplied by a common set of upstream optics that are located in the front end and FOE. At each of these two locations a hutch will house the necessary end station equipment to support the scientific goals of the beamline. The exact location of these hutches will be determined by a number of factors, such as the characteristics of the final nano-focusing optics and details involving conventional facilities (floor space, roof line, egress, utilities, etc.). One way to look at this proposed layout is to consider the 41 m hutch a 1x location and the 76 m hutch a 2x location with regard to beam demagnification. Operationally, the focused x-ray beam can be used in only one hutch at a time. A beam stop located at the back wall of the upstream 1x hutch would allow access to the downstream 2x hutch while beam is present in the 1x hutch. Access to the 2x experimental location during x-ray operation of the 1x location will allow off line work to be performed using the end station equipment. Given the sophistication and complexity of a nano probe end station, this will provide valuable access time for instrumentation development and testing, as well as experiment setup.

The 1x/2x hutch arrangement will play a key role during the early operation phase of the project, when the main activity will be optics testing and commissioning. During this initial phase and well before the 2x hutch (and transport to it) is completed, the 1x location will serve as an early test location where various optics approaches can be evaluated and refined for eventual use in the push to 1 nm in the 2x hutch. There also exists the possibly of achieving a 1nm focal spot at the 1x location if modes such as a waveguide-coupled aperture prove feasible. The two locations can also be instrumented with complimentary end station equipment such as a full-field imaging system in the 1x location providing flexibly and agility in meeting the demands of the user science program.

The optics report section describes five optics modes: two for the 76 m 2x location, and three for the 41 m 1x location. The proposed support optics will be used to configure these five modes and are general enough to provide additional operation modes if necessary. They are also well understood today regarding both performance and cost.

Particular attention should also be given to address vibration issues with the building experimental and outbuilding floor and the principle optical items—namely, the Monochromator and Mirror systems and other key diagnostic and sample hardware. Similarly, the scanning table supports will have to be state-of-he art vibration isolated systems. Novel solutions should also be sort for BPM systems these need to be nanometer accuracy and supported upon thermally stable and vibration-free supports.

2.2 Scientific Objective

This beamline will allow the study of nanomaterials, which play important roles today in many diverse scientific fields, opening up a wide range of scientific problems ranging from studying the structure and function of catalytic nanoparticles, to the mapping of strain in buried grain boundaries, to determining the structure of single molecule devices.

This hard x-ray nanoprobe beamline will be designed and optimized to enable the production and use of a beam of hard x–ray photons with a nm beam size. As such, it will be a world-leading instrument, enabling spatially resolved versions of many powerful structural and spectroscopic x-ray techniques with unprecedented resolution. In particular, it will allow the study of nanomaterials which today play important roles in many diverse scientific fields. This beamline will take maximum advantage of the low emittance beam provided by the NSLS-II lattice.

The primary experimental techniques for this beamline will likely be scanning nanobeam techniques, but it will also have a limited full-field capability. The limited full-field capability will assist in rapidly locating areas of interest, and would thus allow more efficient use of beam time. For the scanning probe techniques, there are a variety of contrast mechanisms that allow one to extract useful information from the real-space mapping of a sample. For example, one can spatially resolve the density, elemental composition, crystallographic phase, strain, texture, chemical state, local atomic environment, and magnetization. It will operate in a number of modes, each of which will place different requirements on the detectors.

In the first mode, a fluorescence detector can be used with the sample to reveal the spatial distribution of individual elements. The second mode will use a large-area, low-spatial resolution high-sensitivity detector, such as a CCD, to obtain a spatial map of selected Fourier components of a crystallographic phase, and also a spatial map of the local strain. Third, by scanning the incident photon energy, it will be possible to access a number of spectroscopic quantities, such as the local environment from EXAFS and the local chemical state from XANES. Finally, from the back-scattered Compton scattering, one can measure the electron density. This will be especially useful for light elements such as carbon.

2.3 Insertion Device

For the nanoprobe, the over-riding design guidance is to improve the chances of attaining a 1 nm spot size. In order to do this, it is clear that the low-beta insertion section with the small source size is the right choice.

2.3.1 Undulator Power

Power density calculations have been performed for an undulator using equations presented by Kim.[1] Table 2.1 details the source, undulator, and beam parameters. Note that these calculations were prepared for a U19 cryogenically cooled permanent magnet device. We currently anticipate that the standard device for NSLS-II baseline hard x-ray undulators will be a room-temperature U20 In proceeding further with the design for this beamline, this choice should be further re-optimized and these calculations performed again.

Table 2.1. Source, Undulator, and Beam Parameters.

Source parameters	Source energy, E_s	3 GeV
	Source current, I	500 mA
Undulator parameters	Period length, λ_u	19 mm
	Number of periods	158
	Deflection parameter, K	2.03
Beam parameters	Horizontal electron size, σ_x	38.5 μm
	Horizontal electron divergence, σ'_x	14.2 μrad
	Vertical electron size, σ_y	3.05 μm
	Vertical electron divergence, σ'_y	3.22 μrad

Normalization factor, G(K). The normalizing factor is defined as:

$$G(K) = K \cdot \frac{(K^6 + 24/7 \cdot K^4 + 4 \cdot K^2 + 16/7)}{(1 + K^2)^{7/2}} \tag{2-1}$$

Substitute known values and calculate the normalization factor.

$$G(K) = (2.03) \cdot \frac{((2.03)^6 + 24/7 \cdot (2.03)^4 + 4 \cdot (2.03)^2 + 16/7)}{(1 + (2.03)^2)^{7/2}} = 0.982 \tag{2-2}$$

Magnetic field strength, B_0. The magnetic field strength of the undulator is defined as:

$$B_0 = \frac{K}{0.934 \cdot \lambda_u}. \tag{2-3}$$

Substitute known values and calculate magnetic field strength.

$$B_0 = \frac{2.03}{0.934 \cdot (19 * mm)} = 1.144 Tesla \tag{2-4}$$

Gamma of synchrotron, γ. The gamma parameter is defined as:

$$\gamma = \frac{E_s}{m_e \cdot c^2} \tag{2-5}$$

where E_s=source energy, m_e=mass of the electron (9.1095 x 10^{-28}grams) and c=speed of light (2.99792458 x 10^{10}cm/sec). Substitute known values and calculate the gamma parameter.

$$\gamma = \frac{3GeV}{(9.1095 * 10^{-28} grams) \cdot (2.99792458 * 10^{10} cm/\sec)^2} = 5871 \tag{2-6}$$

Power density distribution, $P_u(\theta, \psi)$. Power density in the forward direction is given by:

$$P_u(\theta,\psi) = 10.84 \cdot B_0 \cdot {E_s}^4 \cdot I \cdot N \cdot G(K) \cdot f_K(\theta,\psi) \quad (2\text{-}7)$$

where I = source current and N = number of periods. Based on the source, undulator, and beam parameters (Table 2.1) and the detailed functions, Figure 2.1 plots the incident vertical and horizontal heat flux distributions.

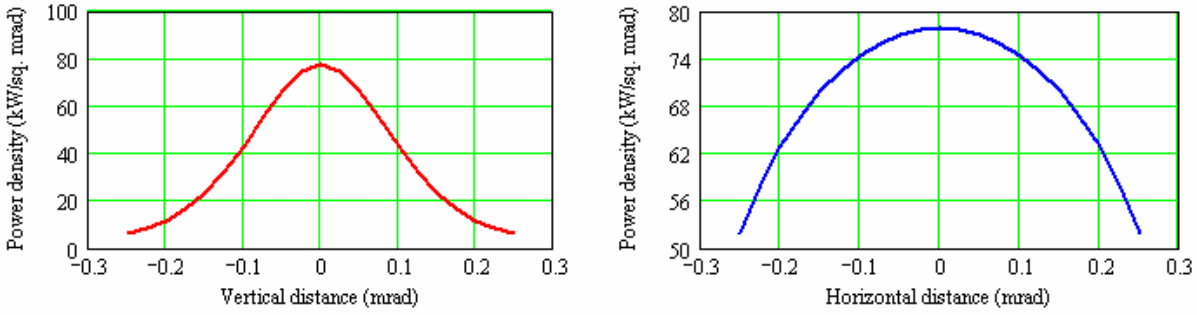

Figure 2.1. Heat flux distributions for the U20 undulator.

2.4 Sector Layout

2.4.1 Front-End Layout

In this section, the components in the front end (upstream of the ratchet wall) are discussed.

2.4.1.1 Front End Differential Pump Mask (FEDPM)

This power limiting mask will allow approximately 90% of the undulator harmonic (at 1 Å) to pass, reduces the total power to a level that is more manageable by the downstream components and protects against mis-steering of the electron beam. It will be located behind the shield wall as close to the undulator as possible with the next component (Front End Defining Aperture Mask, FEDAM) directly downstream. The vertical and horizontal location of this critical component will be defined through survey with additional motorized horizontal positioning over a restricted range to aide the initial alignment of the orbit (its front end location will make it difficult to access manual adjustors). Due to its location and size, this component is ideal for acting as the vacuum conduction-limiting aperture for a differential pump, freeing up space in the optics enclosure.

- distance from source = 14 m
- positioning = Y manual, X motorized (±0.5 mm)
- number of motors = 1

2.4.1.2 Front End Defining Aperture Mask (FEDAM)

To provide some thermal control of the central beam, motorized translation of the FEDPM and the FEDAM will be included to allow the horizontal beam size to be restricted to match the effective vertical coherent source size during nano-focusing.

- distance from source = 15 m
- aperture size = 0.3 mm (vertical) and 1.1 mm (horizontal)
- positioning = Y manual, X motorized (±0.5 mm)
- number of motors = 1
- percent harmonic (at 1 Å) = 90%
- power transmitted = 130.6W – aperture size = 0.3 mm (vertical) and 1.1 mm (horizontal)
- power transmitted = 35.7W – aperture size = 0.3 mm (vertical) and 0.3 mm (horizontal)

2.3.4.2 Beamline Layout

Figures 2.2, 2.3, and 2.4 outline the proposed beamline layout.

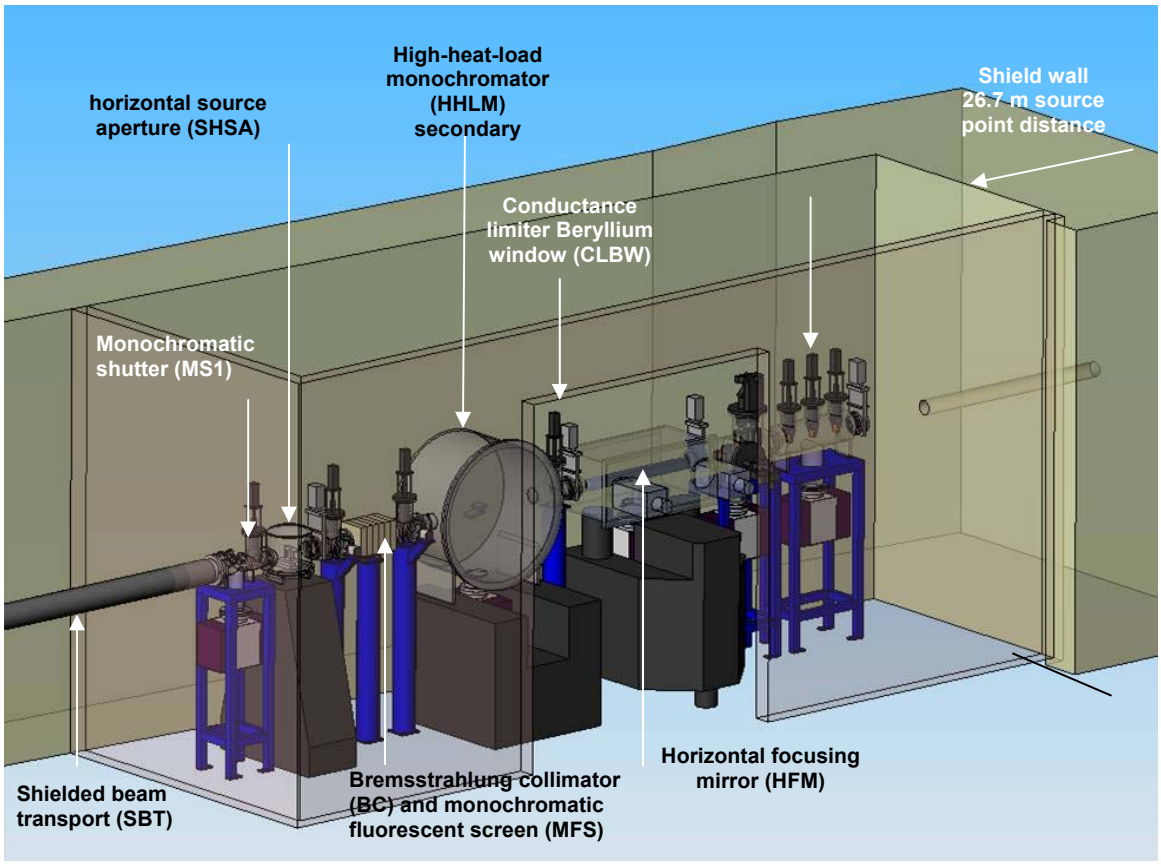

Figure 2.2. Nanoprobe beamline First Optics Enclosure (FOE).

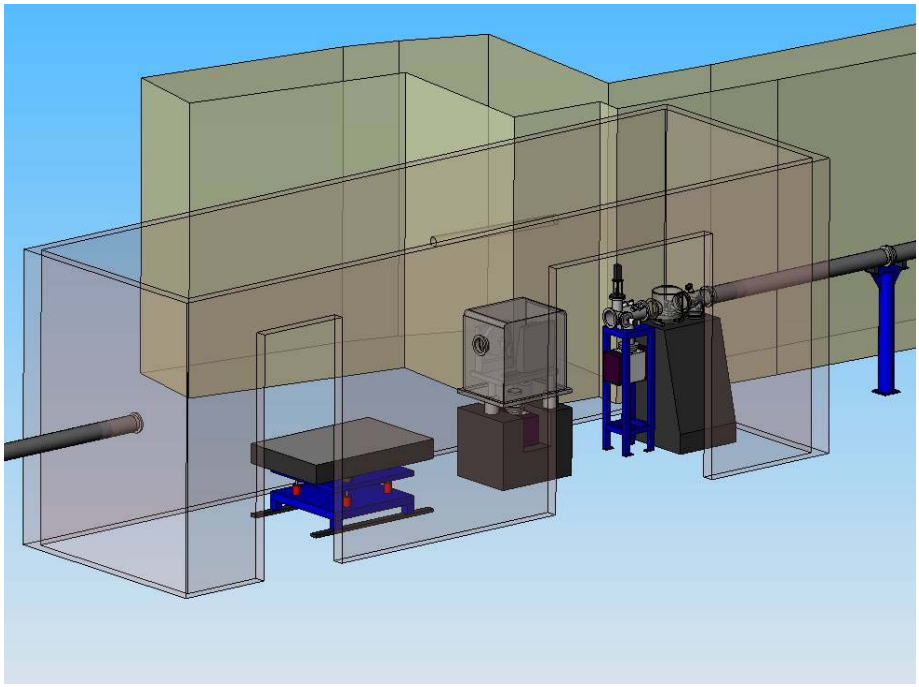

Figure 2.3. Nanoprobe beamline Station A. This station is the “x1” station and is within the experimental hall (see text).

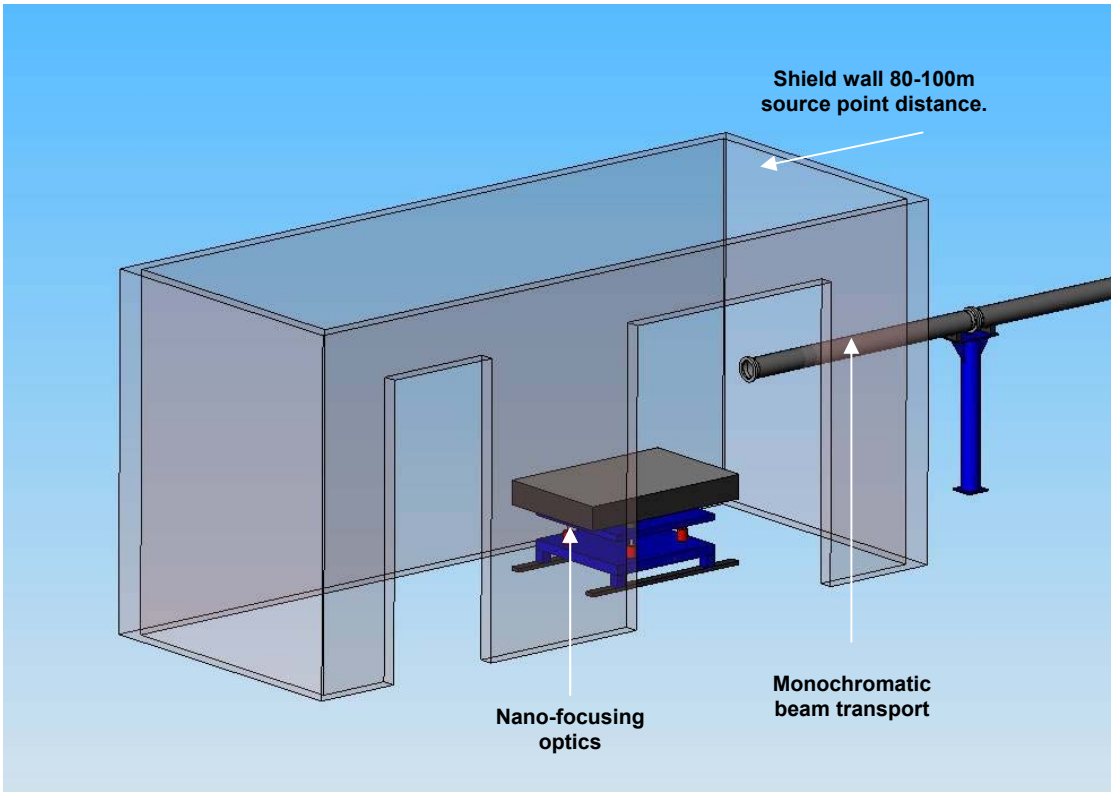

Figure 2.4. Nanoprobe beamline Station B.

2.4.2.1 Survey and Alignment

The NSLS-II nanoprobe sector should commission ~40 survey monuments on the sector, consisting of robust brass monuments countersunk into the floor. In all, there are 20 monuments located on the ID line aligned on the main ID centerline. These monuments, along with additional vertical wall marks and egress aisle locations, constitute the principal fiducial reference points for survey and alignment of the beamlines.

In addition, metallic stick-on targets will be located on the floor offset 1 meter to the main monument lines. These can be used to either establish temporary parallel lines for survey or to act as 90° turn-off points. These monuments should be surveyed relative to the two primary NSLS-II monuments per beamline. After installation, as-built precision coordinate measurements of several of the monuments will be made by the NSLS-II survey and alignment team. The locations of the monuments are shown in the main layout.

Survey and Alignment Guides

Survey monuments. Each FOE and Experiment Station will have brass monuments counter-sunk into the floor, at front and rear, plus approximately every three or four m, for each beamline.

The monuments used in NSLS-II will be compatible with the target mount for a laser tracker. The maximum error is typically ±0.3 mm. An adapter cap will fit over the monument for fitting of a 1.5-inch diameter laser retro-reflector.

Beamline centerline. A 0mrad beamline centerline will be placed in every enclosure, described with dedicated scribed brass monuments.

Beamline equipment. Each piece of beamline equipment will have mounts for laser tracker targets—typically three per piece of equipment. These should be offset to enable measurements of x-y-z and pitch, roll, and yaw adjustments.

Beamline height: 1.4 m. Each beamline will have dedicated survey targets in every enclosure. Wall-mounted targets are very useful for independent survey capability of beamline instrumentation using a Leica auto level with an accuracy capability of 10 μm.

Survey target location. Each radiation enclosure will have survey targets positioned at beam height at front and rear, plus every 3 m, for each beamline. The survey targets will be mounted on the hutch wall or concrete wall.

NSLS-II survey monuments. NSLS-II will provide a pattern of survey monument floor reference locations. These will typically be in the egress aisles plus at other key locations.

Cartesian coordinate framework. All major experimental equipment shall be kinematically mounted on the experimental floor. This will provide the ability to measure complete Cartesian coordinate reference information for experimental equipment. Provision will be made for survey reference floor markings in experiment stations, plus two target spheres on experimental equipment.

Survey Equipment

Survey equipment that has been ascertained to be available for local alignment and survey is as follows.

Beamline height instrumentation. Auto-Leveler - Nikon (accuracy of the scale division ±0.1 mm). The following upgrade may be implemented to achieve 10μm accuracy:

- NA2 Precision Auto Leveler
- GPM3 Parallel plate 10 mm for NA2
- GST-20 Tripod
- GVO-10 Short Focus lens for NA2 (1.8 m – 0.9 m)

Bragg motion axis. Survey targets are to be provided on all Bragg axes, such the device can be aligned to beam height and perpendicular to the beam centerline patch

2.4.2.2 Utility Layouts

Table 2.2 details the estimated coolant usage for the front end and first optics enclosure.

Table 2.2 Coolant Usage – Front End and FOE.

Module	Component description	Source point distance	Coolant	Required flow
1	Front End Differential Pump Mask (FEDPM)	14 m	H_20	8 L/min
	Front End Defining Aperture Mask (FEDAM)	15 m		
	Shield Wall	26.7 m		
2	White Beam Filters (WBF)	27.3 m	H_20	4 L/min
3	White Beam Slits (WBS)	27.8 m	H_20	4 L/min
4	Horizontal Focusing Mirror (HFM)	28.8 m	H_20	4 L/min
5	Conductance Limiter Beryllium Window (CLBW)	29.6 m	H_20	4 L/min
6	High Heat Load Monochromator (HHLM)	30.4 m	H_20	4 L/min
	White Beam Monitor (WBM)		LN_2	4 L/min
		30.9 m	H_20	4 L/min
			H_20	32 L/min
	TOTAL		LN_2	4 L/min

Table 2.3 details the estimated motor usage for the front end and first optics enclosure.

Table 2.3 Motor List – Front End and FOE.

Module	Component description	Source point	Number of motors	Motor	Amps / phase
1	Front End Differential Pump Mask (FEDPM)	14 m	1	Stepper	1.4
	Front End Defining Aperture Mask (FEDAM)	15 m	1	Stepper	1.4
3	White Beam Slits (WBS)	27.8 m	1 (horizontal position)	Stepper	1.4
			1 (horizontal aperture)	Stepper	1.4
			1 (vertical position)	Stepper	1.4
			1 (vertical aperture)	Stepper	1.4
4	Horizontal Focusing Mirror (HFM)	28.8 m	2 (mirror incidence)	Stepper	3.0
			3 (mirror alignment)	Stepper	2.0
			2 (mirror bending)	Stepper	2.5
6	High Heat Load Monochromator (HHLM)	30.4 m	1 (Bragg axis)	Stepper	2.5
			3 (2^{nd} crystal – roll, pitch and yaw)	Stepper	0.6
			1 (2^{nd} crystal vertical translation)	Stepper	2.5
	White Beam Monitor (WBM)	30.9 m	1	Stepper	1.4
	Secondary Horizontal Source Aperture (SHSA)	32.0 m	1 (horizontal position)	Stepper	1.4
			1 (horizontal aperture)	Stepper	1.4
	TOTAL		21	Stepper	49.8

2.4.2.3 Life Safety Code Compliance

Egress Aisles. Egress aisles are shown on the architectural layout drawing NSL-100-10-0003-A. All aisles are approximately 44 inches (1.12 m) wide.

2.4.2.4 Beamline Vacuum System

Most of the beamline components will be built to ultra high vacuum specifications with, in general, no vacuum-to-coolant joints. The exception to this are the silicon crystal mount monochromators in the ID beamlines, these will use a Cajon Swagelok VCR-type coupling connected to flexible pipes, for easy connection to the coolant supply.

To isolate the beamline vacuum from machine front end, there will be a differential pumped mask together with a Beryllium window conductance-limiter system. The nanoprobe beamline will utilize ion pumps to pump all beamline sections. In addition, gate valve pumping ports will be used to isolate the monochromator sections, to enable fast pumpdown via permanently installed turbo pump sets. Vacuum will be in the 10^{-7} to 10^{-8} Torr range. All mirror tanks will be isolated by gate valves from the rest of the beamline and will be operated in UHV (~10^{-9} Torr).

Beryllium Window Design

The main design points of the assembly are:

- At least two window thicknesses will be installed between the beamline termination window and the front end, to comply with regulations on the protection of machine vacuum. One thickness is the Be window conductance limiter and the second is the end window.
- The window material will be Brush Wellman IF1. The purity of the Be will be preferentially selected to 99.3% Be assay, with the iron and copper content less than 300 ppm, respectively.
- Coherence of the beam is a significant issue for nanoprobe experiments, so the Be windows will be polished.
- For ID beamline termination windows utilizing white beam, to protect against ozone-induced oxidization and corrosion we intend to investigate the possibility of sub-micron coating with aluminium. Alternatively, we will cap the end of the window flange with a Kapton window and flow dry nitrogen into the inter-space between the Kapton and Be to prevent corrosion. Holes burned into the Kapton due to white beam should be small, and a marginal positive pressure of dry nitrogen should suffice to keep air out and ozone production to a minimum.

Main Vacuum Sections (see also Table 2.4)

Vacuum Section 1

- Pneumatic DN200 all-metal valve (at end of the front end) 10″ CF, 8″ tube
- Tube incorporating machine protection measures: pirani gauge, cold cathode gauge, RGA, right-angled all-metal valve, 300 L/s (nom) ion pump fitted to the tube.
- Graphite Filter and Primary Slits Section – 300 L/s (nom) ion pump
- Pneumatic DN100 all-metal valve

Vacuum Section 2

- Horizontal mirror – water-cooled Si mirror
- 500 L/s (nom) ion pump, pirani gauge, cold cathode gauge, right-angled metal valve

- Diagnostics section (fluorescent screen, tungsten wire)
- Pneumatic DN100 all-metal valve

Vacuum Section 3

- Beryllium conductance-limiter window
- Double crystal monochromator – liquid nitrogen cooled
- Fitted with 500 L/s (nom) ion pump, pirani gauge, cold cathode gauge, right-angled metal valve
- Turbo dry and scroll backing pump fitted to DCM chamber
- Diagnostics section: white beam monitor and mono fluorescent screen
- GB collimator
- Pneumatic DN100 all-metal valve

Vacuum Section 4

- Photon shutter, possibly integrated gas bremsstrahlung (GB-shielding), fitted with 300 L/s (nom) ion pump, pirani gauge, cold cathode gauge, right-angled metal valve
- Secondary horizontal aperture
- Pneumatic DN100 all-metal valve

Vacuum Section 5

- White beam transport pipe 4 m long - 100mm OD tube
- Diagnostics section (fluorescent screen)
- Integrated gas bremsstrahlung/photon shutter, fitted with 300 L/s (nom) ion pump, pPirani gauge, cold cathode gauge, right-angled metal valve

Vacuum Section 6

- Quad diode BPM
- Diagnostics section (fluorescent screen, tungsten wire)
- Tube fitted with 300 L/s (nom) ion pump, pirani gauge, cold cathode gauge, right-angled metal valve
- Tertiary horizontal aperture

Vacuum Section 7

- White beam transport pipe 4 m long – 100 mm OD tube
- Diagnostics section (mono beam fluorescent screen)
- Tube fitted with 300 L/s (nom) ion pump, pirani gauge, cold cathode gauge, right-angled metal valve
- Pneumatic DN100 all-metal valve
- High-resolution monochromator
- Be window: mirror polished to less than 0.5 μm rms

Vacuum Section 8

- Nano focusing optics
- Long beam transport 29 m long

- 4*300 L/sec ion pumps, pirani gauge, cold cathode gauge, right-angled metal valve
- Be window: mirror polished to less than 0.5 μm rms; end window: Kapton foil protection
- Nano focusing optics

Table. 2.4 Vacuum Equipment Inventory.

Item	Approx Number	Comments
500 L/s (nom) ion pump	2	All major optics (mirror/DCMs)
300 L/s (nom) ion pump	5+3	Long beam transport
240 L/sec turbo and scroll set	2	Monochromators
Pirani gauges	6	Distributed down beamline 1 per vacuum section
Cold cathode gauges (IMG)	6	Distributed down beamline1 per vacuum section
RGA	1	Mirror location
Pneumatic DN100 all-metal valve	5	Distributed down beamline
All-metal right-angled valve	6	At strategic places down beamline (see flow)
Portable rough pump/leak detector	1	Not costed for, but required – assume vacuum loan pool at NSLS-II

2.4.2.5 Data Acquisition System and Motion Control

There are many combinations of control and drive electronics available for beamlines, but some general form factor decisions will reduce the options. The NSLS-II controls group will standardize on the high level control form factor.. The decision involves the balance between extra hardware and software costs verses the availability of existing controls software support (see Chapter 6, Control Systems).

Once the high-level user interface computer system has been determined, one can move down to the motor control options. Again, the synchrotron controls group will probably have a preference. The two main paths are either a simple control card (OMS) or a sophisticated intelligent controller (DeltaTau or Newport XPS). Most beamline axes are single drives that do not require any special features. However, there are exceptions, such as a diffractometer that performs trajectory scans or a monochromator that requires encoder averaging.

The final control decision is the drive amplifiers. There are a wide range on the market, with a wealth of different current ratings and features. For example, when choosing a stepper amplifier card one must chose a step size, current rating, holding current, and DC rail voltage. The choice may also be influenced by the packing density within a rack unit and the availability of spares.

2.4.3 Beamline Components

2.4.3.1 Module 1: Front End Differential Pump Mask (FEDPM)

Distance to center of undulator	14 m

A differential pump assembly will be introduced as the first component in the optics to isolate the beamline vacuum from that of the storage ring. Differential pump assembly will consist of a series of pumps separated from each other and from the UHV region by a flow-restricting aperture. The first aperture in the beamline will be fixed by the FEDPM and the FEDAM (directly downstream of the differential pump assembly), and sets the maximum acceptance of the beamline. This maximum acceptance has been set to correspond with the vertical and horizontal FWHM (full width half maximum) sizes and divergences of the

source. Based on the beam parameters detailed in Table 2.1, the maximum size of the front end aperture is given by:

$$X_1 = 4 \cdot \Sigma_x + 4 \cdot \Sigma'_x \cdot (14m) \approx 1100 \mu m \qquad \text{Maximum horizontal opening}$$

$$Y_1 = 4 \cdot \Sigma_y + 4 \cdot \Sigma'_y \cdot (14m) \approx 300 \mu m \qquad \text{Maximum vertical opening}$$

Using the detailed functions given in Section 2.3, the transmitted vertical and horizontal heat flux distributions are shown in Figure 2.5.

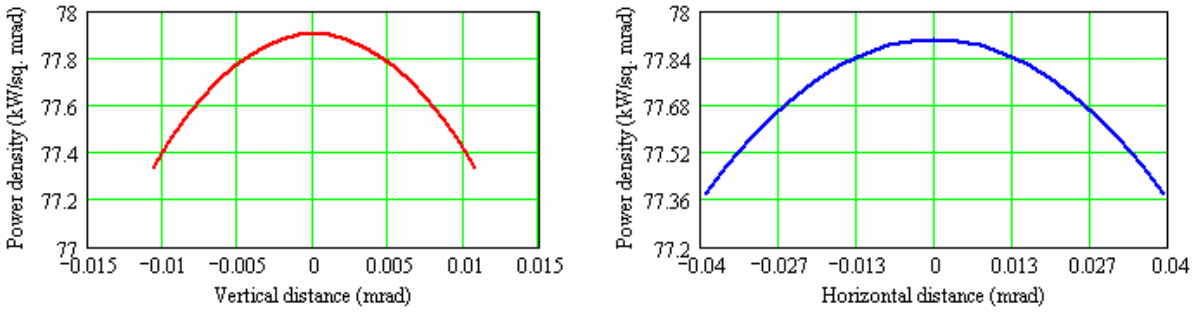

Figure 2.5. Heat flux distributions.

The radiated power for full-field operation is given by:

$$P = \int_{-\left(\frac{0.55mm}{14m}\right)rad}^{\left(\frac{0.55mm}{14m}\right)rad} \left(\int_{-\left(\frac{0.15mm}{14m}\right)rad}^{\left(\frac{0.15mm}{14m}\right)rad} P_u(\theta,\psi) d\theta \right) d\psi = 130.6W \ . \qquad (2\text{-}8)$$

This component is a cooled monolithic block of Glidcop AL-15 with a tapered hole terminating in a rectangular aperture with inclined absorber walls to distribute the heat load (Figure 2.6). Before the ingot is machined, it is first explosion-bonded to AISI 304L stainless steel end plates, which are then fixed to short beam tubes and front and rear entrance flanges. Explosion bonding is a bonding method in which the controlled energy of a detonating explosive is used to create a metallurgical bond between two or more similar or dissimilar materials. This joining technique was first utilized at the APS facility to enable high-strength Glidcop AL-15 materials to be used in high-heat-load components for undulator front ends[2]. The explosion bonded ingots are subjected to the standard ultra sonic tests as outlined by APS in LS 237; this is broadly based on the standard ultrasonic procedure ASTM A578, level I.

The total length, flange face to flange face, has been set at 300 mm. The entire assembly is independently mounted on its own scanning platform and can be translated as a unit by ±2 mm horizontal (motorized) and vertically (manual) adjustments to center the mask on the beam.

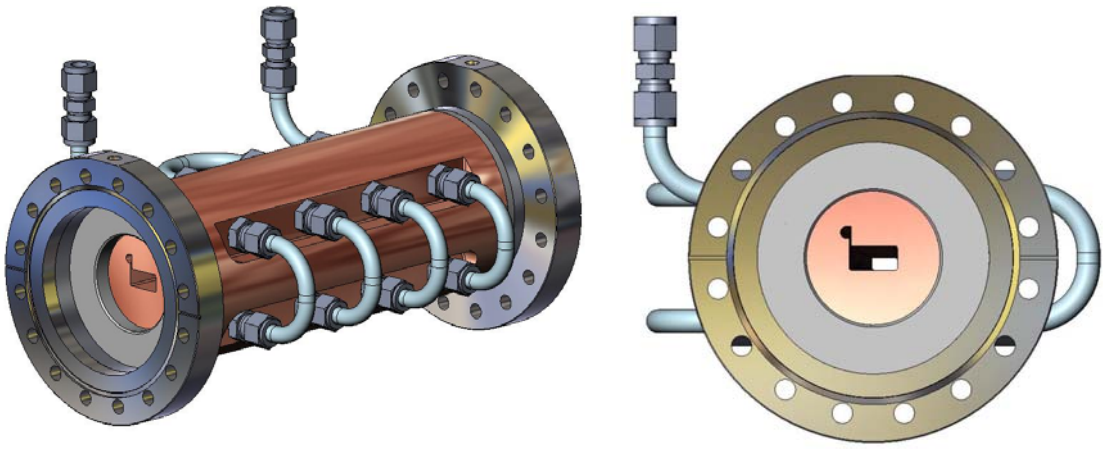

Figure 2.6. Proposed design of the FEDPM.

Motion Specification. Table 2.4 details the required motion specification for the FEDPM assembly.

Table 2.4. Motion Specification for the FEDPM Assembly.

Motion	Range	Resolution	Drive system
Horizontal motorized	±2 mm	<2 μm	Stepper motor driven variable horizontal aperture.
Horizontal manual	±5 mm	0.1 mm	Mask alignment.
Vertical manual	±5 mm	0.1 mm	Mask alignment.
Tilt Φ_X manual	±5°	0.25°	Mask alignment.
Yaw Φ_Y manual	±5°	0.25°	Mask alignment.

2.4.3.2 Module 1: Front End Defining Aperture Mask (FEDAM)

Distance to center of undulator	15 m

To provide some thermal control of the central beam, motorized translation of the FEDPM and the FEDAM will be included to allow the horizontal beam size to be restricted to match the effective vertical coherent source size during nano-focusing. The radiated power for nano-focusing operation is given by:

$$P = \int_{-\left(\frac{0.15mm}{14m}\right)rad}^{\left(\frac{0.15mm}{14m}\right)rad} \left(\int_{-\left(\frac{0.15mm}{14m}\right)rad}^{\left(\frac{0.15mm}{14m}\right)rad} P_u(\theta,\psi)d\theta \right) d\psi = 35.7W \, . \qquad (2\text{-}8)$$

The proposed design for the FEDAM (Figure 2.7) is identical to that of the FEDPM, with the tapered aperture rotated through 180° along the beam centerline. By moving each aperture section independently in the horizontal direction, a variable-sized rectangular aperture can be created. The entire assembly is independently mounted on its own scanning platform and can be translated as a unit by ±2 mm horizontal (motorized) and vertical (manual) adjustments to center the mask on the beam.

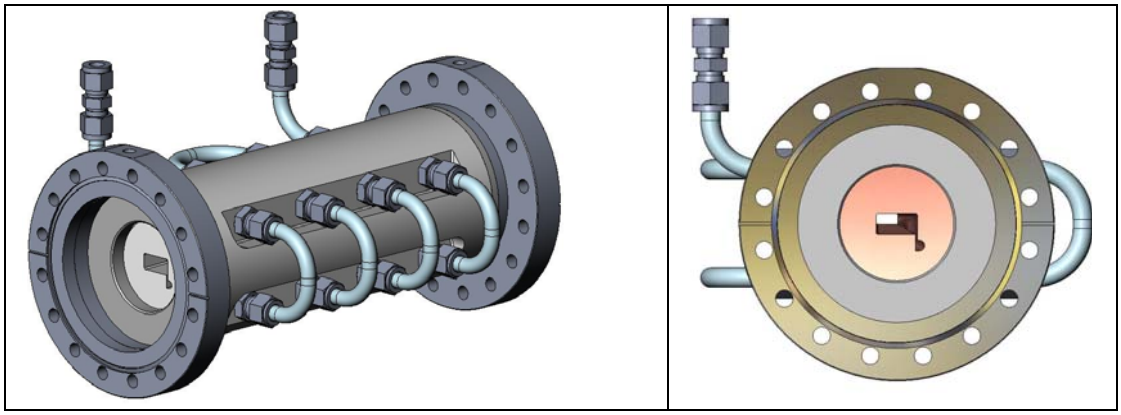

Figure 2.7. Proposed design of the FEDAM.

Motion Specification. Table 2.5 details the required motion specification for the FEDAM assembly.

Table 2.5. Motion Specification for the FEDAM Assembly.

Motion	Range	Resolution	Drive system
Horizontal motorized	±2 mm	<2 µm	Stepper motor driven variable horizontal aperture.
Horizontal manual	±5 mm	0.1 mm	Mask alignment.
Vertical manual	±5 mm	0.1 mm	Mask alignment.
Tilt Φ_X manual	±5°	0.25°	Mask alignment.
Yaw Φ_Y manual	±5°	0.25°	Mask alignment.

2.4.3.3. Shield Wall (SW)

Distance to center of undulator	26.7 m

2.4.3.4 Module 2 - White Beam Filters (WBF)

Distance to center of undulator	27.3 m

The functionality of the filter is to provide variable power absorption upstream of critical beamline components. The design incorporates three water-cooled diamond filters of different thicknesses, each mounted on independent pneumatic actuators with the facility for position translation of the filter in the beam. Diamond filter material is preferred, but there exists uncertainty regarding the degree to which this filter will preserve the source brilliance. There are a number of different types of diamond available, with the best choice for persevering coherence requiring further study. This uncertainty and the need for research and development translate into budget uncertainty. For the purpose of these specifications, commercially available CVD diamond pricing is used.

Based on the source, undulator, and beam parameters, the source spectral power distribution is shown in Figure 2.8. The transmitted spectral power distribution from a 30µm-thick CVD diamond filter is superimposed with the source distribution profile. The transmitted distribution is calculated by multiplying the source spectral distribution with the filter material absorption characteristic. The sum of transmitted

powers at each energy is then divided by the sum of the source power at each energy to give the percentage transmission from the filter. Relative to the source distribution, the power absorption for a 30μm thick CVD diamond filter has been calculated at ~4.1%. Table 2.6 shows foil thickness with calculated absorptions.

Table 2.6. Filter power variation.

Filter thickness (μm)	Transmission (W)	Absorption (W)
30	125.2	5.4
300	107.8	22.8
1000	87.1	43.5

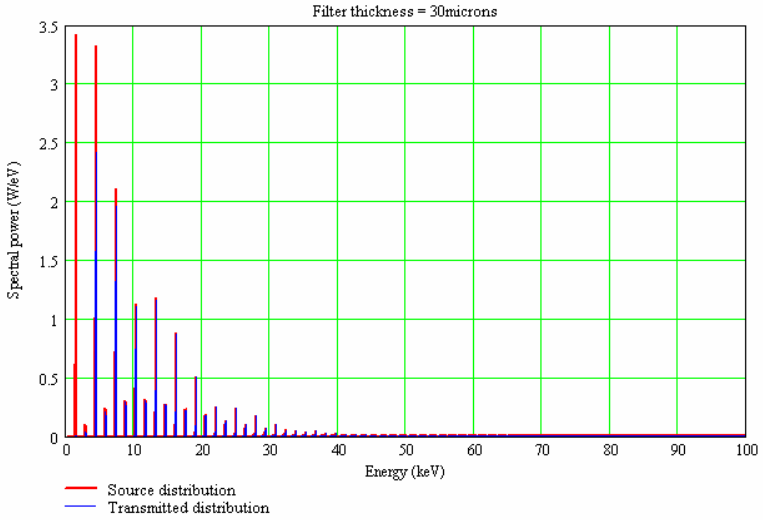

Figure 2.8. Spectral power distributions before and after a diamond filter of 30 microns.

Motion Specification. Table 2.7 details the required motion specification for the WBF assembly.

Table 2.7 Motion Specification for the WBF Assembly.

Motion	Range	Resolution	Drive system
Filter translation	50 mm	<0.5 mm	Pneumatic through vacuum actuator

2.4.3.5 Module 3 - White Beam Slits (WBS)

Distance to center of undulator	27.8 m

The functionality of the primary slits (horizontal and vertical) is to provide an upstream adjustable aperture to regulate the total thermal power exposed to the down stream components. The slits, contained within the same vessel, consist of two actuated jaws positioned serially along the beamline, one mounted horizontally and the other vertically to variably define the beam in the horizontal and vertical direction. Each pair of slits is designed with a single translation drive (up/down for vertical, left/right for horizontal) and with a second drive that adjusts the separation width of the slits (permits precise beam profile measurements with a fixed width slit).

The main design points of the assembly are:

- Each of the slits consists of an inclined block of OFHC copper with a relatively small block of tungsten mounted at the exit end of the slit. Dimensions of slit blade: 80 mm long, 50 mm wide, 30 mm high, and a ~3° incline angle.
- The tungsten edge is precision lapped so that the edge protrudes 0.1 mm above the flat on the OFHC copper incline and defines the beam with a hard edge. The tungsten can be chamfered slightly to further enhance the "hard: defining edge at high energies. The 0.1mm protrusion absorbs very little of the on-axis power density. This "knife-edge" tungsten slit concept has raised no problems in use at sector 13 and 16 at APS.[3, 4]
- The major advantage of this method is that the bulk copper takes the thermal load whilst the tungsten blade provides a hard defining edge for the x-rays.
- The cooling is through copper tubing brazed to the slit blade. No water to vacuum joints.
- The copper blades are mounted in Invar frames for thermal isolation from the support frame and vessel.
- Total length for a pair of actuators (horizontal and vertical) is <50cm.
- The end wall of the chamber can be water cooled to enable any Compton scattering from the slits to be safely absorbed in the chamber walls.
- The drive train has been extensively tested with uni-directional repeatability of 1-2µm and resolution of ~0.5µm. The slits will be equipped with encoders and precision (1micron) limit switches.

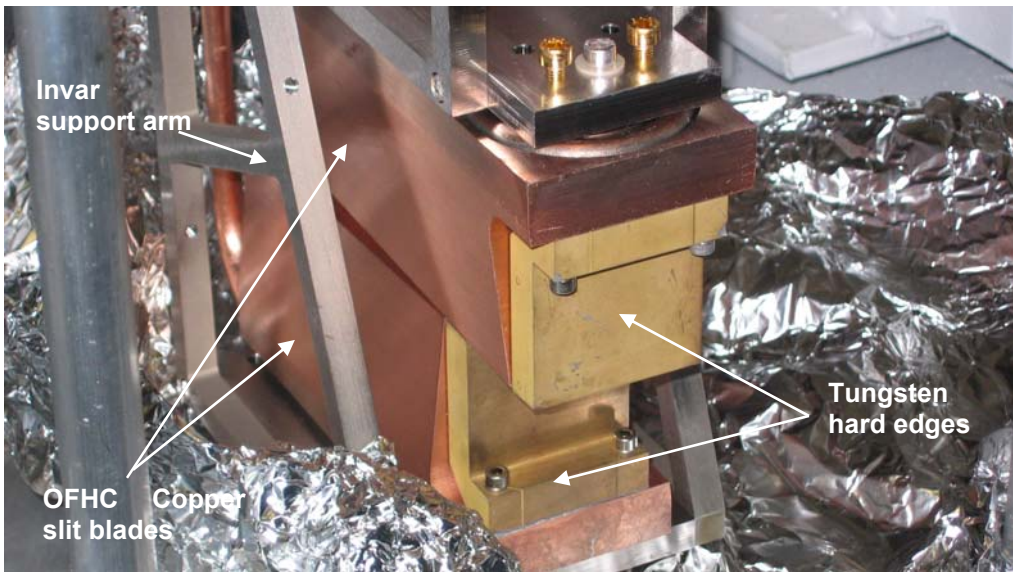

Figure 2.9. High-heat-load slits as used on HXMA ID06 beamline at CLS (designed to operate with >4kW power load).

An FEA model of the slit blade design was run to determine the structural integrity when subjected to the full thermal heat load. To improve the meshing, the FEA model was run with a finer grid than typical, to ensure accurate results. Element sizing can be characterized as fine to very fine, especially around a heat-loaded area and regions considered susceptible to high stress concentrations. The design of the horizontal and vertical slits will be identical; therefore, the incline angle of the slit blades will be fixed by the larger of the horizontal or vertical projected lengths of the beam footprint. The exit aperture of the upstream front end assembly has been set at 1.1 mm (h) by 0.3 mm (v), which at a source point distance of 14 m is equivalent to 78.6 µrad (h) by 21.4 µrad (v). Based on a source point distance of 27.8 m for the white beam slits, the

incident beam is sized at 2.2 mm wide by 0.6 mm high. Therefore, the incline height of the slit blade has been set at 4 mm to allow full acceptance of the beam (including a margin for mis-steer).

When the slit blades are aligned vertically, the incident beam footprint is at a minimum and will therefore produce the highest incident power density. This will be used as the primary design case for the FEA modeling. To apply the thermal load, a small area has been projected onto the optical surface representative of the beam footprint with an applied heat flux 5 W/mm^2 (equivalent to 131 W) to simulate the total thermal load absorbed. Figure 2.10 shows that variation of the horizontal and vertical power densities over the beam footprint are not significant; therefore, using a uniform heat loading for the FEA model is a valid assumption.

Convective cooling has been applied to the feature cut for the brazed coolant pipe. Based on a hydraulic diameter of ~4 mm and a flow rate of 4 L/min, a heat transfer coefficient of 1.8 W/cm^2 K was calculated using the Dittus-Boelter correlation. With the inclusion of thermal contact resistance, the effective heat transfer coefficient on the feature cut has been reduced to 1.5 W/cm^2 K. The results from the thermal models are then loaded into a structural model; with restraints applied to allow free expansion. The results from the FEA model are shown in Figure 2.9.

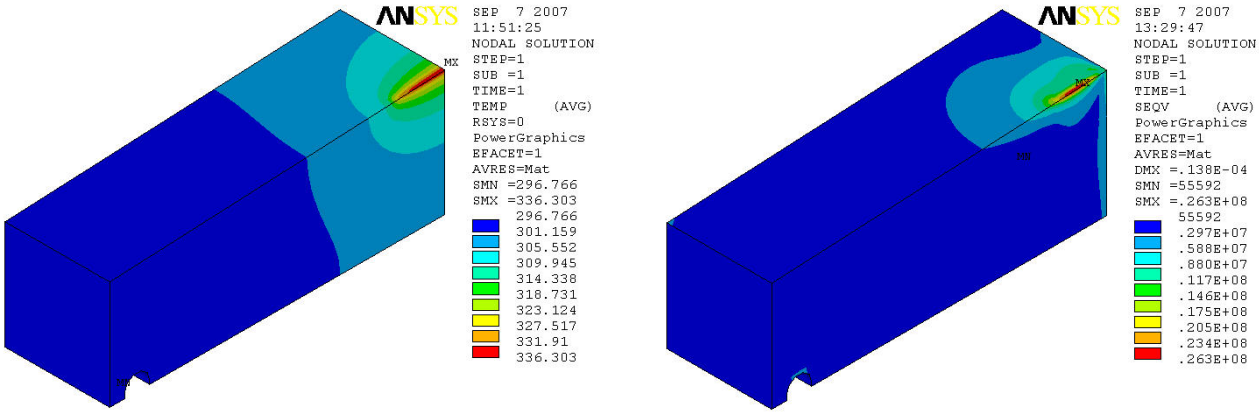

Figure 2.10. Temperature (K) and von Mises stress (Pa) distribution (left and right respectively) of inclined copper block of the white beam slits. The design fatigue stress for OFHC Copper is quoted at 215–254 MPa. The model is therefore not stress critical.

A separate analysis from the main FEA mask model has been undertaken to show the highly localized temperature rise effects on the small at the 0.1mm protrusion of the tungsten jaw into the beam. The 0.1mm element definition required makes the mesh too fine to incorporate into the main mask model. This is a valid model assumption, as the power into the 0.1mm height (by 3.1mm width) is only ~17 W, which makes the local model of the exit aperture almost entirely independent of the main mask model.

- Incident power density = 130.6 W / (2.2 mm x 0.6 mm) = 99 W/mm^2
- Beam footprint area on exit aperture = 0.1 mm x 2. 2 mm = 0.22 mm^2
- Maximum power absorbed into exit aperture = 99 W/mm^2 x 0.22 mm^2 ≈ 22W

To improve the quality of the meshing, the FEA model for the exit aperture was run with a finer grid than is typical, to ensure accurate results. For the thermal model, convective cooling was applied to the contact area between the exit aperture and the slit blade. For reasonable contact pressure exerted by screw fastening (> 4Bar), the effective heat transfer coefficient (representing inverse of thermal resistance) for indium-copper contact[5] is approximately 0.5W/cm^2/K. The bulk temperature for the convective cooling was set to 40°C, this was obtained by probing the contact area from the main FEA model of the slit blade. To apply the thermal load, a small area was projected onto the incident surface and the heat flux (99 W/mm^2) was applied to it. The results from the FEA model are shown in Figures 2.11 and 2.12.

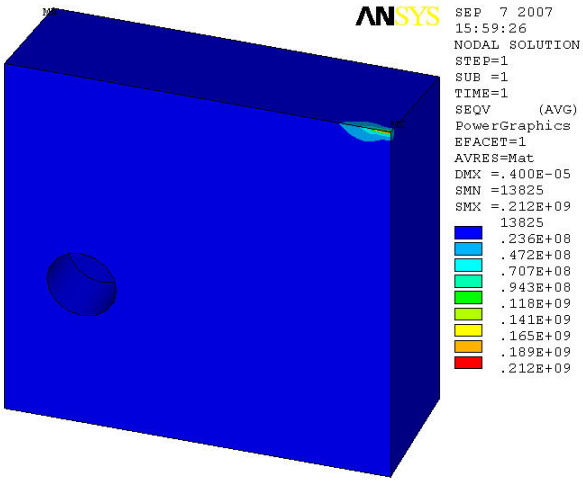

Figure 2.11 Temperature (K) and von Mises stress (Pa) distribution (left and right, respectively) of tungsten jaw of white beam slits. The design fatigue stress for tungsten is quoted at 750 MPa. The model is therefore not stress critical.

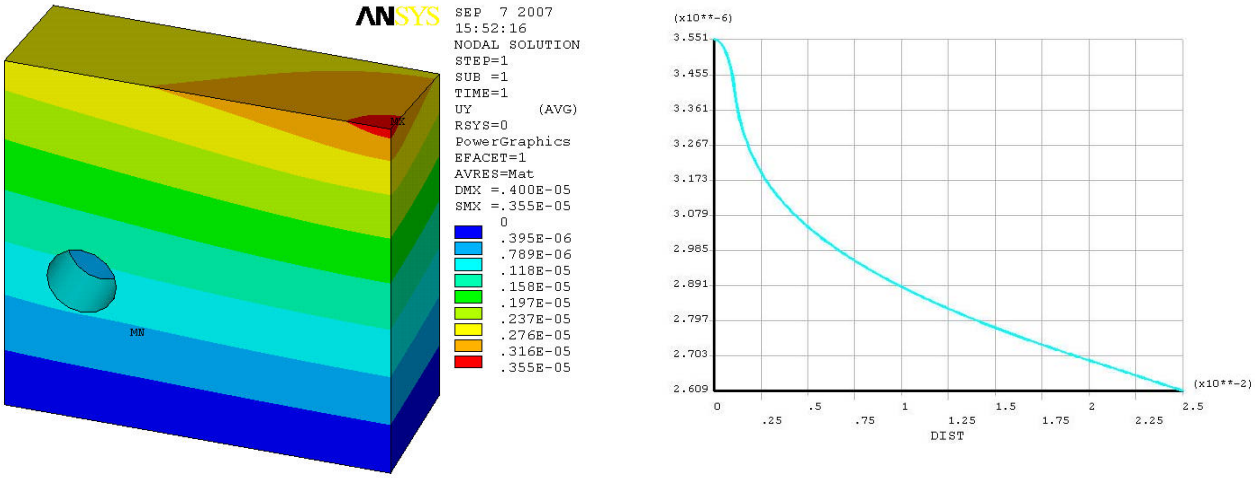

Figure 2.12 Displacement distribution (m) and hard edge displacement profile (m) of tungsten jaw – center at zero (top left and bottom right, respectively). The displacement on the cutting edge is shown to be below 4 microns.

Motion Specification. Table 2.8 details the required motion specification for the WBS assembly.

Table 2.8. Motion Specification for the WBS Assembly.

Motion	Range	Resolution	Drive system
Horizontal and vertical position	±10 mm	<2 µm	Stepper motor driven variable position.
Horizontal and vertical aperture	±5 mm	<0.5 µm	Stepper motor driven variable aperture.

2.4.3.6 Module 4: Horizontal Focusing Mirror (HFM)

Distance to center of undulator	28.8 m

Further power management of the very bright white beam is achieved through a horizontal mirror system. This will be a flat horizontally deflecting mirror used for power management and as a horizontal focusing element in full field mode. To achieve this, two independent moments are applied to either end of the mirror producing a linear moment distribution along the mirror length. The mechanical bender will allow the mirror figure to be corrected for thermal bump when producing unfocused beams as well as allow the horizontal beam to be focused either directly onto the sample or to a secondary horizontal source to be used in a compound focusing mode. In the compound focusing mode nearly the full horizontal source can be made available for full-field imaging.

The principle of the bending mechanism is shown schematically in Figure 2.13. Applying the bending forces to the mirrors through bending holes below the surface allows any distortions resulting from contact strain to dissipate before reaching the optical surface.

The x-ray mirror has two independent functions; suppression of the high energy section of the radiation spectrum and horizontal focusing of the beam. It must be remembered that transmission of photon flux from the source to the sample is the objective of the beamline; therefore reflectivity through the mirror system should be high. The mirror will have an active length of 800 mm, coated with rhodium and bare silicon and operate from 0 – 3 mrad. For low energy reflection (<8 keV), silicon is shown to be an excellent candidate with high reflectivity and harmonic suppression. To maintain mirror reflectivity, a rhodium coating would be used for the operating energies from 8 keV and up.

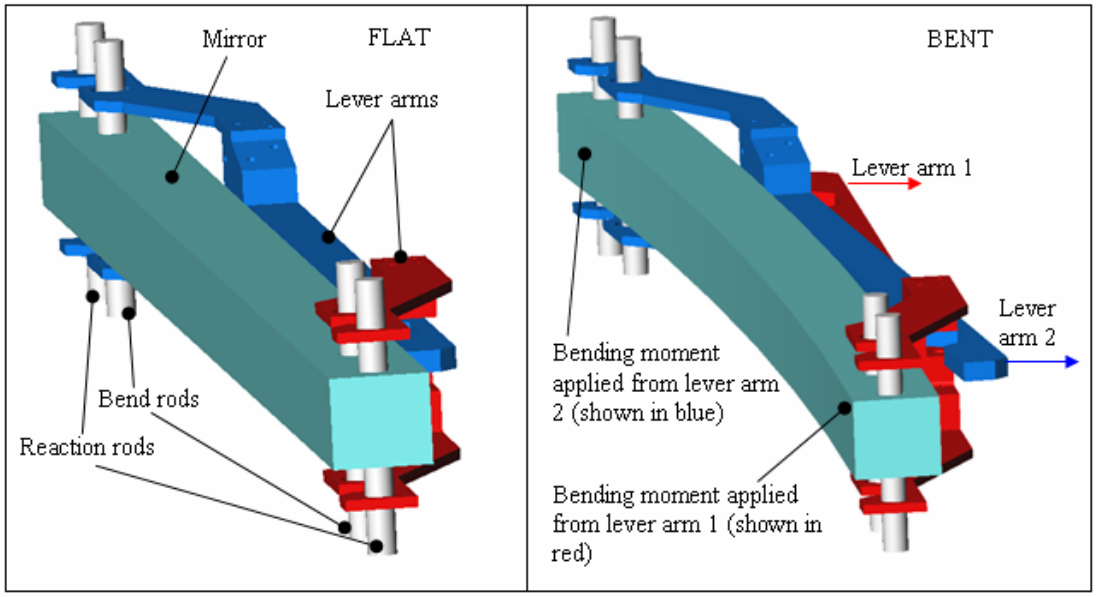

Figure 2.13 Illustrating closed-force bending principle, to be used in horizontal focusing white beam mirror.

Relative to the source distribution (i.e., upstream filters extracted from beam), the mirror power absorption when using each reflective strip is detailed in Table 2.9.

Table 2.9. Mirror Power Absorption, Grazing Angle Set at 3.0 mrad.

Reflective strip	Transmission (W)	Absorption (W)
Silicon	30.9	99.7
Rhodium	80.7	49.9

To determine the mirror displacement due to the thermal heat load, an FEA model of the mirror was run. To improve the quality of the meshing the FEA model for the horizontal mirror has been reduced to half size. Based on the maximum upstream aperture size (differential pump exit aperture), the maximum incident power on the mirror has been calculated at 354 W. To apply the thermal load, a small area has been projected onto the optical surface representative of the beam footprint with an applied heat flux of 213.5 kW/m^2 (equivalent to 130.6 W) to simulate the total thermal load absorbed. Figure 2.6 showed that variation of the horizontal and vertical power densities over the beam footprint are not significant; therefore, using a uniform heat loading for the FEA model is a valid assumption. Convective cooling was applied through the top gallium groove, with an applied heat transfer coefficient of 1 W/cm^2 K. Based on a hydraulic diameter of ~6 mm and a flow rate of 8 L/min, a heat transfer coefficient of 1.5 W/cm^2 K was calculated using the Dittus-Boelter correlation. The heat transfer coefficient value applied inside gallium grooves was lowered to account for the larger wetted area of the grooves relative to the internal area of the coolant pipe. The results from the thermal model are then loaded into a structural model; with restraints applied to allow free expansion. The results from the thermal FEA model are shown in Figure 2.14.

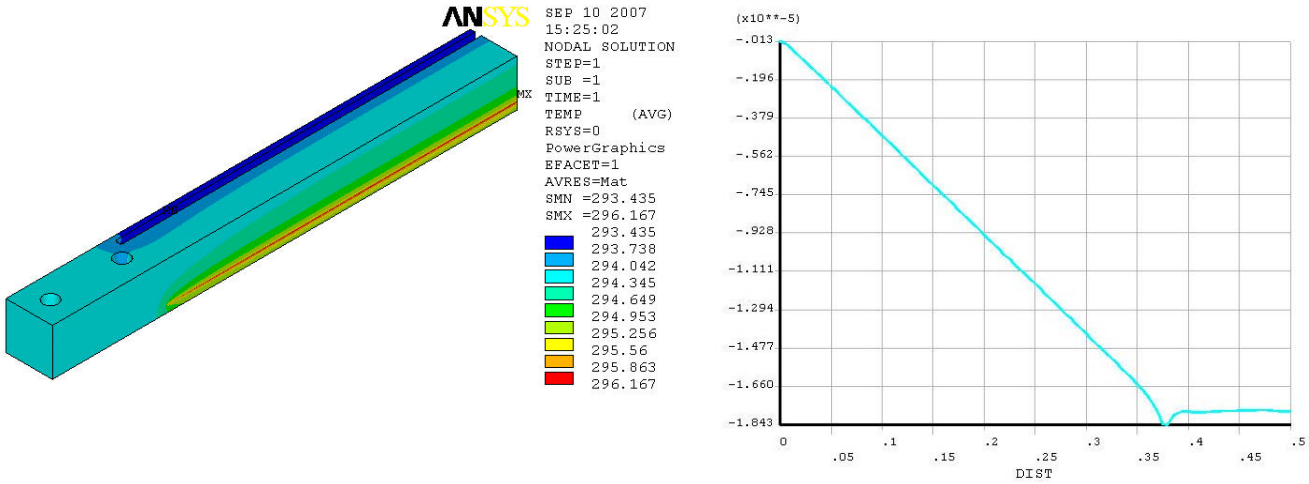

Figure 2.14. Temperature distribution (K) and thermal slope profile (radian) – center at zero (left, top, and right, bottom, respectively).

The ideal mirror bend profile is defined by the focal lengths, the incidence angle, and the optical length of the mirror. To induce the bend and achieve the required central deflection, loads are applied at either end of the mirror through the bending mechanism. However, as thermal bend should also be considered, the bending load applied that is actually applied is calculated to give the corrected mirror profile, as shown in Figure 2.15, taking into account the thermal load.

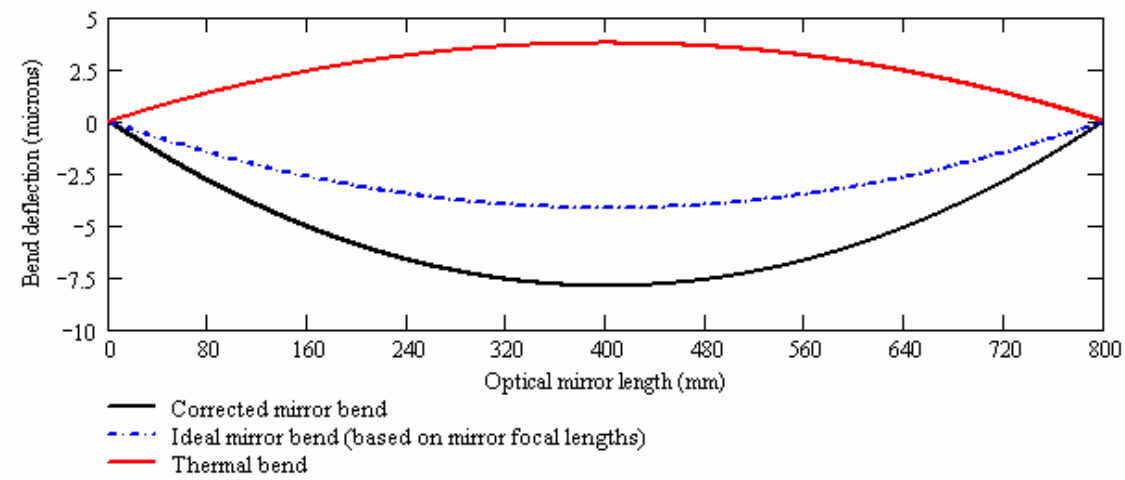

Figure 215. Corrected mirror bend profile, adjusted to include the effects of thermal load.

Since the optical axis normal is perpendicular to the gravity vector (or alternatively expressed, the reflecting optic plane lies parallel to the gravity vector), the requirement for self weight sag appears to be nil. Evidence from previous installations of bent planar mirrors has shown no focus distortion due to possible self weight sag. Based on the corrected mirror bend profile (black line), the deflection at the mid span point along the mirror length was determined. A required bend load of 77 N was then calculated, to give the required deflection at the mid span location. Figure 2.16 superimposes the mirror bend profile (bending loads and thermal bend) with ideal profile based on the mirror's focal length.

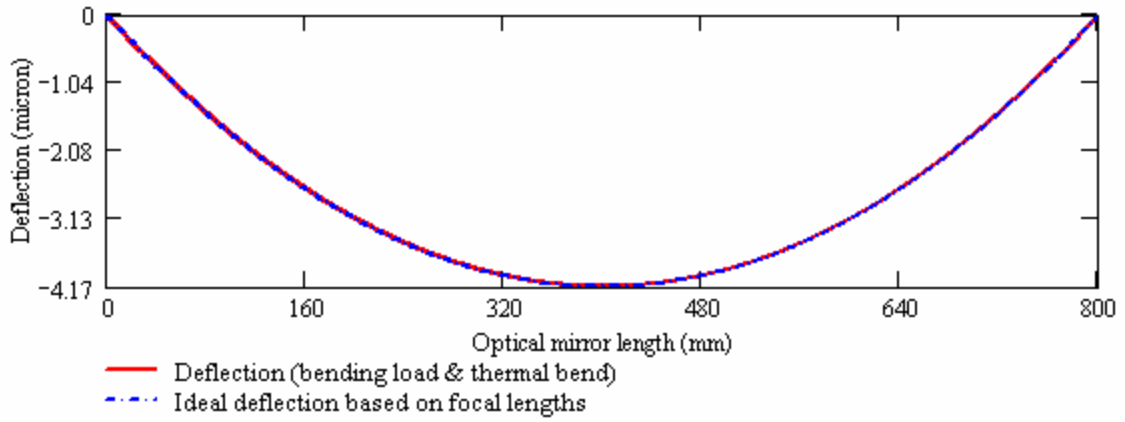

Figure 2.16 Comparison of mirror profiles.

The residual (uncorrectable) slope error is defined as the difference between the mirror slope profile (given by differentiation of its calculated displacement profile) and the slope formed by differentiation of the ideal bend profile (Figure 2.17). The residual slope error of the optically active surface has been corrected to give a root mean squared (RMS) value of 0.32 μrad, calculated over the illuminated length. Note that the optically active area is slightly less than the optical mirror length, due to space taken the bending holes.

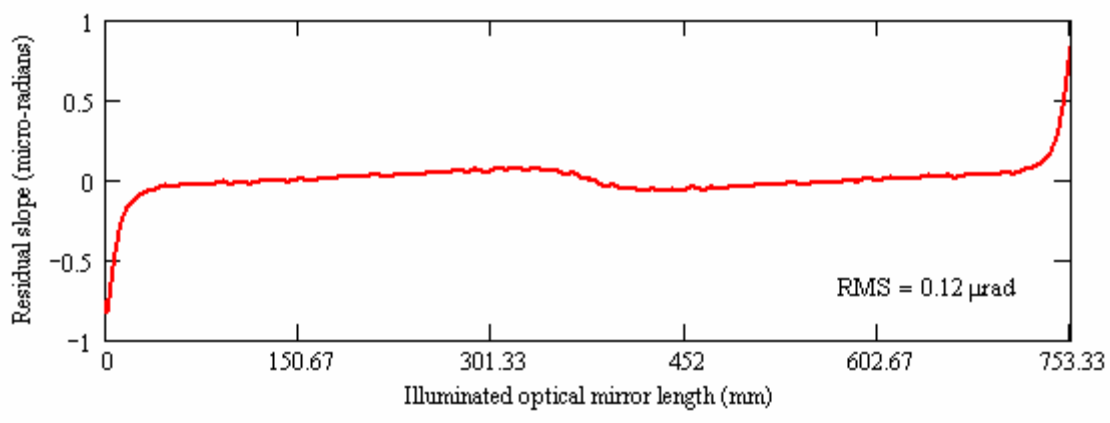

Figure 217 Residual slope error of white beam mirror.

A summary of the key criteria for mirror comparison is given in Table 2.10

Table 2.10 Horizontal Focusing Mirror, Key Criteria.

Description		Focusing mirror, reflecting horizontally
Substrate material		Single crystal silicon
Substrate dimensions		1000 mm long x 50 mm wide x 50 mm deep
Reflective coatings		Rhodium and bare silicon
Focal lengths	F_1	28.8 m
	F_2	∞
Beam acceptance		83 µrad (h) x 56 µrad (v)
Optically active length		754 mm
Incidence angle	θ	3.0 mrad
Radius of curvature	$R = \frac{2}{\left(\frac{\sin(\theta)}{F_1} + \frac{\sin(\theta)}{F_2}\right)}$	19.2 km
Calculated bending load		77 N
Calculated RMS slope error		0.12 µrad
Calculated bending stress	$\sigma = y \cdot \frac{E}{R}$	0.17 MPa

Table 2.11 details the required motion specification for the HFM assembly.

Table 2.11 Motion Specification for the HFM Assembly.

Motion	Range	Resolution	Drive system
Mirror incidence (yaw)	100 mm	<0.05µm	2 stepper motor driven through vacuum actuators.
Motorized fine yaw	±10 µrad	<0.05µrad	Through vacuum piezo driven.
Mirror alignment	±10 mm	<0.2µm	3 stepper motor driven vertical jack systems mounted to base block.
Mirror bending	-10 mm/ +30 mm	<0.2µm	2 stepper motor driven in vacuum actuators.

2.4.3.7 Module 5: Conductance Limiter Beryllium Window (CLBW)

Distance to center of undulator	29.6 m

Located directly upstream of the monochromator, the conductance limiting section is designed to act as a partial vacuum break between the high vacuum (10^{-7} to 10^{-8} Torr) regime in the monochromator and the ultra high vacuum (10^{-9} Torr and better) in the remainder of the beamline. The partial vacuum break is achieved by minimizing molecular flow between regions by providing only very narrow gap between sections, while allowing the beam to pass through (i.e., a vacuum conductance limitation). This is achieved by using an actuated beryllium window such that, when a fixed cooled mask is driven into the beam path, the gap between the frame and the upstream side of the mask is as near zero as possible (~1 mm), limiting the through conductance. There are a number of different designs for mounting the Be foil with the best choice for persevering coherence; these require further study. This uncertainty and the need for research and development translate into budget uncertainty.

Beryllium is a material that is largely transparent to x-rays, and it is therefore well suited to this task, as the beam is affected only in a very small way by passing through. Figure 2.18 shows the mass absorption characteristic for Be, and Figure 2.19 superimposes the transmitted spectral power distribution from the window with the incident distribution profile.

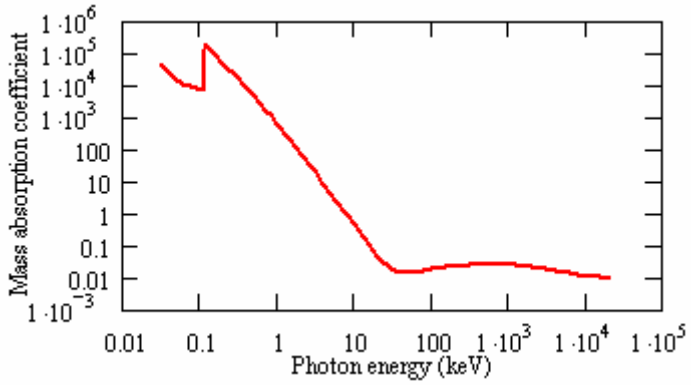

For the 0.003 to 1 KeV energy range, data were taken from:

http://www-cxro.lbl.gov/optical_constants/pert_form.html

For the 1 to 20 MeV energy range, data were taken from:

http://physics.nist.gov/PhysRefData/XrayMassCoef/ElemTab/z04.html

Figure 2.18 Mass absorption characteristic for Be.

The transmitted distribution is calculated by multiplying the incident spectral distribution by the absorption characteristic for beryllium. The sum of transmitted powers at each energy is then divided by the sum of the source power at each energy to give the percentage transmission from the mirror. Relative to the maximum incident heatload (80.7 W – heat load transmitted from the upstream mirror, see Section xx), the power transmission through the window was calculated to be 94.1%.

Motion specification. Table 2.12 details the required motion specification for the Conductance Limiter Beryllium Window assembly.

Table 2.12 Motion Specification for the CLBW Assembly.

Motion	Range	Resolution	Drive system
Filter translation	50 mm	<0.5 mm	Pneumatic through vacuum actuator.

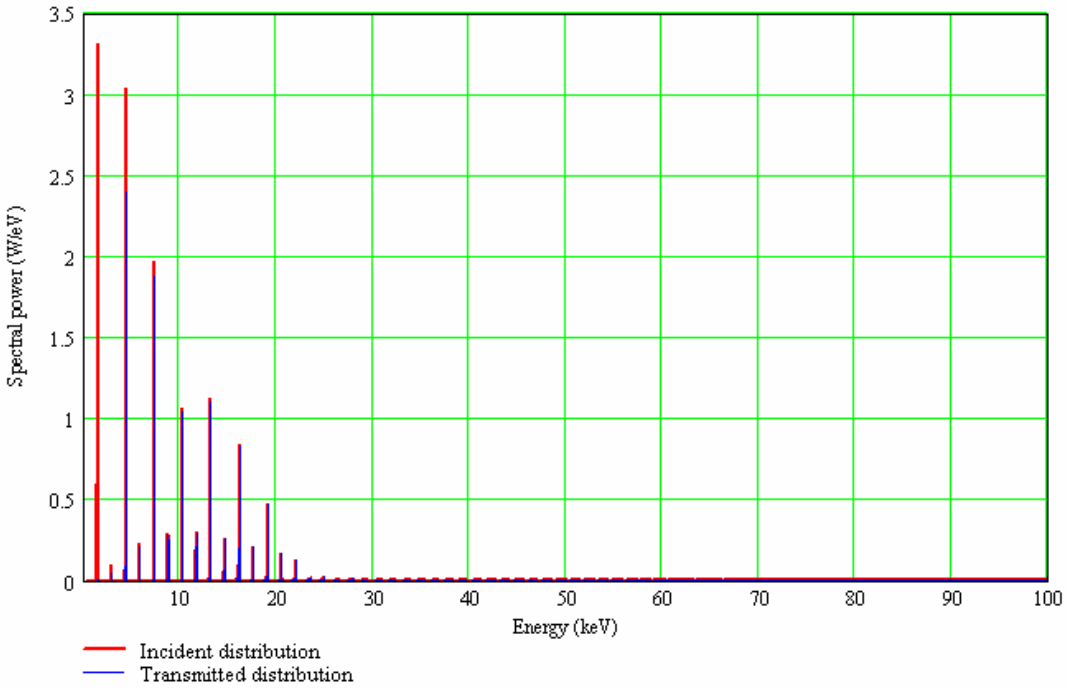

Figure 2.19 Spectral power distributions before and after Be conductance limiter. (Be density = 1850kg/m^3, foil thickness 200 μm).

2.4.3.8 Module 6 - High Heat Load Monochromator (HHLM)

Distance to center of undulator	30.4m

This will be the primary monochromator on the beamline using liquid nitrogen cooled silicon (111) crystals operating with a fixed offset of 20 mm over an energy range of 4 to 24 keV. The energy is changed by rotating the two crystals around a common axis centered on the first crystal surface plane; the output beam height is kept constant by allowing the gap between the faces of the first and second crystal to change (range of motion <1.5 mm) and the beam to "walk" along the surface of a long second crystal. Eliminating the longitudinal translation on the second crystal and replacing it with a long crystal greatly improves ease of tuning energy as well as stability, since the second crystal is more rigidly mounted. Final alignment of the lattice planes of the first and second crystals is achieved with stepper motor-driven actuators for the roll (rotation axis = horizontal axis along the beam), pitch (rotation axis = horizontal axis perpendicular to the

beam) and yaw (rotation axis = vertical axis perpendicular to the beam) adjustment of the second crystal plus a piezoelectric device for the fine pitch and roll adjustment.

Thermal and vibration stability will be of primary importance in this monochromator design. The liquid nitrogen cooling needed to maintain the thermal distortions at acceptable levels has the potential for introducing unacceptable vibration. Managing vibration issues at the level suitable for a nano focus beamline will require research and development effort, including prototypes, and therefore will increase the cost of the final instrument.

The preliminary cooling design for extracting the absorbed heat load is based on the indirect crystal cooling arrangement (similar in principle to that widely used at SPring-8). Since the incident heatload is relatively low, and to improve vibration stability, short lengths of copper braid will be used to connect the liquid nitrogen coolant pipe to the copper blocks. To provide a good thermal contact, indium foil is used between the sides of the silicon crystal and copper blocks. The indium foil has a secondary benefit of absorbing the differential expansion between the copper blocks and silicon crystal and limits the resulting stress and strain transmitted to the silicon at low temperatures. To determine the crystal displacement due to the thermal heat load, an FEA model of the crystal was run. This report shows the FEA results for the silicon crystal only. Element sizing can be characterized as fine to very fine, especially around a heat-loaded area and regions considered susceptible to high-stress concentrations.

To apply the thermal load, a small area has been projected onto the optical surface representative of the beam footprint with an applied heat flux 4.53E+6 W/m^2 (equivalent to 80.7 W – maximum heat load transmitted from upstream mirror, see Section xx) to simulate the total thermal load absorbed. Figure 2.6 showed that variation of the horizontal and vertical power densities over the beam footprint are not significant; therefore, using a uniform heat loading for the FEA model is a valid assumption.

Convective cooling was applied to the cooled contact area between the crystal and the cooled copper heat exchangers. Based the Dittus-Boelter correlation, the heat transfer coefficient through the coolant pipes is given by:

Reynolds number, Re

The Reynolds number is given by:

$$\mathrm{Re} = \rho \cdot \left(\frac{V}{\pi \cdot \left(\frac{D_h}{2} \right)^2} \right) \cdot \left(\frac{D_h}{\mu} \right), \tag{2-9}$$

where

ρ = coolant density (795.52kg/m^3 for liquid nitrogen),

V = volumetric flow rate (4 L/min),

D_h = hydraulic diameter (10 mm), and

μ = dynamic viscosity (0.001465 poise for liquid nitrogen).

Substitute known values and calculate the Reynolds number.

$$\mathrm{Re} = \left(795.52 kg / m^3\right) \cdot \left(\frac{4\, litres/\min}{\pi \cdot \left(\frac{10mm}{2}\right)^2} \right) \cdot \left(\frac{10mm}{0.001465\, poise} \right) = 46092.7 \,. \tag{2-10}$$

Prandtl number, Pr

The Prandtl number is given by:

$$\mathrm{Pr} = \mu \cdot \left(\frac{Cp}{K} \right), \tag{2-11}$$

where Cp = specific heat (2048.2J/kg K for liquid nitrogen) and K = thermal conductivity (0.14086W/m K for liquid nitrogen). Substitute known values and calculate the Prandtl number.

$$\mathrm{Pr} = \left(0.001465\, poise \cdot\right) \left(\frac{2048.2 \frac{J}{kg \cdot K}}{0.14086 \frac{W}{m \cdot K}} \right) = 2.1 \tag{2-12}$$

Nusselt number using the Dittus-Boelter correlation, Nu

For fully developed turbulent flow in smooth tubes, the Nusselt number is defined as:

$$Nu = 0.023 \cdot \mathrm{Re}^{0.8} \cdot \mathrm{Pr}^{0.3} \,. \tag{2-13}$$

Substitute known values and calculate the Prandtl number.

$$Nu = 0.023 \cdot \left(46092.7\right)^{0.8} \cdot \left(2.1\right)^{0.3} = 155.3 \tag{2-14}$$

Heat transfer coefficient through cooling channels, HTC

The heat transfer coefficient is defined as:

$$HTC = \frac{K \cdot Nu}{D_h} \,. \tag{2-15}$$

Substitute known values and calculate heat transfer coefficient.

$$HTC = \frac{\left(0.14086 \frac{W}{m \cdot K}\right) \cdot \left(155.3\right)}{\left(10mm\right)} = 2187.5 \frac{W}{m^2 \cdot K} \,. \tag{2-16}$$

With the inclusion of thermal contact resistance, the effective heat transfer coefficient on the crystal contact surface is given by:

$$HTC = \left[\frac{1}{fa \cdot HTC_0} + \sum R(Cu) + \sum R(In) + Rc \right]^{-1}, \tag{2-17}$$

where

fa = ratio of cooling channel surface area and contact surface area,

HTC_0 = heat transfer coefficient of the coolant in the cooling channels (0.83W/cm^{2}K),

$\sum R(Cu)$ = sum of the thermal conduction resistances in the copper,

$\sum R(In)$ = sum of the thermal conduction resistances in the indium and

Rc = thermal contact resistance at the interface.

As the thermal conductivity of silicon is high at cryogenic temperatures, it is useful to increase the contact surface area by oversizing the crystal height to improve heat transfer (crystal length is limited to prevent interference with the diffracted beam off the second crystal). The ratio of cooling channel surface area and contact surface area is given by:

$$fa = \frac{\text{cooling channel surface area}}{\text{contact surface area}} = \frac{6283.185 mm^2}{7000 mm^2} \approx 0.9 . \tag{2-18}$$

For thicknesses of copper and indium of 3 to 11 mm and 0.5 mm, respectively, the thermal conduction resistance through a single thickness takes the following values:

$$R(Cu) = \begin{pmatrix} 0.75 \\ 2.75 \end{pmatrix} \times 10^{-5} \, m^2 \cdot K \cdot W^{-1} , \tag{2-19}$$

and

$$R(In) = 0.62 \times 10^{-5} \, m^2 \cdot K \cdot W^{-1} . \tag{2-20}$$

Depending on the surface finish, the thermal contact resistance at the interface takes the following values:

$$Rc = \begin{pmatrix} 1 \\ 20 \end{pmatrix} \times 10^{-5} \, m^2 \cdot K \cdot W^{-1} . \tag{2-21}$$

The cooling arrangement includes three copper and two indium interfaces. We substitute known values and calculate heat transfer coefficient at contact surface:

$$HTC = \left[\frac{1}{(0.9) \cdot \left(2187.5 \frac{W}{m^2 \cdot K} \right)} + 3 \times \begin{pmatrix} 0.75 \\ 2.75 \end{pmatrix} \times 10^{-5} \frac{m^2 \cdot K}{W} + 2 \times 0.62 \times 10^{-5} \frac{m^2 \cdot K}{W} + \begin{pmatrix} 1 \\ 20 \end{pmatrix} \times 10^{-5} \frac{m^2 \cdot K}{W} \right]^{-1} \tag{2-22}$$

$$HTC \approx \begin{pmatrix} 1804.4 \\ 1243.5 \end{pmatrix} \frac{W}{m^2 \cdot K}. \tag{2-23}$$

For the FEA model, with the inclusion of thermal contact resistance, the effective heat transfer coefficient on the crystal contact surface has been reduced to 1,200 W/m^2 K. An estimation of the bulk temperature at the contact surface between the crystal and the heat exchanger is given by:

$$T_{crystal\_holder} = \frac{\Delta Q_{Cu}}{K_{Cu}} \cdot \frac{L}{S} \cdot + T_{heat\_exchanger} = \frac{80.7W}{500W/m \cdot K} \cdot \frac{20mm}{300mm^2} + 78K \approx 89K\,, \tag{2-24}$$

where

ΔQ = power dissipated through the copper braids (80.7W),

K_{Cu} = thermal conductivity of copper (500W/m K at cryogenic temperatures),

S = effective section area of braid (300mm^2),

L = braid length (20mm),

$T_{crystal\_holder}$ = temperature at interface between crystal and holder, and

$T_{heat\_exchanger}$ = temperature of liquid nitrogen coolant (78K).

To ensure good thermal contact between the cooled copper block and the silicon crystal, a contact pressure is applied to the side of the copper block, pushing it inward against the silicon crystal. Contact pressure has been set at 350 kPa; this value of contact pressure is based on an approximate relationship of 100 Pa per sq mm of contact area.[6]. This is based on a contact area of 70 mm x 50 mm.

Table 2.13 Summary of Loads Applied to FEA Model.

Case description	E=24 keV	
Thermal model loading	Beam size:	2.26 mm (h) x 0.65 mm (v)
	Heat flux loading:	4.53E+6 W/m^2
	Convection cooling:	HTC = 1200 W/m^2 K
		Bulk temperature = 89 K
Structural model loading	Results from the thermal model are loaded into a structural model, with restraints applied to allow free expansion.	
	Clamping pressure:	350 kPa

Previous thermal analysis of monochromator crystals has shown that the primary design case for selecting the crystal design is generally fixed by the optical performance at the higher energies as a result of the narrower rocking curve widths. The results from the FEA case modeled at 24 keV are shown in Figure 2.20.

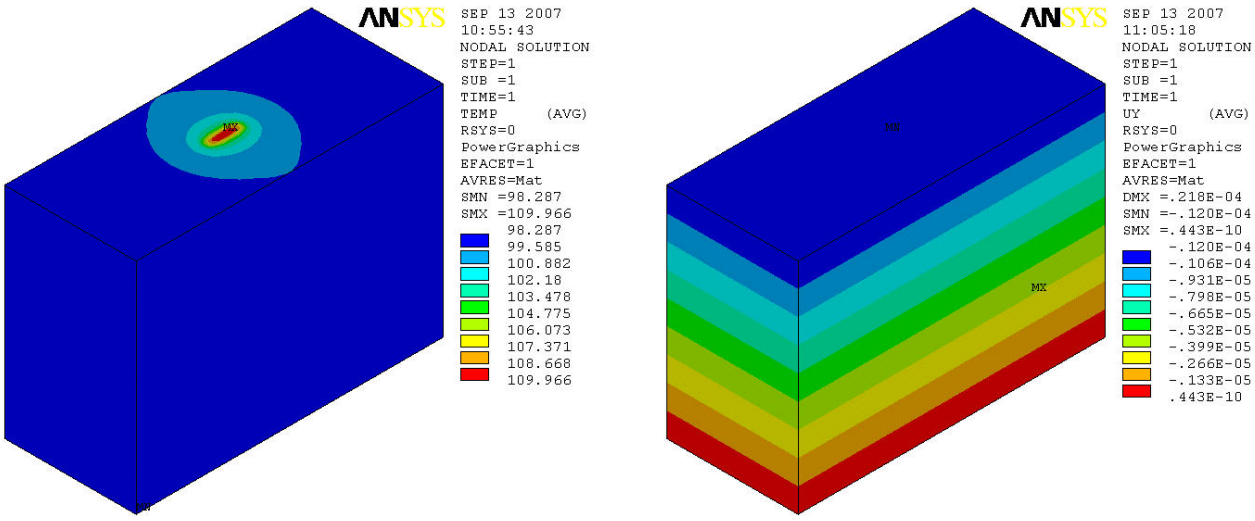

Figure 2.20. Temperature (K) and displacement (m) distribution (left and right, respectively).

To achieve an efficient photon flux transmission at the second monochromator crystal, the slope error on the first crystal should be a fraction of the rocking curve width. Since the rocking curve width is a function of energy, then the slope error for the crystal will also be dependent on the beam's energy. We use this as a basis for a conservative calculation for the first crystal's optical performance. The rocking curve width is the FWHM value for the curve that defines the peak shape on rocking the crystal in the diffracted beam. Assuming a Gaussian curve form, a relative distribution can be determined using the FWHM value. Any slope error on the first crystal surface will result in a shift of this distribution. The quantity of beam reflected is defined by the region shared by the relative distributions, as shown in Figure 2.21. For silicon (111) at 24 keV, the rocking curve width is 11.6 µrad. Based on an integrated reflectivity of 70%, the maximum allowable slope error has been calculated at 3.8 µrad. Approximately 92% of the tangential beam footprint has been shown (Figure.22) to be under the 3.8 µrad slope error limit.

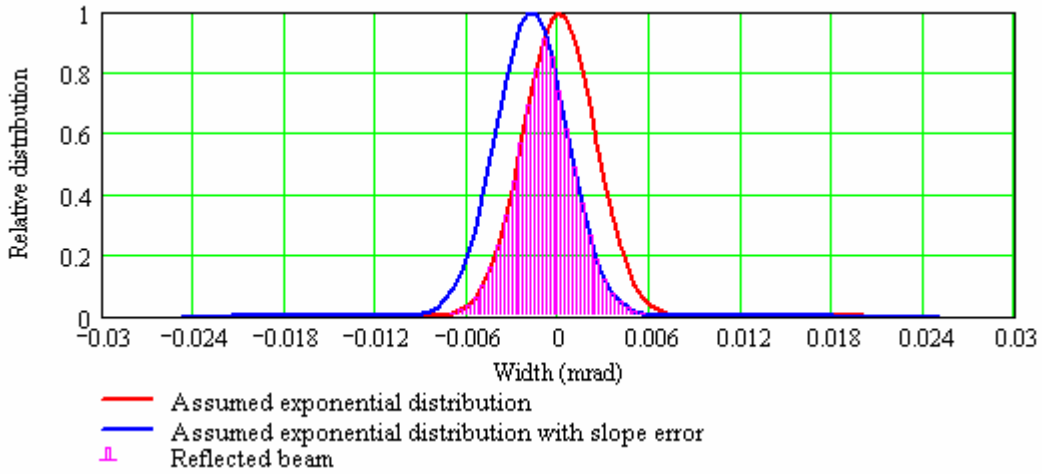

Figure 2.21 Relative distributions with slope error shift.

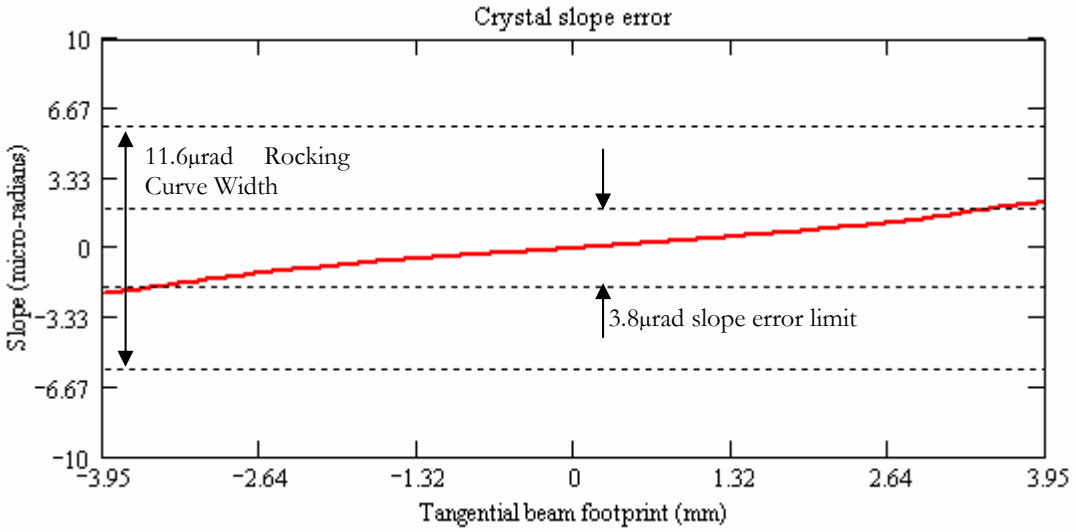

Figure 2.22 Slope profile of the first crystal with white beam incident at 24 keV.

Motion Specification. The origin for each axis will be set at the beamline source point, with the axis arrangement following the right hand rule (see Figure2.23). Some notes are provided below.

- The x-axis will be horizontal and perpendicular to the beam, in the direction away from the ring (outboard).
- The y-axis will be vertical.
- The z-axis will be horizontal and parallel with the beam, in the direction of propagation of the x-ray beam.

All rotations about a given axis are positive if, when looking along the axis in the positive direction, the rotation is clockwise.

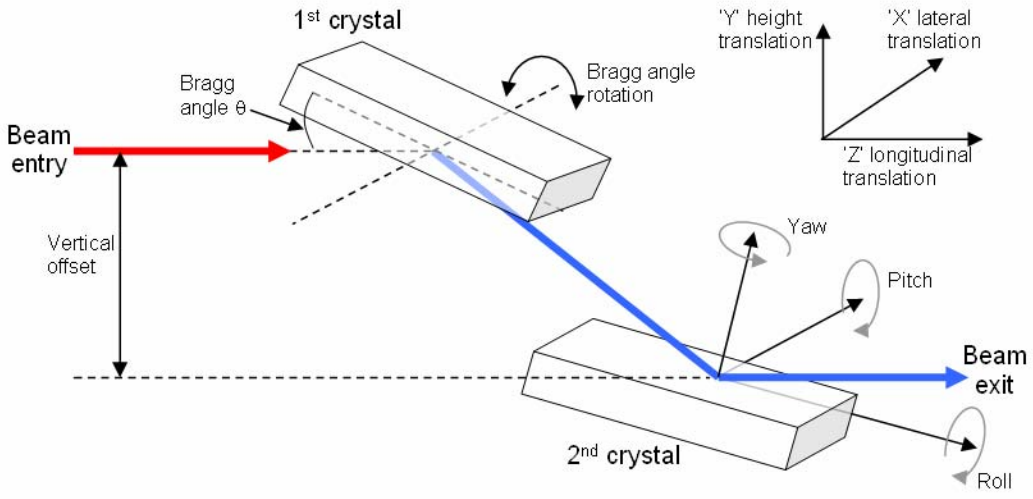

Figure 2.23 Schematic illustration of axis and angle convention.

Table 2.14 details the required motion specification for the HHLM assembly.

Table2.14 Motion Specification.

Motion	Range	Resolution	Drive system
Primary drive			
Bragg angle	-5° to 30°	<1 μrad	In vacuum stepper motor driven.
Support system			
Manual pitch (rotation about x axis)	±1°	<0.25°	System alignment.
Manual roll (rotation about y axis)	±1°	<0.25°	System alignment.
Manual yaw (rotation about z axis)	±1°	<0.25°	System alignment.
Manual lateral (x direction)	±10 mm	<250 μm	System alignment.
Manual height (y direction)	±10 mm	<250 μm	System alignment.
Manual longitudinal (z direction)	±10 mm	<250 μm	System alignment.
First crystal adjustment			
Manual roll (rotation about y axis)	±1°	<0.01°	Crystal alignment.
Manual perpendicular (Y)	±1 mm	<10 μm	Crystal alignment.
Second crystal adjustment			
Motorized coarse pitch (rotation about x axis)	±1°	<5 μrad	In vacuum stepper motor driven.
Motorized fine pitch	200 μrad	<0.05 μrad	In vacuum piezo driven.
Motorized coarse roll	±1°	<5 μrad	In vacuum stepper motor driven.
Motorized fine roll	200 μrad	<0.05 μrad	In vacuum piezo driven.
Motorized coarse yaw (rotation about z axis)	±1°	<5 μrad	In vacuum stepper motor driven.
Motorized perpendicular (to keep fixed offset)	±2 mm	<1 μm	In vacuum stepper motor driven.

2.4.3.9 White Beam Monitor (WBM)

Distance to center of undulator	30.9 m

The retractable White Beam Monitor (WBM) is a combined viewing screen and total intensity monitor for white beam (mirror in) and pink beam (mirror out), positioned directly downstream of the HHLM. It consists of a tungsten screen that is electrically isolated, water cooled, and phosphor coated. The total white and peak beam can be monitored by measuring the photo current. The beam can be visually monitored by locating a UHV window that allows a video camera to see the screen. This device will allow the position of five upstream components in succession to be optimized: 1) FEDPM, 2) FEHAM, 3) WBS, 4) HFM, and 5) HHLM. Once the alignment is complete, the WBM is retracted from the beam with a pneumatic actuator.

2.4.3.10 Bremsstrahlung Collimator (BC)

Distance to center of undulator	31.4 m

The Bremsstrahlung Collimator (BC) acts directly to restrict the size of the bremsstrahlung fan downstream. The use of external clad lead for this collimator is much less expensive than vacuum-prepared tungsten and makes best use of the limited space around this cramped area. The lead bremsstrahlung shield will comprise specially made interlocking bricks with no direct line of sight (shine path) permitted through any interspaces between the bricks. The lead will be security fastened in place to prevent removal and also will be clad in stainless steel sheet metal or Perspex covers. Connection of this standalone component is made to the beamline by flexible bellows at both entrance and exit.

The collimator is classified as a critical survey item which must not be moved once it has been set and aligned.

2.4.3.11 Monochromatic Fluorescent Screen (MFS)

Distance to center of undulator	31.9 m

The Monochromatic Fluorescent Screen (MFS) is a retractable YAG fluorescent screen that will allow the monochromatic beam to be viewed with a CCD camera for initial monochromator setup. Once the alignment is complete, the MFS is retracted from the beam with a pneumatic actuator.

2.4.3.12 Secondary Horizontal Source Aperture (SHSA)

Distance to center of undulator	32.0 m

The SHSA is an adjustable horizontal monochromatic slit intended to act as a backup secondary coherent source. The slit blades will be electrically isolated so the photo current can be measured from each blade. This will allow the SHSA to also function as a horizontal beam position monitor that can be used in a feedback mode with the HFM piezo yaw actuator.

2.4.3.13 Monochromatic Shutter (MS1)

Distance to center of undulator	32.5 m

This is a standard monochromatic shutter located close to the back wall of the optics enclosure.

2.4.3.14 Back Wall (BW)

Distance to center of undulator	33.0 m

2.4.3.15 Optics Enclosure - Incident Power Loads

Table 2.15 Summary of the Incident Heat Loads along the Optical Components within the FOE.

Component	Source Point distance	Beam size	Incident power	Transmitted power
Module 1				
Front End Differential Pump Mask (FEDPM)	14 m	1.1 mm (h) x 0.3 mm (v)		130.6 W
Front End Defining Aperture Mask (FEDAM)	1 5 m	0.3 mm (h) x 0.3 mm (v)		35.7 W
Shield Wall	26.7 m			
Module 2 Notes: Front end aperture set to 1.1 mm (h) x 0.3 mm (v)				
White Beam Filters (WBF)	27.3 m		130.6 W	
Filter thickness (μm)				
30				125.2 W
300				107.8 W
1000				87.1 W
Module 3 Note: All white beam filters removed from x-ray beam.				
White Beam Slits (WBS)	27.8 m		130.6 W	130.6 W →0 W
Module 4 Note: White beam slits open.				
Horizontal Focusing Mirror (HFM)	28.8 m		130.6 W	
reflective strip				
silicon				30.9 W
rhodium				80.7 W
Module 5 Note: Rhodium reflective strip selected on upstream mirror.				
Conductance Limiter Beryllium Window (CLBW)	29.6 m		80.7 W	75.9 W
Module 6 Note: Conductance limiter beryllium window removed from x-ray beam.				
High Heat Load Monochromator (HHLM)	30.4 m		80.7 W	0 W

2.3.6 Radiation Enclosure Design

There are several high-quality vendors for radiation hutches in Europe, as follows:

Calder-UK

Caratelli- France

Innospec-Germany

These suppliers have carried out detail design and build of radiation hutches at DLS, ESRF, SLS, and Soleil. Some of the issues the vendors need to consider are as follows:

- FOE enclosure is required to be designed as white beam enclosure.
- Stations A and B are required to be mono beam enclosures.
- The minimum shielding thickness will be in accord with NSLS-II documents.
- All the doors will be sliding doors – double for equipment and single for personnel.
- All standard enclosure heights will be 3.2 m.
- The roof of each enclosure will be surrounded by a railing to permit safe personnel access.
- Convenient access to the roof areas on the FOE, Station A, and Station B is via three access ladders.

2.4.4 Instruments

2.4.4.1 Endstation 1

Discussion of the endstation specifications and requirements is still under development.

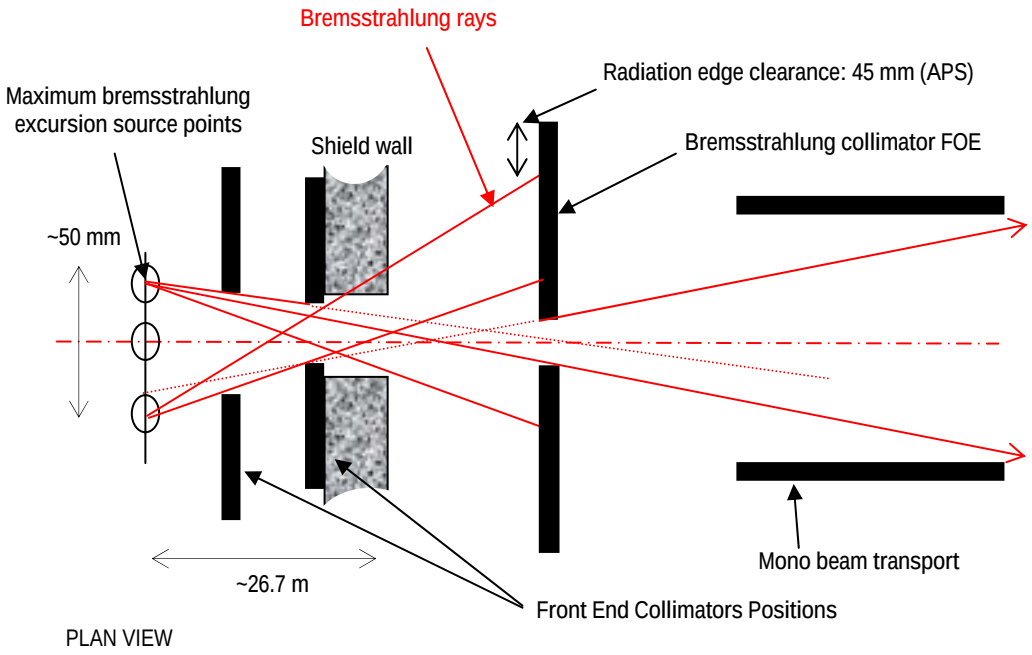

Figure 2.24. Type of bremsstrahlung anamorphic ray diagram required for effective safe beamline design.

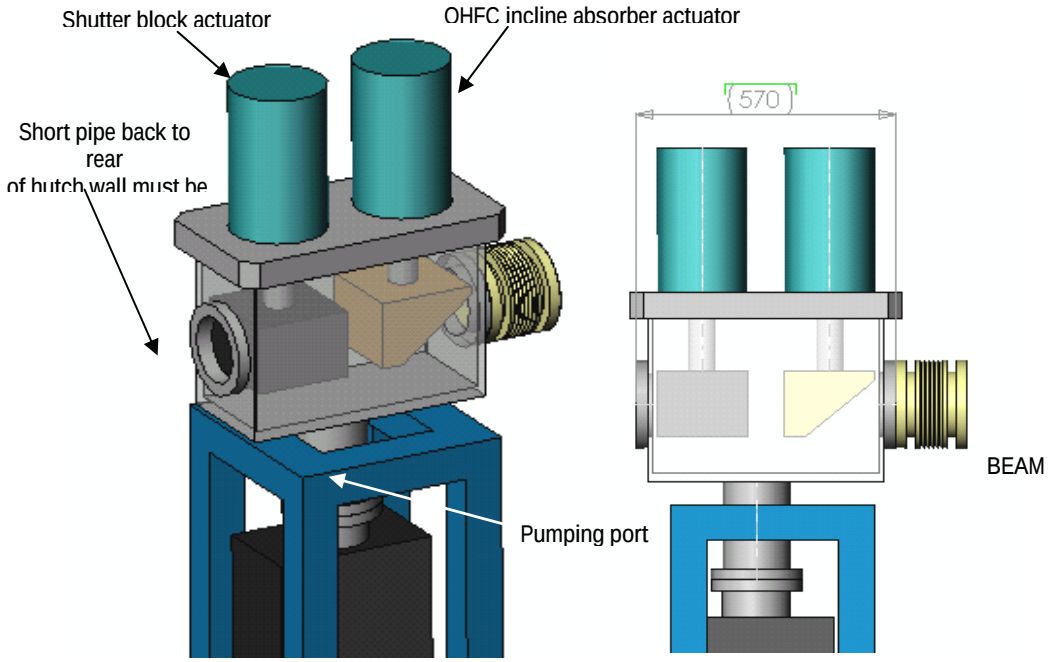

Figure 2.25 Integrated bremsstrahlung/thermal stop shutter.

2.5.3 Equipment Protection System

A Beamline Equipment Protection System (EPS) will also be required: The following table shows the preliminary fault protection logic for the beamline. The EPS protects against damage or failure due to beam heating and inadvertent vacuum let-up.

Component	Type	Action	Consequences
19-A (FOE)			
19-VALV	valve	open requested	opens valve if IMG1 ok
		close requested	closes if FE shutter closed
		air pressure fault	closes FE shutter
19-IMG01	vacuum pressure	trips high	closes FE shutter closes VALV-01 & VALV-02
19-IONP01	ion pump	on requested	turns on if IMG1 ok
19-FILT1/2/3/..	Incident Power Filter	water trips low	closes FE shutter & absorber
19-IONP02	ion pump	on requested	Turns on if IMG1 ok
19-HS1	White Beam horizontal slit	water trips low	closes FE shutter & absorber
19-VS1	White Beam vertical slit	water trips low	closes FE shutter & absorber
19-HS2	White Beam horizontal slit	water trips low	closes FE shutter & absorber
19-VS2	White Beam vertical slit	water trips low	closes FE shutter & absorber
19-VALV01	gate valve	open requested	opens valve if IMG1+IMG2 ok
		close requested	closes if FE shutter closed
		air pressure fault	closes FE shutter
19-IMG	vacuum pressure (HM mirror tank)	trips high	closes FE shutter & absorber VALV02 & 01
19-IMG	vacuum pressure	trips high	closes FE shutter closes VALV-02
19-HM	horizontal mirror	water trips low	closes FE shutter & absorber
19-IONP02	ion pump	on requested	turns on if IMG02 ok
19-VALV02	valve	open requested	opens valve if IMG2+IMG3 ok closes if FE shutter closed
		close requested air pressure fault	closes FE shutter
19-IMG	vacuum pressure	trips high	closes FE shutter closes VALV-02
19-BW1	Be window conductance limiter	water trips low	closes FE shutter & absorber
19-HHM	high heat load monochromator	water trips low	closes FE shutter & absorber
19-IONP04	Ion pump	on requested	Turns on is IMG03 ok
19-WBM	white beam monitor	LN2 trips low	closes FE shutter & absorber
19-STOP1	bremsstrahlung stop	Fixed item Possibly water cooled stop- water trips low	FIXED aperture closes FE shutter & absorber
19-MFS1	monochromatic fluorescent screen	water trips low	closes FE shutter & absorber
19-VALV03	valve	open requested close requested air pressure fault	opens valve if IMG3+IMG4 ok closes if FE shutter closed closes FE shutter
19-IMG04	vacuum pressure	trips high	closes FE shutter closes VALV-03

Component	Type	Action	Consequences
19-SHSA	secondary horizontal source aperture	water trips low	closes FE shutter & absorber
19-IONP05	ion pump	on requested	turns on if IMG04 ok
19-SHUTTER1	monochromatic shutter	open (thru) requested close (stop) requested	opens 19-FE shutter closes 19-FE shutter
19-FOE	back wall for FOE (ID-A)	trips high	closes FE shutter & absorber closes VALV03
19-SBT1	shielded beam transport	on requested	turns on if IMG ok
19-	front wall of hutch (ID-B)		
19-VALV04	valve	open requested close requested air pressure fault	opens valve if IMG4+IMG5 ok closes if FE shutter closed closes FE shutter
19-IMG	vacuum pressure	trips high	closes FE shutter closes VALV-04
19-QDBPM	quad diode BPM		
19-THSA	tertiary horizontal source aperture		
19-IONP	ion pump	on requested	turns on if IMG ok
19-MFS2	monochromatic fluorescent screen		
19-VALV05	valve	open requested close requested air pressure fault	opens valve if IMG5+IMG6 ok closes if FE shutter closed closes FE shutter
19-IMG06	vacuum pressure	trips high	closes FE shutter & absorber closes VALV05
19-IONP07	ion pump	on requested	turns on if IMG06 ok
19-HRM	high-resolution monochromator		
19-BW2	Be window		
19-NFO1	nanometer focusing optics		
19-	back wall of (ID-B)		
19-SBT2	shielded beam transport		
19-	front wall of (ID-C)		
19-NFO2	nanometer focusing optics		

Notes: Vacuum pressure trips using Inverted Magnetron Gauges (IMG) and not Piranis on each gauge cluster

Figure 2.26 is a diagram of the vacuum flow for the HXN beamline. Figure 2.27 is the EPS diagram.

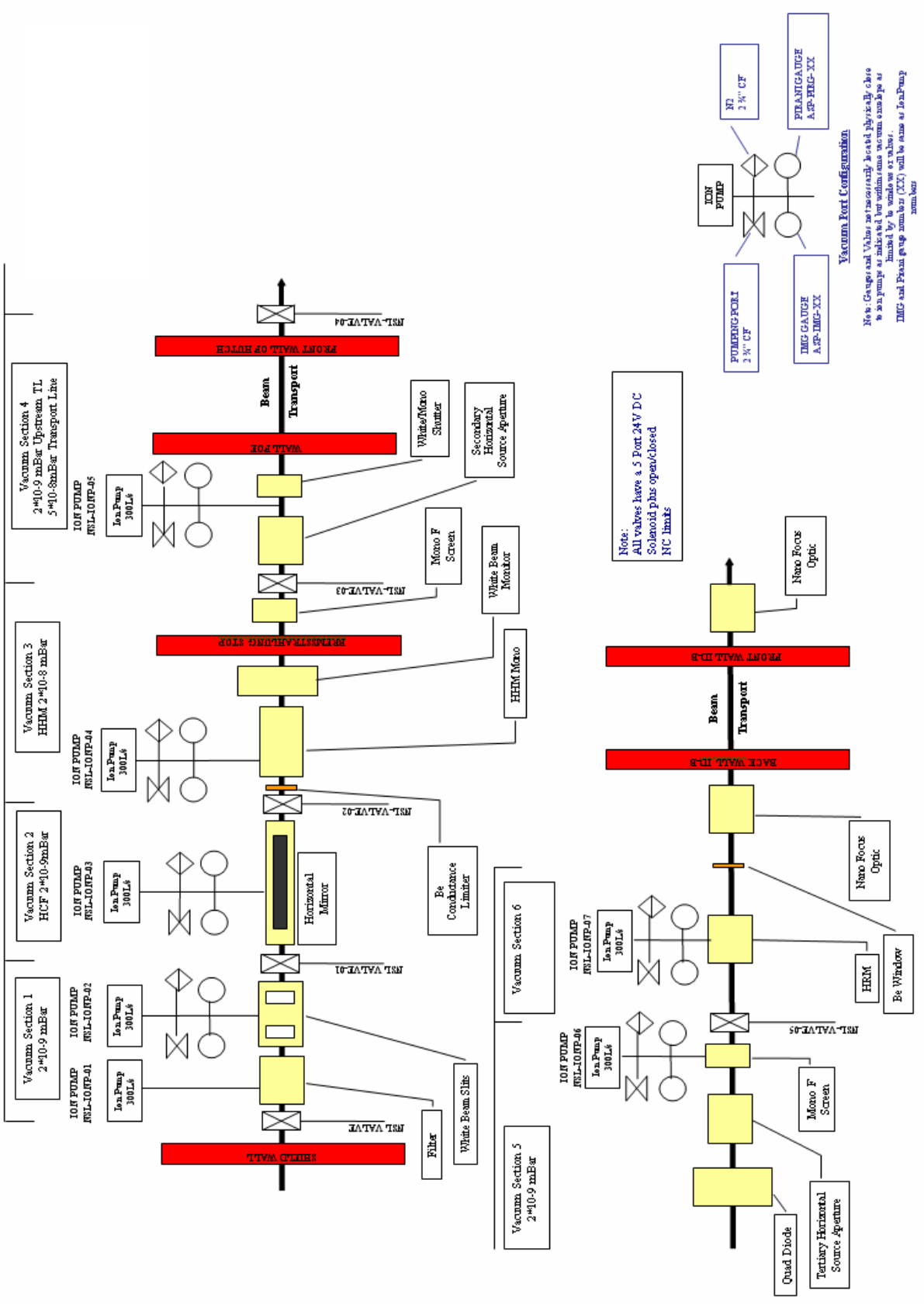

Figure 2.26 Hard X-ray Nanoprobe Beamline Vacuum Flow Diagram

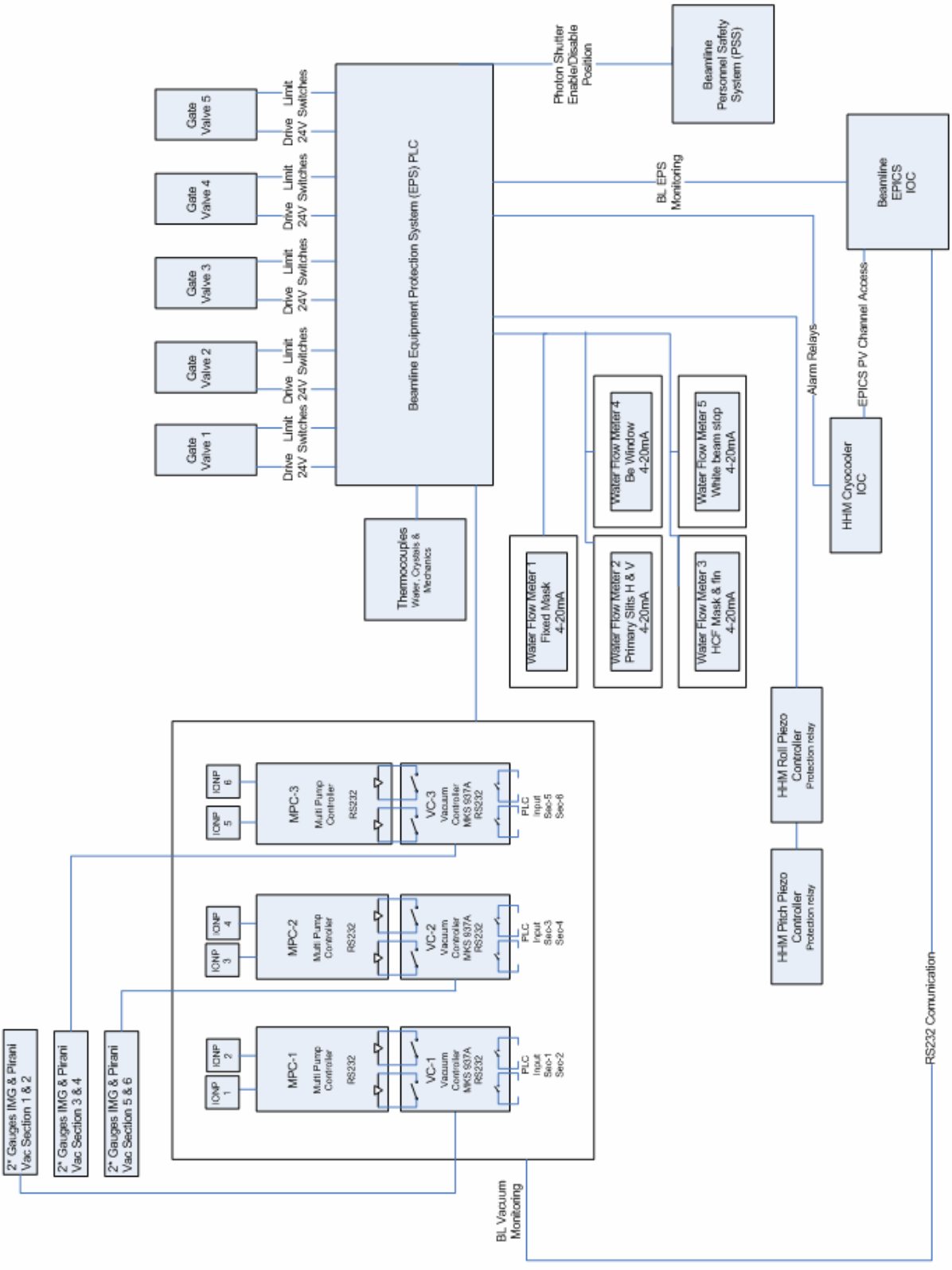

Figure 2.27. EPS Diagram.

2.6 Additional Requirements Imposed on the Conventional Facilities

2.6.1 Vibration Considerations for Synchrotron Beamlines

The beamline vibration is a mammoth subject which ranges from the influence of the distance ocean waves to the local structural resonance. This short discussion has been split in to two sections. The first section addresses vibration sources and the second section presents good engineering design practices.

2.6.1.1 Vibration Sources

Prior to beamline installation it is advisable to characterize the local experimental floor slab. The ambient displacement spectrum will be measured for an extended period of time (>24 h) to increase the likely hood that infrequent vibration sources are observed. NSLS-II should have a sitewide vibration log,, but local structures can affect the results. An example of such a case was a deformed slab at ESRF which, due to the reduced ground contact, increased the displacement amplitude by a factor of 10. The problem was resolved by the injection of grout into the interface.

The vibration source spectrum may be split into three conceptual regions, low-, medium-, and high-frequency. The sources that generate frequencies below 1 Hz (low frequency) tend to be seismic activity, ocean waves, and thermal expansion. The medium-range frequencies (1 – 100 Hz) are generated by machines, pumps, traffic, fluid flow, and mechanical resonances. The high-range (>100 Hz) frequencies are often acoustic, electro-mechanical, and well-designed mechanical resonances.

A proactive approach must be employed when addressing the vibration influence on a beamline. The low-frequency vibration amplitude will be dominated by the quality of the experimental floor and the air conditioning. The associated electron beam and x-ray beam motions may be effectively compensated by the use of closed-loop control systems on the steering magnets and mirrors. The medium-frequency mechanical sources of vibration, such as water chillers or vacuum pumps, should be identified, then moved or isolated. Care must be taken to consider even non beamline components, such as the insertion device (ID) cryostat, or automotive traffic vibrations, which may even be reduced by the removal of speed bumps and drain covers, for example. An instance of a high-frequency vibration source is an optic actuator and the respective support structure stiffness. These effects may often be reduced by the choice of good-quality drive electronics and electrical ground.

2.5.1.2 Good Engineering Design Practices

A wide range of engineering design practices have been empirically developed for synchrotron vibration management. The most basic concept is that only relative motion between the beam and the sample will be detrimental, so all the optics must be mounted from a monolithic floor slab. The most critical components are the mirrors and monochromator. The optical lever arm greatly amplifies vibration effects.

The most common form of vibration isolation within industry is the damping/isolation pad; however, the inherent position instability introduced by an elastic support element can introduce undesirable long-term position drift. For this reason, the optics are usually mounted on stiff supports that are mechanically isolated from their surroundings. Optics are usually mounted on top of a natural or synthetic granite block of high mass and low natural frequency. Granite has good vibration damping properties and a lower thermal expansion coefficient than steel fabrications. The stiffness of the granite may be increased by grouting the block to the floor, although this is often avoided for practical reasons. The upper optic assembly is then designed to be stiff with a high fundamental resonant frequency. Vibration mode analysis and FEA may be used to optimize the design. A high resonant frequency is desirable, as it is less likely to coincide with driving vibration sources and also requires more energy to be driven.

It is possible to extend the high-resonant-frequency philosophy down to the floor. Good results have been achieved using a bolted, lightweight, large cross-section metal structure instead of a massive block. The light

weight and large cross section increase the resonant frequency and the bolted interfaces provide vibration damping.

A number of methods can improve existing mechanical systems, such as the addition of external viscoelastic damping links, which take no mechanical load or tuned dampers.

A closed loop beam stabilization system is commonly employed to effectively lock the beam spot on to the sample position. The signal from a beam position monitor (BPM) is used to drive an upstream mirror or monochromator to compensate for any relative motion via a PID loop. The effectiveness of a closed-loop beam position system to remove vibration reduces as the detrimental frequency rises. In general, the greater the feedback loop frequency the higher the threshold for vibration compensation. A high-frequency, closed-loop beam position system typically runs at ~1 kHz.

It is possible to tune some unavoidable vibration sources to reduce their effect on the beam position. The pump speed and pressure of cryo-coolers may be adjusted to minimize beam influence. Software notch filters may be added to the motion control system to avoid known resonant frequencies.

In summary, vibration will be considered at each stage of beamline design installation and commissioning.

2.6.1.3 Choosing an Optical Top or Breadboard

The broadband damping characteristics are possibly the most important table specification to consider. Tables may employ tuned damping systems; however, these will become invalid as the load mass and location change. The broadband damping may be achieved with oil-based systems or solid dampers. The solid option is preferable, because oil characteristics can change over time and there is the possibility of an oil reservoir being pierced.

The current state-of-the-art system is the TMC Maximum Dry Damping, the performance of which is presented below. TMC offer their leading technology in a range of sizes, all using CleanTop II technology, which insures that fluids are not able to enter the table interior.

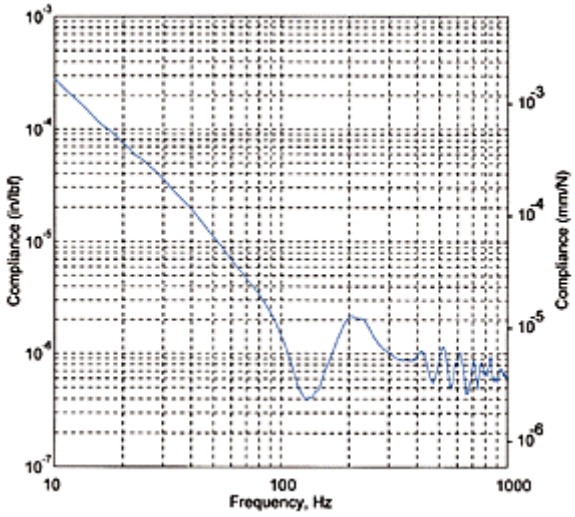

The TMC optical table top can be combined with their cutting edge STACIS active vibration cancellation system. The STACIS system provides a stiff mounting system that effectively reduces vibration in the range from 0.6 – 250 Hz. It was designed for precision microlithography and metrology. Example performance curves are given below.

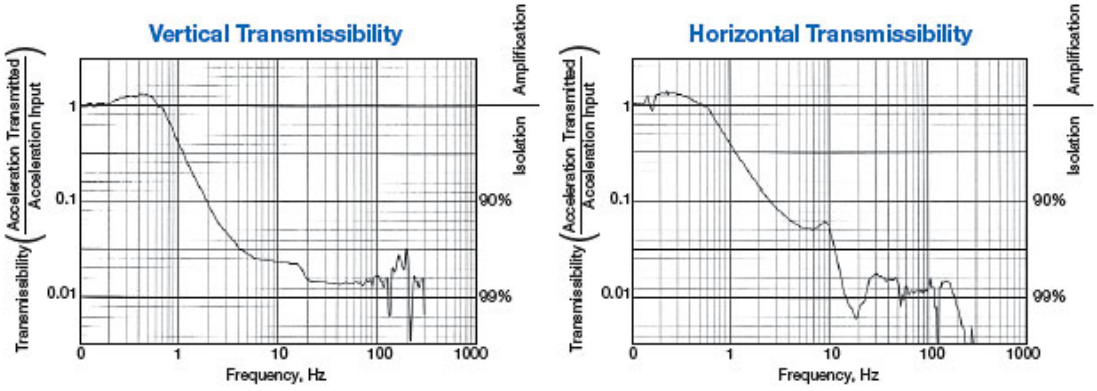

2.7 Additional Requirements Imposed on the Accelerator Systems

The current stability goals for the accelerator performance are sufficient for this beamline.

References

1 K. J. Kim, Angular Distribution of Undulator Power for an Arbitrary Deflection Parameter K, *Nuclear Instruments and Methods in Physics Research,* A246 (1986) 67-70.

2 *LS 237: Explosion Bonding of Dissimilar Materials for Fabricationg APS Front End Components—Analysis of Metallurgical and Mechanical Properties and UHV Applications,* Yuheng Li, Deming Shu, and Tuncer M. Kuzay, Experimental Facilities Division.

3 D. Shu et al. (1995). Precision white-beam a list design for high power density x-ray undulator beamlines at the APS. *Rev. Sci. Instr* **66**(2) Feb 1995.

4 M. Rivers et al. GSECARS Report, First Results from the Sector 13 (GSECARS) Undulator Beamline.

5 B. Fell, K. Fayz, Experimental Investigation of Thermal Contact Resistance for Indirectly Cooled SR Optics, MEDSI 2000.

6 Cryogenic cooling monochromators for SPring-8 undulator beamlines, *Nuclear Instruments and Methods in Physics Research A 467-468 (2001) 647-649.*

2-A Appendix A: Optical Study

2.A.1 Optics Overview

This section presents an overview of the proposed optics plan. It follows the ideas presented in the December 2006 NSLS-II CDR and suggests additional modes. Determining an optics plan for this beamline is complicated by the fact that the required final optics for achieving 1 nm do not yet exist. The uncertainty associated with the optics requires that the beamline be designed with sufficient flexibility to provide the necessary contingency to accommodate an eventual optics solution. The challenge is to provide this flexibly without paying an excessive cost premium or the need to rebuild / replace components, allowing on budget and on time completion of the beamline. The following optics plan incorporates this flexibly and controls risk by utilizing well understood front end and FOE optics components to deliver the x-ray beams generally required for illuminating any successful nano-focusing optics.

The plan is based on two focal points – one at 41 m and the other at 76 m – both supplied by a common set of upstream optics located in the front end and FOE. At each of these two locations a hutch would be constructed that is capable of housing the necessary end station equipment to support the scientific goals of the beamline. The exact location of these hutches will be determined by a number of factors such as the characteristics of the final nano-focusing optics and details involving conventional facilities (floor space, roof line, egress, utilities, etc.). One way to look at this proposed layout is to consider the 41 m hutch a 1x location and the 76m hutch a 2x location with regard to beam demagnification. Operationally, the focused x-ray beam can be used in only one hutch at a time. A beam stop located at the back wall of the upstream 1x hutch would provide access to the downstream 2x hutch while beam is present in the 1x hutch. Access to the 2x experimental location during x-ray operation of the 1x location will allow off line work to be performed using the end station equipment. Given the sophistication and complexity of a nanoprobe end station, this will provide valuable access time for instrumentation development and debugging as well as experiment setup.

The 1x/2x hutch arrangement will play a key role during the early operation phase of the project when the main activity will be optics testing and commissioning. During this initial phase and well before the 2x hutch (and transport to it) is completed, the 1x location will serve as an early test sight where various optics approaches can be evaluated and refined for eventual use in the push to 1 nm in the 2x hutch. There also exists the possibly of achieving a 1nm focal spot at the 1x location if modes such as a wave guide coupled aperture prove feasible. The two locations can also be instrumented with complimentary end station equipment such as a full-field imaging system in the 1x location providing flexibly and agility in meeting the demands of the user science program.

Below, five optics modes are presented – two for the 76m 2x location and three for the 41m 1x location. The five modes are:

- direct focusing at 76 m
- compound horizontal focusing at 76 m
- waveguide mode at 41 m
- direct mode at 41 m
- compound horizontal KB focusing mode for full-field imaging at 41 m.

The proposed support optics will be used to configure these five modes and are general enough to provide additional operation modes if necessary. They are also well understood today regarding both performance and cost. The order of presentation in this document follows the flow of the x-rays from the storage ring to the sample. The components common to all five modes will be presented first followed by discussion of each mode.

2.A.2 Critical Optics Components

In this section we discuss only optical components of primary importance to the five operation modes. For a complete component description of the please see full beamline description.

2.A.2.1 Storage ring and Insertion Devices

The first optical component to be considered in a beamline plan is the storage ring and insertion device. For this report we used the source parameters found in the NSLS-II July 2007 user workshop report. The values used are listed in Table 2.A.1 for a low-beta straight. The NSLS-II U19, 3m long undulator is an excellent source of hard x-rays. It has the advantage of effectively utilizing the storage ring's brilliance and producing hard x-rays from 2 to 30 keV that are well matched to the required optics.

2.A.2.2 Front End Fixed Mask (FEFM) and Differential Pump (DP)

This power limiting mask will allow approximately 90% of the undulator harmonic (at 1 Å) to pass, reduces the total power to a level that is more manageable by the downstream components and protects against miss-steered of the electron beam. It will be located behind the shield wall as close to the undulator as possible (~14 m) with the next component (horizontal source aperture) directly downstream. The vertical and horizontal location of this critical component will be defined through survey with additional motorized horizontal positioning over a restricted range to aide the initial alignment of the orbit (its front end location will make it difficult to access manual adjustors.) Due to its location and size this component is ideal for acting as the vacuum conduction limiting aperture for a differential pump, freeing up space in the FOE. See power management report section for thermal performance analysis.

2.A.2.3 Front End Adjustable Horizontal Source Aperture (FEHA)

This adjustable horizontal mask at ~ 14.5 m will allow the horizontal beam size to be restricted to match the effective vertical coherent source size during nano-focusing. The aperture can be opened to match the FEFM horizontal size for full-field operation mode. The aperture will be constructed as two wedges with one motor adjusting the aperture size and the other it's horizontal position. See power management report section for thermal performance analysis.

2.A.2.4 Horizontal Focusing Mirror (HFM)

This will be a flat horizontally deflecting mirror located at 28.8 m used for power management and as a horizontal focusing element for compound horizontal focusing modes. It will be water cooled with a two moment bender. The mechanical bender will allow the mirror figure to be corrected for thermal bump when producing unfocused beams as well as allow the horizontal beam to focused either directly onto the sample or over a ranged of secondary horizontal source locations from 3.2 to 9 m, resulting in demagnifications from 9 to 3.3. In compound horizontal KB focusing mode for full-field imaging at 41m nearly the full horizontal source can be collected and focused onto the sample using this mirror. The mirror will be fabricated from silicon have an active length of approximately 600 mm, coated over ½ its width with Rh and operate from 0 – 3 mrad. At its maximum incidence angle (3 mrad) working off the Rh stripe it will have an entrance aperture of 1.8 mm with an energy cut off of approximately 20 keV and capable of collecting 89% of the full horizontal undulator source. With a ½ Rh coating the bare silicon stripe can be used to achieve higher harmonic rejection for low energy operation.

Table 2.A.1 Source Parameters from NSLS-II July 2007 User Workshop.

	Based on July 2007 Workshop
Electron Energy	$E = 3GeV$
Stored Current	$I = 500\ mA$
Electron Beam Emittance	
Horizontal	$\varepsilon_x = 0.55\times10^{-9}\, m-rad$
Vertical (1.5% Coupling)	$\varepsilon_y = 8.25\times10^{-12}\, m-rad$
Betatron Function§	
Horizontal	$\beta_x = 1.5m$
Vertical	$\beta_y = 0.8m$
Electron Beam Size§	
Horizontal	$\sigma_x = 28.7\mu m$
Vertical	$\sigma_y = 2.57\mu m$
Electron Beam Divergence§	
Horizontal	$\sigma_x^{'} = 19.2\mu rad$
Vertical	$\sigma_y^{'} = 3.21\mu rad$
Intrinsic Photon Size*	$\sigma_r = 1.95\mu m$
Intrinsic Photon Divergence*	$\sigma_r^{'} = 4.08\mu rad$
Total Photon Source Size§*	
Horizontal	$\sum_x = 28.8\mu m$
Vertical	$\sum_y = 3.2\mu m$
Total Photon Source Divergence§*	
Horizontal	$\sum_x^{'} = 19.6\mu rad$
Vertical	$\sum_y^{'} = 5.19\mu rad$

§ = Low b straight.

*Quantities evaluated for 12.4 keV x-rays and a 3m long undulator.

2.A.2.5 High Heatload Monochromator (HHM)

This will be the primary monochromator on the beamline located at approximate 30.4 m, with LN2 cooled Si 111 crystals operating with a fixed offset of 20 mm over an energy range of 4 – 24 keV. The fixed offset will be maintained by allowing the gap between the faces of the first and second crystal to change (range of motion < 1.5 mm) and the beam to walk along the surface of a long (115 mm) second crystal. Eliminating the

"z-stage" on the second crystal and replacing it with a long crystal greatly improves ease of tuning energy as well as stability since the second crystal is more rigidly mounted. Thermal and vibration stability will be of primary importance in this monochromator design. The direct LN2 cooling needed to maintain the thermal distortions at acceptable levels has the potential for introducing unacceptable vibration. Managing vibration issues at the level suitable for a nano focus beamline will require R&D effort and prototypes resulting in additional cost. See power management report section for thermal performance analysis.

2.A.2.6 Secondary Horizontal Source Aperture (SHSA) + BPM

This is a high quality monochromatic aperture located at 32 m and adjustable horizontal. It will provide a secondary horizontal coherent source as well as a horizontal beam position monitor that can be used in a feedback mode with the HFM PZT pitch actuator. It will be of a relative open and center position type. The blades will be electrically isolated so that the photo current can be measured from each blade.

2.A.2.7 Quad Diode BPM (QDBPM)

This device located at 37.5 m and just inside the upstream wall of the 1 x experimental hutch. For this device the x-ray beam is incident on the face of a 1 micron thick foil generating x-ray florescence that is collected by vertical and horizontal pairs of diodes. As the beam moves on the face of the foil the solid angle of the florescence intercepted by each diode changes. The beam position is determined by computing the difference over the sum of the diode pairs. The foils are mounted on a filter wheel with six positions (one left empty) so that foil with an edge close to the beam energy can be used. Since both vertical and horizontal position information is available this device can be used in a closed loop feedback mode with the PZT's (pitch and roll) of the monochromator and or the horizontal mirror pitch PZT. This closed loop feedback can be used to stabilize the beam position. The QDBPM will be mounted on a vertical translation stage supported off the same structure as the tertiary horizontal source aperture (THSA) – see next item.

2.A.2.8 Tertiary Horizontal Source Aperture (THSA)

This is a high quality aperture located at 37.8 m that will be used to control the size of the horizontal source image produced by the HFM when operating in horizontal compound focusing mode. It will be of a relative width and center slit type with sufficient range to follow the horizontal deflected beam.

2.A.2.9 High-Resolution Monochromator (HRM)

The high-resolution monochromator located at 39 m will operate in a back scatter geometry (first crystal downstream of the second crystal) to achieve the energy resolution required for nanometer size beams. It will consist of diamond 111 crystals allowing use of higher order reflections to cover the required energy range. The crystals will be mounted on a water cooled heater stage held at constant temperature using feedback. Each crystal will be mounted on an independent high-resolution rotation stage. The first crystal rotation stage will be fixed and the second will be free to travel on a z stage so that the monochromator can be operated in fixed offset mode.

2.A.3 Optics Modes

In this section we present an analysis of five optics mode. Common to each mode is a working distance of 10 mm. A working distance of 10 mm or less is most likely needed to reach a 1nm goal. Such short working distances will severely limit the space available for items such as detectors and sample viewing optics and will require that the final focusing optic (i.e., MLL, Kinoform lenses) support structure be optimized to reduce their transverse size. Setting the working distance goal as long as 10 mm provides a safety factor should higher demagnifications be required.

The ray trace analysis presented here were conducted using a program written in IDL at the University of Chicago Center for Advanced Radiation Sources that is optimized for large and small KB optics and capable of optimally figuring both straight and tapered mirrors through the application of upstream and downstream moments. All ray-tracing is performed using realistic mirror shapes and in the case of the small KB mirrors the well established approach (see Eng et al. SPIE Proc. 3449, 145 (1998)) of dynamically figuring the mirror shape by applying two adjustable moments to a trapezoidal shaped mirror is used.

2.A.3.1 Direct Focusing at 76 m

Figure 2.A.1 shows the vertical and horizontal optics layout for the direct focusing mode at 76 m. The inserts shows scatter plots of ray traces of the source at the front end aperture and at the location of the final focusing optics. The location of the final focusing optics is defined simply by the 7.6 μm FWHM vertical source size, the 10 mm working distance, and the desired 1 nm beam size. In addition to the final focusing optics, the only other components required are the front end aperture and high-resolution monochromator. The transverse coherence angle of the vertical source at 1 Å is 6.6 μrad and is achievable with a vertical aperture at 14.5 m of 120 μm, resulting in a vertical optical aperture at 76 m of 500 μm.

In the horizontal dimension, the source is nearly 10 times larger. In order to match the vertical focus, the horizontal size of the front end aperture must be 10 μm or less. The divergence through such an aperture is defined by the size of the horizontal source and the distance to the aperture and is approximately 5 μrad. This matches well the transverse coherence angle of the new horizontal source, defined by this aperture as 5.5 μrad, resulting in a horizontal optical aperture at 76 m that is well matched to the vertical.

The scatter plots in A.2.A to the left of the front end aperture show the full beam available from the undulator. The top panel is a plot of the vertical and horizontal source, with the missing center rectangle indicating the portion of the beam that can be used by the final focusing optics. The lower panel shows a phase space plot in the horizontal direction with the vertical white band showing the portion of horizontal phase space used by the final focusing optics. To the right of the aperture are the same plots, but they now show just the transmitted beam. Figure A.x.x shows a detail view of the source that illuminates the final focusing optics, where a little less then 1% of the total undulator beam is accepted.

2.A.3.2 Compound Horizontal Focusing at 76 m

In the compound horizontal focusing mode at 76 m the horizontal focusing mirror located at 28.8 m is used to produce a secondary horizontal source at 32 m. In this mode the vertical optics are identical mode discussed above. The horizontal optics layout and ray trace scatter plots are shown in Figure A.2.x. This horizontal mirror geometry results in a horizontal demag = 9 and produces a horizontal focus with a FWHM of 7.6 μm. To be able to achieve a 1nm horizontal focus, this secondary source must be reduced to 4 μm using the secondary source aperture. The divergence of this secondary source in very large (~0.5 mrad), and the horizontal transverse coherence angle of this source is about 11 μm, requiring that nearly a factor of 50 of the full divergence be masked out of the beam that illuminates the final focusing optics. The scatter plots at the secondary source aperture show full and the masked secondary source. The scatter plots at 76 m show the beam that will illuminate the final focusing optics, showing that approximately 1 % of the total undulator beam can be made available to the optics.

One possible advantage of this mode is that the horizontal source size can be tuned by adjusting the secondary source slit. An additional advantage is that the secondary horizontal source could be stabilized on the secondary source aperture, using a feedback loop that adjusts the pitch of the horizontal mirror.

2.A.3.3 Waveguide Mode at 41 m

Figure A.2.4 shows the waveguide mode used at 41 m. In this mode primary focusing optics with a working distance of 30 mm and an aperture of 269 μm would produce a secondary source that is 50 μm FWHM. This source is then coupled to an x-ray wave guide. The waveguide will pass only a coherent source and will act as a secondary source for the secondary focusing optics. A demagnification of only 50 is now needed to achieve 1 nm focus. The secondary focusing optics would have an optical aperture of 500 μm and a working distance of 10 mm.

2.A.3.4 Direct Mode at 41 m

The direct focusing mode at 41 m is the same concept as the direct mode at 76 m. The final focusing optics would have a demagnification of 4133 and an optical aperture of 273 μm and would focus the beam to 1.89 nm at a working distance of 10 mm.

2.A.3.5 Compound Horizontal KB Focusing Mode for Full-Field Imaging at 41 m

Full-field imaging greatly benefits from the high photon flux, divergence, and small spot size produced using the compound horizontal small KB focusing mode. Figure A.2.x and Figure A.2.x show the horizontal and vertical optics layout respectively. In this mode the horizontal focusing mirror at 28.8 would focus the beam 9 m away at the tertiary horizontal aperture with a demagnification of 3.3. The horizontal beam size at this aperture is 51 μm FWHM and is re-imaged by a small KB mirror located 3.33 m away. This small KB mirror with a demagnification of 16 and a working distance of 90 mm produces a final focus of 1.4 μm FWHM. In the vertical (Figure A.2.x), only a single small KB mirror is used with a demagnification of 91, producing a vertical focus of 92 nm FWHM. The first two scatter plots in Figure A.2.x show the tertiary focal spot with the aperture fully open and set to 2 μm. The third and fourth scatter plot show the final focus produced by the small KB mirror pair for the case the tertiary aperture fully open and closed to 2 μm, resulting in a horizontal focus that ranges between 1.4 to 0.1 μm FWHM and transmitting 69% to 6% of the undulator source.

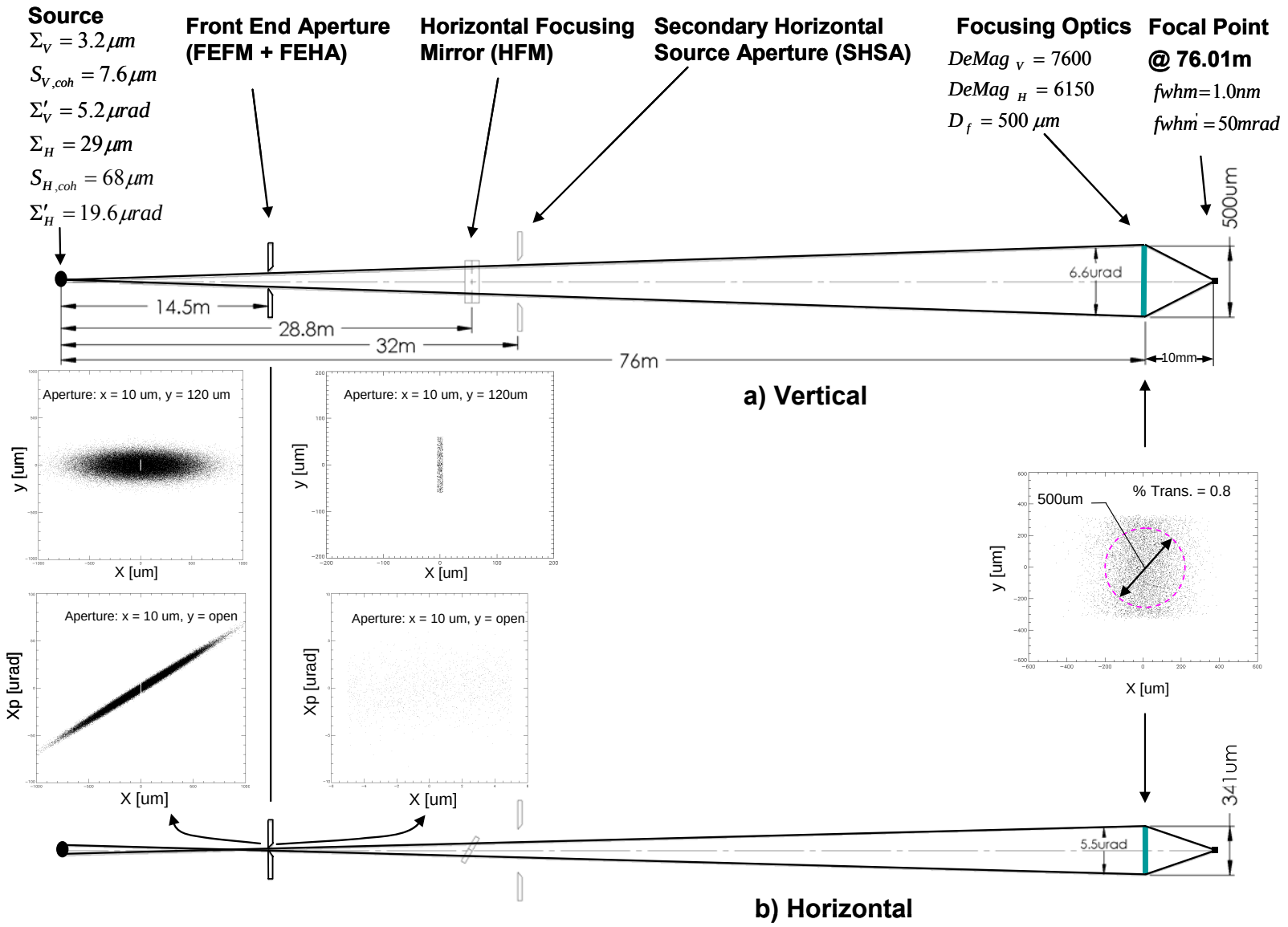

Figure 2.A.1. Optics layout and ray trace for a direct focusing at 76 m, focusing the beam to 1 nm with a working distance of 10 mm. a) vertical ray trace, b) horizontal ray trace.

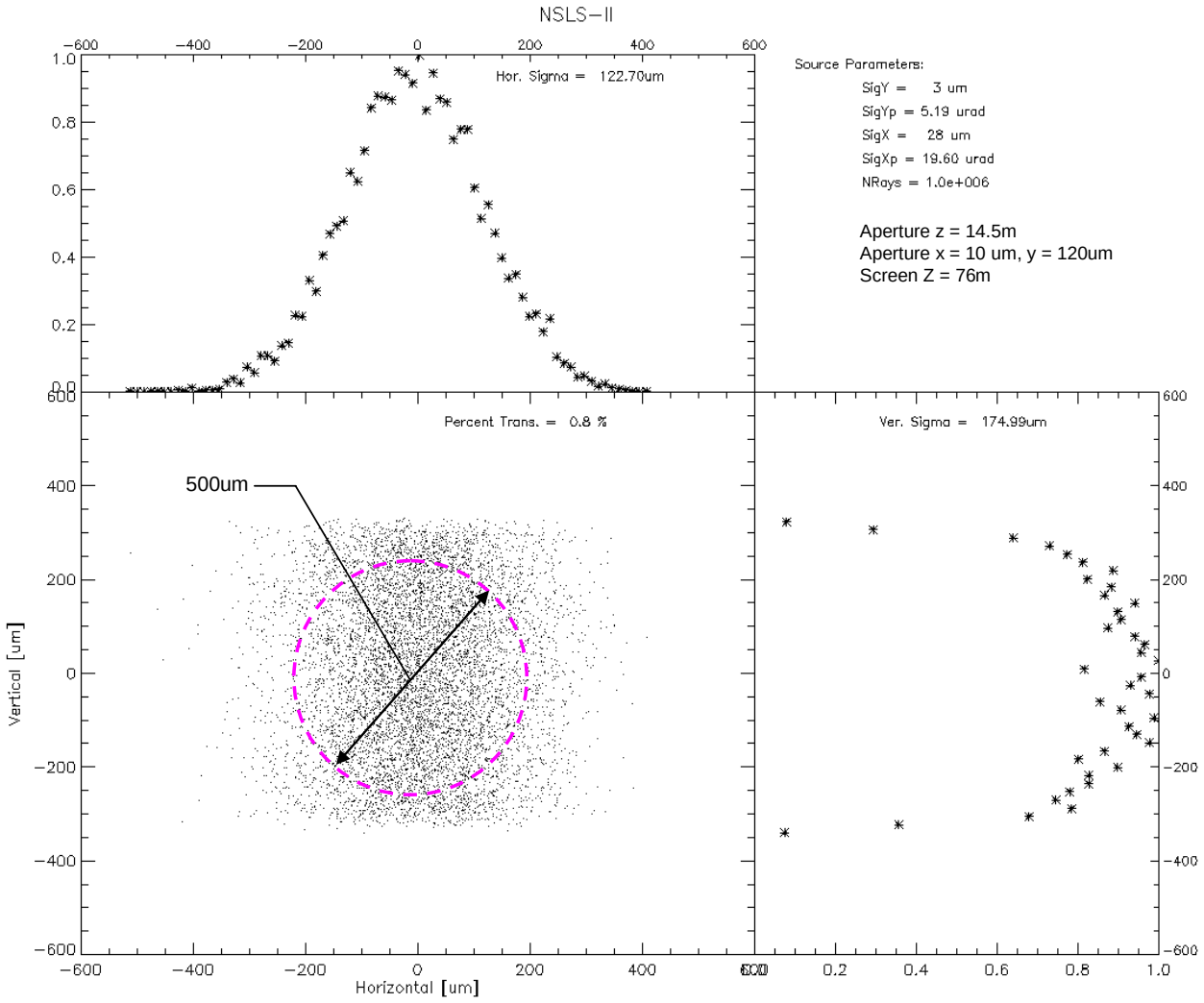

Figure 2.A.2. Scatter plot of coherent beam illuminating the nano-focusing optics for direct focusing at 76 m. 0.8 % of the total undulator harmonic is transmitted to the final optic.

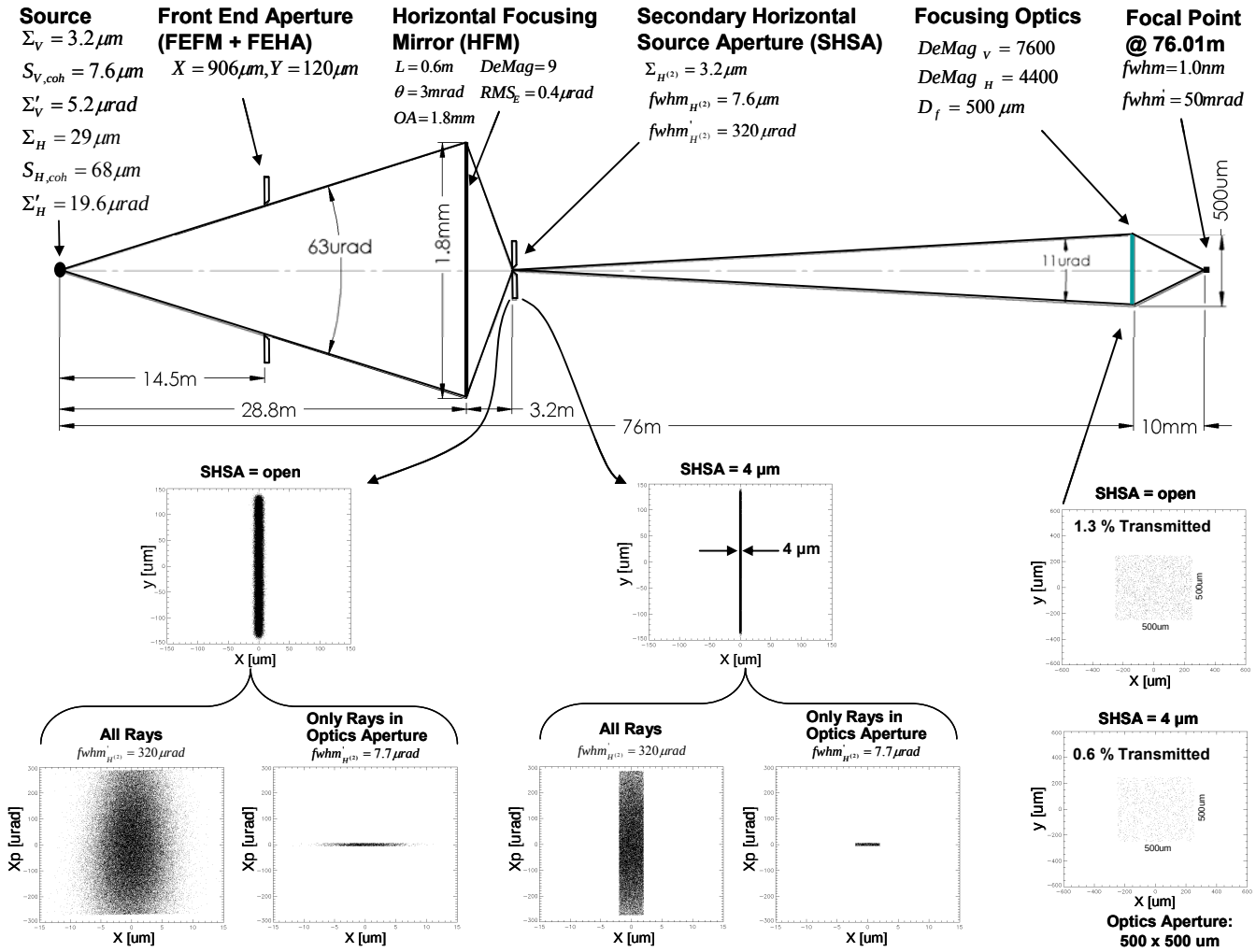

Figure 2.A.3. Optics layout and ray trace for a compound horizontal focusing at 76 m, focusing the beam to 1 nm with a working distance of 10 mm.

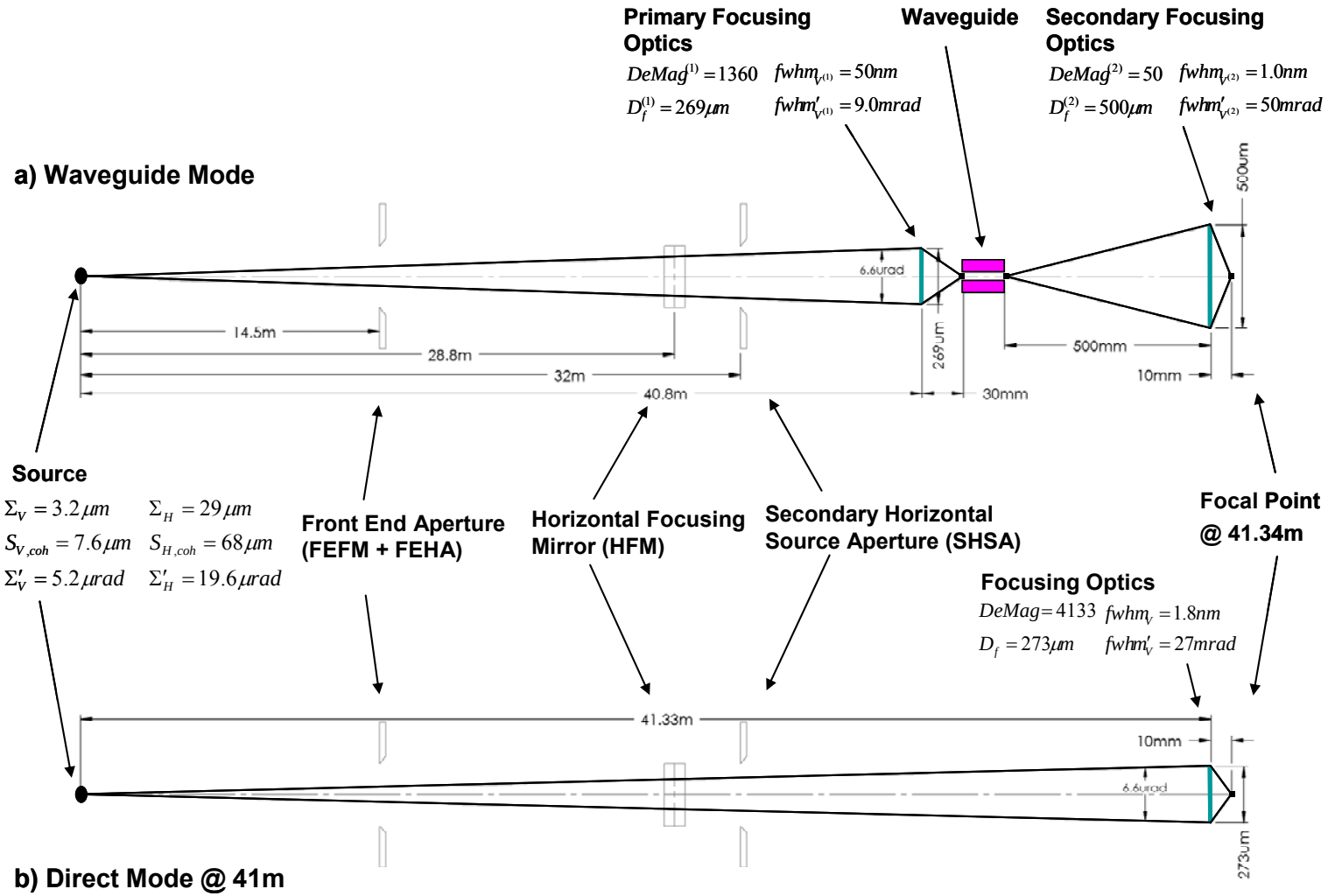

Figure 2.A.4. Optics layout for focusing at 41 m. a) Waveguide mode achieving 1 nm at 41 m with a working distance of 10 mm. b) Direct beam mode with the beam focused to 1.8 nm at 41 m with a working distance of 10 mm.

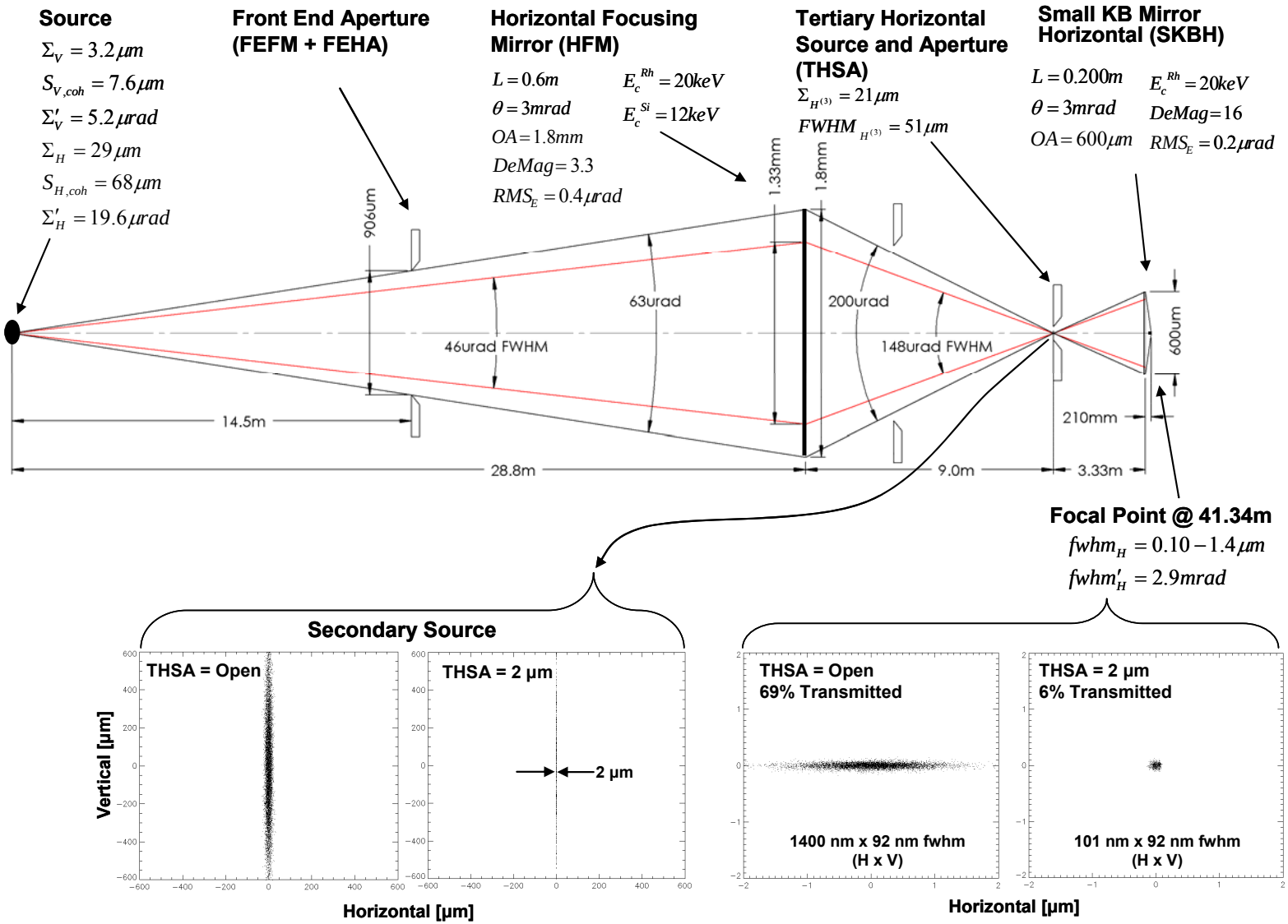

Figure 2.A.5. Optics layout and ray trace for a compound horizontal focusing at 76 m, focusing the beam to 1 nm with a working distance of 10 mm.

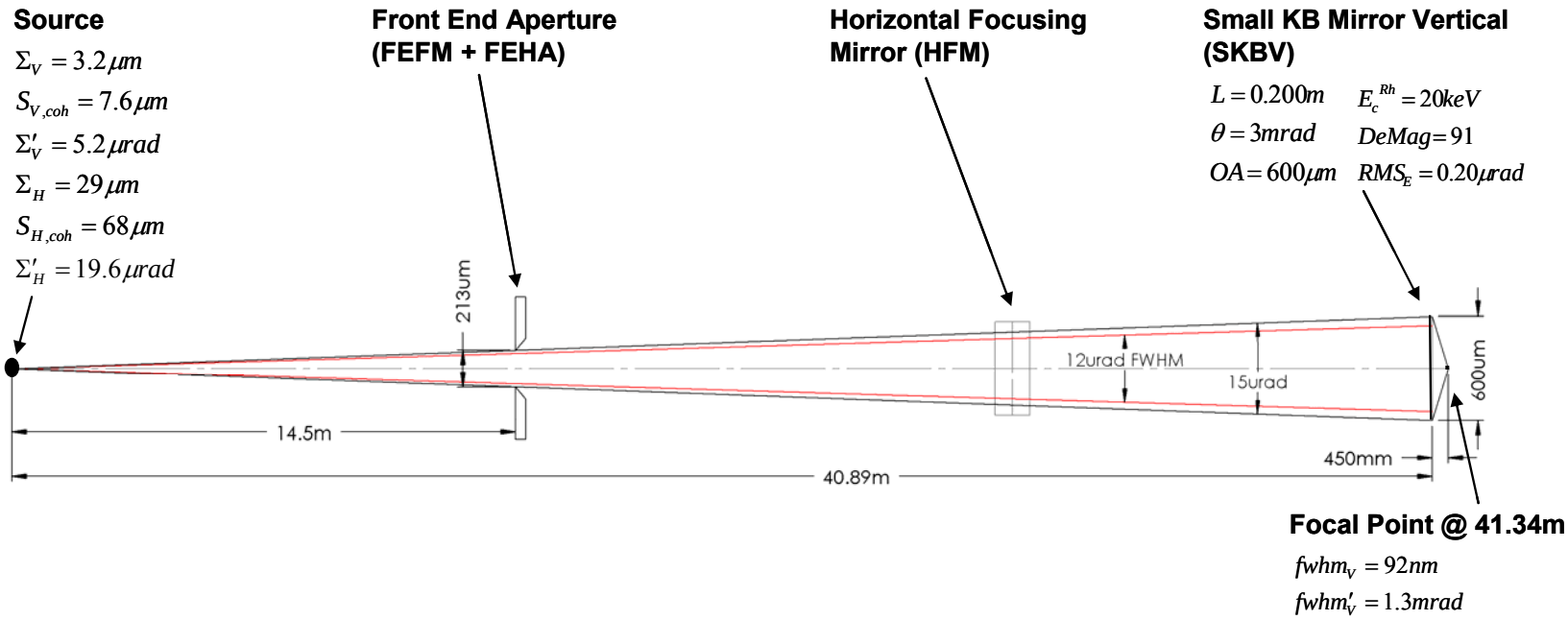

Figure 2.A.6. Vertical optics layout and ray trace for compound horizontal KB focusing mode for full-field imaging at 41m using a small vertical KB mirror, together with horizontal compound reflective optics.

3.1 Executive Summary

This section provides an overview of the conceptual design of the Coherent Hard X-Ray (CHX) Beamline at NSLS-II at Brookhaven National Laboratory.

The technique will take advantage of very high flux of the NSLS-II source. The basic concept of the proposed design of the CHX beamline is to substitute the intrinsic source with a secondary source that is controlled by the end user. A secondary source is employed only in the horizontal direction. The aim is to enlarge the lateral coherence seen at the sample position and bring the horizontal and vertical coherence lengths closer to each other [1]. The beamline design embraces two branches, the small angle branch and the coherent diffraction and large angle branch, although just one of these branches (the small angle branch) will be built as part of the NSLS-II project. The edges of the mirrors will be used to separate the branches. The main energy range for the beamline is 7 – 20 keV.

Each beamline branch will have one endstation, one for small-angle X-Ray Photon Correlation Spectroscopy (XPCS) and one for Coherent X-ray Diffraction (CXD), although only the XPCS beamline and endstation will be built as part of the project. They will be used either simultaneously (most likely and desirable mode) or sequentially, i.e. only one at a time to preserve most of flux available from the source [2]. Splitting the beam into two sections for different branches of the beam line will be done using reflecting mirrors.

The length of the XPCS beamline will be about 60 m and the length of the CXD beamline will be about 250 m.

Mirrors and monochromators should be water cooled to avoid vibration issues and simplify maintenance.

To maximize beam brilliance surfaces of the optical elements should be polished to state-of-the-art standards and the slope errors minimized.

Floor vibrations and temperature fluctuations should be minimized.

A 3 m long U19 undulator placed in a high-beta 8 m straight will be used. The minimum deflection parameter value is K=1.8. The working values for 1-sigma photon beam sizes and divergences are estimated as σ_x =100 μm, σ_y = 6 μm, σ'_x = 15 μrad and σ'_y = 12 μrad. An upgrade is being considered of adding a second undulator in-line with the first one to double the flux. It is anticipated the energy range from 7 – 9 keV will be covered using the third harmonic and a 9 – 12 keV range using the fifth harmonic.

Maximum size of the opening aperture is expected to be about 500 μm (H) x 500 μm (V) or 0.02 mrad (H) x 0.02 mrad (V).

Higher harmonics should be cut off by the mirror and lower ones by use of thin absorber. A CVD diamond crystal of approximately 100 μm thick is being considered as a suitable high-pass filter. Mirrors are expected to operate at 3 mrad incidence angle.

Scientific Objective

X-ray photon correlation spectroscopy also utilizes the very high coherent flux at NSLS-II, in this case to probe the equilibrium or steady-state dynamics of condensed matter. In this endeavor, the XPCS technique offers the significant strengths of being able to study length scales shorter than can be achieved with optical
techniques and longer time scales than can be achieved via neutron scattering. Even on optically accessible length scales, it permits the study of opaque and metallic samples, presenting new opportunities for studies of colloidal and other soft-matter systems.

XPCS involves creating a partially coherent x-ray beam, which is allowed to impinge upon a sample. The dynamics of any fluctuations within the sample are then determined by characterizing the intensity autocorrelation function, g2 = g2(Q,t), of the resultant x-ray speckle pattern versus delay time (t) and wave vector (Q). In a certain sense, this may be thought of as the time-resolved counterpart to coherent diffraction discussed above. Importantly, the quantity g2(Q,t) is related to the sample's normalized intermediate scattering function (ISF) [f(Q,t) = S(Q,t)/S(Q,0)] via g2(Q,t) = 1+A[f(Q,t)]2, where A is the optical contrast. The ISF (equivalent to the sample's Q- and t-dependent density–density autocorrelation function) is a quantity of central interest for any condensed matter system, and is usually key in comparing theory to experimental
results.

However, PCS is much more challenging with x-rays than with light. This is due to a combination of the fact that there are many fewer photons in x-ray beams from even the brightest synchrotrons than from laser sources, and the fact that x-ray scattering cross-sections are invariably many times smaller than light scattering cross-sections. As a result, the crucial aspect of any XPCS experiment is generally the signal-to-noise ratio. The XPCS SNR is linearly proportional to the source brightness.

NSLS-II will drive a revolution in the kinds of samples that will be accessible to XPCS studies. Interestingly, while the SNR scales linearly with brightness, it only scales as the square-root of the sample time (which should be a few times smaller than the sample's correlation time). It follows that for samples of a given scattering strength, meaningful XPCS measurements will be possible at NSLS-II on time scales that are about 100-1000 times faster than currently possible anywhere. Since the current state-of-the-art for diffuse scattering measurements (not from liquid crystal Bragg peaks, or surface specular reflection) corresponds to sample times of about 1 millisecond, we expect time resolutions at NSLS-II of 1 microsecond or less to be feasible, which will enable entirely new science. Indeed, with a time resolution of 0.1 microseconds, it may be possible, in favorable circumstances, to overlap with neutron spin echo measurements.

There are several classes of XPCS experiments that will be possible at NSLS-II but are impossible at current facilities. These include:

Membrane Dynamics. Studies of the dynamics of membrane-based complex fluid phases, consisting of oil–water and an amphiphilic surfactant. Such phases—including the sponge phase and the bicontinuous microemulsion phase, for example—have been the subject of intense interest over the past 20 years, not least because of their possible utility in enhanced oil recovery applications. There are detailed predictions for the equilibrium dynamics of such phases for the wave vectors most characteristic of these materials, namely wave vectors at and near the peak of the static scattering. However, these dynamics are typically too slow for neutron spin echo (NSE) measurements and occur at wavevectors that are too large for optical studies. The faster time scales made accessible by the enhanced brightness of NSLS-II will enable XPCS studies to test these predictions.

Nanoparticles in Suspension. Studies of the collective dynamics of suspensions of nanoparticles. At NSLS-II, it will be possible to study fluctuation dynamics of smaller nanoparticles than is possible

now. This will, for example, permit studies of the motions of nanoparticles confined within block copolymer matrices, or on surfaces. Such studies will be critical in understanding the processes underlying how small particles self-assemble into potentially, technologically useful structures. Especially interesting will be studies examining mixtures of differently-sized nanoparticles of differing compositions, which can self assemble into a variety of different structures, depending on their relative sizes, and which it may be possible to selectively probe via anomalous scattering methods.

Polymer Dynamics. A longstanding question in polymer science concerns so-called *reptation*, which is the process by which polymers in an entangled polymer melt diffuse. The enhanced brightness of NSLS-II will permit XPCS studies on shorter length scales than is now possible, allowing such studies to critically examine the reptation model and relaxations associated with reptation in polymer melts in a much more direct fashion—by actually looking at the polymer motion—than has been possible previously.

Surface Fluctuations. Surface XPCS studies carried out at NSLS-II will probe shorter length scales and faster time scales than are possible now and will therefore elucidate the dynamical behavior of thin liquid and polymer films, and permit definitive answers to questions concerning the role of surface roughness in quenching dynamical fluctuations, or of a polymer's radius of gyration in determining a polymer thin film's capillary mode spectrum.

Biological Applications. The increase in source brightness provided by NSLS-II presents new opportunities for XPCS measurements in systems with low electron density contrast, such as those that consist of biological materials. It is useful to note that the signal-to-noise ratio in the time correlation function obtained in XPCS measurements is proportional to the source brightness, the scattering cross-section of the sample and the square root of the fastest probed time scale. Biological samples have intrinsically low electron density contrast (e.g. the electron density contrast of proteins against water is ~0.1e/Å^3, in contrast to ~0.4e/Å^3 for Si against water). The scattering cross-section of a biological sample is therefore approximately an order of magnitude lower than an inorganic sample of comparable structure features. NSLS-II will permit accessing sub-millisecond time scales for biological samples. Such a time scale is relevant to many important biological processes. For instance, the internal motion of proteins can be described by a series of normal modes. While the high frequency normal modes can be as fast as sub-picosecond, the low frequency, global collective normal modes are on the time scale of millisecond or slower. These normal modes are related to conformation changes that are important to the proteins' function and their time scale is comfortably within the range of XPCS measurements. Membrane inclusions, such as membrane proteins and peptide induced pores, are also good candidates to be studied by XPCS. The intrinsic diffusion coefficient of lipid molecules in a fluid membrane is on the order of 1μm^2/s. The membrane inclusions are likely to have lower diffusion coefficients (e.g. 0.004μm^2/s for CFTR Cl^- channels) and the relevant length scale corresponds to scattering vector q~0.1Å^{-1}. The time scale relevant to the diffusion of membrane inclusions in XPCS measurements is therefore just below millisecond. It should be noted that this time scale is nearing what the best (longest) molecular dynamics simulations can do today. The XPCS measurements therefore could provide a validation for computer simulations. At the same time, the combined information also provides a more complete understanding of the studied system.

Insertion Device

The beamline will be using a 3 m U19 insertion device as a source of x-rays. Key storage ring and undulator parameters are summarised in Table 0.1. The parameters have been compiled from the information provided in references [1,3].

Initially one U19 undulator will be used in a high β 8.6 m straight section [1]. There will also be eight damping wigglers reducing the horizontal emittance to 0.55 nm-rad [3] from the 2.1 nm-rad specified for the bare lattice, Table 1 of reference [3]. But at the start there will only be 3 damping wigglers [2] and hence higher horizontal emittance of 0.9 nm-rad [3].

Table 0.1 Storage ring and ID parameters.

Parameters	Values	Units	Reference
Electron Energy	3	GeV	3
Storage ring current	500	mA	3
Period length	19	mm	3
Length of magnet array	3	m	3
Number of full periods	158	-	3
Field strength (max)	1.14	T	3
Maximum deflection parameter K(y)	2.03	-	3
Horizontal and vertical emittance			1-3
ε_x	0.55 / 0.9	nm · rad	
ε_y	0.008	nm · rad	3
Beta function horizontal and vertical			
β_x	18	m	3
β_y	3.1	m	3
Energy spread	0.0005 - 0.001	-	3
Beam size (sigma) horizontal and vertical			
σ_x	99.5 / 127.3	μm	Calculated
σ_y	5.0	μm	Calculated
Beam angular divergence (sigma) horizontal and vertical			
σ'_x	5.5 / 7.1	μrad	Calculated
σ'_y	1.6	μrad	Calculated
Total power	11.18	kW	3
On-axis power density	77.86	kW/mrad^2	3

Photon beam parameters are summarized in Tables 3.1 and 3.2.

Table 0.2 Source size and angular divergence. The FWHM is calculated using σ values as $FWHM = 2\sigma\sqrt{2\ln 2}$.

A. ε_x =0.55 nm-rad

K	n	E, keV	$\sigma_{r'}$, μrad	σ_r, μm	Source size, μm				Angular divergence, μrad			
					(σ)		(FWHM)		(σ)		(FWHM)	
					H	V	H	V	H	V	H	V
1.0	3	9.0	4.79	2.29	99.5	5.5	234.4	12.9	7.3	5.1	17.2	11.9
1.73	5											
2.03	1	1.47	11.85	5.66	99.7	7.5	234.7	17.8	13.1	12.0	30.8	28.2
2.03	11	16.2	3.57	1.71	99.5	5.3	234.3	12.4	6.6	3.92	15.5	9.2

B. ε_x =0.9 nm-rad.

1.0	3	9.0	4.79	2.29	127.3	5.5	299.8	12.9	8.6	5.1	20.2	11.9
1.73	5											
2.03	1	1.47	11.85	5.66	127.4	7.5	300.1	17.8	13.8	12.0	32.5	28.2
2.03	11	16.2	3.57	1.71	127.3	5.3	299.8	12.4	7.9	3.9	18.7	9.2

Table 0.3 Effective beam size and angular divergence at different positions along the beamline. The FWHM is calculated using σ values as $FWHM = 2\sigma\sqrt{2\ln 2}$.

A. ε_x =0.55 nm-rad

Distance from sourse, m	Beam size, μm				Beam angular divergence, μrad			
	(σ)		(FWHM)		(σ)		(FWHM)	
	H	V	H	V	H	V	H	V
27.9	227.2	141.0	535.0	332.0	8.1	5.1	19.2	11.9
50	379.3	252.6	893.2	594.7	7.6		17.9	
75	558.0	378.8	1313.9	892.0	7.4		17.5	
100	738.7	505.0	1739.6	1189.3	7.4		17.4	

B. ε_x =0.9 nm-rad

27.9	271.6	142.4	639.6	335.3	9.7		22.9	

50	448.5	255.1	1056.0	600.6	9.0	5.1	21.1	12.0
75	657.4	382.5	1548.2	900.8	8.8		20.6	
100	869.4	510.0	2047.2	1201	8.7		20.5	

Figure 0.1 shows the calculated brilliance of different harmonics at values of the deflection parameter K<2.03 using the XTC program from the XOP package [6,7].

The first harmonic of the radiation is available at energies from approximately 1.47 keV to 4.5 keV, i.e. within the energy range that will not be used on the beamline. Useful undulator harmonics for the particular beam line for selecting energies from 7 to 20 keV are harmonics from 3 to 9 or possibly up to 11. Variation of K versus energy is given in Figure 0.2. Assuming the deflection parameter of the undulator, K, of any practical use will be between 2.03 and 0.4, Figure 0.2, maximum undulator gap will be less than 15 mm.

Data in Figure 0.1 show that different undulator harmonics should be used to keep maximum flux over the range of energies from 7 keV to 20 keV: the 3rd harmonic below approximately 8.1 keV, the 5th at 8.1 – 11.2 keV, the 7th at 11.2 – 13.7 keV, the 9th at 13.7 – 16.2 keV and the 11th at 16.2 – 20 keV. The most important energy range of 7 -12 keV could essentially be covered with the 3rd and 5th harmonics.

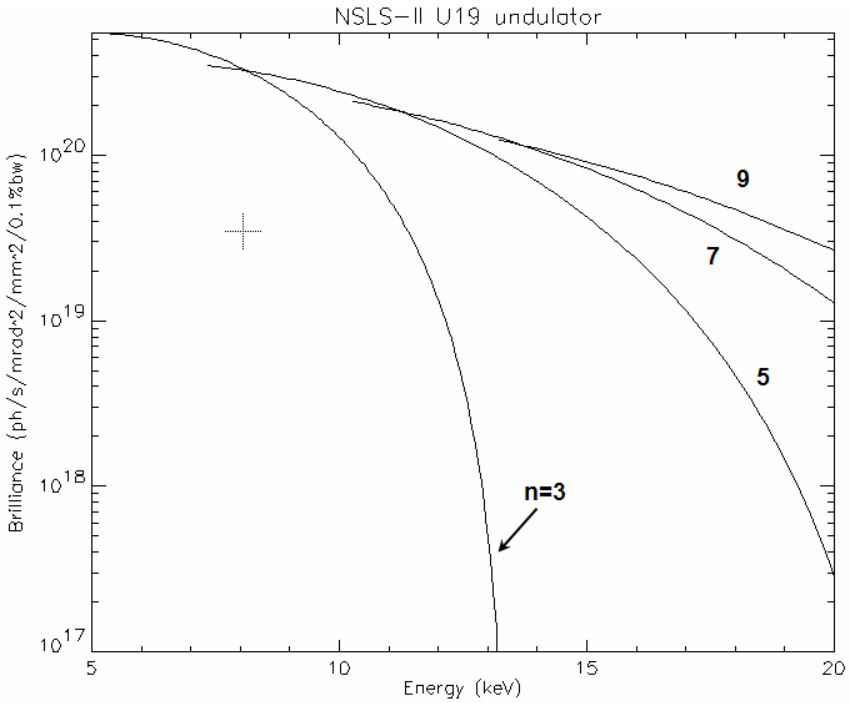

Figure 0.1 Calculated variation of the on axis brilliance of first few odd harmonics (from 3 to 9) of radiation from the U19 undulator versus energy at K<2.03.

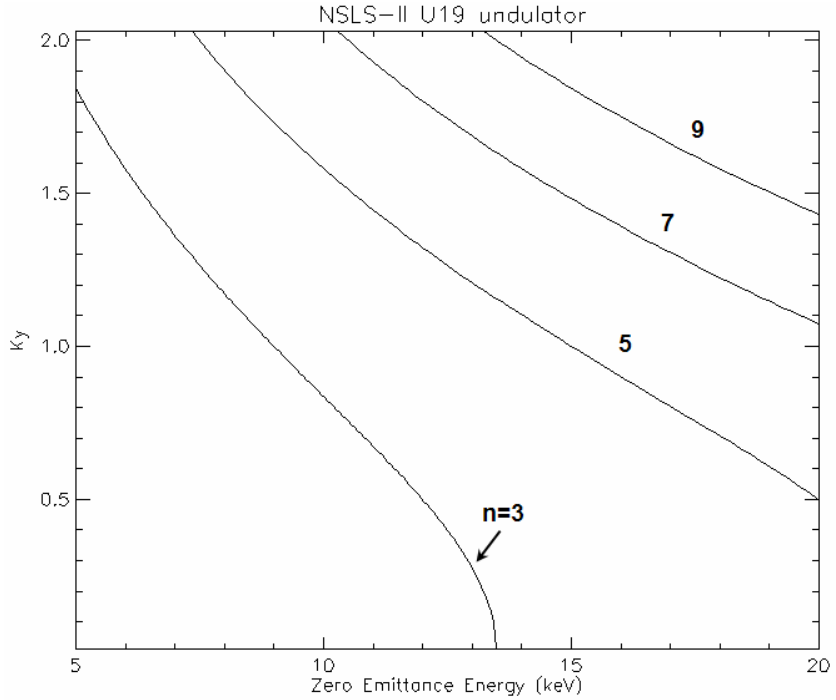

Figure 0.2 Calculated variation of the deflection parameter *K* corresponding to odd harmonics (from 3 to 9) of radiation from a U19 undulator versus energy.

Calculated heat loads for different operating modes of the U19 undulator are shown in Table 3.3. Power density distributions are shown in Figures 3.3 and 3.4. The heat load associated with a 20 μrad x 20 μrad aperture placed at 29.7 m from the souce is summarized in Table 3.4.

Table 0.4 Calculated heat loads at different operating modes of the U19 undulator. The opening angle of 100 μrad (H) x 100 μrad (V) corresponds to the size of a fixed mask. The 20 μrad (H) x 20 μrad (V) opening of the beam is the maximum opening required by experiments.

Distance from source, m	**K**	**FWHM of power distribution (H x V), μrad**	**FWHM of flux distribution[1] (H x V), μrad**	**Total Power, W**	**Power density, W/mm^2**	**Power through 0.1 (H) x 0.1 (V) mrad aperture, W**	**Power through 0.02 (H) x 0.02 (V) mrad aperture W**
27.9	1	281 x 207	20.2 x 11.9	2704	47.6	343	14.8
	1.73	490 x 217		8093	84.8	624	26.3
	2.03	579 x 218	32.5 x 28.2	11143	100.1	737	31.1

Note(s): 1) See Table 0.2, B.

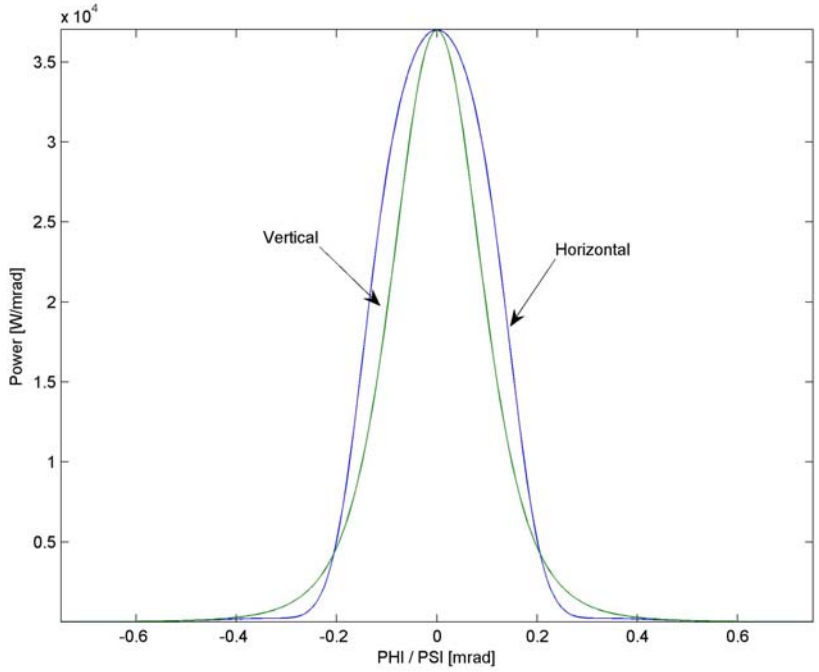

Figure 0.3 Calculated cross-section of power distribution in horizontal (FWHM=0.281 mrad) and vertical (FWHM=0.207 mrad) planes at K=1.0 and beam opening angle of 1.5 mrad (H) x 1.5 mrad (V).

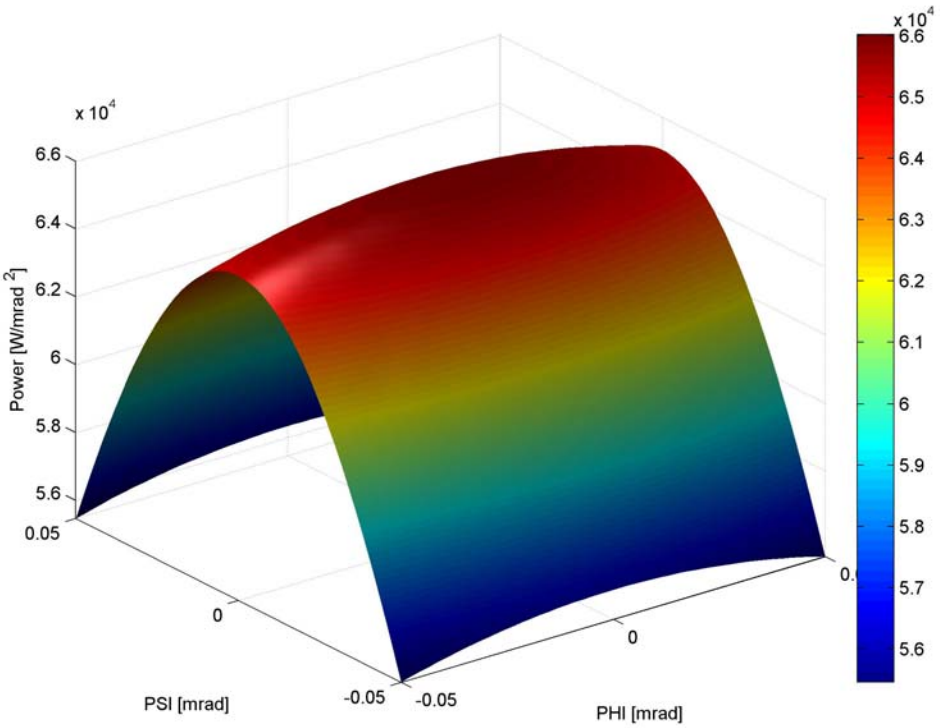

Figure 0.4 Power density distribution versus horizontal, *Phi*, and vertical, *Psi*, opening angles at a 100 μrad (H) x 100 μrad (V) aperture at *K*=1.73.

Table 0.5. Heat load at a 20 μrad x 20 μrad aperture placed at 29.7 m from the souce. The source consists of two in-line U19 undulators tuned to the same gap. Heat load is calculated without any windows/filters or mirrors and taking into account a 200 μm thick CVD diamond filter and heat loss at a Rh coated deflecting mirror at an incidence angle of 3 mrad.

Distance from source, m	**K**	**Power density, W/mm^2**	**Power, W**	**Power, W (after 200 μm CVD diamond + mirror)**	**Power through central cone $\sigma_{r'}$, W**	**Power through central cone $\sigma_{r'}$ (after 200 μm CVD diamond + mirror), W**
29.7	1.0	95.1	30	9.3	1.7	0.5
	1.73	169.7	53	29	3.0	1.6

The results in Table 0.5 show that if only coherent part of the beam is selected using slits the heat at the monochromator will only be few Watts. If however the 0.02 μrad x 0.02 μrad aperture is used, the heat at the monochromator will be much bigger, 29 W, at power density of about 170 W/mm^2.

3.2 Sector Layout

3.2.1 Beamline Layout

Table 0.6 shows the position and size of the beamline components. Space between the main components will be filled with vacuum bellows and pipes of suitable length. The table also shows different sections of the beam line vacuum system.

A CAD drawing of the beam line and the end stations showing general layout of the beam line components is given in Attachment 1.

Table 0.6 Beamline layout.

Beamline Component	Starting position, mm	Length, mm	Vacuum section[1]	Centre of Optical Element
End of shield wall	27900			
Fixed mask	**28200**	**229**	0/1	**28315**
Differential Pump	28429	420	1	
Bellow	28849	180	1	
Blade BPM	29029	319	1	
Bellow	29348	180	1	
CVD Diamond Window / Filter	**29528**	**303**	1	**29680**
Bremsstrahlung collimator	29831	388	1	
Bellow	30219	167	1	
White beam Slit (H)	30386	229	1	
Bellow	30615	167	1	
White beam Slit (V)	30782	229	1	
Bellow	31011	180	1	
Fluorescent screen	31191	340	1	
Bellow	31531	180	1	
Gate valve	31711	70	1/2	
Outbound deflecting Mirror	**31781**	**700**	2	**32131**
Gate valve	32481	70	2/3	
Bellow	32551	137	3	
Inboard White beam Slit (H)	32688	229	3	
Bellow	32917	167	3	
Inboard White beam Slit (V)	33084	229	3	
Bellow	33313	167	3	
Pipe	33480	300	3	
Gate valve	33780	70	3/4	
Inboard deflecting Mirror	**33850**	**700**	4	**34200**
Gate valve	34550	70	4	
Bellow	34620	200	4/5	
Pipe	34820	800	5	
Beam mask and white beam stop	35620	450	5	
Bellow	36070	200	5	
White Beam Shutter	36270	230	5	
Bellow	36500	200	5	
Hutch wall	36890	300		37040
Beam Transport pipe	36700	9145	5	
Beam mask and Bremsstrahlung stop	45395	450	5	
Hutch wall	45250	300		45400
Bellow	45550	200	5	
Gate valve	45750	70	5/16	
Pipe outbound	45550	295	5	
Bellow	45845	200	5	
Fluorescent screen	46045	345	5	
Gate valve	46390	70	5/6	
DCM and pink beam stop	**46460**	**745**	6	**46832.5**
Gate valve	47205	70	6/7	

Bellow	47275	200	7	
Pink Beam Shutter	47475	230	7	
Pipe	47705	604	7	
Hutch wall	48100	300		
Fluorescent screen	48309	340	7	
Quadrant BPM	48649	35	7	
Bellow	48684	150	7	
Pink beam Guard slits	48834	65	7	
Gate valve	48899	70	7/8	
VFM	**48969**	**700**	8	**49319**
Gate valve	49669	70	8/9	
Pipe	49739	290	9	
Pink beam Slits	50029	65	9	
SiN / CVD Diamond Window	50094	20 / 303	9	
Pink beam/Bremsstrahlung stop	TBD	400	14	
End station 1 equipment	TBD			
Hutch wall	60000	300		

3.2.1.1 Data Acquisition System and Motion Control

The 8-axis motion control boxes having RS232, USB and Ethernet interfaces are customized to suit the beam line motorised axis. They also have built in micro IOCs.

Separate micro IOCs control vacuum pump controllers, vacuum gauge controllers, DPT controllers, current amplifiers and CCD cameras.

EPS PLC has analogue input and digital input and output and is linked to solenoid valve actuators, fluorescent screen actuators limits, thermocouples, water flow meters, vacuum interlocks, vacuum gauge controllers, cooling water flow meters in the heat exchangers, thermocouples in the heat exchangers and water conductivity probes.

PSS shutter is controlled from the PSS and sends and receives status signals to/from EPS PLC.

Vacuum schematic is shown in a separate drawing. Vacuum gauge controllers are monitoring vacuum level measured by Pirani and ion gauges mounted on different beamline components. Ion pump controllers provide power to each of the ion pumps used on the beamline. High voltage splitter units are used where necessary to power more than one pump per output channel.

Micro IOC controlling the vacuum system uses RS485 protocol for communication with the pump and gauge controllers. Vacuum gauge controllers are integrated with the EPS system to monitor vacuum level in different sections of the beamline.

Piezo actuators need to have vacuum interlocks linked to the vacuum gauge controllers.

Table 0.7 Controls schematic of the CHX beamline.

Beamline Component	No. of units	Number of elements per unit											
		Controlled by 8 axis Motion Control units					Controlled by EPS PLC			Controlled by micro IOC			PC
		Stepper /Pico Motor	Server Motor	Limit/ datum switch	Enco-der	Refe-rence point	Flow meter	Thermo-couple	Sole-noid valve actuat.	CCD camera	DPT control unit	Current amplifier	
Beamline control system	1												1
Fixed mask	1						1	1					
Blade BPM	1	2		4			1					1	
CVD Diamond windows	1						1	1					
Bremsstrahlung collimator	2						1	1					
Slits (H **or** V)	12	1		2	1								
Gate Valve	14			2					1				
Horizontally Deflecting Mirror (water cooled)	2	6		10	5	5	1	1					

VFM	2	5		10	5	5					1		
HFM	1	5		10	5	5					1		
Pink Beam shutter	3			4			1	1	1				
Fluorescent screen	5			2			1		1	1			
DCM (water cooled)	2	5	1	8	7	6	1	3			1		
White/pink beam stops	5						1	1					
QBPM	2	1		2								1	
Water cooled wndows (diamond or Be)	2						1	1					

3.4.3.3 High Heat Load Monochromator

A water cooled Si(111) DCM with no sagittal focusing on the second crystal should provide energy resolution of ~10^{-4}, fixed exit beam height and operate across the requested energy range from 7 keV to 20 keV. Expected performance parameters of the DCM and some useful information are given in

Table 0.8. We also assume 25 mm vertical offset between the incoming and outgoing beams and that the beam 'walk' alone the second crystal as the energy changes will be taken by longitudinal translation of the crystal.

The results in

Table 0.8 show that

- The energy resolution is expected to be from $1.34\cdot10^{-4}$ to $1.42\cdot10^{-4}$.
- The Bragg angles are from 5.67° to 16.4°. The Bragg angle calculation assumes the lattice constant of Si(111) of 5.4309 Å.
- Perpendicular translation of the 2nd crystal over the energy range is about 0.44 mm.
- Longitudinal translation of the 2nd crystal over the energy range is approximately 82 mm.
- The footprint of the beam at the crystals of the Si(111) monochromator at all energies is less than 0.22 mm x 2.2 mm assuming 4.8 μrad (H) x 4.8 μrad (V) opening of the beam (coherent beam).If the aperture is 20 μrad (H) x 20 μrad (V) the maximum beam footprint increases to 0.9 mm x 9 mm.

The design of the DCM should meet stability requirements and be able to withstand heat loads as discussed earlier.

Table 0.8 Performance parameters of the Si(111) DCM.

Parameters	**Energy, keV**		
	7	12	20
Wavelength, Å	1.7712	1.0332	0.6199
Bragg angle θ_B, deg	16.4058	9.483	5.6732
Reflectivity (double reflection)	0.85	0.94	0.98
Energy resolution			
Rocking (Darwin) width[1], μrad	39.1586	22.2161	13.2122
Bandpass due to source size	$4.3\cdot10^{-10}$	$7.1\cdot10^{-10}$	$1.2\cdot10^{-9}$
Bandpass due to accepted angular divergence	$1.6\cdot10^{-5}$	$2.9\cdot10^{-5}$	$4.8\cdot10^{-5}$
Resolution of the DCM	$1.34\cdot10^{-4}$	$1.36\cdot10^{-4}$	$1.42\cdot10^{-4}$
Resolving power[2]	7463	7349	7067
Crystal size and position			

Vertical offset between incoming and outgoing beams, *D*, mm	25		
Perpendicular offset between 1st and 2nd crystals[3], mm	13.0	12.7	12.6
Longitudinal offset between the crystals[4], mm	44.3	75.9	126.4
Maximum beam footprint[5] transverse to the beam, mm along the beam, mm	0.22		 2.21

Notes: 1) Intrinsic resolution of Si(111) is $\left(\frac{\delta\lambda}{\lambda}\right)_{cryst.}$ = 1.33 $\cdot 10^{-4}$ [30]. The rocking (Darwin) width is

$$\Omega = \frac{\delta\lambda}{\lambda}\tan\theta_B \ .$$

2) The resolution is determined by the width of the rocking curve of the crystal, beam opening angle and size of the source

$$\frac{\Delta E}{E} = \sqrt{(\Delta\theta^2_{source} + \Delta\theta^2_{slit})\cot^2\theta_B + \left(\frac{\delta\lambda}{\lambda}\right)^2_{cryst.}} \ ,$$

$$\Delta\theta_{source} = \sigma_y / p \ \text{ and } \ \Delta\theta_{slit} = \min(\sigma_y^{'}, s_v)/p \ ,$$

where σ_y is the vertical source size (FWHM), $\sigma_y^{'}$ is the vertical divergence of the beam (6σ), s_v is the opening of the monochromator vertical entrance slit and *p* is a distance from the source.

Resolving power of the monochromator is reverse to the total band pass, i.e. it is $\frac{E}{\Delta E}$.

3) The distance, *X*, measured perpendicular to the optical surfaces of the crystals: $X = \frac{D}{2\sin\theta_B}$, where *D* is the constant vertical offset between incoming and outgoing beams.

4) The distance, *Y*, measured along the surface of the crystals: $Y = \frac{D}{2\cos\theta}$, where *D* is the constant vertical offset between incoming and outgoing beams. The longitudinal offset shows beam walk parallel to the surface of the crystals as the Bragg angle changes. To maintain the constant beam offset, *D*, the *X* and *Y* should satisfy the condition $\frac{1}{X^2} + \frac{1}{Y^2} = \frac{4}{D^2}$.

5) The beam footprint depends on the rms size and divergence of the incoming beam, DCM distance from the source and the Bragg angle so that

$$F = \sqrt{\sigma^2_{x,y} + (\sigma^{'}_{x,y} \cdot p)^2}; \ F_x = F; \ F_y = F/\sin\theta \ ,$$

where $\sigma_{x,y}$ and $\sigma'_{x,y}$ are the size and divergence of the source, correspondingly, *p* is the distance from the source and θ is the Bragg angle.

3.4.3.5 Mirrors (White Beam and Monochromatic)

As has been discussed earlier, the beam line is expected to have few mirrors for collimating and focusing the beam in horizontal and vertical planes. Preliminary analysis shows that full energy range of 7 -20 keV can be covered without changing the angle of incidence while providing good transmission of the x-ray beam over the whole range.

Increase of the angle of incidence is favourable for reducing the cut-off energy, lengths of the mirrors and improving harmonic rejection, but the reflectivity of the mirrors decreases. We have considered using bare Si, Pt, Pd and Rh coatings and concluded that Rh and bare Si are most suitable for the energy range. Pd is very similar to Rh but the latter has slightly better reflectivity. Reflectivity of Pt shows few absorption edges and it is more suitable for higher energies.

Most mirror suppliers will guarantee densities of Rh in the coatings to be better than 90% of the bulk material which is 12.41 g/cm^3 [17,18]. We therefore assume in this analysis the density of Rh of 11.17 g/cm^3 for calculating reflectivity of the mirror stripes. The densities are usually lower, about 85% of the bulk, for bimorph mirrors. The lower density means slightly lower reflectivity and lower cut-off energies at similar incidence angles. As the density of Rhodium decreases from 90% to 85%, the cut-off energy decreases by about 550 eV.

The density of Si, 2.33 g/cm^3 [28], is slightly higher than the density of Silica, 2.2 g/cm^3 [18]. Usually Silica is used as a substrate for making mirrors to focus monochromated beam and Silicon is used to make mirrors operating in a white beam. The data in Figure 0.5 show that replacing Silica with Silicon as a mirror substrate increases the cut-off energy by approximately 300 eV.

Figure 0.5 shows variation of the critical angle of the mirrors versus energy for Si, Silica, Rh (and Pt). The critical angles were calculated as $\alpha_c = \sqrt{2\delta}$, where δ is a real part of the refractive index of material. Incidence angle of the mirrors should ensure that the low energy beam is not contaminated by the beam of higher energy. Also it is desirable to keep the mirrors reasonably short. But the reflectivity of the mirrors decreases as the angle of incidence increases. Therefore the incidence angle should be optimised taking into account these factors and ease of use.

The useful energy range is defined from 7 keV to 20 keV [2] and from the point of view of ease of use changing the mirror incidence angle should be avoided. In that case the mirrors could be set at an incidence angle of approximately 3.0 mrad to achieve about 95% reflectivity using Rh stripe. Higher reflectivity can be obtained using Si or Silica stripe, Figure 0.6.

We therefore suggest operating at fixed angle of incidence and use bare Si (cut off energy 10.4 keV) below approximately 10 keV and Rh (cut off energy 20.8 keV) from 10 keV to 20 keV. Reflectivity of Si and Rh at 3 mrad is shown in Figure 0.7. We suggest using Silica rather than Silicon with monochromated beam.

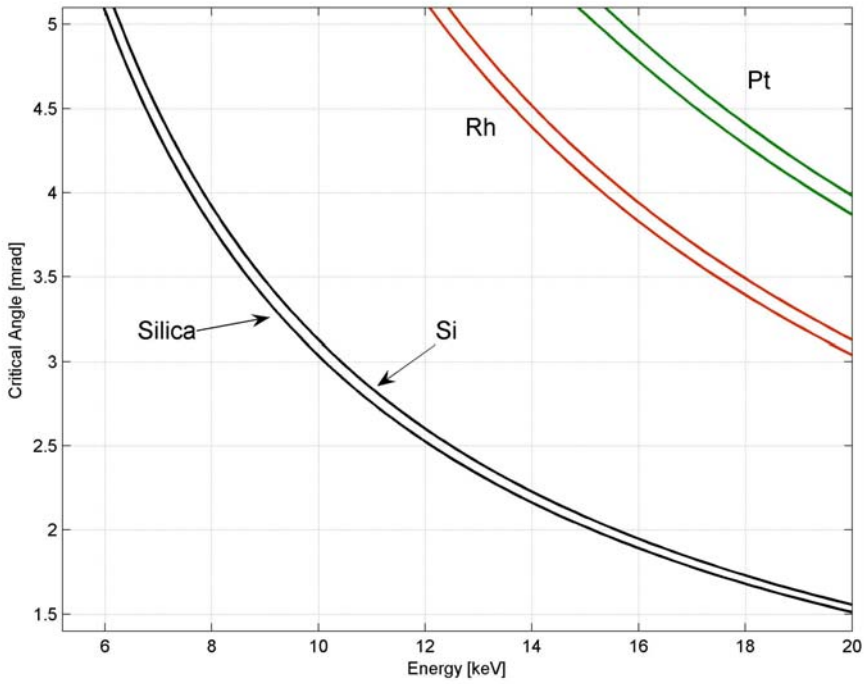

Figure 0.5 Variation of the critical thickness versus energy for bare Silica, Silicon, Rhodium and Platinum. The double lines for Rh and Pt correspond to different densities of the materials: 85% density of the bulk for the lower line and 90% for the upper line.

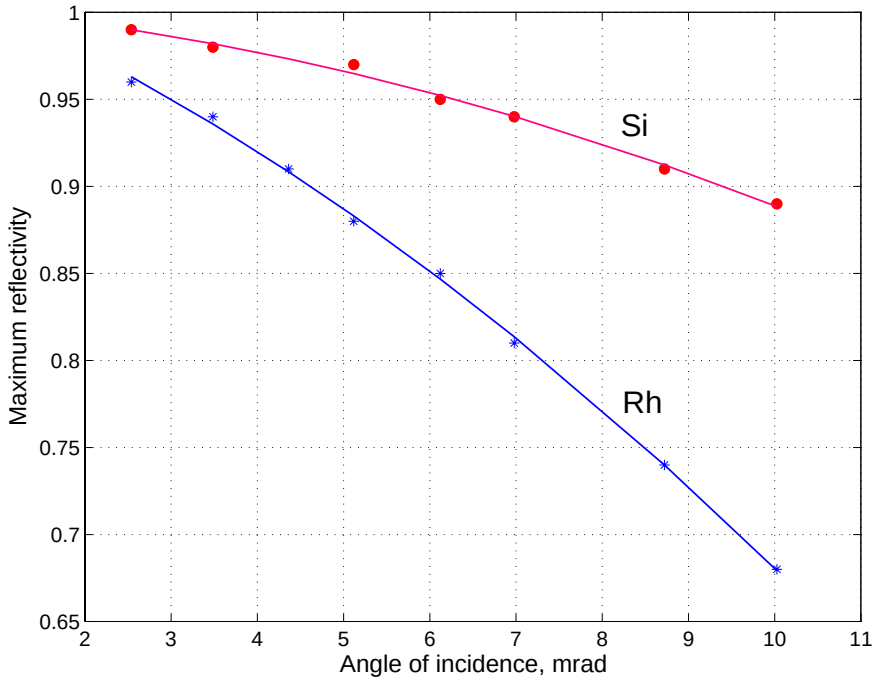

Figure 0.6 Variation of maximum reflectivity of Rh and Si versus angle of incidence.

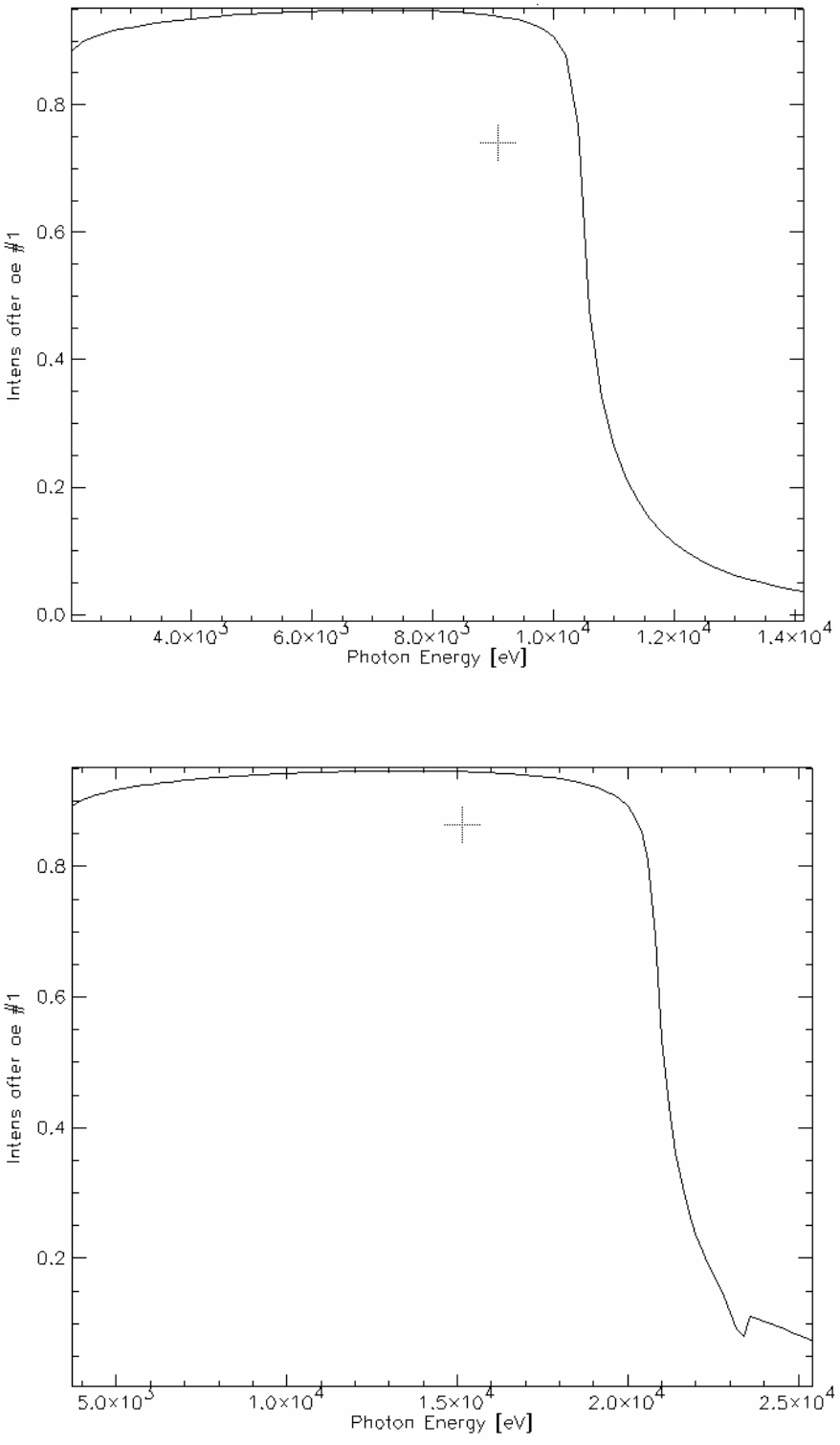

Figure 0.7 Reflectivity of Silicon (top) and Rhodium of 90% density of bulk (bottom) at 3.0 mrad.

Some useful characteristics of the mirrors are shown in Table 0.9.

The lengths of the mirrors are calculated for the case of 0.02 mrad x 0.02 mrad opening of the beam and for beam divergence of the central cone.

Table 0.9 Parameters of the mirrors. The *p* and *q* are source-to-mirror and mirror-to-image distances.

Mirror	**Optical distance from source, m**	**Inci-dence angle, mrad**	**Coating**	**Beam Footprint, mm**		**Bent radius m**	***P*, m**	***Q*, m**
				Aperture 20 μrad x 20 μrad	**Aperture 4.8 μrad x 4.8 μrad**			
HDM1	26.89	3	Si, Rh	179	43	N/A	-∞	∞
HDM2	28.96	3	Si, Rh	193	46	N/A	-∞	∞
VFM	47.13	3	Silica, Rh	314	75	TBD	-∞	TBD

3.4.3.6 FEA and Ray Tracing Analysis

The calculations are based on the assumptions that the horizontally deflecting mirror (HDM) at an incidence angle of 3 mrad uses a bare silicon reflecting surface and is located at 32.13 m from the source. The beam opening aperture is 0.020 mrad x 0.020 mrad. The Si(111) DCM after the deflecting mirror is at 46.83 m from the source. The primary beam is attenuated by the 200 μm thick CVD diamond window/filter located upstream of the mirror. The horizontally deflecting mirror selects 0.02 mrad of the beam to the side from the centre.

The results of the ray tracing using XOP and Shadow packages are given in Tables C1 and C2. To compensate for defocusing of the beam by slope errors at the HDM and DCM the bend radius of the HDM was optimized to achieve a single spot and maximize the intensity. Only for the Case 1 in Tables C1 and C2 representing the worse case of heat load and thermal slope errors the optimum radius was smaller than the nominal radius.

Table C1. Results of FEA analysis at different heat loads at the horizontally deflecting bare Silicon mirror (at 32.13 m, incidence angle 3 mrad) and 1st crystal of the Si(111) DCM (at 46.83 m, Bragg angle of 12.69^{o} corresponding to 9 keV). Beam opening aperture is 0.02 mrad x 0.02 mrad. The 200 μm thick CVD diamond window is assumed upstream of the mirror. Single or double U19 undulator source is operating in high-beta straight and in low emittance (0.55 nm-rad) mode.

Beamline Component	Final Case No.	Source	Max slope X, μrad	Max slope Y, μrad	RMS slope X, μrad	RMS slope Y, μrad
Horizontally Deflecting mirror	1	2xU19, K=1.731, Power= 20.5 W	2.63	0.94	1.15	0.78
	2	1xU19, K=1.0, Power= 2.1 W	0.27	0.09	0.12	0.08
	3	1xU19, K=1.731, Power= 10.0 W	1.28	0.45	0.56	0.38

	4	2xU19, K=1.0, Power= 4.2 W	0.53	0.19	0.23	0.16
DCM	1	2xU19, K=1.731, Power= 11.7 W	16.6	22.1	7.6	7.8
	2	1xU19, K=1.0, Power= 3.0 W	4.1	5.4	1.9	1.9
	3	1xU19, K=1.731, Power= 5.7 W	7.9	10.4	3.6	3.7
	4	2xU19, K=1.0, Power= 6 W	8.3	11.0	3.8	3.9

Table C2. Results of ray tracing analysis (final) of the hard coherent beamline at 9 keV. Flux was calculated over the 1000 µm x 20 µm aperture placed at the sample position at 50 m from the source. The primary beam, I_o, is assumed to be of 0.020 mrad x 0.020 mrad. The mirror is 250 mm (L) x 50 mm (W). Bending radius of the VFM was optimised by changing the focal distance. Nominal radius before any optimisation is 447.2 m.

Case No.	Incoming Flux I_o, ph/s	Spot size, µm	Flux, ph/s	Spot size, µm	Flux, ph/s	Optimised R_m (VFM), m
		no crystal distortion		Slope errors at HDM and DCM		
1	5.39×10^{14}	314 x 4.7	5.52×10^{13}	287 x 1.8	1.41×10^{13}	264.5
2	1.28×10^{14}	321 x 4.7	1.29×10^{13}	291 x 1.7	6.58×10^{12}	492.5
3	2.18×10^{14}	329 x 5.3	2.19×10^{13}	307 x 2.6	7.37×10^{12}	812.7
4	2.93×10^{14}	300 x 3.7	2.96×10^{13}	272 x 2.8	1.24×10^{13}	876.0

3.4.4 Instruments

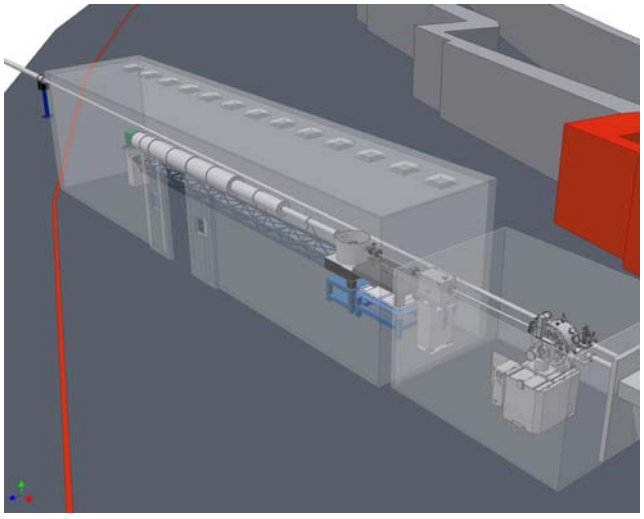

The source brightness at NSLS-II will enable XPCS experiments to study dynamics in disordered system at time scales well below milliseconds. The goal of the instrumentation in this endstation is to turn this potential into reality. To do so, the instrumentation must not compromise the superior coherence quality of the source and a state-of-art detector is needed to actually measure the intensity fluctuations in x-ray speckles that correspond to sample dynamics. Detailed requirements have already been set forth in the CDR and will not be repeated here. This document will only describe the actual instrumentation that will satisfy these requirements.

The first component inside the endstation is a vertical focusing mirror that will reduce the vertical coherent length to match that in the horizontal direction. The mirror is followed by 3 sets of slits to select coherent flux and clean up parasitic scattering from the slits. Between the mirror and slits are an attenuator and a fast shutter. The attenuator is necessary for samples that produce strong scattering. The x-ray absorbing material in the attenuator will be double-side polished silicon so that it will not introduce significant phase error to the propagating x-ray wave front. The shutter is

necessary when a CCD-type detector is being used and to avoid sample exposure to x-rays and radiation damage when data are not being collected.

The sample will be housed in a vacuum sample chamber just downstream of the 3rd set of slits. For solid samples, a hexapod will be used to position the sample into the beam and translate the sample before the expose part is damaged x-rays. The advantage of the hexapod is that an arbitrary point on the sample can be programmed as the rotation center. This is particularly useful for thin film samples that are measured in grazing incidence geometry. A rotary stage under the hexapod makes up for the hexapod's limited azimuthal rotation range. Liquid samples will be continuously flowed through a flow cell to reduce radiation damage.

The length of the flight path downstream of the sample chamber will be 10m long to produce x-ray speckles comparable to the pixels (assuming 100μm) in size. It is made up of several sections so that shorter sample-to-detector distance is possible if desired. Because of the long length of the flight path, it also needs to be large enough in diameter in order to capture enough *q*-range. With the current design of 20" tube, the highest q accessible at 12keV and 10m sample-to-detector distance is ~0.15$Å^{-1}$. The flight tube can be offset so that the beam is not centered on the exit window and higher *q*-range can be accessed on one side. The tube size is most likely larger that that of the detector itself. The detector will therefore be mounted on an x-z stage so that it can multiple images can be collected and tiled to cover the entire available *q*-range.

A beamstop assembly is located at the end of the flight path. This assembly consists of x-z-rotary stages that can position multiple beamstops (e.g. with different size or beam intensity detector) into the beam to block the direct beam and measure its intensity. A similar assembly is currently being built at beamline X9 of NSLS.

The detector group at NSLS is planning to develop a pixel array detector with auto-correlator built-in in each pixel. Such a detector will be ideal to realize the full potential of XPCS measurements at NSLS-II. In case that the development of such a detector is not successful, a pixel array detector without auto-correlators will be used instead. Specifically, a pixel array detector with 75um pixels and 10kHz frame rate is being designed by DECTRIS, who is currently marketing its 170um, 200Hz frame rate pixel array detector, PILATUS. In this case, a large computing facility must be established to store and post-process collected data.

3.5 Additional Requirements Imposed on the Conventional Facilities

Special attention must be given to stability requirements. These are determined by temperature stability and vibration (natural and self-inflicting) and they have been extensively discussed at the recent NSLS-II Stability Workshop in April 2007 [10-12].

The beam stability requirements for different components are based on achieving less than 10% variation of the beam size. To conduct different experiments like the ones mentioned by Sandy [10] or Shen [11] horizontal and vertical position stability should be 0.2 μm, vertical angle stability 0.2 μrad and horizontal angle stability 1 μrad [12]. For SAXS high beam stability (<1%) is desirable.

Typical temperature variations measured at ESRF are about 0.5^{o} [13]. At ID22 beam line at ESRF temperature variations are < 0.1^{o} over 24 hours [12]. Similar or better stability should be achieved for the beamline especially taking into consideration extremely big length of the beamline. For demanding beam lines new high flow rate air conditioning units (air renewal rate 20 cycles/hour) are used. Vibrations from air flow are reduced using porous ducts [12].

Measures allowing reducing thermal effects include choosing low expansion materials, cooling local heat sources, thermal insulation of vessels, moving all control electronics outside the hutches [13], using thermally insulated sand-filled stands, aiming at achieving first natural frequency at above 50 Hz [14] and high thermal inertia [13]. It has been pointed out that angular vibration drifts are much worse than linear [13]. This is particularly true for long beam lines like IXS.

Temperature control requires high resolution industrial grade instruments and controls with excellent repeatability. At DESY, for example, narrow span thermistor/transmitters with 0.01^{o} C sensitivity and programmable controllers with 14 bit resolution will be used [15].

Vibrations generated by water chillers, fans, compressors etc. can be reduced by selecting rotating equipment with stringent balancing requirements, using spring support for rotating equipment and inertia bases [16].

References

1. NSLS-II Conceptual Design Report, Brookhaven National Laboratory (2006).

2. BNL staff, Private communications (2007).

3. Summary of NSLS-II Source Properties, NSLS-II User Workshop 17-18 July 2007, http://www.bnl.gov/nsls2/project/source_properties.asp, 31 July 2007 (2007).

4. J. Hill, Experimental Facilities, NSLS-II User Workshop, 17-18 July 2007, http://www.bnl.gov/nsls2/07_Hill_XFD_NUW_July07.ppt (2007).

5. K-J. Kim, Optical Engineering **34**, 2, 342 (1995).

6. M.S. del Rio, R. J. Dejus, XOP Home Page: http://www.esrf.fr/computing/scientific/xop2.1/

7. M.S. del Rio, SPIE Proc. 3448, 230 (1998).

8. L. Berman, ID Beamline Optics and Damping Wigglers, EFAC May 10th 2007 (2007).

9. J.-C. Biasci, B. Plan and L. Zhang, J. Synchrotron Rad., **9**, 44 (2002).

10. A. Sandy, A hard X-ray Coherent scattering beamline for NSLS-II and …SAXS?, NSLS-II User Workshop, 17-18 July 2007, http://www.bnl.gov/nsls2/workshops/docs/UserWorkshop/BOS/coherent/Shen_Soft_Coherent.ppt (2007).

11. Q. Shen, Overview on Coherent Diffraction Imaging and Its Applications, NSLS-II User Workshop, 17-18 July 2007, http://www.bnl.gov/nsls2/workshops/docs/UserWorkshop/BOS/coherent/Shen_Soft_Coherent.ppt (2007).

12. Stability Requirements for NSLS-II Beamlines, Report of the NSLS-II Stability Task Force, NSLS-II Stability Workshop, April 18-20, 2007, http://www.bnl.gov/nsls2/docs/StabilityTaskforceReport.pdf ; updated on June 18, 2007.

13. Y. Dabin, Stability of instruments at ESRF, NSLS-II Stability Workshop, April 18-20, 2007, http://www.bnl.gov/nsls2/workshops/docs/Stability/Dabin_ESRF_Stability.ppt

14. S. Sharma and V. Ravindranath, Stability of Mechanical Systems, NSLS-II Stability Workshop, April 18-20, 2007, http://www.bnl.gov/nsls2/workshops/docs/Stability/Sharma_mechanicalSystems.ppt

15. C. Channing, Conventional Facilities. Temperature Stability, NSLS-II Stability Workshop, April 18-20, 2007, http://www.bnl.gov/nsls2/workshops/docs/Stability/Channing_CF_Tempstablity.ppt

16. J. Sidarous, Engineering Approaches to Reducing Floor Vibration at the APS and CNM, NSLS-II Stability Workshop, April 18-20, 2007, http://www.bnl.gov/nsls2/workshops/docs/Stability/Sidarous_CF.ppt

17. X-Ray Mass Attenuation Coefficients, NIST, http://physics.nist.gov/PhysRefData/XrayMassCoef/tab1.html

18. Densities (g/cm^3) of some Common Materials, LBL, http://henke.lbl.gov/cgi-bin/density.pl

19. W.B. Peatman, Gratings, mirrors and slits, Gordon & Breach Sci. Publ., Amsterdam (1997).

20. M.C. Wilson, Diamond Personnel Safety System, Proc. ICALEPCS2003, Gyeongju, Korea, 2003, http://accelconf.web.cern.ch/accelconf/ica03/PAPERS/WP515.PDF

21. A. Boron, 30ID Beamline Requirements Document for the Generation-3 Personnel Safety System (PSS) of the Advanced Photon Source at Argonne National Laboratory, Document No. 4104013001-000122004, March 2004, http://www.aps.anl.gov/asd/safetyilocks/PSS/Gen3/30id/Requirements_30ID_V00_2004_03_05%20.pdf

22. J. Hawkins, Personnel Safety System for the beamlines at the Advanced Photon Source, Rev. Sci. Instrum. 67, 3370 (1996).

23. F. Schrever, New Australian Synchrotron uses safety PLCs, http://www.industrial-embedded.com/articles/schrever/

24. M. Ramanathan, Preliminary Design Report. Inelastic X-ray Scattering CDT. Sector 30, March 2004, http://www.ixs.aps.anl.gov/IXS_PDR_final.pdf .

Appendix A: Ray Diagram

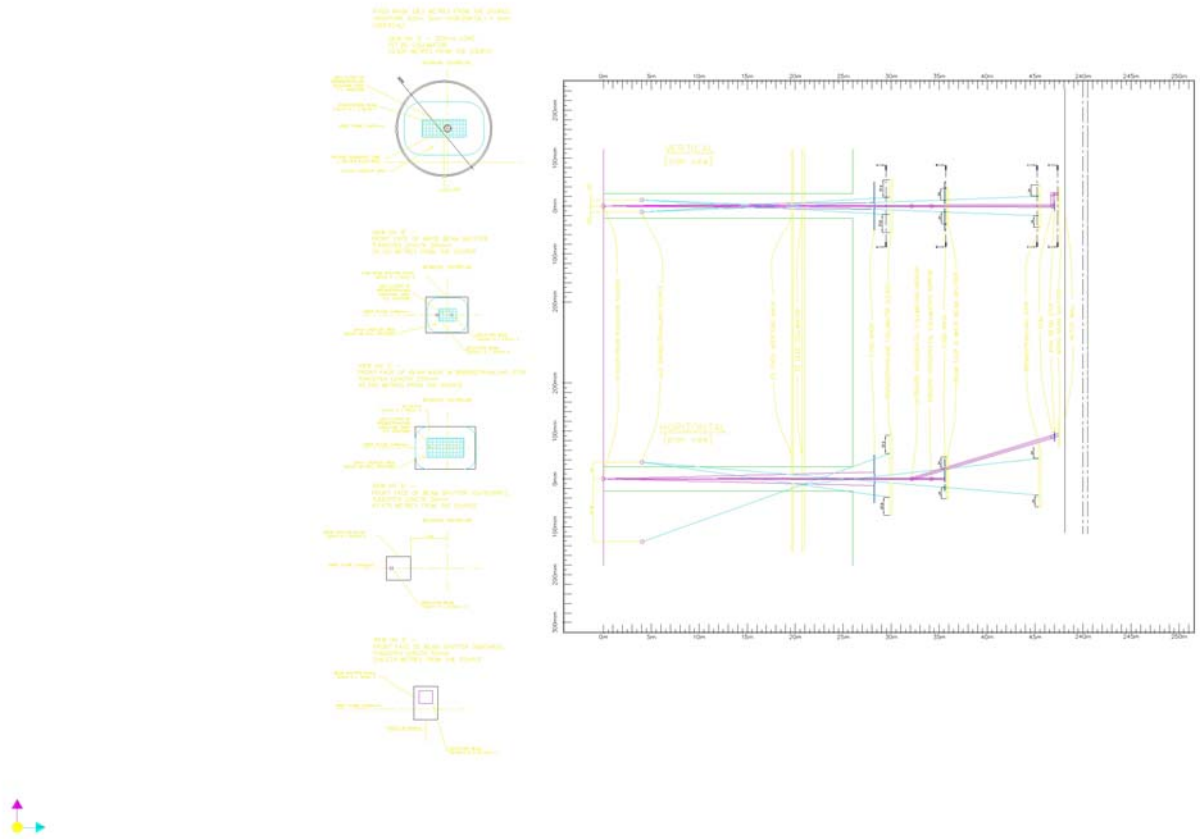

Figure A1. Bremsstrahlung and photon beam ray tracing drawing for XPCS beamline.

Appendix B: Beamline Layout Drawings

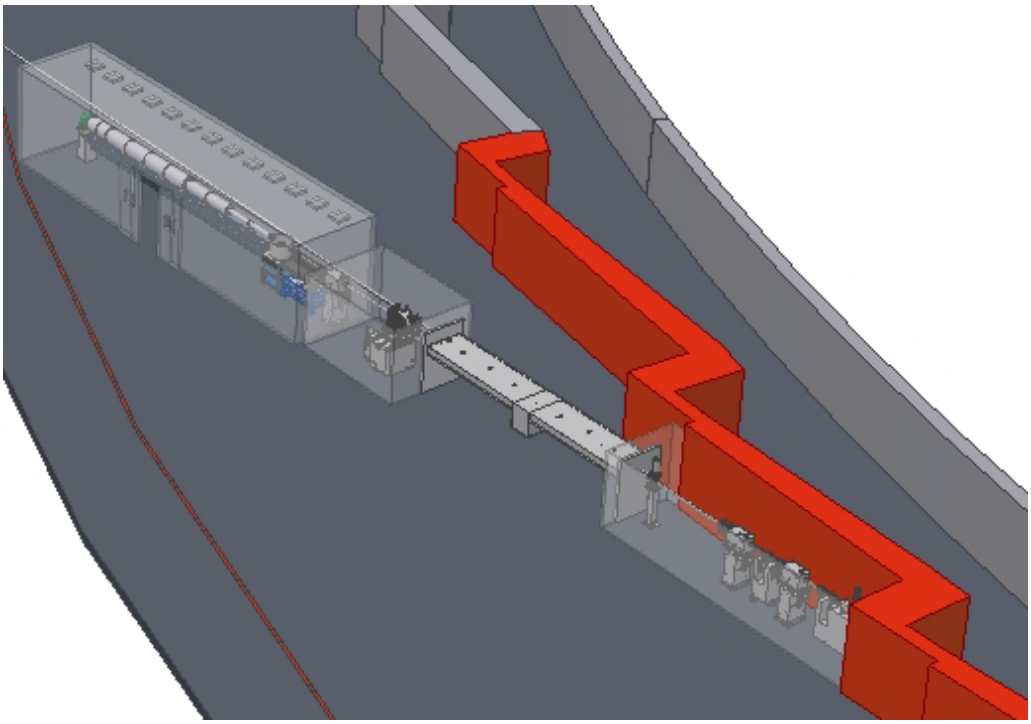

Figure A1. General view of the Hard Coherent X-Ray beamline.

Appendix C: List of Key Beamline Components

CVD Diamond Windows

Chemical Vapour Deposition (CVD) Diamond offer extreme hardness, high thermal conductivity, chemical inertness, and high transparency over a very wide spectral range. Stronger and stiffer than Beryllium, with lower thermal expansion and lower toxicity, it is ideal for UHV isolation windows in X-ray beamlines. Windows can be supplied embedded in UHV flanges and with efficient water cooling.

CVD Diamond windows, Figure 0.1, developed in cooperation with the Fraunhofer Institute of Germany and Paul Scherrer Institute of Switzerland, with the support of Argonne National Laboratory in the USA, are manufactured by Diamond Materials GmbH.

Specifications

Thickness:	200 µm
Diameter:	5 – 50mm
Vacuum performance:	<10-9mbar l/sec
Surface finish:	10nm RMS roughness

The window will be used when a monochromatic beam mode is replaced with the pink beam regime. The window will be put in place of SiN windows that are used in a monochromatic mode as last windows before the sample.

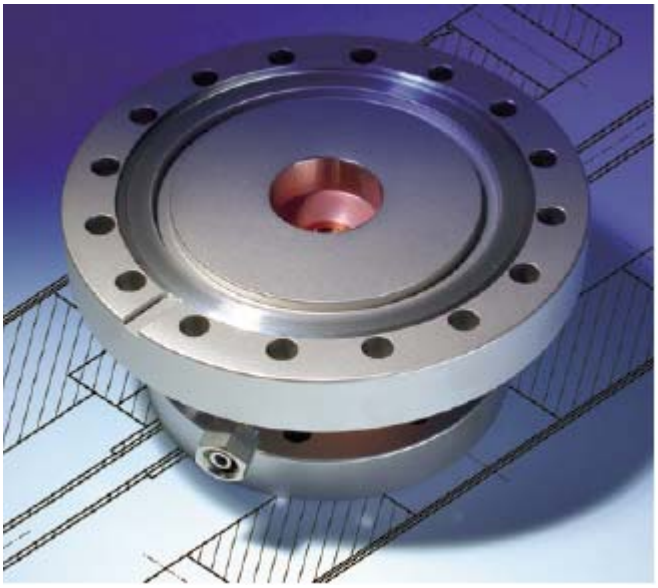

Figure 0.1 Water cooled CVD Diamond window.

Fixed mask and CVD Diamond window / filter

Description:

Window material:	CVD diamond, optical quality
Thickness:	180 µm ± 30 µm
free aperture:	10.0 mm
Surface Roughness :	R_a less than 20 nm

Mounted to a watercooled OFC copper joint with CF 63 flanges on each side and a central conical hole (20x10 mm on one side, 7.2x3.6 mm at the other side)
Assembly leak tight to a rate of 1x10e-10 Torr L/sec of He
CVD diamond window pressure tested at 1 atm pressure

Schematic drawing:

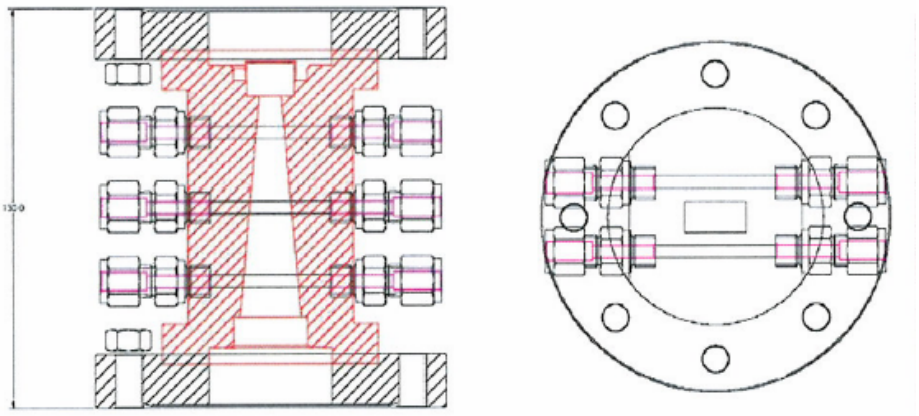

Figure 0.2 Outline specification and schematic drawing of a typical diamond window.

Blade BPM

The White Beam (BBPM) consists of a vacuum vessel containing the sensor mechanism, a support stand, and associated electronics.

The sensor mechanism consists of 2 insulated blades fixed a known distance apart in a vacuum chamber. The signals from these electrodes provide a measurement of the position of the beam.

The gap between the blades and their orientation are chosen to provide a usable current without significant disturbance to the usable x-ray beam.

Quadrant BPM

The QBPMs are available in HV and UHV configurations. The QBPMs will need to be taken out of the beam when the end station is used in a pink beam regime.

Fluorescent Screens

The screens are made in two modifications: water cooled and not water cooled. For using with pink beam water cooled option should be chosen.

Slits

High Heat Load Slits for Undulator Beams

The slit system, **Figure 0.3**, consists of 2 L-shaped absorbers arranged in series along the beam (the downstream being rotated through 180°) to define the aperture,

Figure 0.4. Each mask therefore defines two edges of the beam. Each absorber is moved laterally and vertically by external translation stages to define the beam. There are edge-welded bellows before, between and after the two absorbers, which allow the movement of the slits relative to the beam. The slit mechanism is mounted on a synthetic granite-filled mild steel frame for stability and vibration rejection.

Slits of this type will be used to define the size of the white beam.

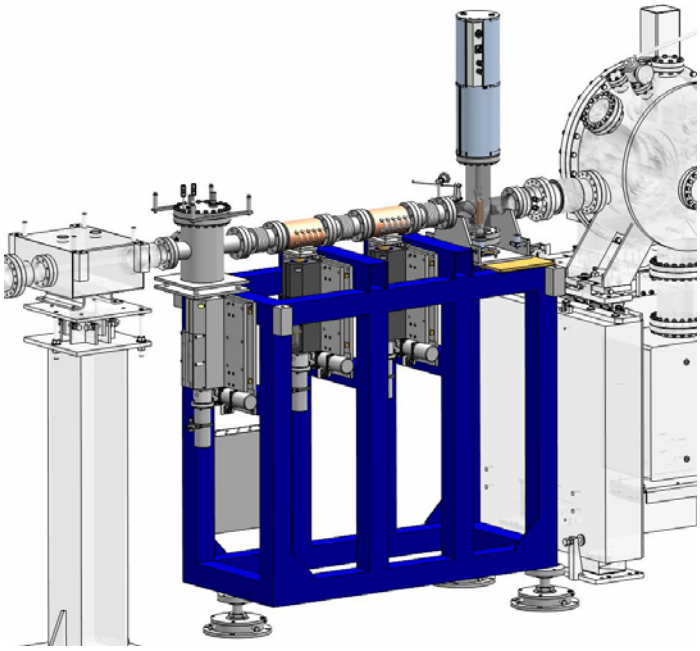

Figure 0.3 High Heat Load Slits

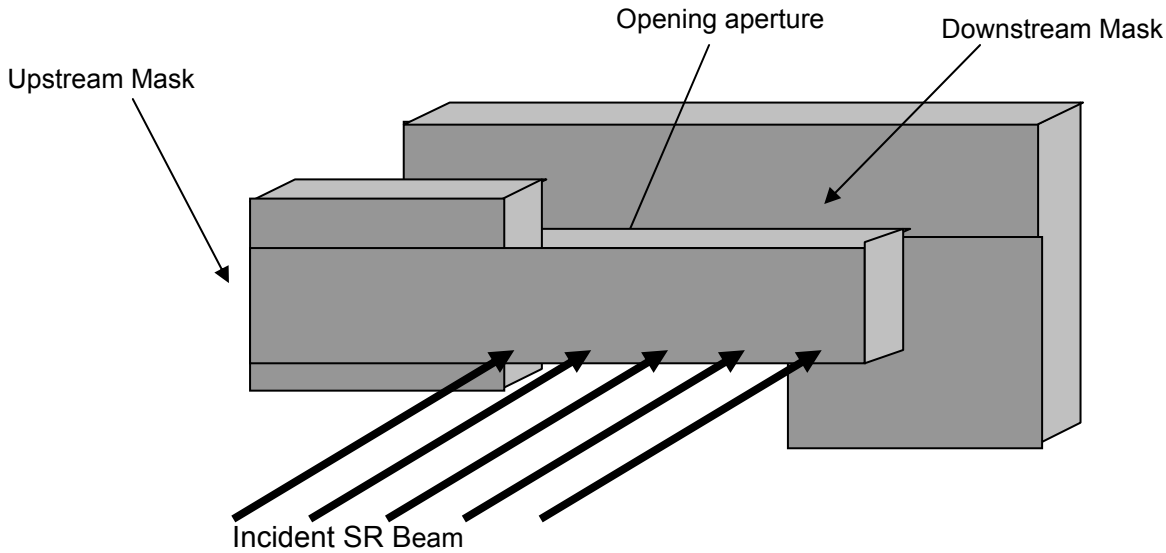

Figure 0.4 High Heat Load Slits schematic.

Pink beam Slits

The cooled Slit Unit comprises two independently actuated slit blades, mounted on the same flange. Each Slit System has a horizontal slit unit and a vertical slit unit, each of which is mounted on a flange on a vacuum vessel, one on top of the vessel and one at the side of the vessel. Each pair of blades defines either the horizontal or vertical dimension of the beam, Figure 0.5.

Each cooled slit unit consists of two slit blades, each of which is mounted onto a water-cooled Glidcop body and connected to an external actuator mechanism through a flange on the slit vessel. Indium foil is clamped between the slit blade and the copper body to enhance heat transfer by conduction, Figure 0.6. On each slit blade the edge nearest the beam is chamfered, at 3°, to produce a sharp defining (knife) edge. The chamfered face is positioned on the downstream side of the blade (on the side of the blade furthest from the source). On each cooling block the edge nearest the beam is chamfered, Figure 0.7, to reduce the power density of the beam on the block at the operating condition. The chamfered face is positioned on the upstream side of the block. An additional tungsten disaster plate is added to prevent damage over the full range of operation. The slit blades are manufactured from 5 mm thick tungsten alloy. The blade defining edge protrudes 0.5 mm above the cooling block.

The slits are specially designed for high heat loads where conventional water cooled slits can not be used.

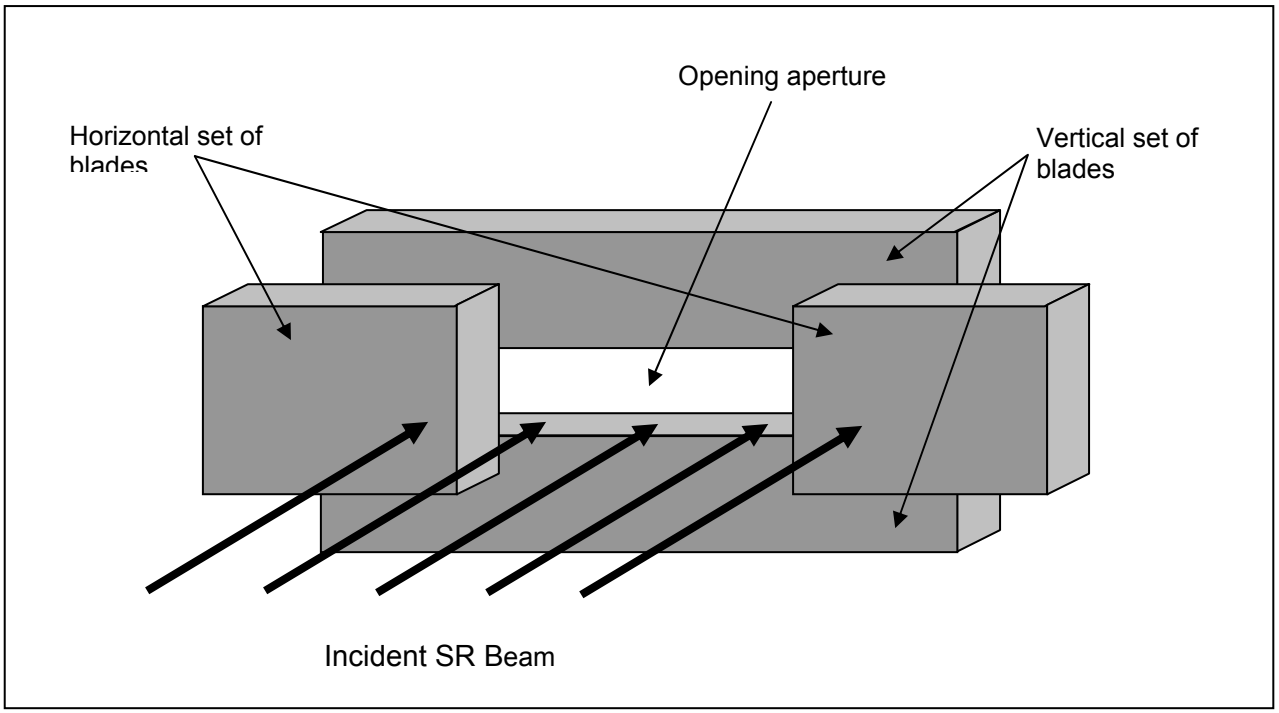

Figure 0.5 Schematic set-up of a horizontal/vertical slit system.

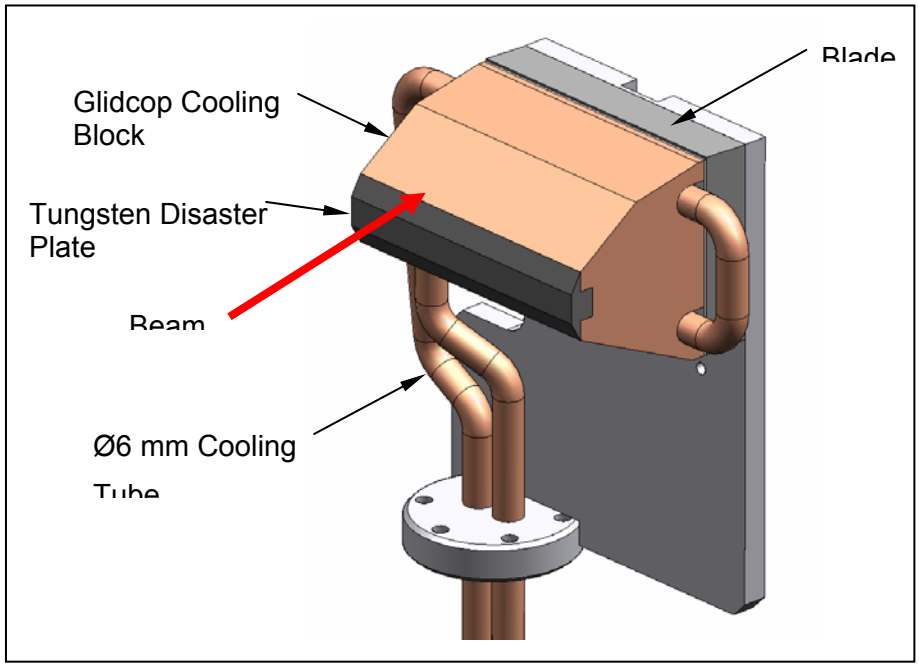

Figure 0.6 Cooling block & slit blade arrangement.

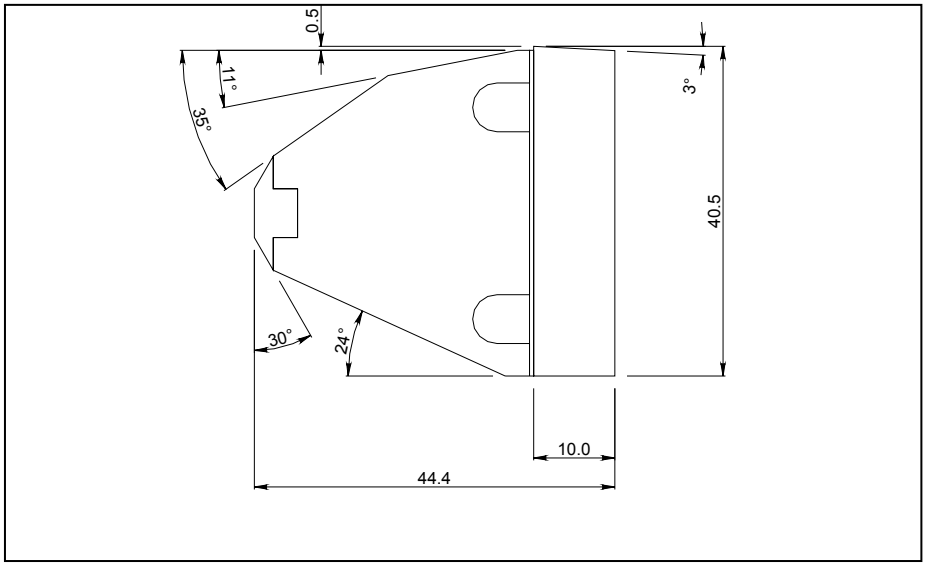

Figure 0.7 Cooling block & slit blade schematic.

Conventional water cooled slits

Each cooled slit unit consists of two slit blades, each of which is mounted onto a water-cooled OFHC copper body and connected to an external actuator mechanism through a flange on the slit vessel. Indium foil is clamped between the slit blade and the copper body to enhance heat transfer by conduction, Figure 0.8. On each slit blade the edge nearest the beam is chamfered, at 3°, to produce a sharp defining (knife) edge. The chamfered face is positioned on the downstream side of the blade (on the side of the blade furthest from the source). On each cooling block the edge nearest the beam is chamfered, at 20°, to reduce the power density of the beam on the block. The chamfered face is positioned on the upstream side of the block. The slit blades are manufactured from 10 mm thick tungsten alloy (95% tungsten or more with the remainder of nickel and iron). The blade defining edge protrudes 0.2 mm above the cooling block.

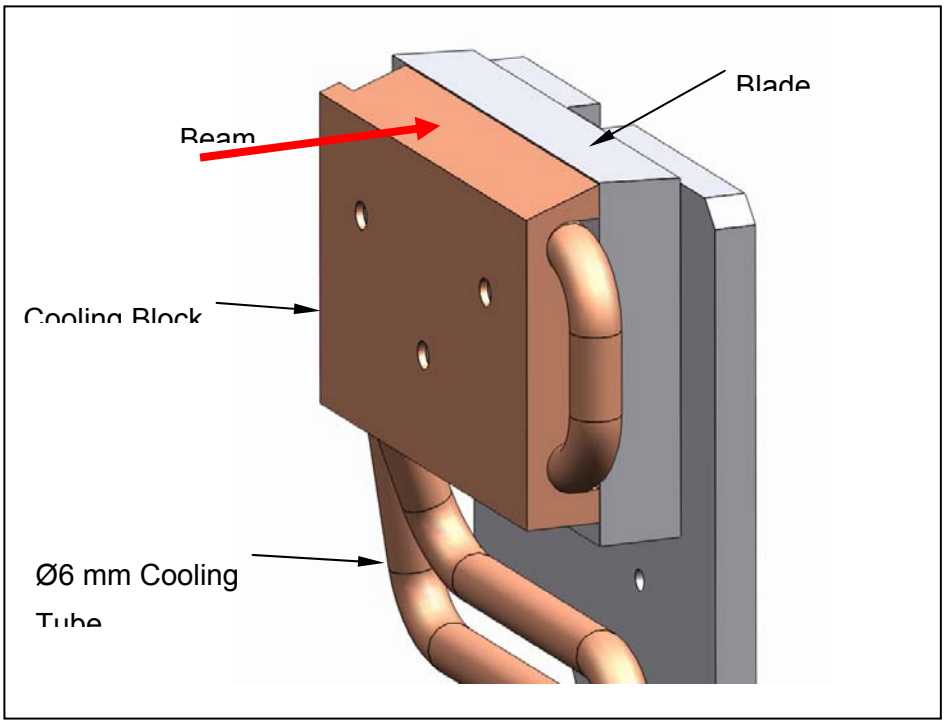

Figure 0.8 Cooling block & slit blade arrangement.

For the cooled slits a spare port is provided on the vessel. This port can accommodate an electrical feedthrough thus allowing thermocouples to be fitted to the slit blades should this be required. Thermocouples are not fitted as standard but can be retrofitted as an upgrade.

Bremsstrahlung collimator and beam stops

The Bremsstrahlung collimators are typically made of 300 mm of lead and their dimensions are calculated from the ray tracing. We will use one of the collimators immediately after the CVD Diamond window/filter.

First Bremsstrahlung stop will be specially designed to be put at the downstream end of the long beam transport pipe entering the outbound beamline. This is done to ensure sufficient separation

of the beam deflected by the mirrors. The Bremsstrahlung stop will be assembled with the water cooled beam mask.

As the end stations are designed for the pink beam Bremsstrahlung stops are needed after the sample positions. Exact location is to be decided when the end stations are designed.

Brehmsstrahlung stops are also anticipated after the DCMs. Depending on the detailed design they will be made of lead (out of vacuum) or Tungsten (in vacuum). The beam stops will need to be translated up and down when the operating mode is changed from monochromatic to pink beam mode.

Mirrors

Parameters of the mirror that will be used on the beamline are given in Table 0.9. It is not immediately clear whether bimorph mirror will offer any significant advantage. Adaptive optics for a VFM mirror can be particularly useful a water cooled DCM is used because residual slope errors could be compensated.

Plane deflecting mirrors will be water cooled and specially designed to cut out part (about one half) of the whole beam. They will operate at a fixed angle of incidence to simplify operation of the beamline. The deflecting mirrors will be made of Silicon, whereas the other mirrors can use Silica as a cheaper alternative.

The downstream vertical focusing mirror will operate in the monochromatic beam only. The mirror system will have capability of removing the optics from the beam to allow operating in pink beam regime.

Quality of the optical surface that can be achieved is being continuously improved by makers of the mirrors.

Double Crystal Monochromators

The water cooled monochromator system will most likely use a vertical beam offset of about 25 mm and a long second crystal to eliminate longitudinal translation and improve stability. The second crystal will be translated vertically to keep fixed offset of the beam.

The DCM is designed to operate at energies of 5-20 keV, has a fixed offset of 25 mm and uses a set of Si(111) crystals. The DCM is designed to achieve angular beam stability of 200 μrad that should be adequate for the current application.

Some useful characteristics of the monochromator of that type are shown in

Table 0.8.

White and pink beam shutters

Pink beam shutters will also be used. They will be positioned after the DCMs and before the hutch wall. Essentially pink shutters are made of a 15 mm thick water cooled Copper plate clamped to a 35 mm thick Tungsten block.

SiN 200 nm window

Supplier	SPI supplies
Outside frame dimensions	7.5mm x 7.5mm
Window size	1.5 mm x 1.5 mm
Membrane thickness	200 nm
Frame thickness	200 μm
Quantity	Pack of 50

4 CSX: COHERENT SOFT X-RAY BEAMLINE

4.1 Executive Summary

The coherent soft x-ray beamline design described in this chapter is state-of-the-art and will be able to fully exploit the brightness and flux provided by the NSLS-II storage ring. The source, an EPU45 Elliptically Polarizing Undulator, will allow full control of the polarization (circular and linear) of the incident photons. The beamline optics design will either preserve this polarization or, additionally, will allow fast-switching of the polarization state of the photon beam on the sample. In addition to providing very high photon flux at high energy resolution, the beam on sample will have a high degree of transverse spatial coherence.

The current design, presented here, will satisfy the requirements of "photon hungry" experiments that demand high photon flux (~10^{13} photons/sec), at high resolving power (~10^4), coherent (a few transverse modes), focused into a small spot (~1.5 μm x 3μm 1-σ).

4.2 Scientific Objective

The scientific motivation for this beamline is that its superior properties will expand the very exciting field of "photon hungry" experiments that currently are limited by their long acquisition times. This set of experiments includes any the uses the coherent part of the photon beam, such as coherent diffraction, phase retrieval imaging using coherent scattering, coherent based microscopy, phase contrast microscopy, and STXM. In addition and in particular, soft X-ray Photon Correlation Spectroscopy (XPCS) experiments demand very high coherent photon flux and have been severely limited by count rates available to date. In a different direction, but equally important, are the studies driven by a scientific case or interest in the understanding of the properties of new materials or artificially engineered systems. Examples of those systems are highly diluted materials, the study of micrometer size single crystals, nanosized-materials and interfaces. Obviously these systems could also be studied using the previously cited techniques, but in many cases other experimental techniques, so called standard, will provide with more precise information about their specific properties.

In general, either justifying the beamline from a technique or the scientific motivation point of view, a beamline working in the soft x-ray energy range will dramatically enhance its scientific capabilities with the possibility to select the incident polarization. This is a characteristic that in the past ten years has been extensively proven in the study of soft-matter and magnetic materials.

The beamline has been designed to host experiments in the soft x-rays energy range from 200eV to 2000eV requiring high coherent photon flux The current CSX beamline design provides high photon flux (~10^{13} photons/sec), at high resolving power (~10^4), coherent (a few transverse modes), focused into a small spot (~1.5 μm x 3μm 1-σ). Taken together, the CSX beamline performance is expected to be better than any other soft x-ray beamline currently operational in the US.

4.3 Insertion Device

This insertion device chosen for the CSX beamline is a pair of 45mm-period Elliptically Polarizing Undulators (EPU45's) that can operate either as one insertion device (same gap and polarization) or in canted mode, where the two EPU45's, separated in angle by ~0.16 mrad, can provide a beam with different polarization. Having two statically-canted (in horizontal angle) insertion devices allows one to control the

polarization switching rates outside the storage ring by the use of a mechanical chopper that selects beam from one of the EPU45's at a time. The switching rate for such a chopper can be quite high, up to kHz rates. Use of switching rates from 10 Hz to 1 kHz are well matched to lock-in technique detection techniques. The use of the lock-in technique has been demonstrated to be very effective in the detection of small signals from magnetic systems, especially in highly dilute samples.

4.4 Sector Layout

4.4.1 Front-End Layout

This is a soft x-ray beamline that will operate windowless and under ultrahigh vacuum conditions. Under these conditions there is no need for a differential pumping section in the front end, although one could be included in order to provide an extra degree of vacuum protection. A 15 mm-square fixed aperture will be located at 18.25 m from the center of the insertion device straight section. Non-absorbing type x-ray beam position monitors (XBPM) should be located at approximately 18.85 meters and 24.15 meters from the center of the straight. An adjustable white beam aperture should be located in the section between the fast gate valve and the second beam position monitor, to define the beam size in real time.

4.4.2 Beamline Layout

The equipment layout for this beamline allows many options. Before discussing the details of the equipment it will be helpful to have an overview of the beamline and define some names. There are three undulator configurations and two branches allowing six major modes of operation. The undulators could be configured to provide one straight beam, two canted circularly polarized beams (upstream and downsteam), two canted linearly polarized beams (upstream and downstream). It would also be possible to configure the accelerator so the beam is steered alternately though the two undulators producing a straight beam with time dependant polarization oscillations. While this case was considered, the decision was made to complete this conceptual design considering the constant **canted** and **straight** cases. For any undulator configuration the beam(s) can be directed along the **short** branch with the branching mirror retracted or along the **long** branch by deflecting off the branching mirror.

The CAD model in Figure 4.1 show an isometric overview of the beamline from the ratchet wall to the end of the short branch. Figure 4.2 shows a side view and Figure 4.3 a top view. Starting at the ratchet wall the major components are:

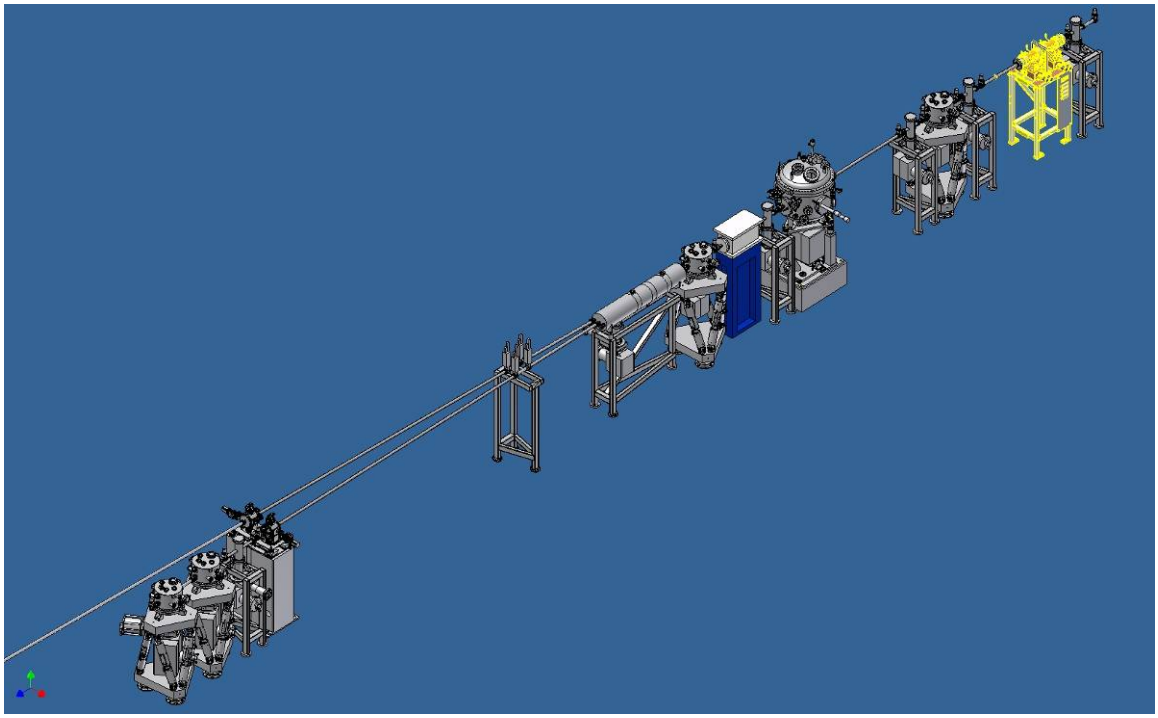

Figure 4.1

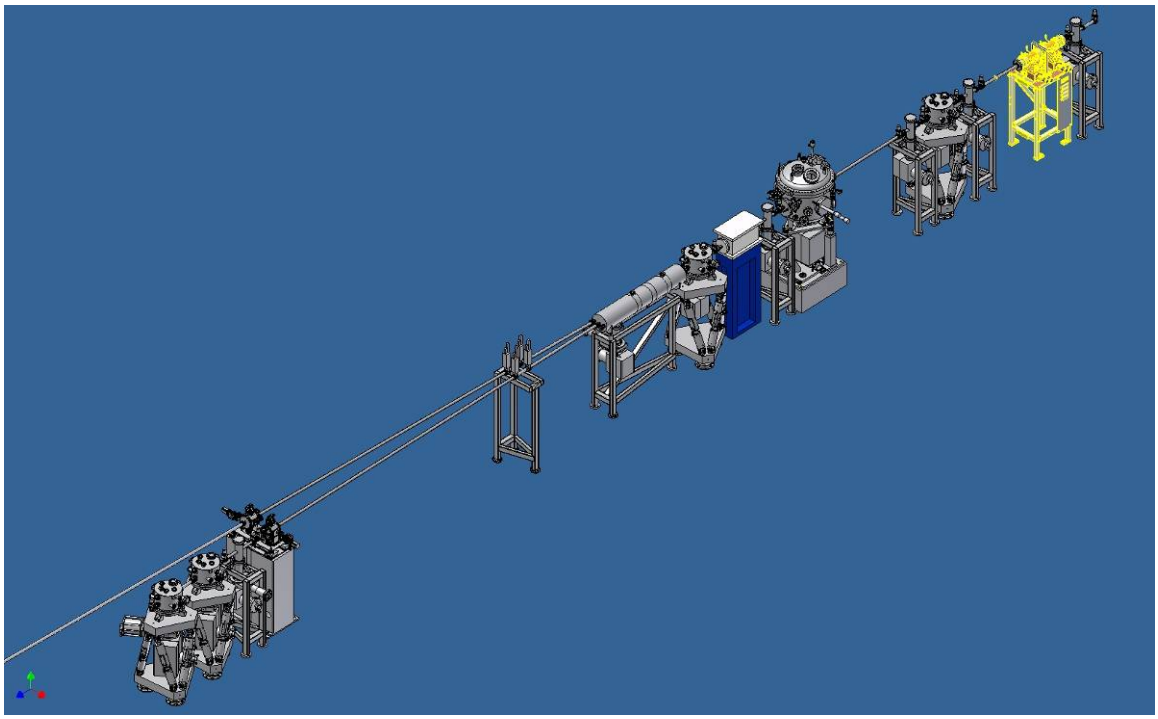

Figure 4.2

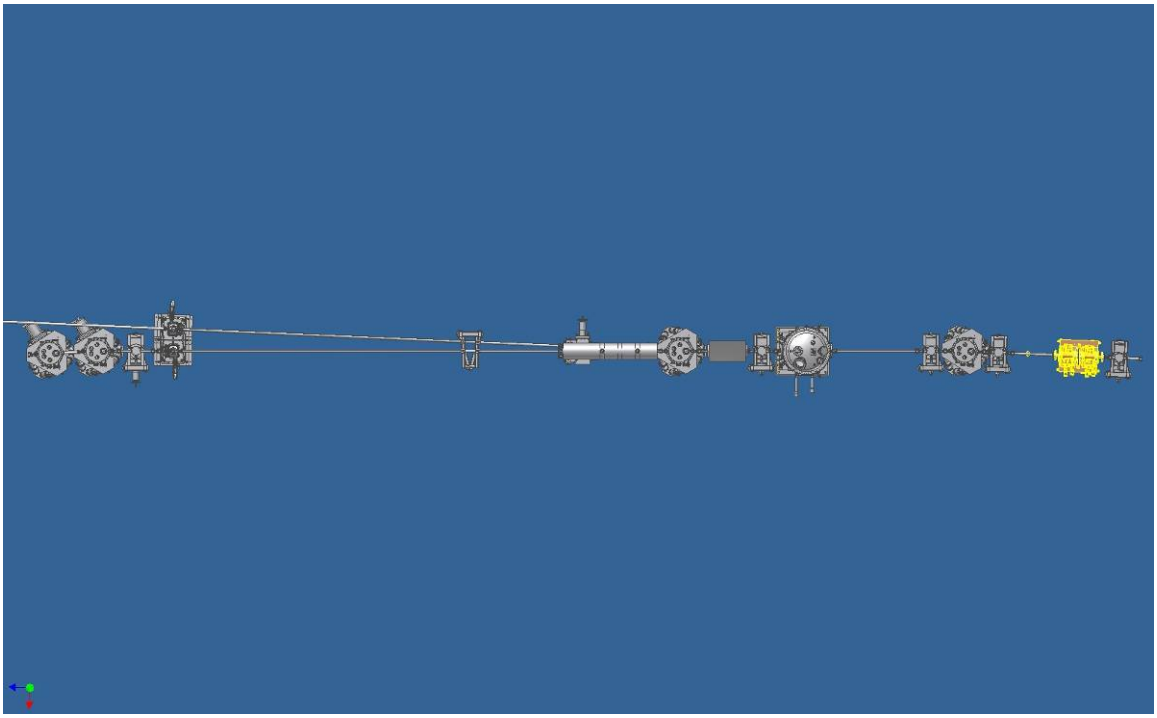

Figure 4.3

White Beam Aperture – rough beam sizing and power absorption

M1 – absorbs high energy beam reducing heat load on downstream optics and collimates the beam vertically

Monochromator – uses M2 and one of three gratings to vertically focus a selected energy on the slit

Chopper – blocks alternating polarizations when operating in canted mode

Branching Mirror – allows diverting the beam into the long branch. Each branch has the following components

Exit Slits – allows the selected energy radiation to pass to the refocusing optics

Beam Defining Slits and Gas Cell – combined chamber allow sizing of the beam, measurement of photon current, and energy calibration

M3 – Horizontal refocusing mirror

M4 – Vertical refocusing mirror

End Station

The mirrors along the beamline are supported with hexapod mounts. To the extent possible these will be made the same and share common mirror boxes. A close up of a hexapod with mirror box, pump, and valves for M3S and M4S can be seen in Figure 4.4.

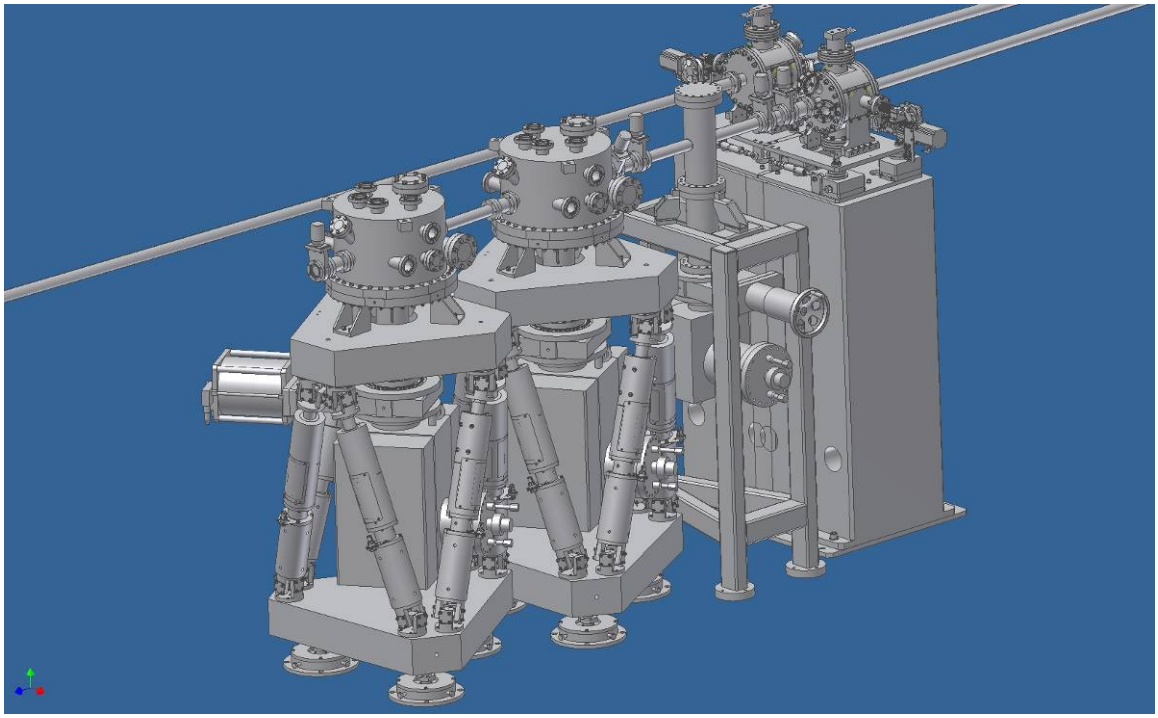

Figure 4.4

Diagnostic chambers are also standardized and placed between mirrors. in the diagnostic chambers shown in the drawings are missing many ports. The design contemplates the use of a Kimball Physics expanded sphere cube as the basic element adding the necessary equipment to the different available ports.. The space between the exit slit and the short M3 is very cramped to include beam defining slits, a gas cell, and a diagnostic chamber. The exit slit was moved as far downstream as possible to maximize the resolution and M3 was moved upstream as far as possible to maximize the space for the end station. The gas cell is included in the diagnostic chamber in front of M3. While it may be possible to fit the beam defining slits in as well, it would be more prudent to move M3 0.5 m downstream in the next design pass. In this CAD model we have only shown the beam defining slit chamber on the long line.

i) CAD model of beamline and hutch layout.

ii) Appropriate shadow model of beamline

4.4.2.1 Survey and Alignment Plans

All beamline components will be surveyed and aligned in place by the facility. In order to facilitate ease of alignment, all components will be fiducialized to external reference points on their table during assembly. All components are designed with a liberal tolerance allowance greater than 0.5 mm.

4.4.2.2 Utility Layouts

The utilities will require the coordination between the beamline and the project infrastructure. At this point in the beamline design the goal is to identify the utility requirements at a high level. Appendix C, List of Key Components, has a spreadsheet with some columns included for utility requirements. Here is a brief summary.

Cooling will be all by chilled water. The total beam heat load of about 12 kW should end up in the cooling

water. There is also the need of cooling for vacuum components including pumps and Titanium sublimator pumps (TSP). The system is envisioned to be a pressurized supply pipe of good quality water and a return pipe supplied by the lab infrastructure. This water should be low-conductivity (LC) to allow electrical isolation of cooled parts. If the water provided by the lab is not LC water, then a separate deionizing and water circulation system will be need for the beamline. The beamline will need about 24 taps into the supply and return for cooling loops. 3 of these taps would go to heat exchangers for separate temperature controlled loops for M1, M2, and the gratings. If we need to cool these below room temp a compressor-based chiller could be added to each of these loops. No cryogenic cooling is envisioned for this beamline. There will be cryogenic requirements for the end stations.

Electricity will be primarily 120 V 60 Hz, but it would be beneficial to have access to 240 V. A rough estimate is 91 duplex 120 V outlets and 9 outlets at 240 V. It would be convenient to have some clean power available in a subset of these outlets. Some of these outlets should be provided with UPS protection. Pneumatics will be required for valve actuation. This could be a pipe with local taps for valves. A rough estimate is 29 air taps. Some of these will be critical safety systems so need to be guaranteed pressure. If the project does not supply this there should be a N2 backup system to guarantee valve operation.

4.4.2.4 Beamline Vacuum System

The details of the design do not allow detailed vacuum calculations. Using the experience of Diamond I06 as a guide, each mirror box was fitted with a 500 l/s pump with TS(After consultation with Diamond beamline responsible beamline I06 does not have the TSPs and wishes they did). Smaller 150 l/s ion pumps were placed at each of the diagnostic chambers, chopper, exit slits, gas cells, and long transport lines. A valve was placed between the chambers and the pumps to allow isolation of the pumps while working on the chamber. These were cost as metal valves. Potentially some of the valves could be changed to O-ring or eliminated. In the spreadsheet of Appendix C, List of Beamline Components, there are columns detailing pump and gauge locations. Each chamber with a pump was fit with a cold cathode gauge. There is a controller for each 6 gauges. Each mirror box was fit with an RGA head. There is one RGA controller. Additional piezo axis on the mirrors may limit the bakeout temperatures to 110 C as they did at Diamond. It would be good to find a work around for this.

There are three fast isolation valves associated with this beamline. One is in the standard front end. There is one on each line between the branching mirror and the exit slit. In the final design there will need to be enough vacuum impedance down steam of these valves to allow leak detection and valve actuation before the pressure wave reaches the valve. The distances between the endstations and the branch valves are long enough that this is not expected to be a problem. The location of the valve in the front end is not defined, but the beamline will have appropriate restriction to insure 15 ms of shutting time if there is a leak in the white beam apertures. Pressure sensing switches were included in each mirror box and the white beam apertures. They should also be included in the end stations as well. The control of these valves will be through the EPS system

4.4.3 Beamline Components

The major beamline components are discussed in this section. Table QQQ covers all the optics and provides information on position, size, spot size, thermal load, and distortion requirements. In the discussion below the numbers for location are referenced from the center of the straight which is the source for the linear straight mode of operation. The mirror sizes referenced are the size of the good optical surface so actual physical size may be larger to accommodate manufacturing. Some ray tracing results are included below but the original reports from Ruben Reininger can be found in appendix A.

Mirror Summary - NSLS-II Soft X-ray Coherent Beamline

Mirror	Mirror Name	Beam Along Beam from Source	Radius	Mirror Material	Mirror Coating	Bend Plane Figure Required - D	Length urad	Width urad	Heat Absorbed B 5.2mm@M1 Bend Angle 183eV Total W	Heat Absorbed B Beam Size - A Density W/mm^2	Heat Absorbed C Beam Size - A Sigma X mm	Heat Absorbed C Sigma Y mm	Density W/mm^2	Heat Absorbed C 4.0mm@M1 Mirror Length	Total W	Heat Absorbed C 7.1mmx5.2mm @M1 Shape and Properties 183eV Width	Density W/mm^2	Total W	Density W/mm^2
M0	M0	No Longer in Beamline																	
M1	M1	Silicon	Internal		0.25	8	966.558	0.9221		1900		0.92				1160	Sagital Cylinder		
M1 central	M1 central	2.80	29.50	Horz			88.75	0.8644	@183eV	47.617	250	50	1287.08	mm rad					
M1 upstream	M1 upstream							*0.9828*	*47.935*		250	50	1338.89	mm rad					
M1 downstream	M1 downstream							*0.9066*	*44.543*		250	50	1234.89	mm rad					
M2	M2	Silicon	Internal		0.17	3.5	101.624	0.3653		236		0.36				132			
		5.15	31.83	Vert			87.11	1.2150		17.145	380	50	Planar						
					@183eV, 150l/mm -A			*1.1331*	*21.853*										
			31.66				88.725		@183Ev										
					@2.3keV, 400l/mm -A														
			31.93				84.012												
					@183eV, 1200l/mm -B														
																a0	a1	a2	c
	Grating LEG	Silicon	Edge		0.13	5.5	1.8125	0.0041		40		0.06				l/mm	l/mm^2	l/mm^3	
Grating LEG		5.30	32.00	Vert			87.69, 86.53	1.1267		21.425	130	25	150	0.0540	8.09E-06	~1.5			
	Grating MEG				@183, 150l/mm -A			*1.1388*	MEG@183eV	27.340									
Grating MEG			32.00				88.98, 88.47				130	25	400	0.1438	2.15E-05	~1.5			
	Grating HEG				@2.3keV, 400l/mm -A														
Grating HEG			32.00				86.24, 81.78				130	25	1200	0.3018	4.51E-05	~2.2			
					@183eV, 1200l/mm -B														
	BM	Silicon	Edge		0.22	8.8							3	0.004					
BM		7.30	34.00	Horz			88.70	1.1532		55.745	600	30	Plane						
	SLIT												10	0.24					
SLIT		15.30	42.00					1.4784	0.00846										
	M3S							1.4804	0.00573										
	M3S central	Silicon	None		0.17	14							0.002	2.2E-05					
M3S	M3S upstream													Plane Elliptical - Bimorph					
M3S central	M3S downstream	16.50	43.20	Horz			88.5	0.1560	0.30 x 138.0 spot (+/-1 sigma)	69.421	350	50	22475	mm rad		189.68	mm rad		
M3S downstream	M4S							*0.2017*		*66.822*	350	50	23125	mm rad		191.51	mm rad		
		Silicon	None		0.37	14		*0.1417*		*68.144*	350	0.002	2.3E-05	mm rad		186.8	mm rad		
M4S		17.25	43.95	Vert			88.5	0.8672		11.589	75	50	Plane Elliptical - Bimorph						
	End Station S							*0.9627*		*13.224*		0.008	1841455	mm rad		30.463	mm rad		
End Station S		18.25	44.95					0.00188	0.0038 x 0.0054 spot (1 sigma)	0.00269									
								0.00205		*0.00248*									
	M3L																		
	M3L central	Silicon	None																
M3L	M3L upstream												Plane Elliptical - Bimorph						
M3L central	M3L downstream	24.50	51.20	Horz			88.5				450	50	26600	mm rad		220.75	mm rad		
M3L downstream	M4L															217.54	mm rad		
		Silicon	None					*1.2742*		*75.034*	450	50	25950	mm rad		217.93	mm rad		
M4L																			
	End Station L													5600	mm rad	69.67	mm rad		
End Station L		26.50	53.20					*0.00188*		*0.00046*									
								0.00164		*0.00047*									

Reference Sources - all by Ruben Reininger

A	Traces 070827.pdf	APPLE II, 85 Period, 45 mm/period, 183eV, X=46.4 um, Y=37.2 um, dX=35.1 urad, dY=29.2 urad
B	abs_M2_183eV_HEG.xls	5.2 mm square apperture at 29.5 m, 183eV, 1200l/mm (HEG), Zeiss drawing lower case
C	Power_deformations 070917.doc	Various cases with different appertures and gratings
D	Slope Errors 070904.doc	Limits required so resolution, horizontal spot and vertical spot do not degrade by more than half the
E	Traces 070911.doc	Canted Beam cases

4.4.3.1 White Beam Apertures

The power produced by the undulators is about 12 kW with power densities up to 40.1 kW/mrad^2. The white beam apertures, located at 28 m, would see a power density of up to 51 W/mm^2. They will have sufficient cooling to be able to absorb 12 kW at these power densities. An appropriate choice for these would be the IDT design used at Diamond. This consists are two water cooled copper cylinders with tapered square holes mounted on a translation stand. One cylinder is translated to define the bottom and right edge of the beam while the other is translated to define the top and left edge of the beam. The cylinders are water cooled but there are no water joints exposed to vacuum. This design has been used at Diamond I06 at similar power levels. The aperture needs to be adjustable to allow a spot size as large as 7.1 mm vertically (to over illuminate M2 for thermal stability) and 9.5 mm horizontally (canted beam case). The Diamond set incorporates some tungsten to help better define the beam.

4.4.3.2 M1 Mirrors

The first mirror makes a horizontal bend of 2.5° (88.75° from normal) so it absorbs a considerable amount of power passing only the softer X-rays to the downstream optics. With a 7.1 x 5.2 mm beam in the M1 plane at 29.5 m the mirror absorbs 1160 W with the undulators in the straight mode and adjusted for 183 eV. This gives a maximum power density of 0.92 W/mm2. These mirrors will be cylindrically ground to vertically collimate the beam. Thermal distortions in the length direction (meridional) beyond 0.25 μrad will increase the size of the horizontal beam spot and in the width direction (sagittal) beyond 8 μrad will decrease the energy resolution. Internally water cooled silicon mirrors have been selected for the M1s to provide the maximum thermal control. Cryogenic cooling would provide better thermal stability due to the lowered coefficient of thermal expansion (CTE) and the improved thermal conductivity of silicon at low temperatures, but with soft X-rays even a small layer of ice build up is a problem. Thermal modeling done for the Diamond I06 beamline showed expected rms slope errors of 20 μrad sagittally and 3 μrad meridionally at similar power levels (0.92 W/mm2) for an internally cooled silicon mirror. Preliminary ray tracing results have shown that this level of distortion can be compensated for by adjusting the operating angles of the monochromator and curvature of the M3 optic. Reduction of the levels of distortion may be obtained by reducing the coolant temperature enough to gain some improvements in silicon properties but not enough to produce ice build up. Both the optical correction and distortion minimization need further study to insure thermal distortions in M1 do not significantly reduce the beamline performance. The use of an M0 mirror before M1 was investigated. To split the power between the two mirrors, the M0 would need to be at a very shallow angle. This makes the mirror very large, expensive, and prone to distortion at the high power levels. There was significant cost saving in eliminating this option.

There are three M1 mirrors in this design. One for the straight operation mode and two (an upstream and a downstream) mirrors for the canted operation mode. Several options were considered to reduce the number of mirrors and some of these options may end up working. However, the three mirror option is the only one we could adequately verify during this design pass. It may be worthwhile to reopen this issue when answers to some of the accelerator related questions can be definitively answered. The three mirrors have slightly different shapes because the distance to the source varies between the operation modes. The size of the M1 mirrors was set to 250 mm long x 50 mm wide. This length is 5 σ from the expected spot size for a 5.2 mm horizontal beam size in the plane at 29.5 m. Figures QQQ, QQQ, and QQQ produced by Ruben Reininger show the expected spot on M1 with undistorted optics for the straight, canted upstream, and canted downstream configurations. Internally cooled silicon mirrors of this size with the required ~1300 mm sagittal cylindrical radius and meridional figure slope error of 0.5 μrad rms are within the normal manufacturing capability of InSync. This beamline requires meridional figure slope error of 0.25 μrad rms which may

require the addition of profile coating to the process. Detailed thermal modeling may show a longer mirror would be useful to reduce the effects of distortion at the ends of the heated stripe. The width should be enough to allow multiple stripes to be used. Wider mirrors would increase the vertical movement requirement to switch between the straight and canted modes (see below).

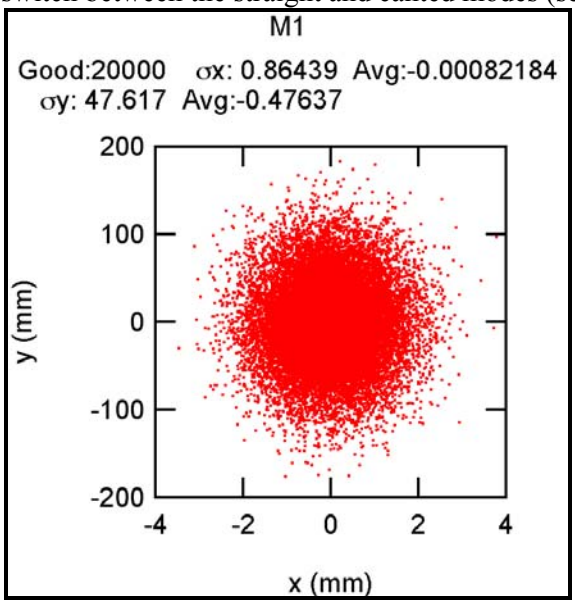

Figure 4.1. M1 illumination, undulator 183eV linear straight mode

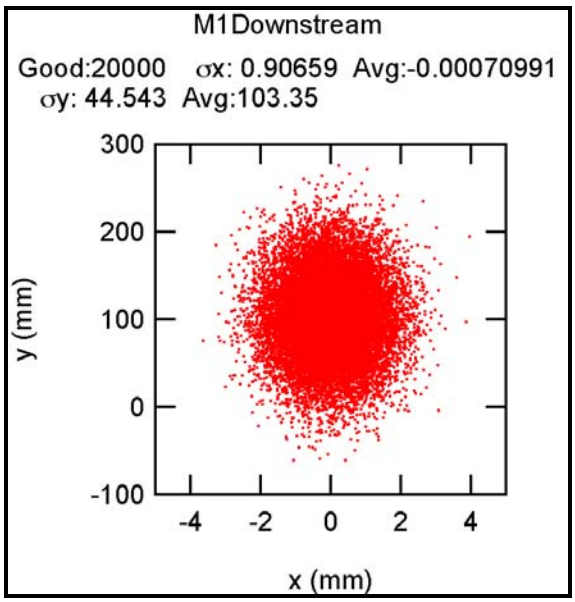

Figure 4.2. M1 illumination, undulator 230eV circular canted mode

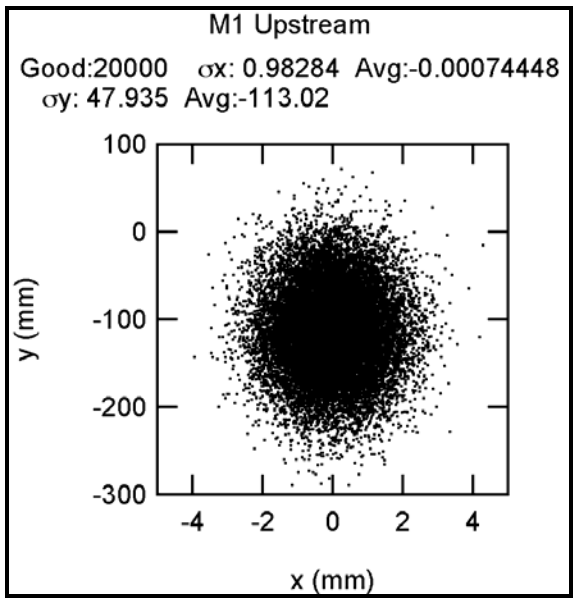

Figure 4.3. M1 illumination, undulator 230eV circular canted mode

The support system for mirrors is a hexapod system. The hexapods build by Oxford Danfysik for the Diamond I06 beamline would be a good choice. By standardizing on a flexible support the beamline will be easier to install, maintain, and operate. Controlled changes to the lengths of the six supporting legs can

Figure 2 M1 illumination, undulator 230eV circular canted mode

provide translations and rotations about convenient axis. The repeatability of motion is 1 μm and 2 μrad at the 2 σ level. This would be sufficient for single mirror alignment requirements except the bending angle. For this, additional piezoelectric axes in the vacuum chamber will be used. In the canted beam case the first mirror can be aligned with the hexapod, but the second mirror will require additional alignment. The second mirror will be fit with four in vacuum axes. With detailed study of the kinematics of the hexapod and alignment sensitivities it may be possible to reduce this number. The large translation required to change between the one mirror straight mode and the two mirror canted mode is outside the normal 25 mm range of the hexapod. A larger range can be accommodated but at some loss in repeatability. If the repeatability degradation is too large an additional vertical axis may be required. This will need additional study. The stiffness (vibration modes) of the hexapods has proven adequate for operation at Diamond I06 with similar requirements.

4.4.3.3 Monochromator

The beam enters the monochromator, makes an upward vertical bend at the M2 mirror and then another vertical bend at one of the three variable line spaced gratings. The angles of the M2 and gating are set so the beam exiting horizontally with a 15 mm vertical offset (aimed at the exit slit) is of the selected energy. The line spacing of the grating is set so the light of the selected energy hitting the bottom of the grating is exiting at a slightly upward direction and the light of the selected energy hitting the top of the grating is exiting at a slightly downward direction thus focusing the light to a minimum vertical size at the exit slit. There are three sets of grating, LEG 150 l/mm, MEG 400 l/mm, and HEV 1200 l/mm to allow a trade off between energy resolution and delivered photons. Consideration was given to adding a fourth grating position with a spherical mirror to direct a “hot pink” beam to the experiment station. The decision was made that the 150 l/mm grating could provide enough pink beam power by opening the exit slit to the desired size. This keeps the number of gratings to three allowing use of more standard monochromator designs and reduces concerns for heating of downstream optics.

The M2 mirror makes a vertical bend of 12.0° (84.01° from normal) when operating at 183eV with the HEG grating so it absorbs a considerable amount of power passing only the softest X-rays to the downstream optics. With a 5.2 x 5.2 mm beam in the M1 plane at 29.5 m the M2 mirror absorbs 102 W with the undulators in the straight linear mode and adjusted for 183 eV. This gives a maximum power density of 0.36 W/mm2. M2 is a flat mirror that does no intentional focusing. Thermal distortions in the length direction (meridional) beyond 0.17 μrad will reduce the energy resolution and in the width direction (sagittal) beyond 3.5 μrad will increase the horizontal spot size. Internally water cooled silicon mirrors have been selected for the M2 to provide the maximum thermal control. Cryogenic cooling would provide better thermal stability due to the lowered coefficient of thermal expansion (CTE) and the improved thermal conductivity of silicon at low temperatures, but with soft X-rays even a small layer of ice build up is a problem. Thermal modeling was done with Finite Element Method by Ken Kriesel. A detailed report can be found in Appendix E. The thermal load produces a raised bump on the M2 surface. This bump has the largest slope changes near the ends of its length. With a beam size of 5.2 mm square at M1 the ends of the thermal bump on M2 are still part of the active optical path and greatly degrade the vertical optical performance doubling the vertical beam size at the exit slit. Increasing the aperture to 7.1 mm vertically increases the total heat load on M2, but moves the high slope areas out of the active optical path. The remaining thermally induced distortions can be corrected. The figure change in the central part of the M2 thermal bump can be approximated by a convex radius of ≈1.8×107 mm, which means the beam incident on the grating is not vertically collimated as in the optical design. This change in the virtual source position can be corrected by operating the grating with a c value of 2.193 instead of the nominal value of 2.184 at this energy. This change in operation essentially restores the vertical size of the beam at the exit slit. While 183eV appears to be the worst case, further work needs to be done to verify that this correction method can be done at higher beam energies. The horizontal distortion of M2 increases the horizontal spot size at the end station. The plan is to correct this by changing the shape of

the focusing mirror. The M3 and M4 mirrors are planned to be bimorphs. Preliminary work suggests that this method will work. Reduction of the levels of distortion may be obtained by reducing the coolant temperature enough to gain some improvements in silicon properties but not enough to produce ice build up. Both the optical correction and distortion minimization need further study to insure thermal distortions in M2 do not significantly reduce the beamline performance.

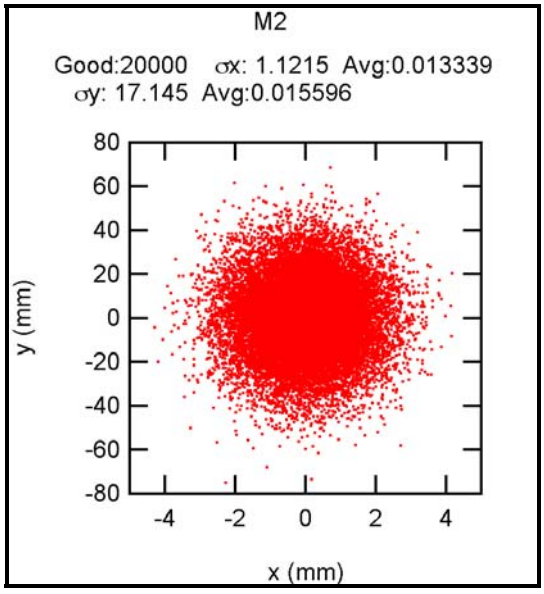

Figure 4.4. M2 mirror illumination, undulator 183eV linear straight mode

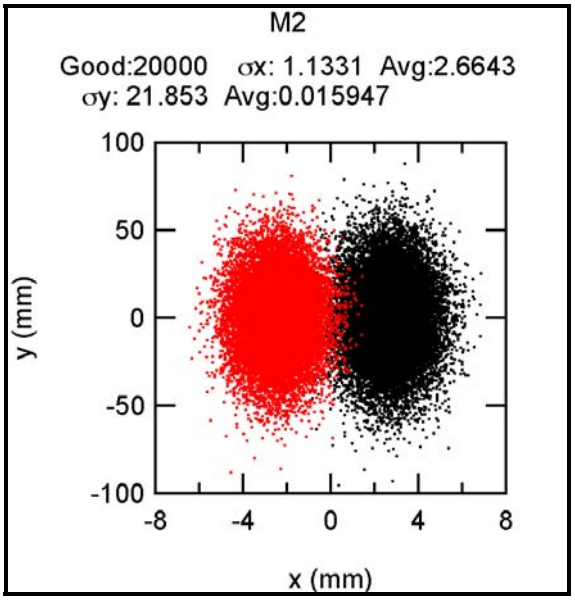

Figure 4.5. M2 mirror illumination, undulator 230eV circular canted mode

The size of the M2 mirrors was set to 380 mm long x 50 mm wide. The monochromator motion rotates M2 about a point 7.577 mm above the optical face of the grating. This changes the distance along the beamline that the center of the beam strikes the mirror from 31.66 m at 2.3 keV (88.73° from normal to beam) to 31.93 m at 183 eV (84.01° from normal to beam). This effective translation of the mirror relative to the beam helps determine the length requirement of the optic. Figures QQQ, and QQQ produced by Ruben Reininger show the expected spot on M2 with undistorted optics for the straight, canted configurations. Internally cooled silicon plane mirrors of this and figure slope error of 0.17 µrad rms are slightly pushing the current state of the art manufacturing capability of InSync. However, InSync is currently quoting 0.25 µrad rms and has produced somewhat better, without using profile coating. Addition of profile coating should allow achievement of the required figure with current technology.

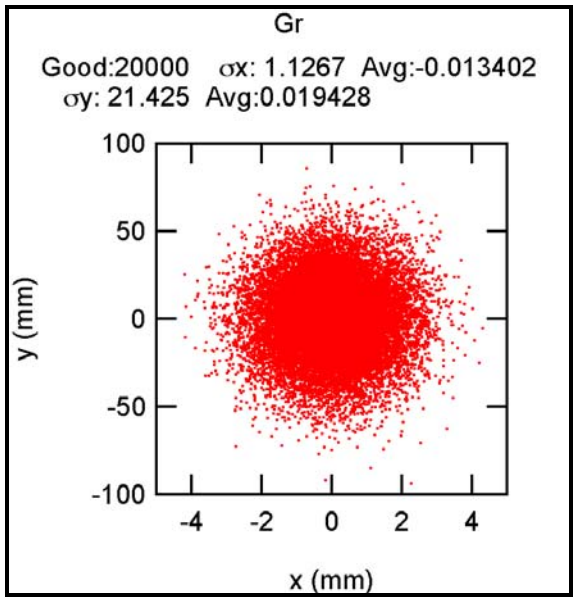

Figure 4.6. Grating illumination, undulator 183eV linear straight mode

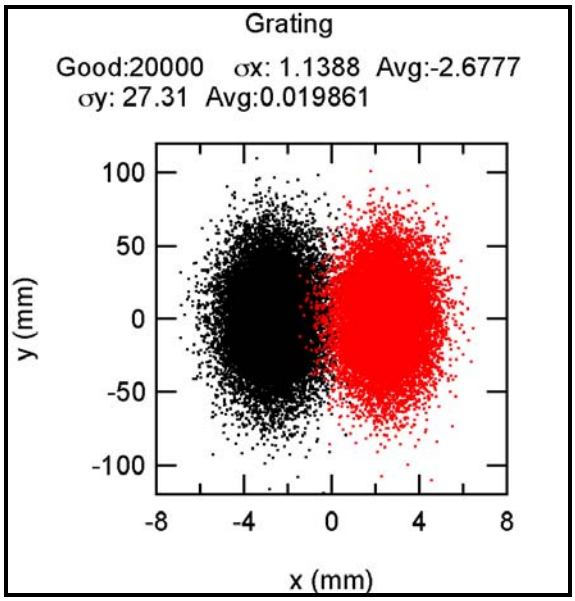

Figure 4.7. Grating illumination, undulator 230eV circular canted mode

The size of the gratings was set to 130 mm long x 25 mm wide. This length is 5 σ from the expected spot size for canted beam operation at 230eV. The monochromator motion rotates the grating about the central face of the grating and can translate the grating support to place any of the three gratings into the beam. The gratings will be edge cooled silicon because the expected heat load is less than 40 W in the worst case with a power density of 0.016 W/mm^2. Figures QQQ, and QQQ produced by Ruben Reininger show the expected spot on the gratings with undistorted optics for the straight, canted configurations. These gratings are within standard manufacturing capability.

JenOptik makes a CPGM that is suitable for this beamline. The required resolution in angle is 0.03 μrad for the gratings and 0.05 μrad for the mirror. These requirements are better than the advertised capability of the JenOptik monochromator.

4.4.3.4 Chopper

The chopper is a mechanical device with a double function, block the non-desired radiation to come down to the end stations from the two canted insertion devices and provides with the switching frequency between the two different polarizations delivered by the EPU's selecting in time the beam from one of the two canted insertion devices serving this beamline. The chopper will also have a neutral position were x-rays from both insertion devices may pass without any being blocked. The preferred location of this piece of equipment will be between the monochromator and the branching mirror. It is desired that the switching frequency of the chopper could be selected from a few Hz up to several kHz. Having the possibility to select the different frequencies will allow choose a noise free frequency without interfering with noise from other frequencies. This can be achieved utilizing a rotating blade using ferrofluidic© style feedthroughs to connect with the driving motor and the switching control mechanism located outside of the vacuum chamber. A new design of an existing chopper located at the NSLS X13A beamline, is being improved. The X13A beamline requires a chopper because of the fast switching 22Hz characteristic of its unique source an Elliptically Polarizing Wiggler (EPW).

4.4.3.5 Exit Slit

The exit slits used by the Diamond I06 beamline were manufactured by Bestec. They would also be appropriate for this beamline. The power at the exit slits is expected to be less than 10 W with a power density less than 0.24 W/mm. According to Bestec this will not require cooled slits. The two exit slits are pretty close together on the branching line, but do fit without interference. The standard stands do interfere but can be easily modified. Pictures of the spot size at the exit slits for various conditions can be found in the reports from Ruben Reininger in Appendix A, SAS Optics Reports.

4.4.3.6 M3 and M4

The final focusing mirrors, M3 & M4 are Silicon Elliptical Bimorph mirrors. The same Hexapod mounting strategy is used for these as for M1 and the branching mirrors. The heat load at these mirrors is small so they do not require cooling. Correction for the thermal distortions of the M1 mirror and M2 mirror can be made respectively by changing the curvatures of M3 and the monochromator to recover the small spot size. Preliminary investigation suggests that this could be accomplished with a simple bending of the mirrors. The bimorph technology is exciting and would allow more complete correction at a small cost premium. This cost was included. For the canted beam case there needs to be three M3 mirrors just like there are three M1s. This will require additional in vacuum axis to get precision alignment of the mirrors as with M1. Each line has just one M4. The short branch M3s and M4 are 350 mm and 75 mm long respectively. The long branch M3s and M4 are 450 mm and 350 mm long respectively. The spacing between the long branch mirrors was increased to 1 m from the 0.75 m for the short branch. The tentative distance to sample spot from the M4 is 1 m for both lines. Pictures of the spot size on the final focusing mirrors for various conditions can be found in the reports from Ruben Reininger in Appendix A, SAS Optics Reports.

4.4.3.7 Diagnostics

Diagnostics are included for vacuum, beam current monitoring, beam position monitoring, temperature and flow sensing, and energy measurement. Vacuum RGAs and cold cathode gauges are discuss in the vacuum section. Costs were included to monitor the temperatures of all 25 cooled surfaces and the flow of the corresponding 14 coolant paths. Sensor signals would be conditioned and readout over a network to the central computer. This can provide a warning for temperatures going out of range and possibly be used as input into beamline operating setting. 4 fluorescent screens are anticipated to help locate the beam. These will be housed in the diagnostic chambers. Instrumented mesh will allow measurement of beam current upstream of the exit slits. Photo diode will monitor beam current after the exit slits. These will also be housed in the diagnostic chambers. The photo current on mirror surfaces, and beam defining slits will also be monitored. These devices will also report to the network either directly or through signal conditioners. A gas cell is included on each branch to allow energy calibration. The length of these was set to 0.5 m. A decision was made to use a Kimbal Physics Expanded Sphere for the diagnostic chambers, but there was not time to include this in the CAD model.

4.4.4 Endstations

The beamline has been designed to have two branches, each of which has the capability to host one or more independent endstations, depending on user demand. The angular separation between the two branches will be 2.5° and the two branches will be of unequal length, in order to provide adequate non-interfering floor space for endstations. This beamline will be able to host a wide variety of types of endstations, including diffractometers, spectrometers, and microscopes. The only restrictions on endstation types compatible with this beamline will be space and vacuum compatibility for windowless connection to the storage ring vacuum. A very important component of the beamline equipment protection system will be interlocks that

continuously monitor the end station vacuum pressure and temperature to avoid accidental venting of the storage ring. The endstation design and hardware will provide experimental capabilities (detectors, sample environments, and sample and detector motions) with enough degrees of freedom to permit users to carry out specific experiments using focused, high-resolution, high flux, coherent soft x-rays from the beamline. The endstation will also provide pinholes and/or specific coherent soft x-ray focusing optics (e.g. Fresnel zone plates) to perform experiments using the coherent part of the photon beam.

One example of an endstation well-matched to the capabilities of the CSX beamline is a multipurpose ultrahigh vacuum compatible four-circle diffractometer that will fully utilize the energy range, high photon flux, extraordinary brightness, and polarization control provided by the beamline. Conceptually, this endstation will emphasize scattering experiments, but at the same time will have the flexibility to introduce optical elements such as pinholes, Fresnel zone plates, and polarization analyzers, allowing one to conduct an wide range of experiments. The use of pinholes of different sizes in the chamber will enable coherent scattering and/or small angle scattering experiments to be performed, depending on the pinhole size. Combining polarization control of the soft x-rays incident on the sample with the capability to analyze the polarization of the soft x-rays reflected/emitted from the sample will provide an extremely powerful tool to study orbital and spin magnetic moments and molecular orientation in crystalline and partially ordered samples.

In more detail, a multipurpose endstation would consist of a high vacuum compatible vacuum vessel containing a basic four-circle in-vacuum diffractometer, two independent concentric circles dedicated to the detector and the sample rotations. The detector arm should be able to move a wide angular range exceeding 180 degrees. It is desirable that the incident beam on the sample and the beams detected by a number of detectors be unimpeded by any other instruments in the chamber over their full intended ranges of motion. The chamber should incorporate an electromagnet, using high T_c superconducting technology that will provide with homogeneous (1% in a distance +- 5 mm from the center of the magnet) magnetic fields up to 1 Tesla in x, y and z directions. This magnet will be able to rotate together with the sample keeping constant the direction of the magnetic field relative to the sample surface, or will be able to rotate independently of the movement of the sample, without disrupting in either case the incidence of the beam on the sample. The sample stage will be mounted on a cold finger that will cover a sample energy temperature range from 4K up to 300 K. Currently it is under study the possibility to raise the temperature of the samples above room temperature, but we are aware that this could cause the quench of the superconducting magnet. The chamber it self is conceive to have a sample transfer system that will allow to transfer samples when they are cool without breaking the vacuum, reducing the down time when samples get changed.

The design of the endstation and its vessel provides space for a motorized system of pinholes or refocusing optics in the front part of the chamber to allow the use of the coherent characteristics of the x-ray beam. The design of the detector arm includes space for the future a polarization analyzer. The vessel and its ports have been designed to allow the insertion of these two instruments during a maintenance period.

The endstation will also be provided with a pressure and temperature monitoring system connected to the beamline Equipment Protection System that will protect the beamline vacuum and instruments from possible errors in the operation of the end station that could lead to loss of vacuum.

4-A Appendix A: SAS Optics Reports

Canted Beams for the Coherence Beamline.

August 23, 2007

Questions were raised about the required separation between the canted beams when the insertion devices are operated to deliver right and left circular polarized light. Since there is no horizontal focusing until the plane elliptical mirrors downstream the exit slit, the horizontal acceptance for the beams and the canting angle between them should be as small as possible. However, a too small canting angle is not desirable since the two polarizations will overlap.

Since only the first harmonic is emitted on axis when the ID is tuned to deliver circular polarized radiation, higher harmonics will be in the acceptance of the other ID. Furthermore, there could be some "at energy" flux emitted by one ID in the horizontal acceptance of the other ID.

To address these issues, we calculated the angular flux and angular power density over a wide horizontal angle when the upstream insertion device (ID) is tuned to emit circular polarized radiation. The calculations were performed with the SPECTRA code [1] at three photon energies. In the calculations we assumed that the ID center is 1.3 m upstream the center of the straight section. The machine parameters at this position are listed in Table 4.A.1. The parameters of the ID and photon energies are given in Table 4.A.2.

Figure 4.A.1Figure 4.A.2, and Figure 4.A.3 show the angular dependence of the flux density when the upstream ID is tuned to 231, 501, and 1008 eV, respectively. From these data, we obtained the integrated flux as a function of the horizontal aperture and full vertical aperture. As seen in Figure , a horizontal aperture of 0.16 mrad allows to collect practically the whole central cone flux at 501 and 1008 eV and most of this flux at 231 eV. The "at-energy" flux leaked in the acceptance window of the downstream ID was integrated from the data in Figure 4.A.1Figure 4.A.2, and Figure 4.A.3 assuming that the separation between the beams axis is equal to the acceptance angle. The leaked flux is plotted in Figure 4.A.5 for the three energies. Clearly, there is no optimal aperture for all energies. A reasonable compromise, which gives at most a 3% leak at the three energies, is a canting angle and an aperture of 0.16 mrad. A smaller leak percentage could be achieved with a canting angle of 0.2 mrad or larger and a (variable thickness) beam stop inserted in between the two beams. at high energies.

The angular power densities when the upstream ID is tuned to the three photon energies are shown in Figure ,4.A.6, Figure 4.A.7, and Figure 4.A.8. For an horizontal aperture and canting angle of 0.16 mrad the power obtained at 231 eV in the upstream ID aperture is 10.5 W and in the downstream ID aperture 22.7 W. At 501 (1008) eV the values are 45 (97) W for the upstream and 95 (71) W for the downstream.

References

1. T. Tanaka and H. Kitamura, J. Synchrotron Rad., **8**, 1221, 2001

Tables

Table 4.A.1. Machine parameters used in the calculations. Upstream ID.

Energy (GeV)	3.0
Current (mA)	500
εx (pm rad)	550
εy (pm rad)	8
βx (m)	2.61
βy (m)	2.88
αx (μrad)	0.914
αy (μrad)	1.58

Table 4.A.2: ID parameters used in the calculations.

ID type		APPLE II	
Number of periods		44	
Period length (mm)		45	
Energy (eV)	230.6	501.3	1008
kx and ky	2.69	1.67	0.94

Figures

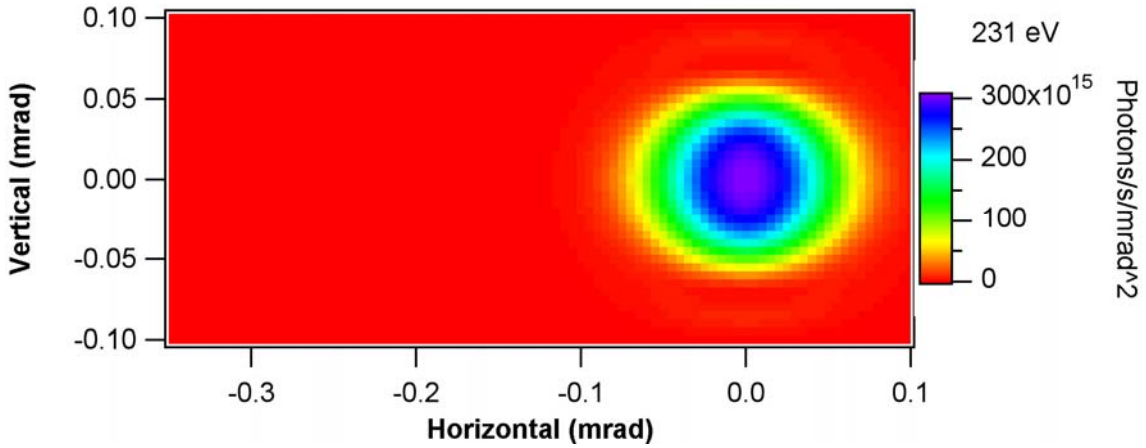

Figure 4.A.1. Angular flux density (in 0.1% BW) when the upstream ID is tuned to 231 eV.

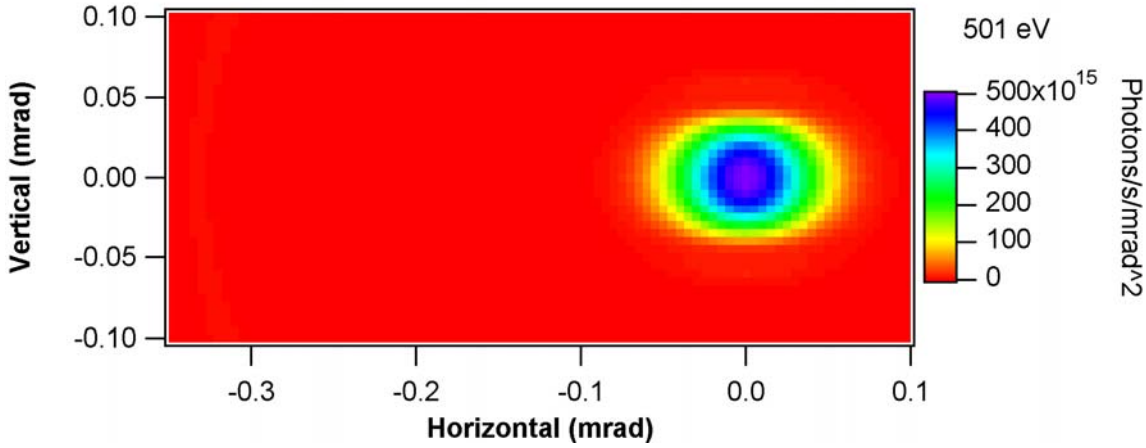

Figure 4.A.2. : As Figure 4.A.1 when the upstream ID is tuned to 501 eV.

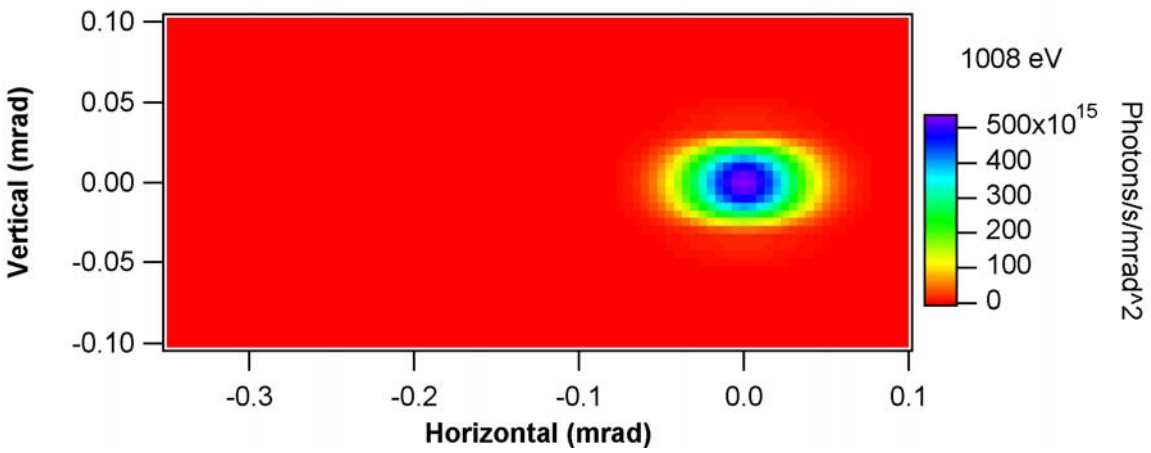

Figure4.A.3. As Figure 4.A.1 when the upstream ID is tuned to 1008 eV.

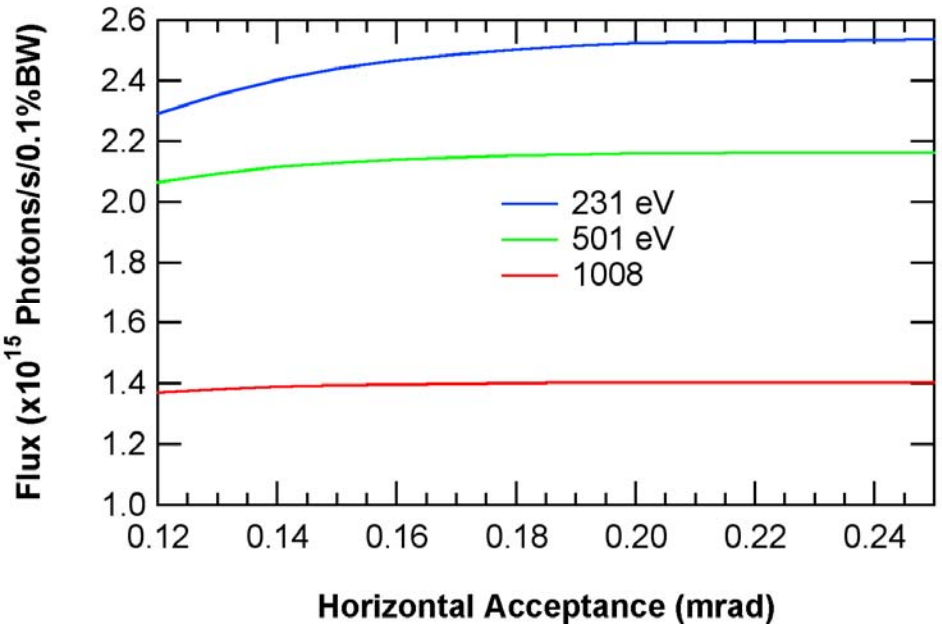

Figure 4.A.4. Flux as a function of the horizontal aperture (over full vertical aperture) for 231, 501, and 1008 eV.

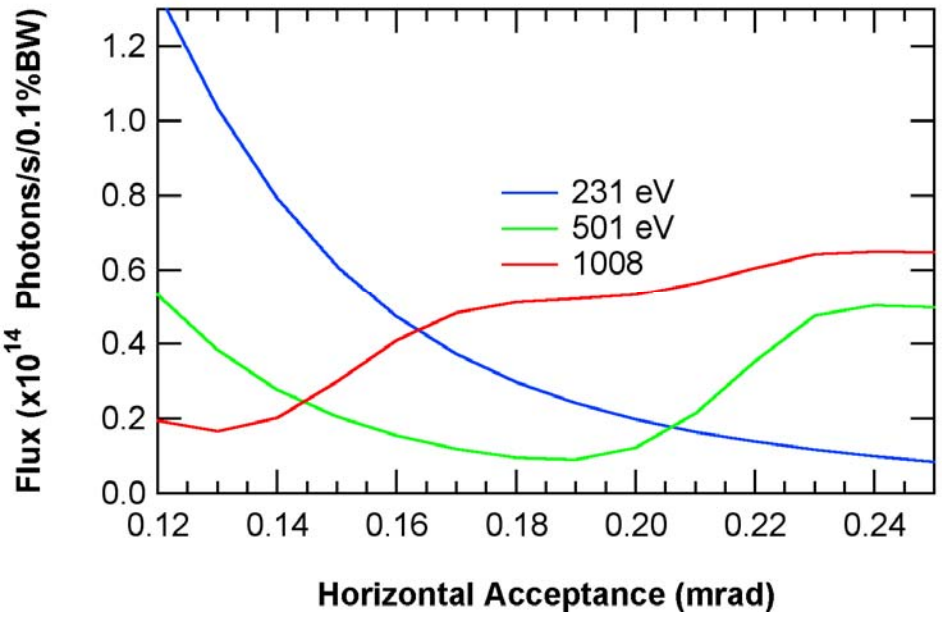

Figure 4.A.5. At–energy flux leaked onto the acceptance of the other ID as a function of the horizontal aperture (over full vertical aperture) for 231, 501, and 1008 eV. The canting angle is equal to the horizontal aperture.

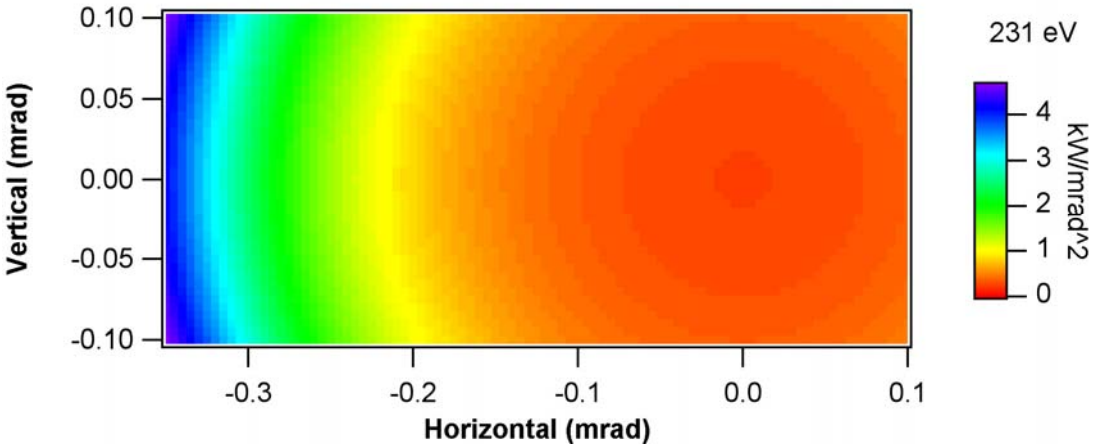

Figure 4.A.6. Angular power density when the upstream ID is tuned to 231 eV.

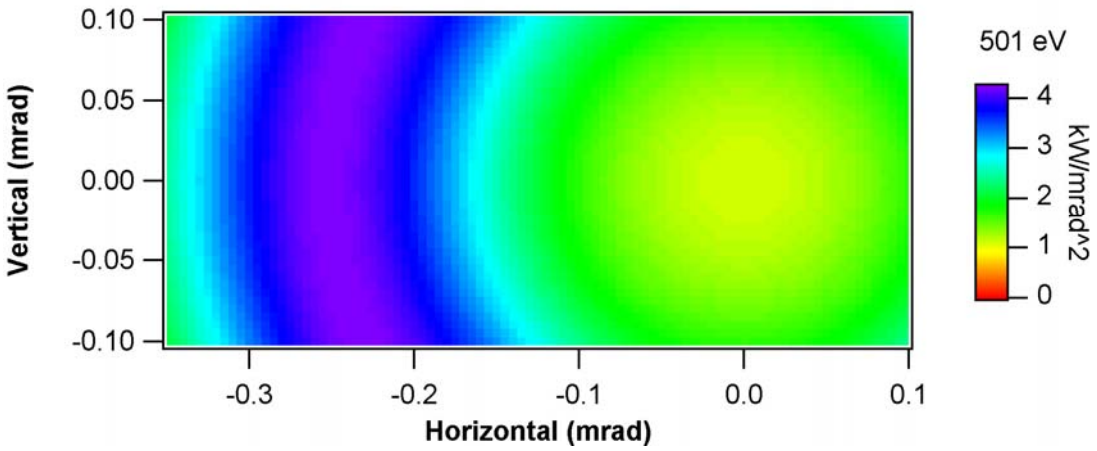

Figure 4.A.7. Angular power density when the upstream ID is tuned to 501 eV.

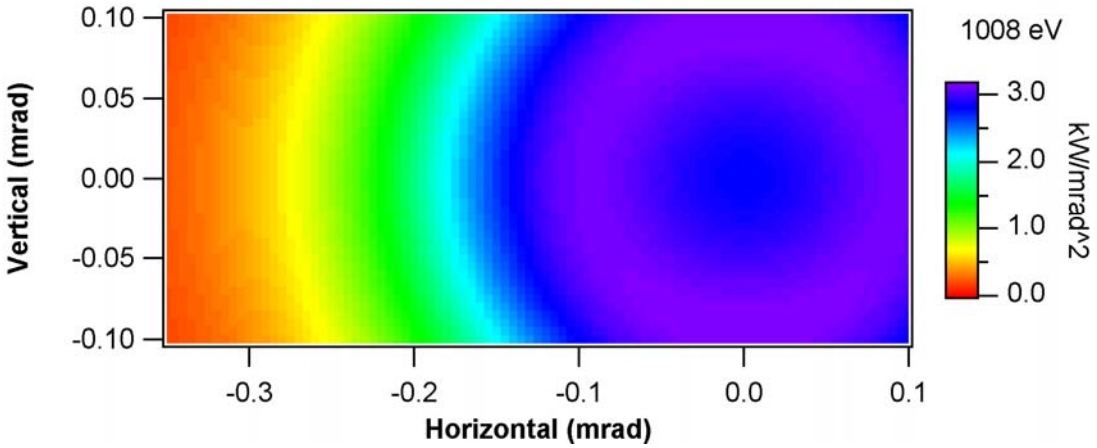

Figure 4.A.8. Angular power density when the upstream ID is tuned to 1008 eV.

4-A Appendix B: SAS Optics Reports

Preliminary Ray Tracings, Single Beam.

The purpose of this brief report is to give a first impression on the optical sizes and the size at the sample with the parameters we have discussed until now.

The machine parameters used are those at the straight center and are listed in Table 4.B.1. The parameters of the ID as well as the total source size and divergence calculated (as in our report dated July 16, 2006) at 183 eV are given in Table 4.B.2.

The distances from the source, angles of incidence, and deflection of the optical components are given in Table 4.B.3. M2 and the grating, a 150 l/mm VLS operating with c≈1.5, are tuned for 183 eV.

Figure 4.A.1, Figure 4.B.2, Figure 4.B.3, Figure 4.B.4, and Figure 4.B.5 show the illumination on M1, M2, grating, M3 and M4 with the above parameters. The ray tracings at the slit are shown in Figure 4.B.6. The spot at the sample when the slit width is set to 20 μm is seen in Figure 4.B.7. No slope errors have been assumed on the optical elements.

Tables

Table 4.B.1: Machine parameters used in the calculations.

Energy (GeV)	3.0
Current (mA)	500
σx (μm)	28
σy (μm)	2.6
σx' (μrad)	19.7
σy' (μrad)	3.1

Table 3.B.2: ID parameters used in the calculations.

ID type	APPLE II
Number of periods	85
Period length (mm)	45
Energy (eV)	183
Σx (μm)	46.4
Σy (μm)	37.2
Σx' (μrad)	35.1
Σy' (μrad)	29.2

Table 4.B.3: Distance from the source, angle of incidence, and deflection of the optical components. (183 eV, LEG)

Element	Distance (mm)	Angle (deg)	Deflection
M1- Sagittal Cylinder	29500	88.75	horizontal
M2- Plane	31851.8	87.11	vertical
Gr - Grating	32000	87.69 (inc.)	vertical
Slit	42000		
M3 - Plane Elliptical	43200	88.5	horizontal
M4 – Plane Elliptical	43950	88.5	vertical
Sample	44950		

Figures

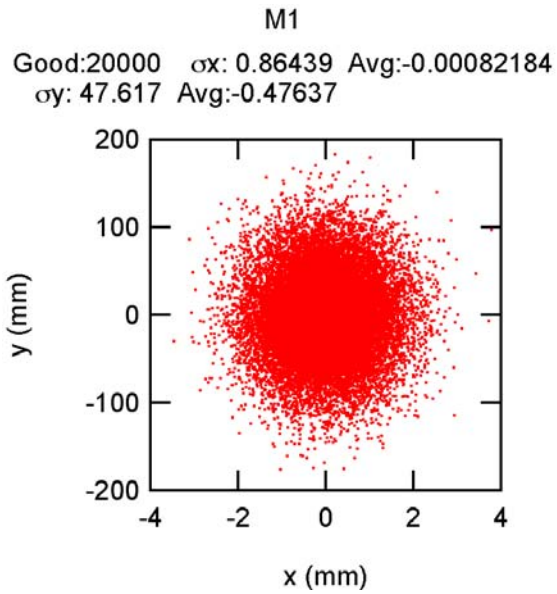

Figure 4.B.1. M1 illumination

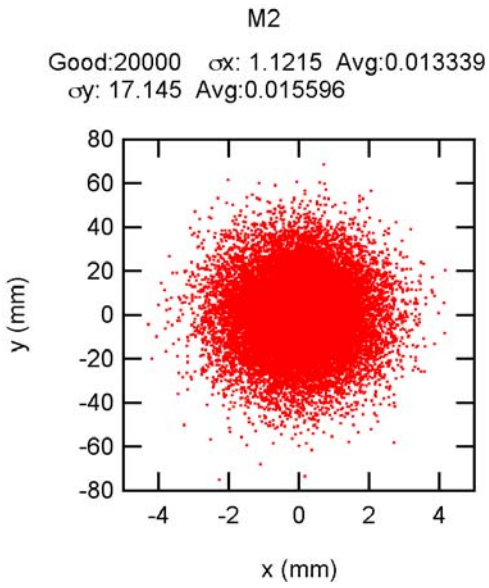

Figure 4.B.2. M2 illumination

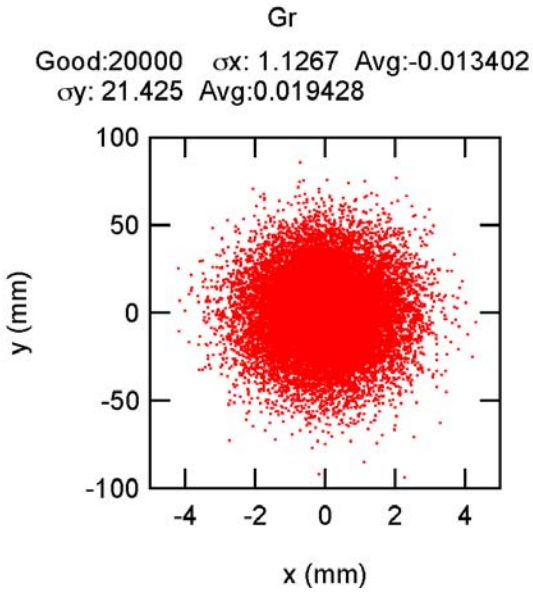

Figure 4.B.3. Grating illumination

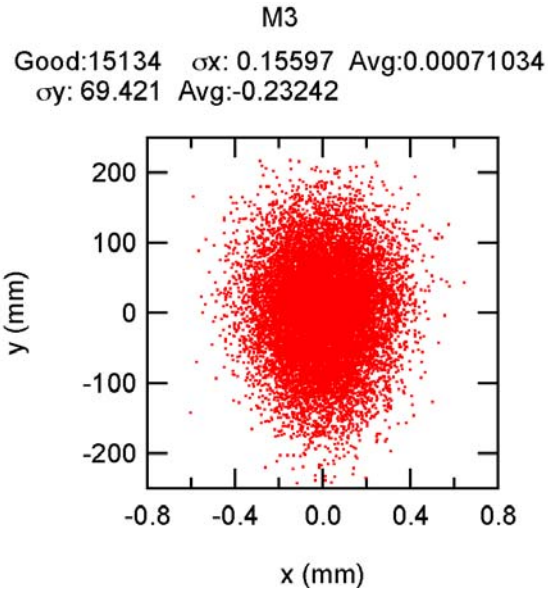

Figure. 4.B.4. M3 illumination

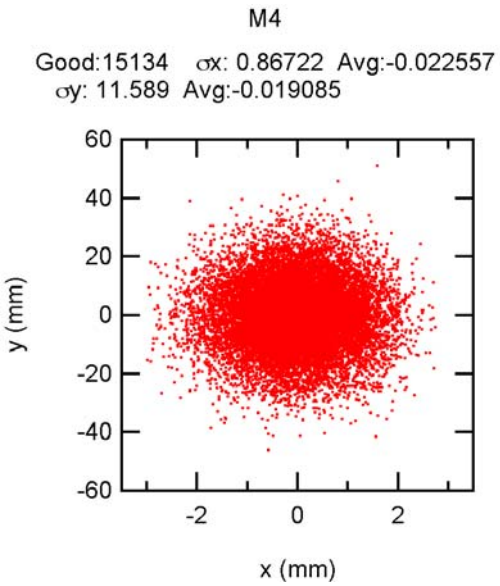

Figure 4.B.5. M4 Illumination

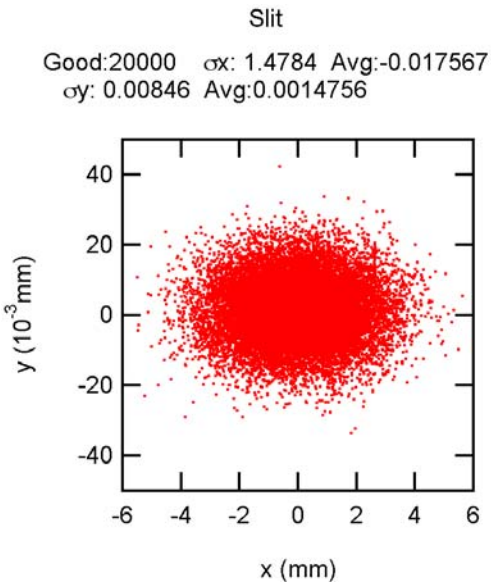

Figure 4.B.6. Image at slit

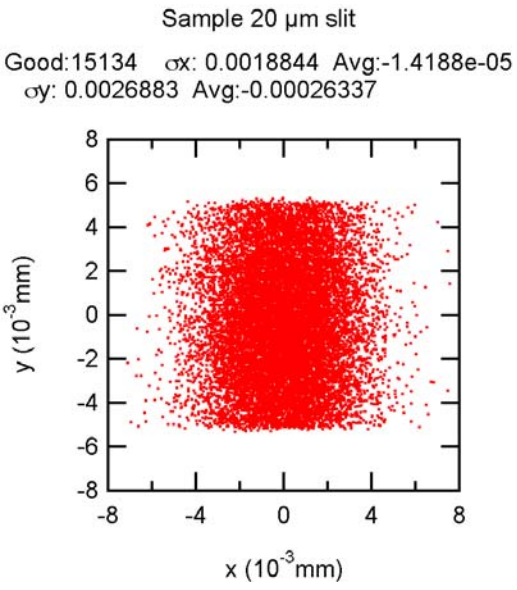

Figure 4.B.7. Image at sample position.

4-A Appendix C: SAS Optics Reports

Slope Errors on the Optical Elements.

The meridional slope errors on M1, diverting mirror, and M3 contribute to the horizontal spot size. The sagittal slope errors on M2, grating, and M4 also affect the horizontal spot size. The required slope errors were obtained from the condition that each contribution is less or equal half the minimum RMS horizontal spot size at the sample.

The meridional slope errors on M2 and the grating contribute to the resolution. The sagittal slope errors on M1 and diverting mirror also affect the resolution. The required slope errors were obtained from the condition that each contribution is less or equal half the combined resolution due to the source and a 10 μm exit slit.
The meridional slope error on M4 and the sagittal errors on M3 contribute to the vertical spot size at the sample. The required slope errors were obtained from the condition that each contribution is less or equal half the minimum RMS vertical spot size at the sample with a 10 μm slit.

The required RMS slope errors (and the condition determining it) are given in the table below.

Table 1. Maximum RMS slope errors on the optical elements

Element	Meridional(μrad)	Condition	Sagittal(μrad)	Condition
M1- Sagittal cylinder	0.25	Hor. spot size	8.0	Resolution
M2- Plane	0.17	Resolution	3.5	Hor. Spot Size
Gr - Grating	0.13	Resolution	5.5	Hor. Spot Size
Div. Mirror – Plane	0.22	Hor. Spot Size	8.8	Resolution
M3 - Plane Elliptical	0.17	Hor. Spot Size	14	Ver. Spot Size
M4 – Plane Elliptical	0.37	Ver. Spot Size	14	Hor. Spot Size

4-A Appendix D: SAS Optics Reports

Position of the Optical Elements, Optics Parameters, and Ray Tracings with Canted Beams

Position of the Optical Elements

The coordinates of the optical elements in the case of a single beam are given in Table 4.D.1. The center of the coordinate system is in the middle of the straight. The y coordinate is along the beam propagation, x is in the horizontal plane and perpendicular to y, and z is along the vertical. The distance between M3 II and M4 II was increased to 1 m.

Table 4: Coordinates of the optical elements**.**

Element	x (mm)	y (mm)	z (mm)
Source	0.000	0.000	0.000
M1	0.000	29500.000	0.000
M2	-102.583	31849.537	0.000
Grating	-109.0485	31997.621	-15.000
Slit	-545.242	41988.103	-15.000
M3	-597.586	43186.961	-15.000
M4	-662.952	43934.107	-15.000
Sample	-750.025	44929.353	28.619
Branching Mirror	-196.287	33995.717	-15.000
Slit II	-893.533	41965.275	-15.000
M3 II	-1695.366	51130.266	-15.000
M4 II	-1825.892	52121.711	-15.000
Sample II	-1956.294	53112.212	28.6193

Optical parameters

Table 2. Parameters of the optical components.

Element	Figure	Major axis (mm)	Minor axis/sagittal radius (mm)
M1 Center	Meridional Cylinder		1287.08
M1 Upstream	Meridional Cylinder		1338.89
M1 Downstream	Meridional Cylinder		1234.89
M3 Center	Meridional Elliptical Cylinder	22475.	189.68
M3 Upstream	Meridional Elliptical Cylinder	23125.	192.51
M3 Downstream	Meridional Elliptical Cylinder	21825.	186.80
M4	Meridional Elliptical Cylinder	1475.	30.463
M3 II Center	Meridional Elliptical Cylinder	26600.	220.75
M3 II Upstream	Meridional Elliptical Cylinder	27250.	223.54
M3 II Downstream	Meridional Elliptical Cylinder	25950.	217.93
M4 II	Meridional Elliptical Cylinder	5600.	69.67

Grating Parameters

The line density of the gratings is given by $k(w) = a_0 + a_1 w + a_2 w^2 + \ldots$ where w is positive towards the slit. These parameters and the c parameter are listed in Table 3.

Table 3. Grating parameters

Grating	a_0 (mm^{-1})	a_1 (mm^{-2})	a_2 (10^{-6} mm^{-3})	c parameter
LEG	150	0.05397	8.09	≈1.5
MEG	400	0.14381	21.5	≈1.5
HEG	1200	0.30181	45.1	≈2.2

Accuracy in Optics Positioning.

The resolution of the hexapods is 1μm for the translations and 1 μrad for the rotations[1]. These values are sufficient for most of the required movements besides the pitches of M1, the branching mirror, M3 and M4. Since the goal is to overlap the beams from the two IDS, lets say within 0.2 the sigma value, one needs a resolution better than 0.07 μrad on the most sensitive element, M3. We note that this resolution is 2/5 the meridional slope error specified previously for M3.

Ray Traces with Canted Beams

As in the case of the IDs emitting linearly polarized light[2], we determined the source sizes as a function of the longitudinal position using SRW. In this case, the upstream ID (located at 1.3m upstream the center of the straight) was tuned to emit circular polarized radiation at the lowest possible energy (230 eV). As seen in Figure 2, the RMS vertical size is 26 μm and it is located very close to the ID center. The vertical RMS size is 42 μm and occurs close to the ID end. The lines in the right part of the figure are linear fits to the RMS size giving RMS divergences of 32 μrad for the vertical and 34 μrad for the horizontal. In the ray tracings described below, we used these divergences and vertical RMS sizes. For the horizontal RMS size, we used the RMS beam size at the center of the ID, i.e., 45 μm.

In the canted mirrors, y=0 corresponds to the coordinates of the mirror collecting the central beam.
Figure and Figure show the illumination of the M1 mirrors collimating the upstream and downstream beams, respectively.

Figure , Figure , and Figure show the illumination of the plane mirror, the grating, and the slit plane with both beams when using the 150 l/mm grating and c=1.5. Note that the upstream beam is wider (diverging beam) but the vertical image at the slit is smaller for the upstream beam due to the larger demagnification.
The illumination of M3 with the upstream beam is seen in Figure and with the downstream beam in Figure 9. Note that due to the mirror orientation in Shadow, the y coordinates have the opposite sign. The illumination of M4 with both beams is presented in Figure 10.
The spot at the sample position with the upstream beam is displayed in Figure 11 and that of the downstream beam in Figure 12. Note that the image of the downstream beam is narrower due to the higher

[1] According to Ken Kriesel.
[2] Report "ID's Source Positions" dated September 9, 2007. The same electron beam parameters were used.

demagnification. This can be corrected by detuning the plane elliptical mirror as done in the initial beamline design.

The illumination of the mirrors of the branch line are shown in **Figure 13** (diverting mirror), **Figure 14** (M3 II upstream ID), **Figure 15** (M3 II downstream beam), and **Figure 16** (M4 II). The sample illumination with both beams is seen in **Figure 17** and **Figure 18**.

Figures

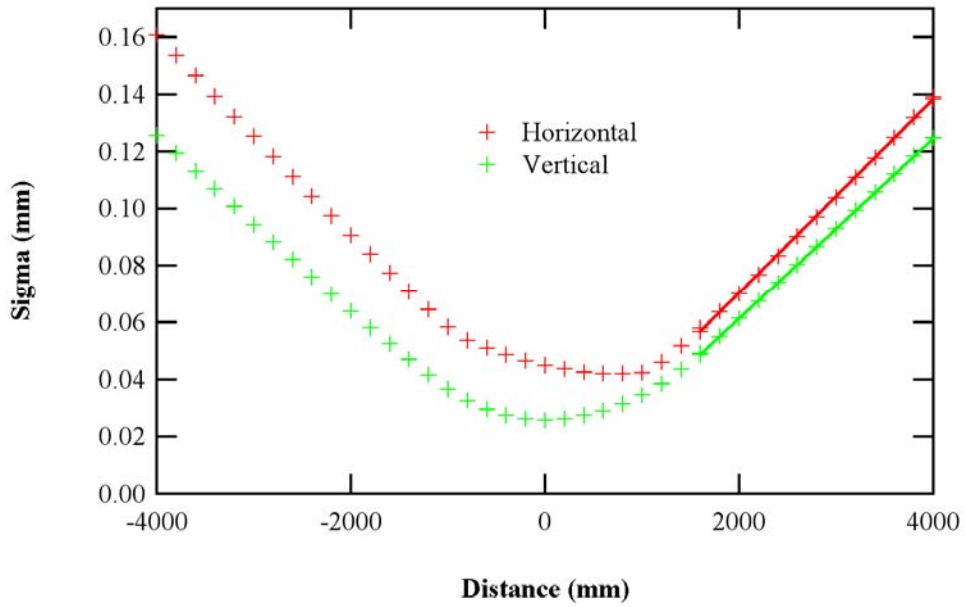

Figure 2. RMS image size of the upstream ID radiation as a function of the longitudinal position. The photon energy is 230 eV and the straight center is at +1.3 m.

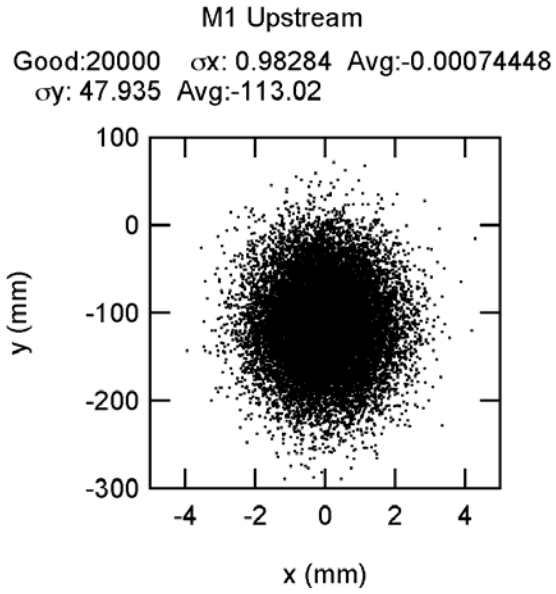

Figure 3. M1 illumination. Upstream ID.

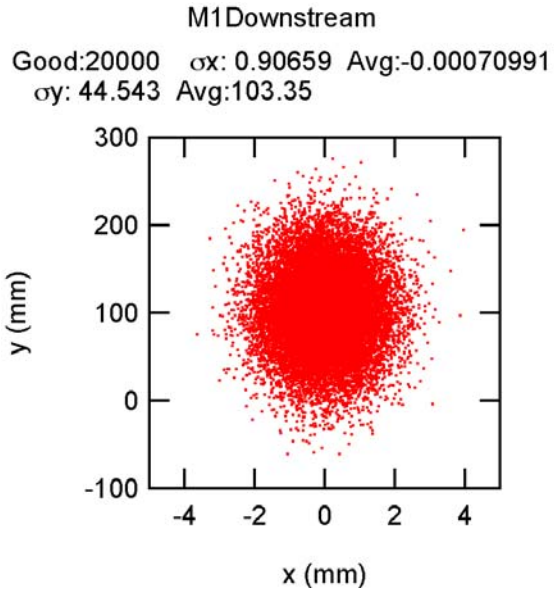

Figure 4. M1 illumination. Downstream ID.

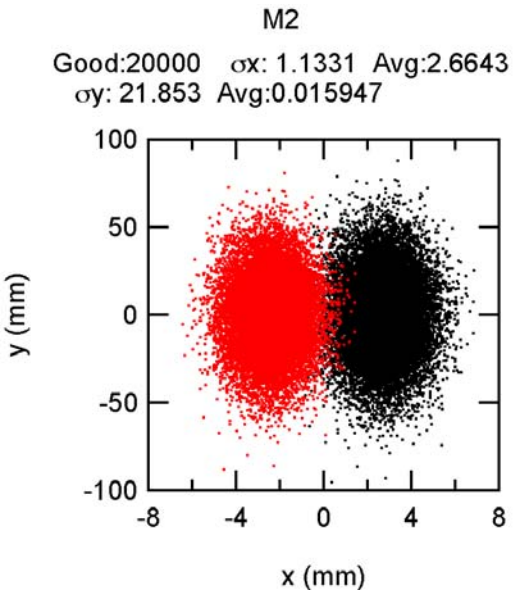

Figure 5. M2 illumination. Black: Upstream ID, Red: Downstream ID.

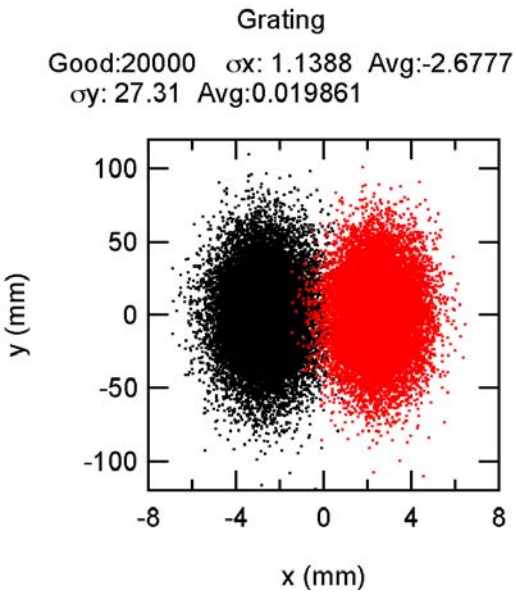

Figure 6. Grating illumination. Black: Upstream ID, Red: Downstream ID.

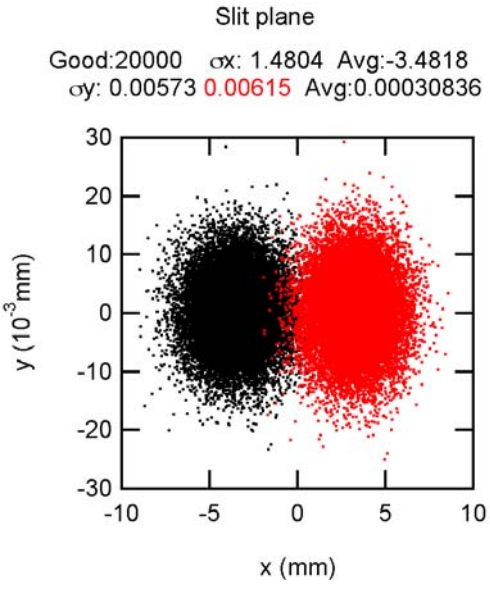

Figure 7. Slit plane. Black: Upstream ID, Red: Downstream ID.

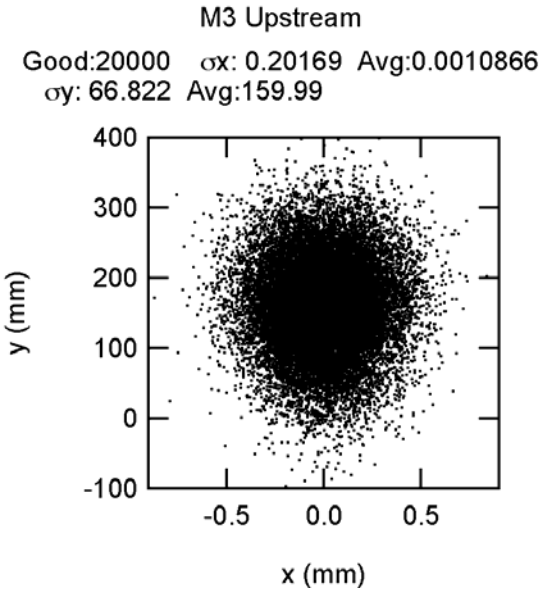

Figure 8. M3 illumination. Upstream ID.

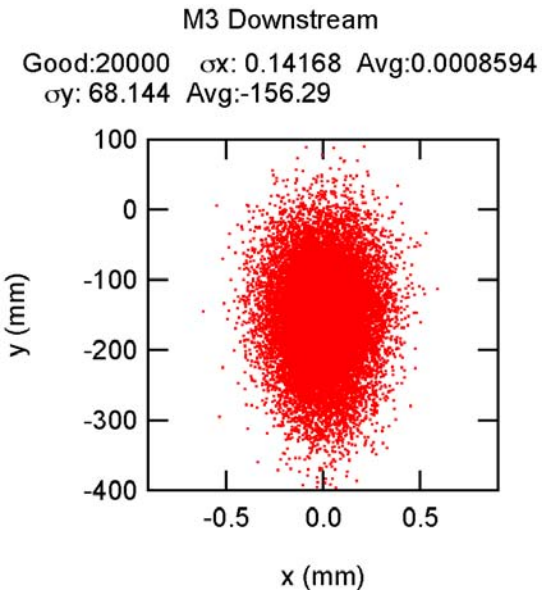

Figure 9. M3 illumination.
Downstream ID.

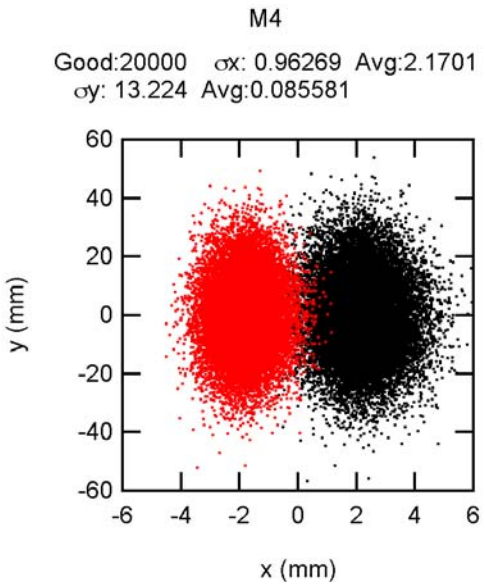

Figure 10. M4 illumination.
Black: Upstream ID, Red: Downstream ID.

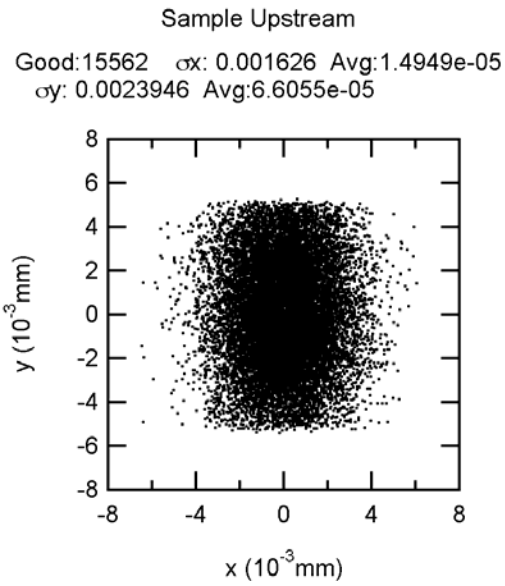

Figure 11. Sample illumination.
Upstream ID.

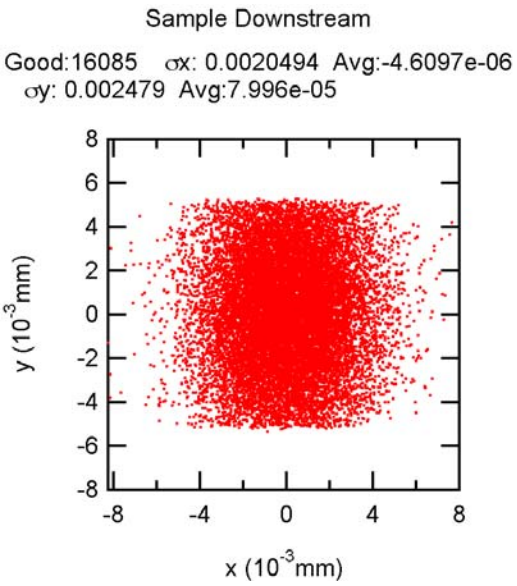

Figure 12. Sample illumination.
Downstream ID.

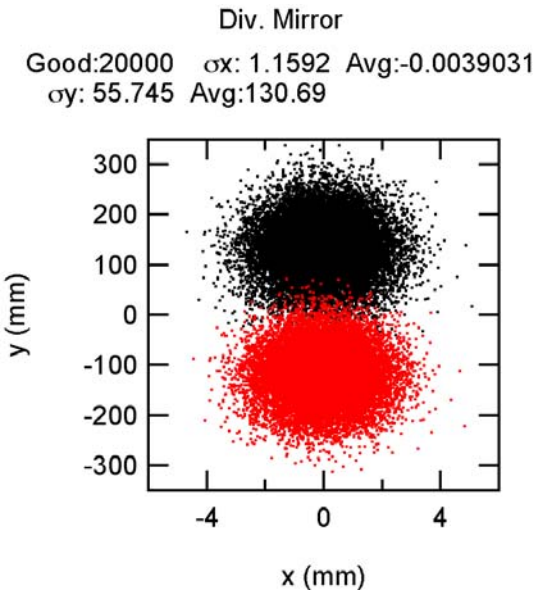

Figure 13. Illumination of the diverting mirror. Black: Upstream ID, Red: Downstream ID.

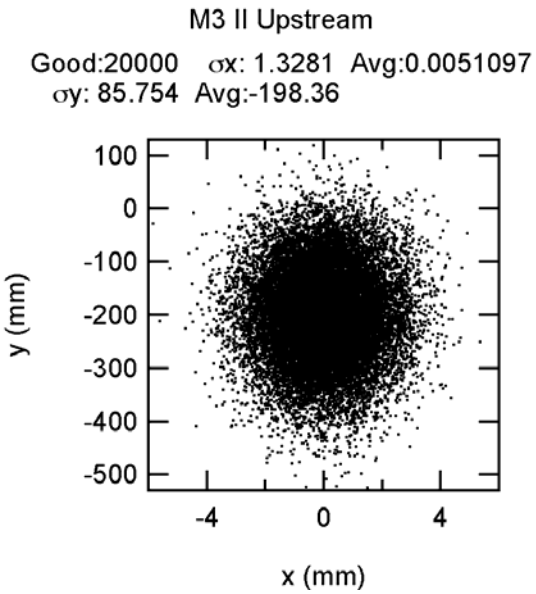

Figure 14. M3 II illumination. Upstream ID.

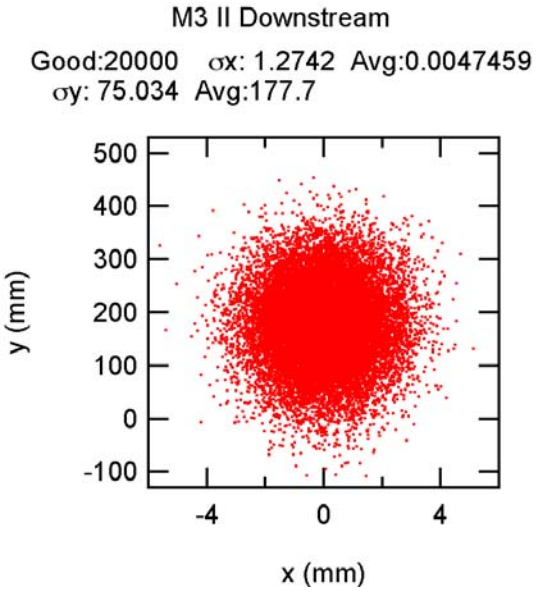

Figure 15. M3 II illumination. Downstream ID.

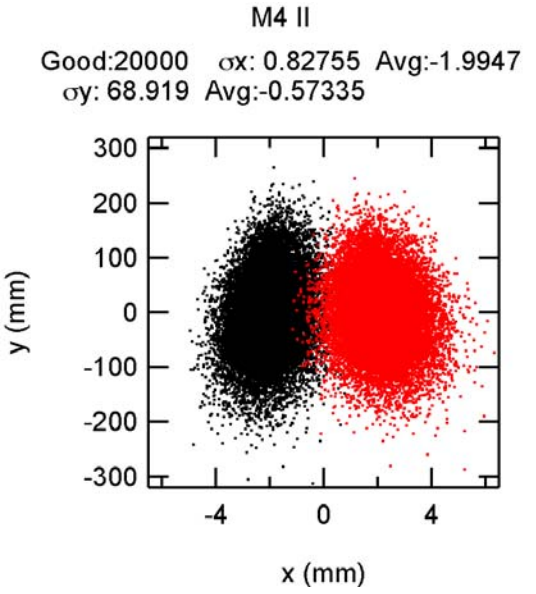

Figure 16. M4 II illumination. Black: Upstream ID, Red: Downstream ID.

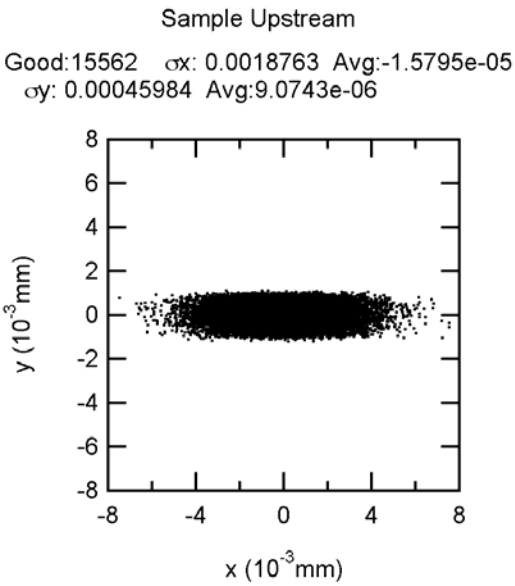

Figure 17. Sample II illumination. Upstream ID.

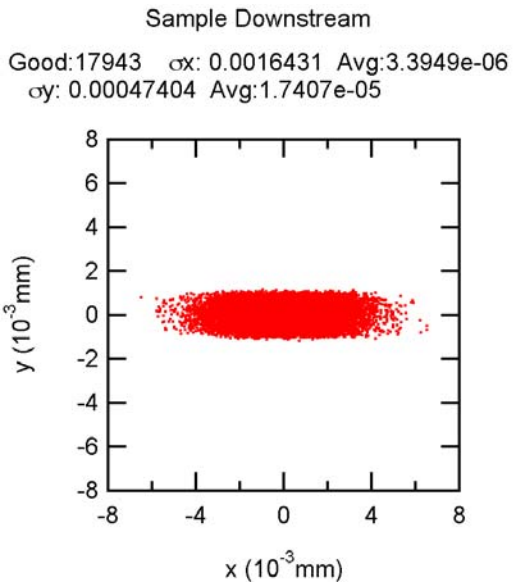

Figure 18. Sample II illumination. Downstream ID.

Power Absorbed by Optical Elements.

Corrected for the values used by Ken Kriesel on the FEA.

NOTE: Ken Kriesel corrected the illuminated length he used in the FEA of M2 in section 2 from (what I wrote) 80 mm to 68 mm. I calculated the total power on M1, M2 and the grating, for an aperture of 8×8 mm^2 at the position of M1. I added to the table (in parenthesis) the power values for the aperture used by Ken, i.e., 7.1×5.15 mm^2 at the position of M1. The effect of the reduced horizontal aperture on the slope errors along the horizontal direction needs to be investigated.

Power Absorbed by the Optical Elements

The power and power densities absorbed by M1, M2, and the grating were calculated with the IDPower routine in SRCalc with the machine and ID parameters listed in our report dated August 27, 2007. We assumed Au as the reflective coating on all optics. Table 7 summarizes the maximum power values for elements up to the slit.

The highest absorbed power and power density in M1 and M2 occur when the two IDs are operated in tandem and tuned to the lowest photon energy, 183 eV. The worst case for M2 is when it is used with the high energy grating (HEG) since its angle of incidence is the smallest, 84.0º. As described in section 2, the power incident along the length of M2 needs to extend beyond the central cone of the "good" radiation to minimize the meridional slope error. Therefore, the horizontal and vertical apertures at the position of M1 were set to 8×8 mm^2. The power densities absorbed by M1 and M2 are shown in Figure 2 and Figure 20. The total absorbed power in M1 is 1.9 kW and in M2 236 W. The maximum power densities in M1 and M2 are 0.92 and 0.36 W/mm^2, respectively.

The maximum power density on the gratings (obtained from a few cases at different energies using the LEG) is less than 16 mW/mm^2. This value was obtained with the ID tuned to 555 eV (Figure 21). The total power absorbed with the aperture mentioned above is almost 40W. The horizontal aperture could be reduced to half, which will decrease the total power to 20 W. However, this could have a negative effect on the figure of M1, which will impair the horizontal spot at the sample.

The grating efficiencies and the diffraction angles are required to obtain the power densities and power downstream the grating. Since we already calculated the monochromatic flux for this beamline with a slightly different ID (42 mm period instead of 45 mm) we used those results to estimate an upper limit for the power and power densities on those elements.

The calculated flux at the sample at 1 keV with the LEG and 10 μm slit is 5×10^{13} photons/sec, or a power of 8 mW. With an aperture of 4×4 mm^2 at the position of M1, the illuminated vertical (horizontal) size at the slit with this grating is approximately 7.2 (5.7) mm. This means that the power at the slit plane is less than 10 W and the power density is less than 0.24 W/mm^2. Approximately the same power will be incident on the diverting mirror but the absorbed power and absorbed power densities are less than 3 W and less than 4 mW/mm^2.

With a 10μm slit, the power absorbed in M3 and M4 is less than 2 mW. The total power will increase linearly with the slit width. The power densities are negligible.

The power on the chopper in the CP fast switching mode is less than 10 W and the power density is less than 0.2 W/mm^2.

Slope Errors on M2

Ken Kriesel did a FEA analysis to obtain the temperature rise and surface deformation due to the power absorbed in M2. He initially performed[3] the calculations assuming a homogeneous power density of 0.362 W/mm^2 over a length of 48 mm and a width of 5.4 mm. Ken included in the model the fact that that beam is not centered on M2 but at 307 mm from its end.

We ray traced the system up to the exit slit with the deformed surface obtained by Ken and realized that the RMS spot at the exit slit increased from 5.8 μm to more than 11 μm. The reason for the large increase is mainly due to the sharp discontinuity in the absorbed power along the mirror length, giving a large slope error in the region of the central cone.

At our request, Ken increased the length over which the power is absorbed to 68 mm. The surface deformation he obtained (assuming a constant power density instead of the small variations seen in Figure 20) is displayed as an image plot in Figure 22. From these results we extracted the surface deformation along the mirror length (at zero width) and along the mirror width (at zero length). The height profiles and the calculated slope errors are shown in Figure 23 and Figure 24.

The maximum surface deformation is actually not at the center of the beam, i.e. at 307 mm (Figure 23). As Ken pointed out, this is due to the fact that the long M2 mirror is not illuminated at the center[4]. The sharp increase in the slope error towards the edge of the region being heated by the beam is clearly seen in Figure 23. However, the beam in the central cone sees only an RMS slope error of ≈0.9 μrad and not the high slope error region.

Ray Traces with Deformed M2

The spot at the exit slit plane when the ID is tuned to 183 eV, the high energy grating is used, and there are no deformations on the optics, is shown in Figure 25. The effects of the induced figure error on M2 due to the absorbed power are evident when comparing Figure 26 to the previous one.
The figure change in the central part of M2 can be approximated by a convex radius of $\approx 1.8\times10^7$ mm, which means the beam incident on the grating is not vertically collimated as in the optical design. This change in the virtual source position can be corrected by operating the grating with a c value of 2.193 instead of the nominal value of 2.184 at this energy. The spot at the exit slit plane with the deformed M2 and the corrected c value is presented in Figure 27. The vertical RMS size is reduced to 6 μm, very close to the initial value.

The above example shows the possibility of correcting the spot size at the slit for the highest absorbed power in M2. At this energy (183 eV) the beam size is the largest. Further studies at higher energies (where the beam is smaller) need to be performed to verify that this "correction" is also possible. Still to be tested is whether the deformations along the meridional direction on M1 can be corrected with a change in the curvature of M3. FEA of this mirror are then required.

[3] I proposed that length since it is the part illuminated by the central cone.
[4] Ken Kriesel checked that illuminating the mirror center gives a symmetric deformation.

Effect of Single M1

We discussed the option of performing the fast switching of CP with the electron beam instead of canting the beams. This requires using a single collimating mirror. To assess the effect of using a single M1, we have ray traced the system when each ID has an M1 with the correct sagittal radius and when the radius is the one required when the two IDs are operated in tandem.

The ray tracings at the exit slit plane when the upstream ID is tuned to 230 eV, M1 has the correct sagittal radius, and the LEG is used, are seen in Figure 28. Changing the radius to that required for the case when the IDs are operated in tandem increases the vertical spot by almost a factor of two (Figure 29). This means that the contribution to the resolution due to the source will degrade by the same factor. Practically the same results are obtained for the downstream ID.

Table 5. Maximum power and power densities absorbed by the optical elements. Values in parentheses are for an aperture of 7.1×5.15 mm^2 at the position of M1.

Element	Power Absorbed (W)	Power Dens. Abs (W/mm^2)	Case
M1	1910 (1160)	0.92	183 eV
M2	236 (132)	0.37	183 eV HEG
Gr	40 (22)	0.016	555 eV LEG
Div. mirror	<3	<0.004	1 keV LEG
Chopper	<10	<0.2	1 keV CP LEG
Slit	<10	<0.24	1 keV LEG

Figures

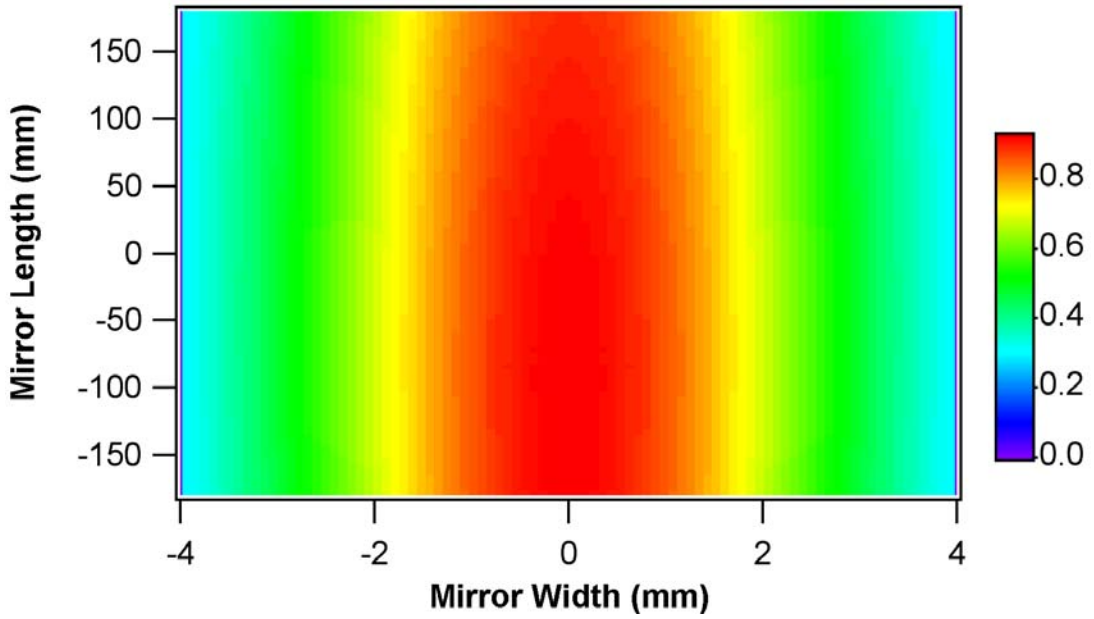

Figure 19. Power density (W/mm^2) absorbed in M1. 183 eV.

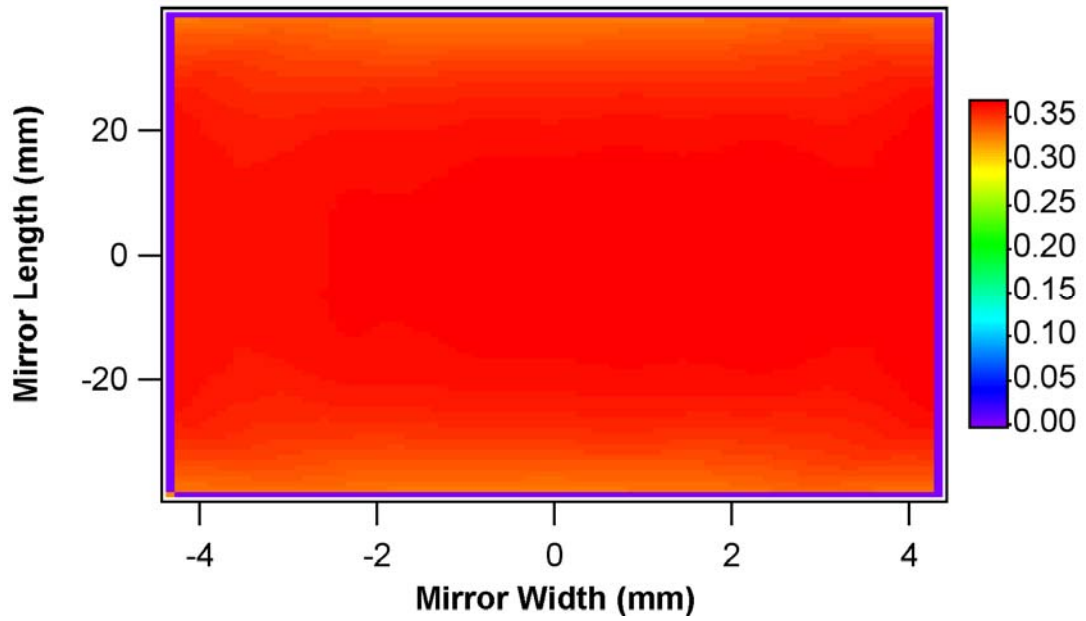

Figure 20. Power density (W/mm^2) absorbed in M2. 183 eV HEG.

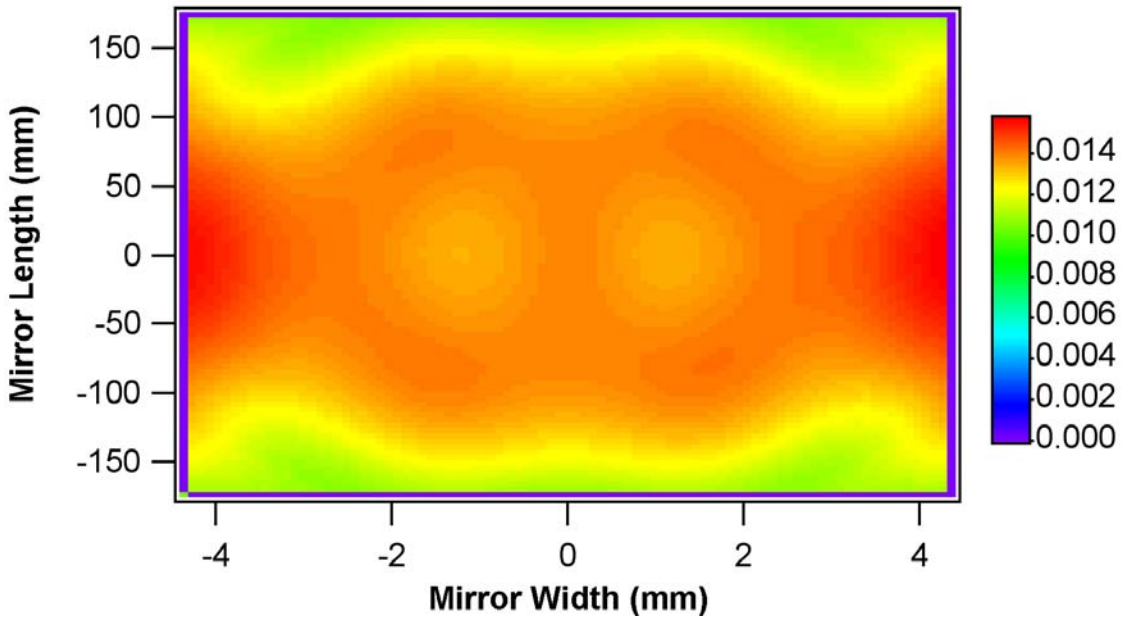

Figure 21. Power density (W/mm^2) absorbed in the LEG at 555 eV.

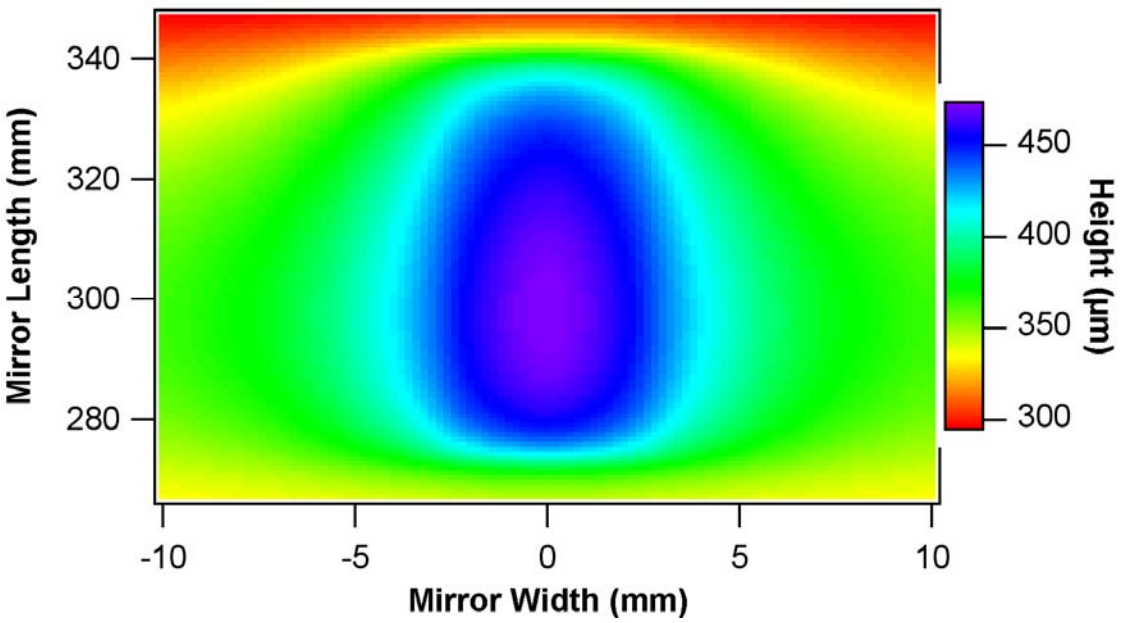

Figure 22. Height change on M2 due to the absorbed power density.

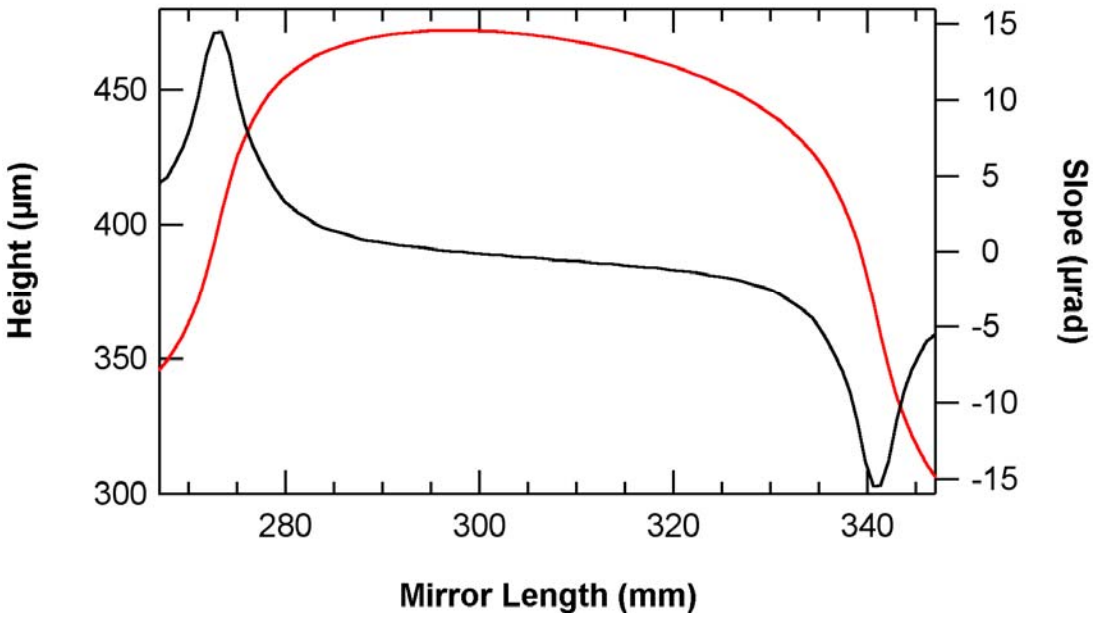

Figure 23. M2 Surface deformation (red trace) and meridional slope error (black trace) at zero width.

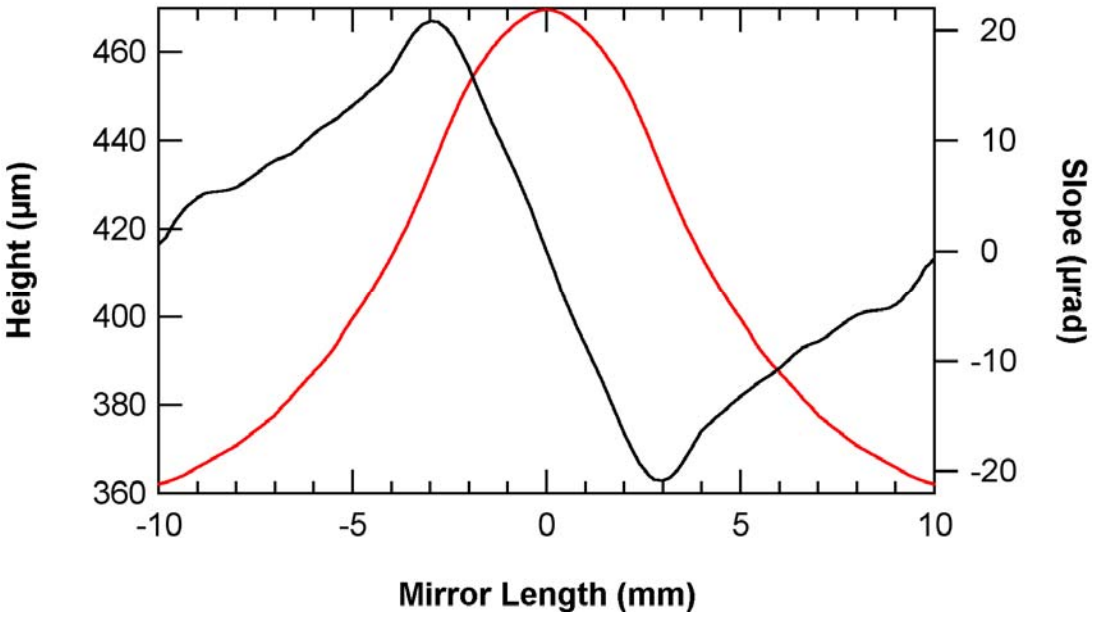

Figure 24. M2 Surface deformation (red trace) and sagittal slope error (black trace) at zero length.

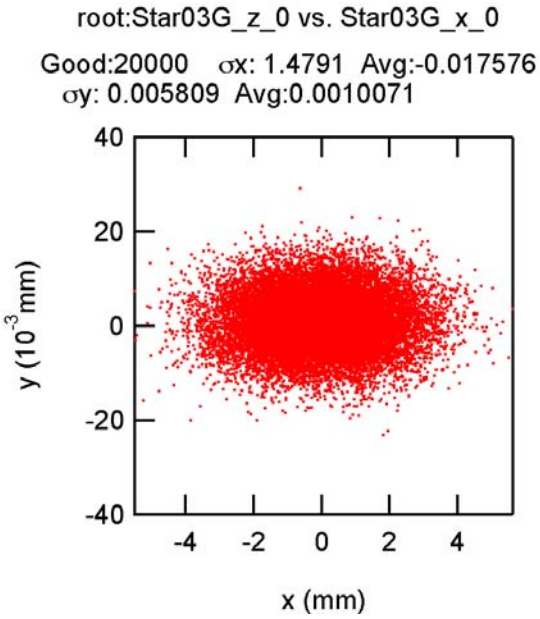

Figure 25. Ray tracings at the exit slit plane with perfect optics

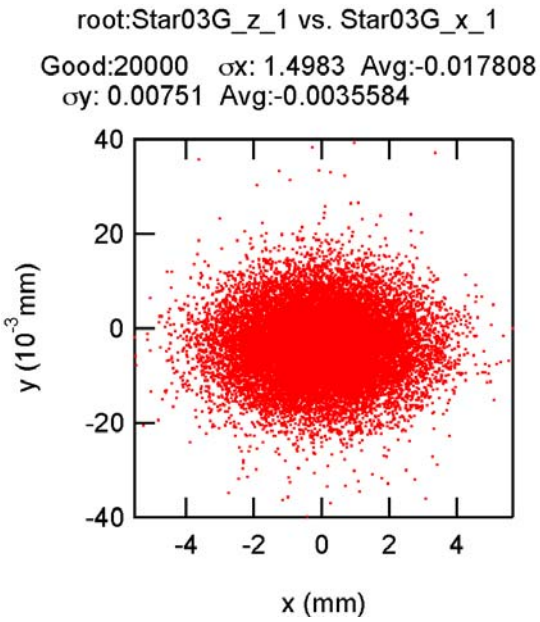

Figure 26. Ray tracings at the exit slit plane with deformed M2.

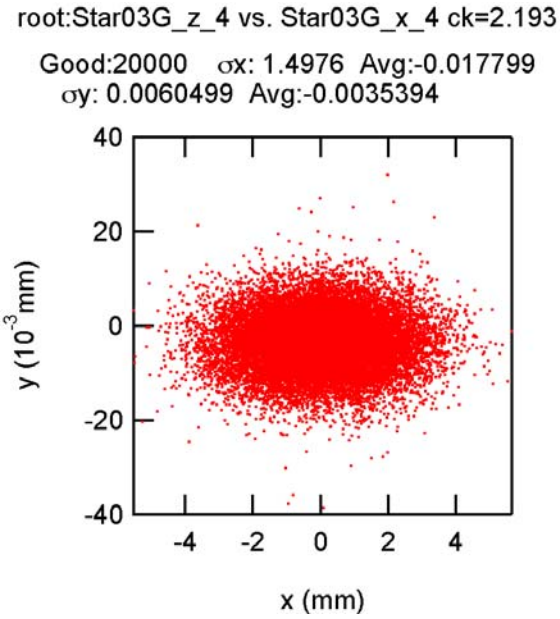

Figure 27. Ray tracings at the exit slit plane with deformed M2 and optimized c value.

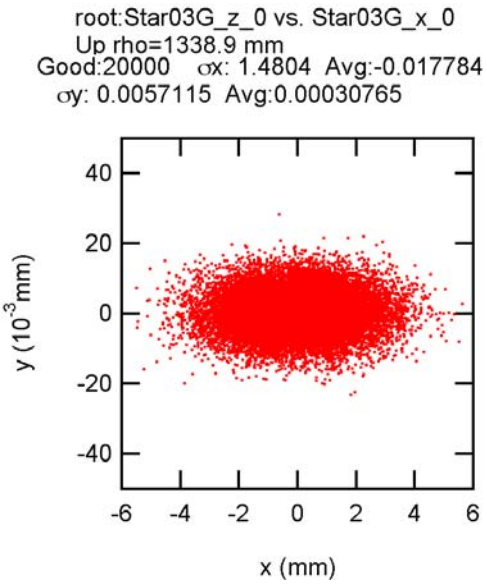

Figure 28. Ray tracings at exit slit plane for the upstream ID with correct M1 radius.

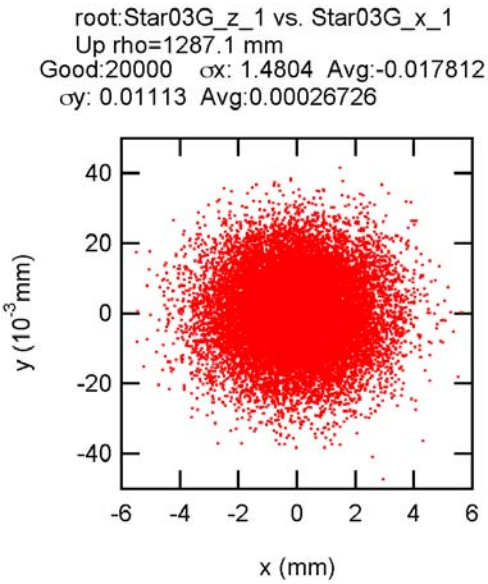

Figure 29. Ray tracings at exit slit plane for the upstream ID with M1 radius of phased IDs.

Appendix E. M2 Finite Element Analysis

A parametrically driven ANSYS input file was developed and employed for 3-D thermal-structural analysis of the M2 mirror in the NSLS2 soft x-ray coherent scattering and imaging beamline. It solves for surface deflections in two passes. The first is a thermal analysis. The second pass has the thermal solution's resulting temperature field as input along with symmetry and other structural constraints and solves for thermal stresses and deflections. It allows for temperature dependencies of some properties; varying number, dimensions, and depth below heated surface of rectangular longitudinal coolant passages; variation in overall dimensions of the mirror substrate, changes in size, location or intensity of mirror heating; and certain other variations, with single parameter value changes in some cases and modest editing of the model file in others. Currently these variations are constrained by interaction with the definition of the heat load. Further development to support significantly spatially varying power densities will allow simulation of additional load cases. This work was performed with perhaps the most demanding defined load case, single-beam 183eV operation of the beamline.

Properties of bulk single-crystal silicon were gathered. Temperature dependencies of thermal conductivity and thermal expansion coefficient[1] were included in the model file. Data[2] for directional thermal conductivity below 40 degrees K was found, showing the anisotropy disappears in the range above 30 K, so the conductivity was treated as isotropic in our range of interest. No data for directionality of thermal expansion was found. (It would seem reasonable that if structural stiffness varies with direction that there would be some variation in thermal expansion as there is in other anisotropic materials. But in the absence of directional property data, we do not model directionality of thermal expansion.)

Beginning with coolant and heat transfer parameters as well as coolant passage geometry matching the Diamond I06 beamline, some simple optimization simulations were made. Peak temperature was used as a proxy for the optical surface deformations we desire to minimize. These preliminary optimization runs resulted in a move to 1.5mm thick silicon between coolant passages and a reduction to 1mm between the optical surface and the beginning of the coolant passages. These parameters are within the range of what is workable for silicon optics manufacturers such as InSync to produce with good optical figure. A number of ANSYS FEA runs were then made using this basic set of parameters. A subset will be documented here. Initial results were compared to the closest case documented in the Diamond I06 TDR as an additional check on the modeling accuracy in this work. Several models were rerun to generate graphics files from model development to results path plots.

There are a number of simplifications and approximations in common among all ANSYS models of the M2 mirror to date. The silicon is treated as isotropic rather than orthotropic structurally. This is a significant approximation structurally (in how the silicon responds structurally to the thermally produced strains). The coolant passages as modeled run the full length of the optic, and the back of the optic is solid; a real optic will require UHV-tight end manifolding of the coolant slots and inlet & outlet connections on the back with air guarding. The optic is modeled with symmetry constraints to exploit left-right symmetry. (Because the location of the heat load in general is not centered axially, only bilateral symmetry is present in the model, not four-fold as is often modeled.) The thermal effects of the glass frit bond are treated as negligible, which is rather optimistic given the thermal resistance of the approximately 50 micron layer can equal that of several mm of silicon. The bulk temperature of the coolant is held constant at 23°C. Heat transfer coefficient is treated as constant, invariant to both silicon surface temperature and location in the flow channel. Geometric effects such as the slope increasing on the front portion of the heat bump and thereby raising its power density are minor and safely ignored; peak meridional slope of about 14 microradians change was observed at the front & back of the heat input area of 6 degrees grazing incidence, giving about ±0.013% power density change. The effect of mirror coating is trivial since the gold over chromium is nominally only 30nm thick, one millionth the substrate thickness or less. It is also likely that the thin film's conductivity being lower than that of bulk properties[3], approximates that of silicon, reducing this error further. The change in shape of the optic due to other influences including manufacturing tolerances, gravity load, support clamp loads etc. are

ignored. Structural effects of the thin coating and frit layers including residual stress and differential thermal expansion are also ignored. Differential pressure between the coolant passages and vacuum surface are ignored. Optical figure error as manufactured is ignored.

1. Basic Mechanical and Thermal Properties of Silicon, Virgina Semiconductor Inc. http://www.virginiasemi.com/pdf/Basic%20Mechanical%20and%20Thermal%20Properties%20of%20Silicon.pdf

2. Anisotropic Heat Conduction in Cubic Crystals in the Boundary Scattering Regime, Physical Review B, Volume 2, No. 10, pages 4077-4083.

3. Strain and size effects on heat transport in nanostructures, Journal of Applied Physics, Volume 93, No. 6, pages 3535-3539.

Thermal load & optic parameters were as follows.

Table 1. Parameters comparison.

Parameter	As initially described	As modeled in ANSYS
Power deposition, W/mm^2	Nearly flat at 0.354 to 0.365 (maximum variation from average is 2.36%)	Flat at average 0.36223
Size of region with power deposition	5.4 x 48.045 mm	5.4 x 48.046mm
Location of center of beam spot	307 or 307.3mm downstream of upstream end	307mm downstream of upstream end
Taper in area illuminated due to beam divergence	(not described)	Divergence treated as zero
Mirror substrate overall length mm	<380	380
Mirror substrate overall width, mm	100	60
Mirror substrate overall thickness, mm	unstated	30

Following are details of a coarsely meshed run for 5 coolant partitions ("fins") per mirror half. For modeling convenience the optic was modeled upside down as shown in the figure below. The heat load is applied on a 48.046 mm long stripe 2.7 mm wide from the origin to the slanted line shown in the figure. Note, the system of units defined & used through the simulation runs is mm, gm, second, degrees C, coulomb, newton, & joule. Consequently stresses are displayed in N/mm^2 (MPa).

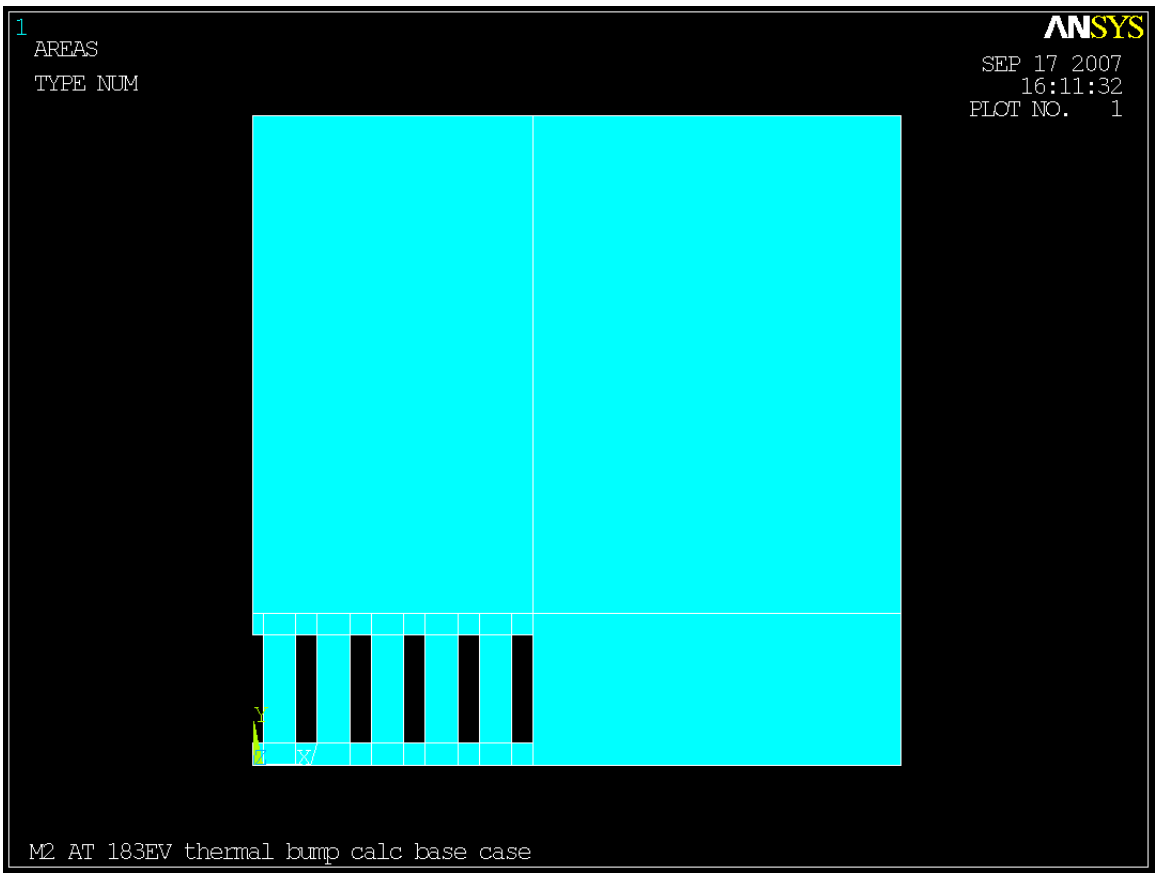

Figure 30. Silicon area shown in color; symmetry plane is at left.

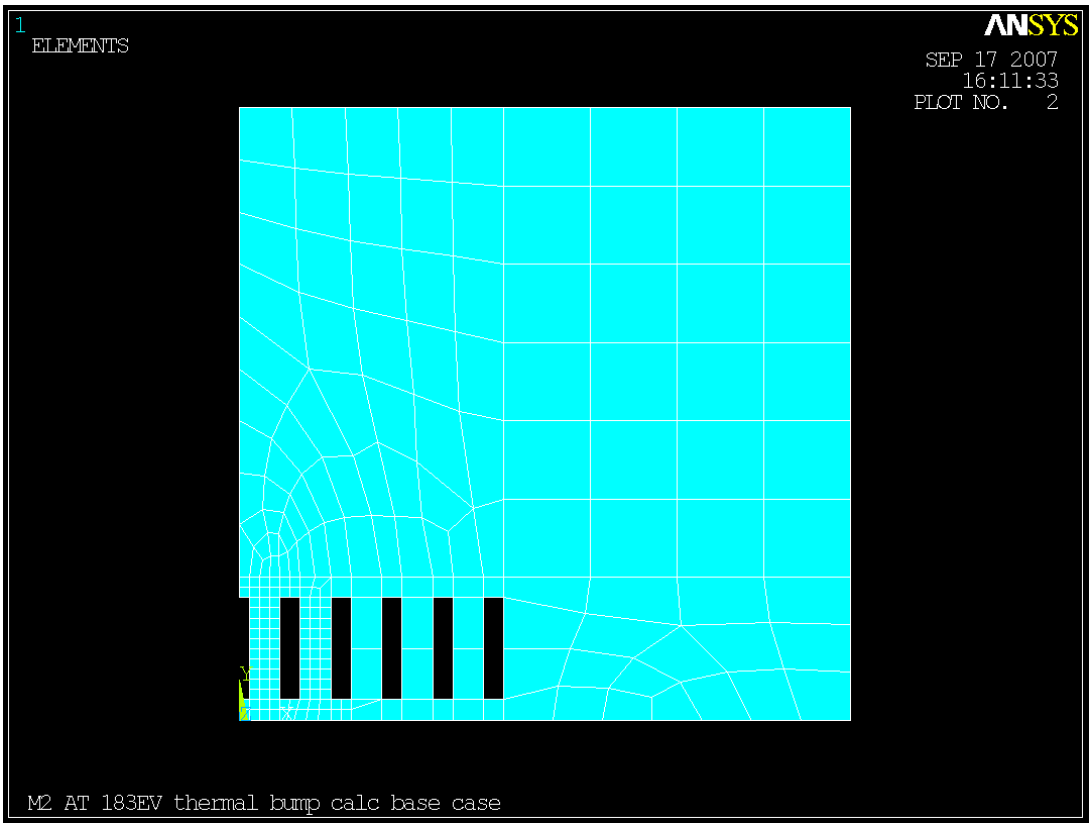

Figure 31. Initial meshing end view

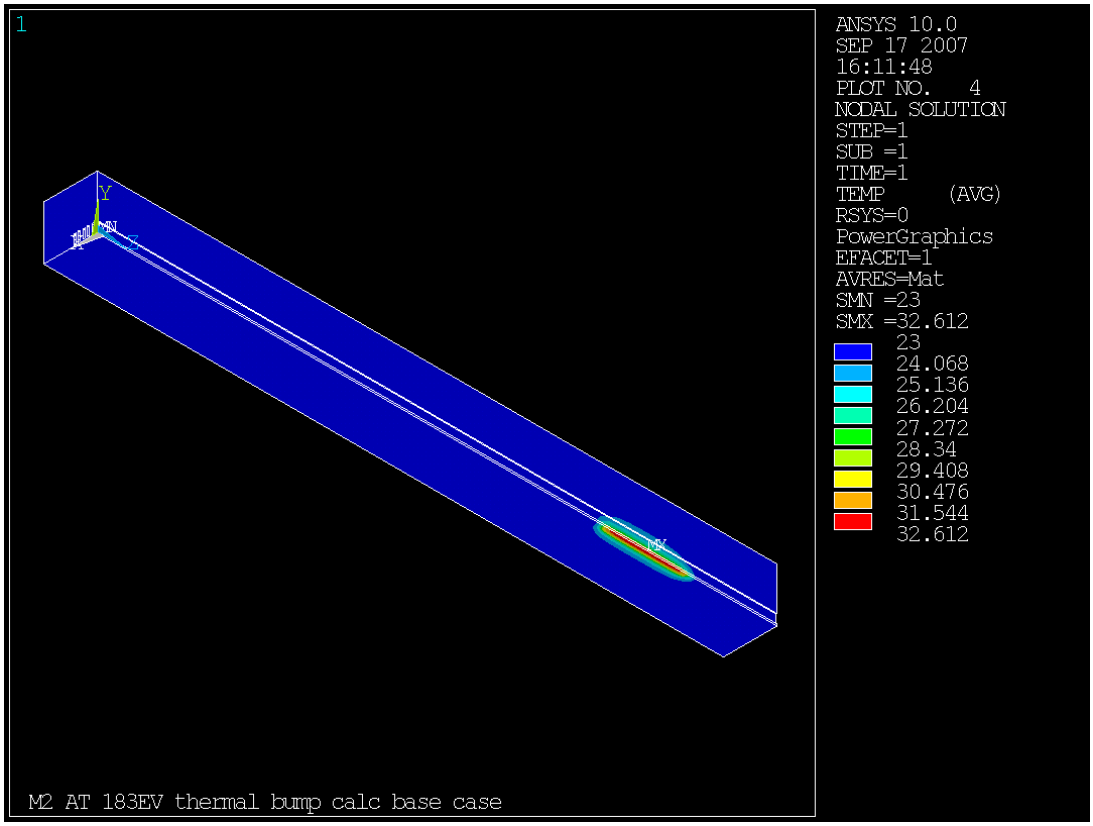

Figure 32. Thermal response, degrees C.

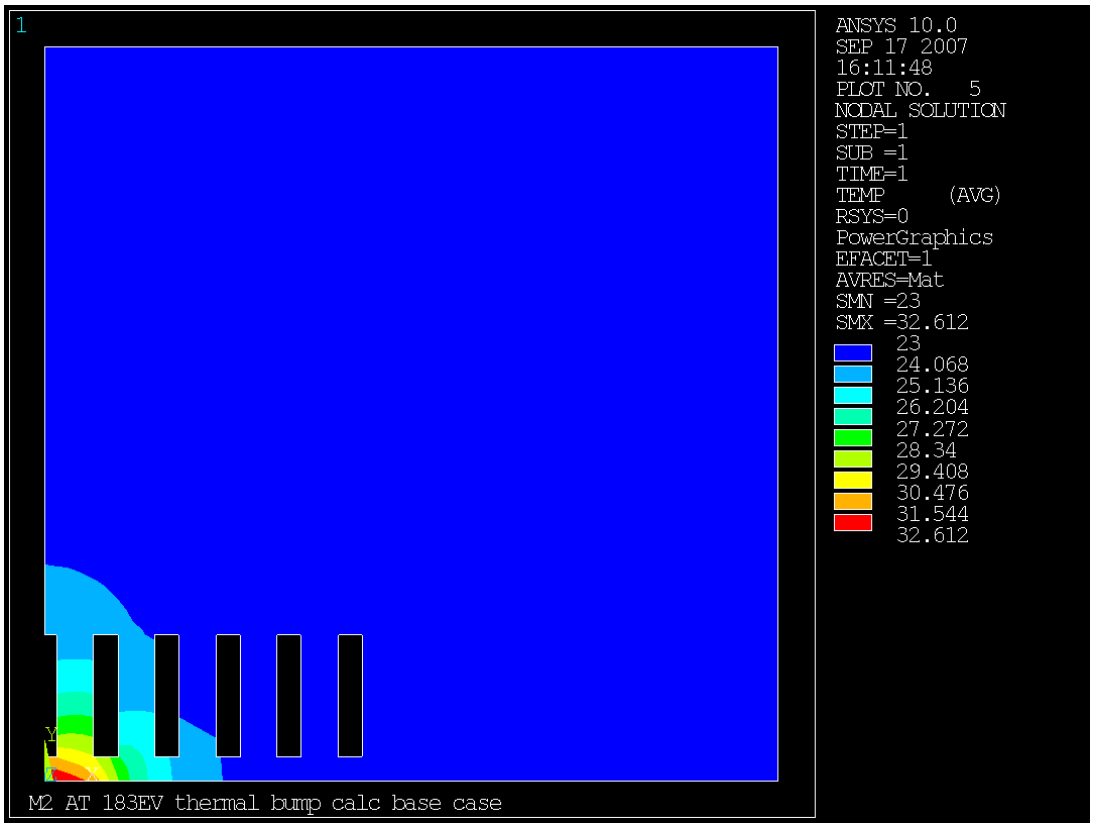

Figure 33. Thermal response at section through midpoint of heat load (Z=307mm).

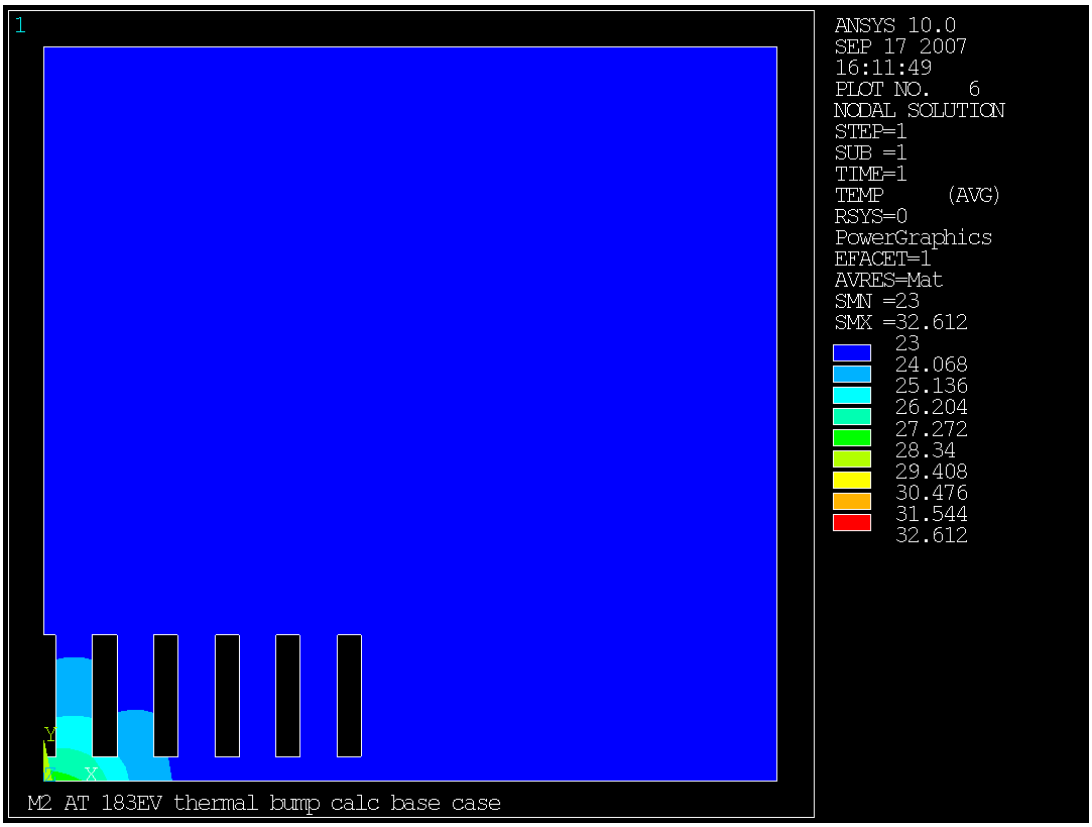

Figure 34. Thermal response, section through upstream edge of heat load (Z=283mm).

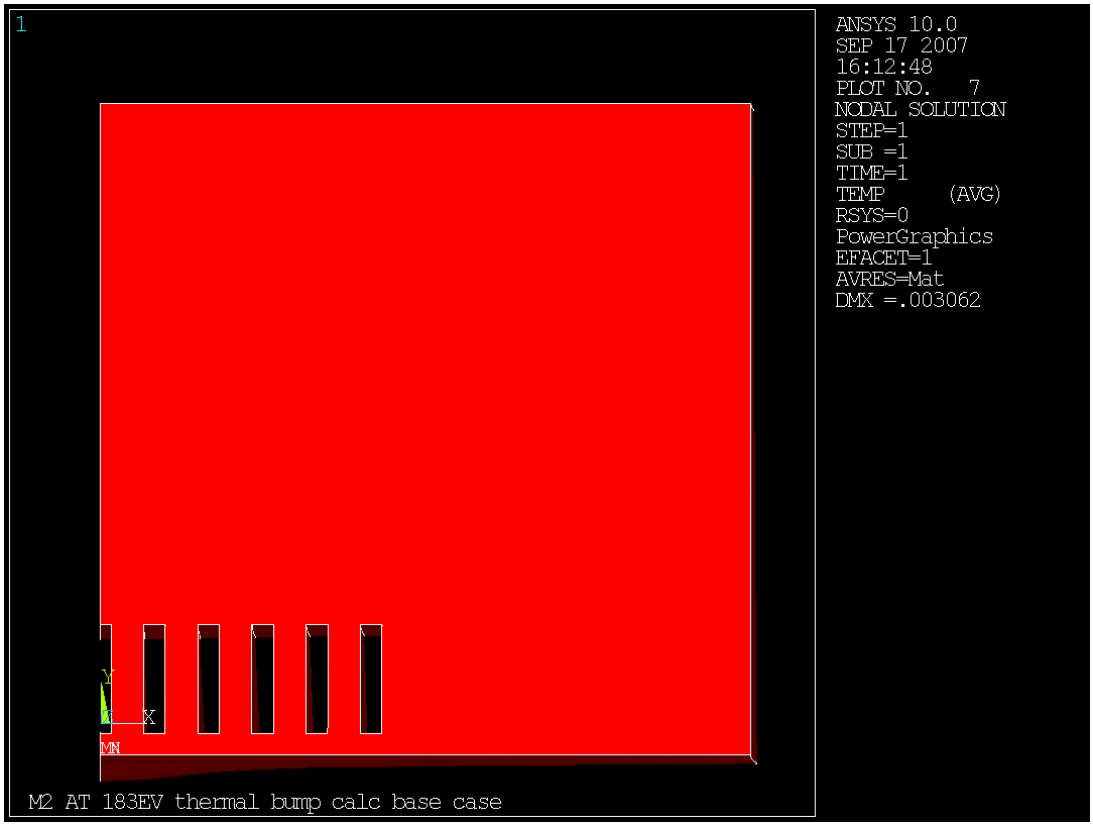

Figure 35. Exaggerated deformation end view.

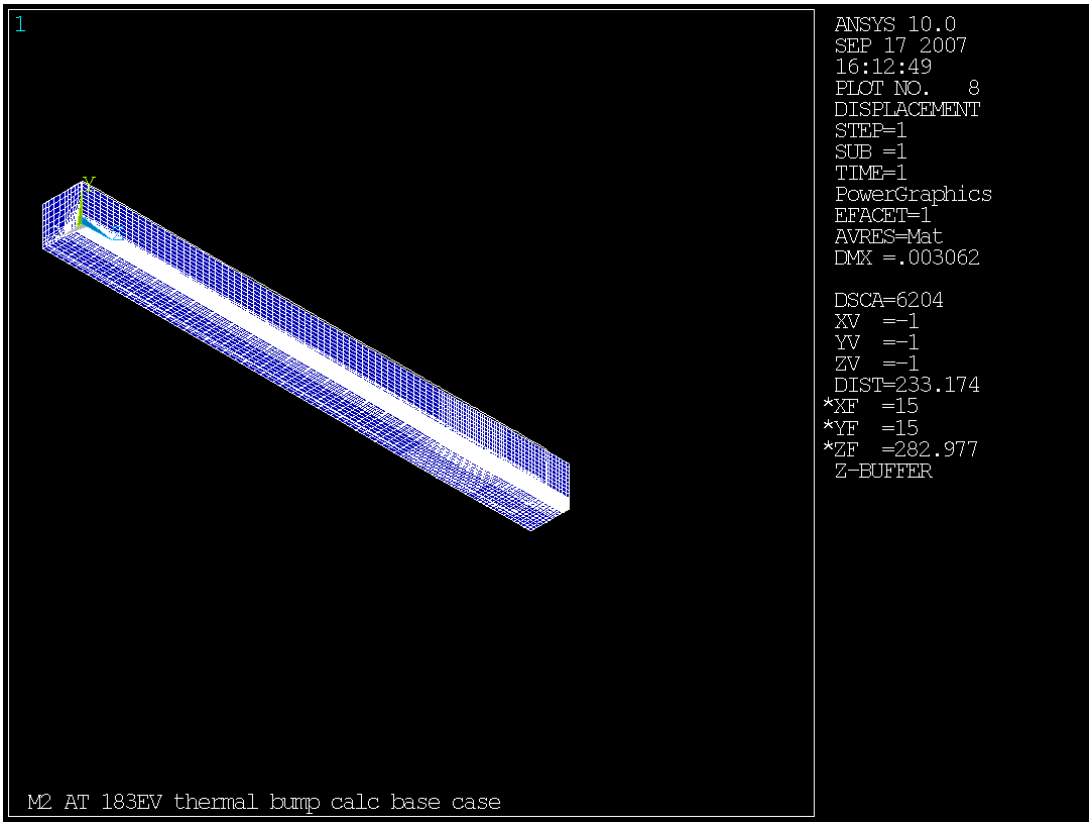

Figure 36. Displacement plot showing deformed and undeformed mesh; uniform thermal expansion dominates under the modeled conditions.

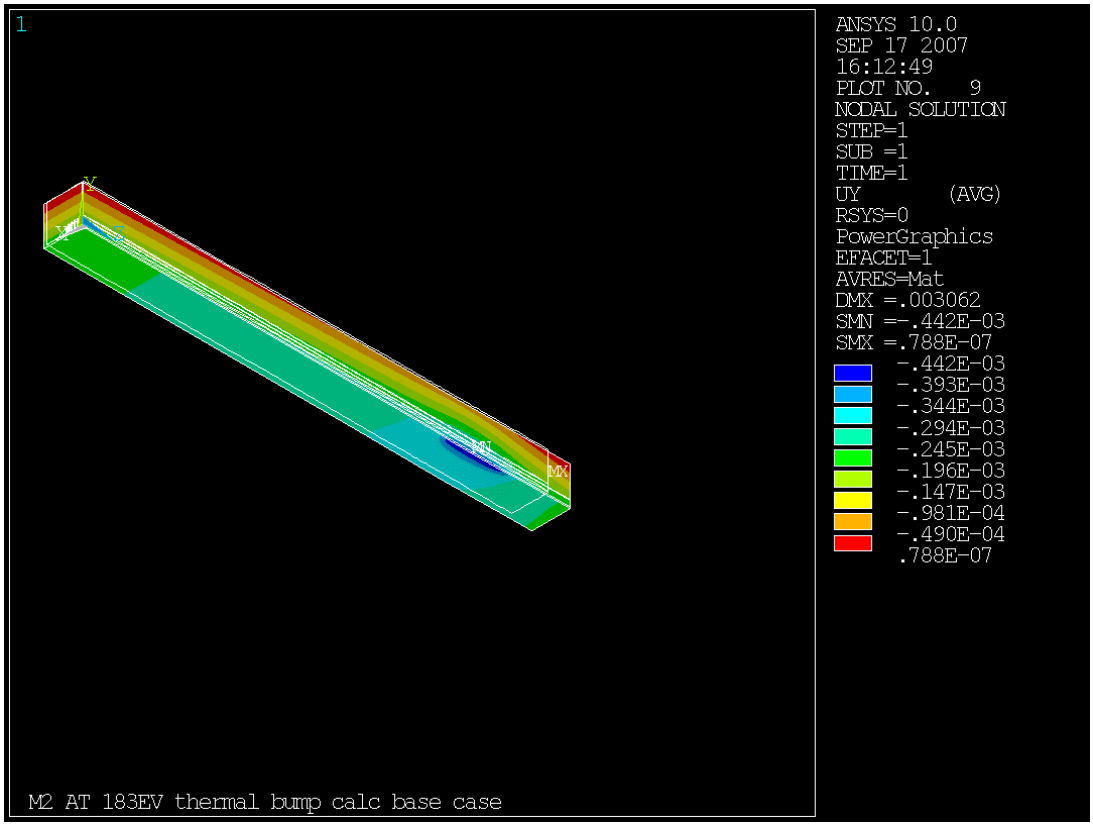

Figure 37. Displacement normal to the optical surface. Longitudinal bending and uniform thermal expansion dominate in producing the gross deflections.

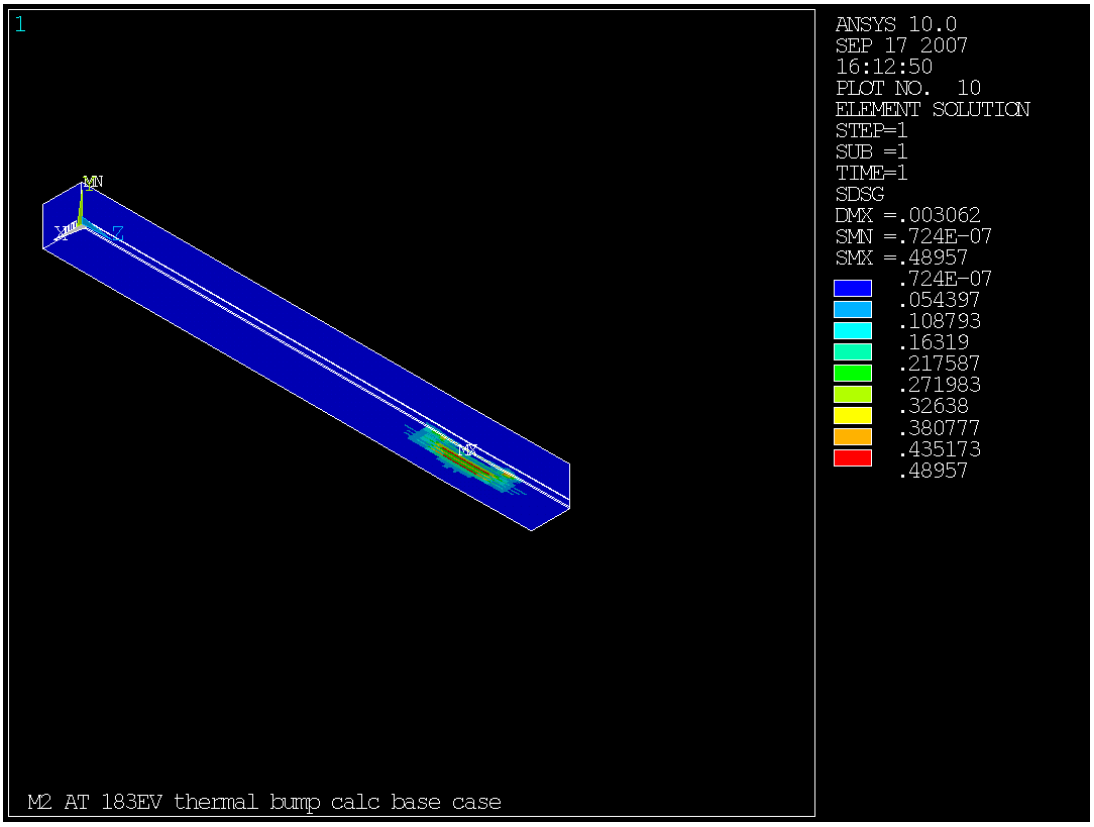

Figure 38. Absolute value of the maximum variation of any nodal stress component. Magnitude is high enough that calculated stresses should be regarded as very approximate.

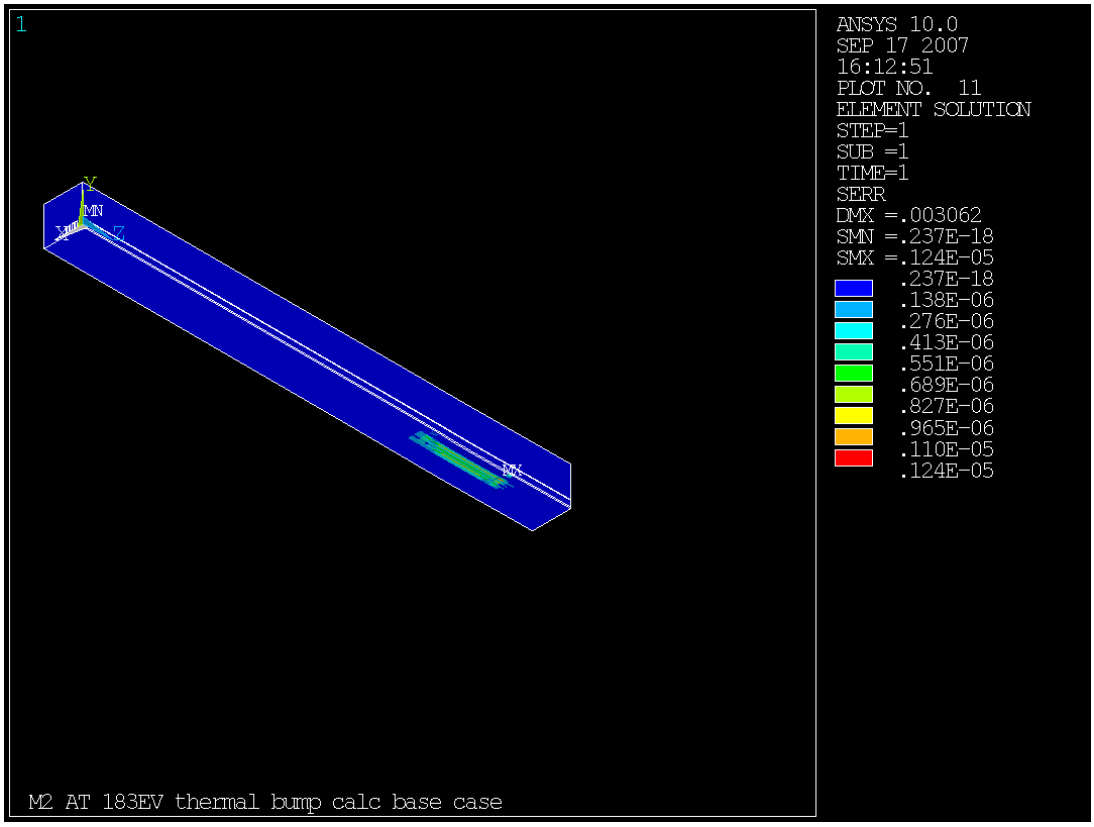

Figure 39. Energy error for the elements.

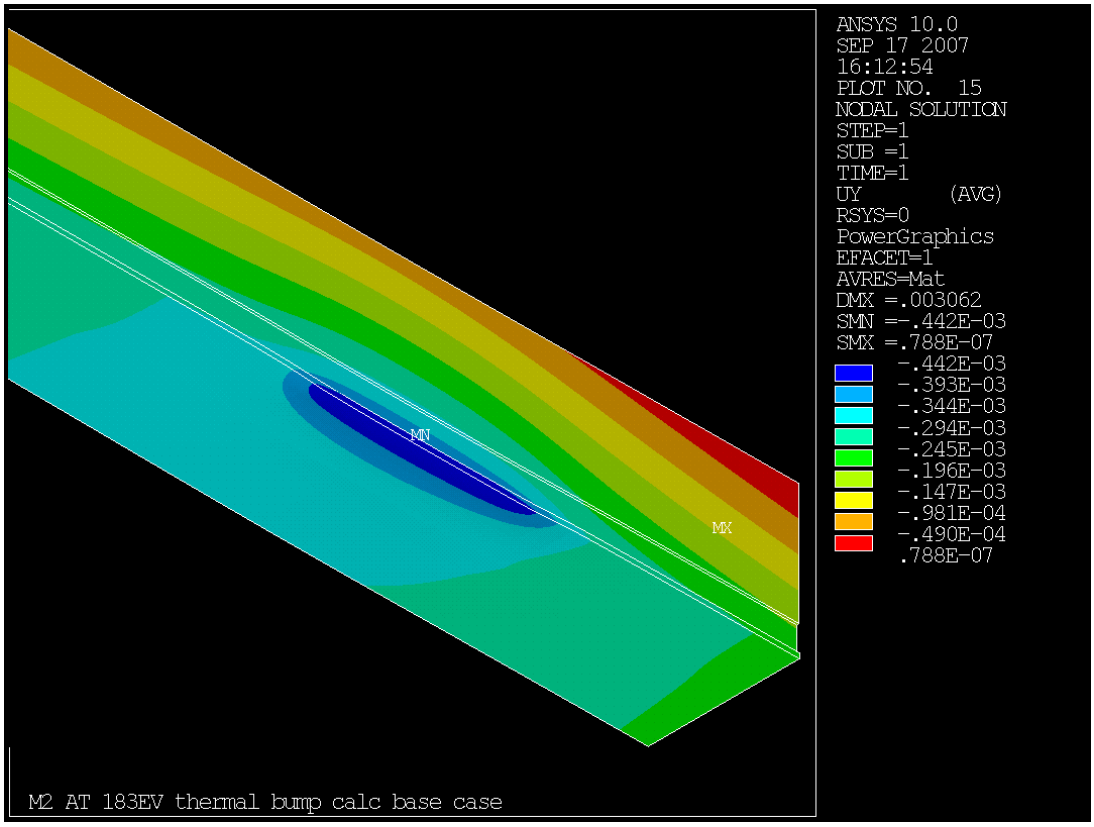

Figure 40. Displacements normal to optical surface at heat load and downstream end.

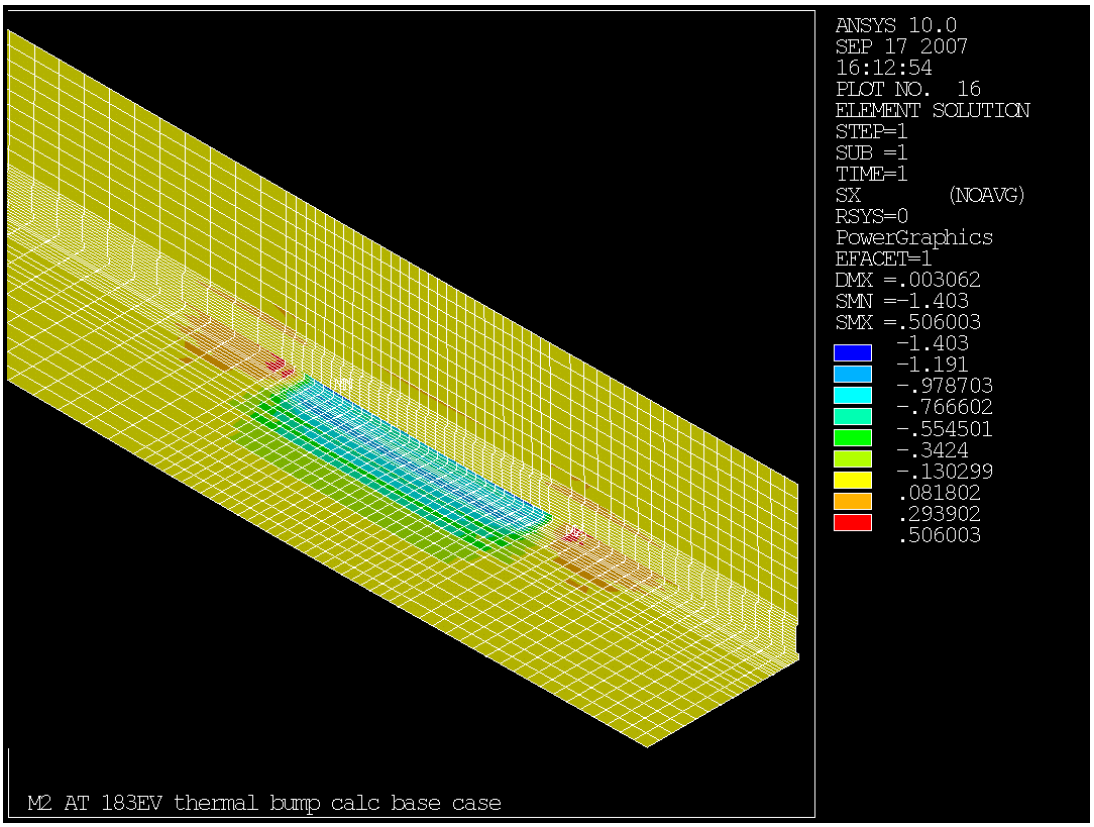

Figure 41. X axis stresses.

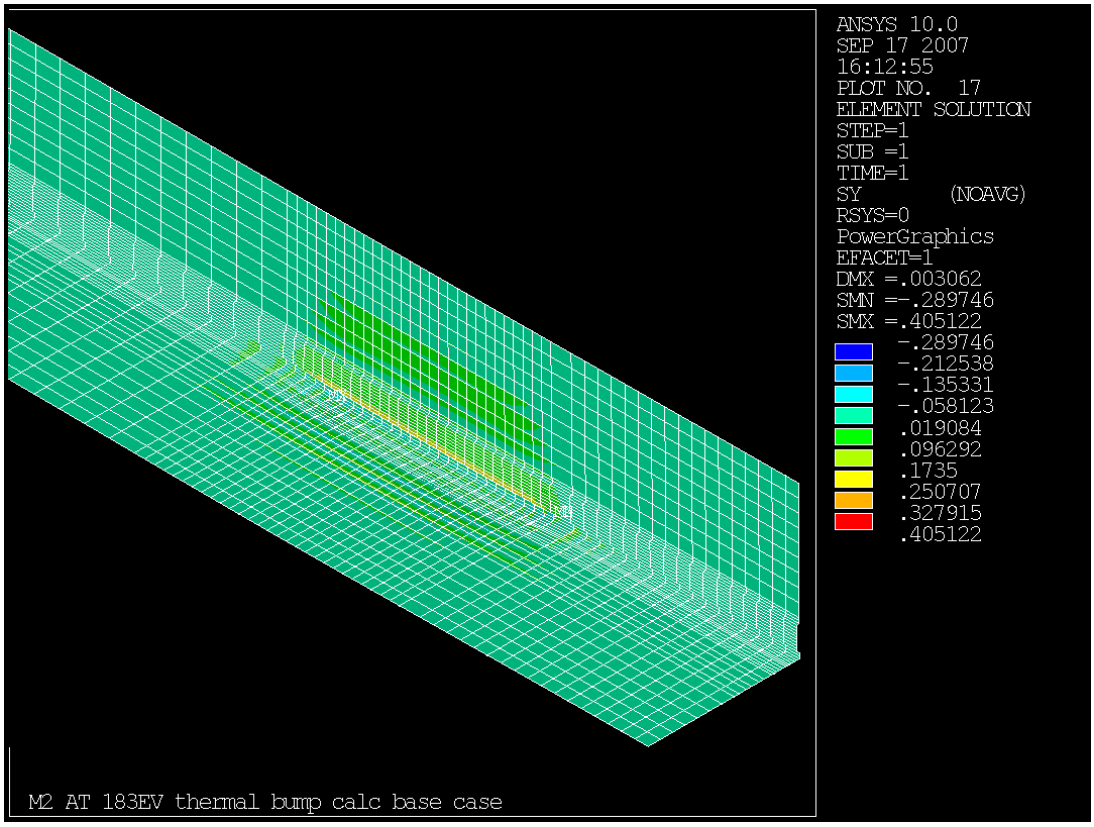

Figure 42. Y axis Stresses.

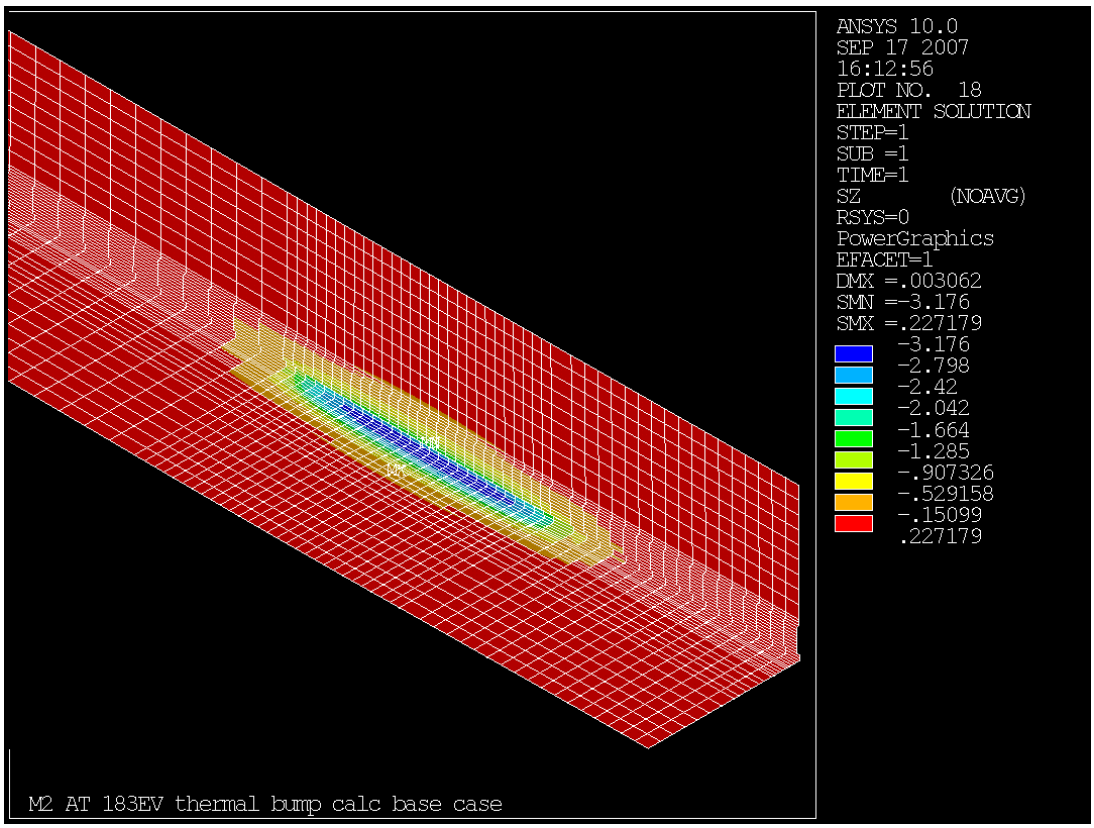

Figure 43. Z axis stresses. Contours resemble the temperature contours and the surface normal displacements.

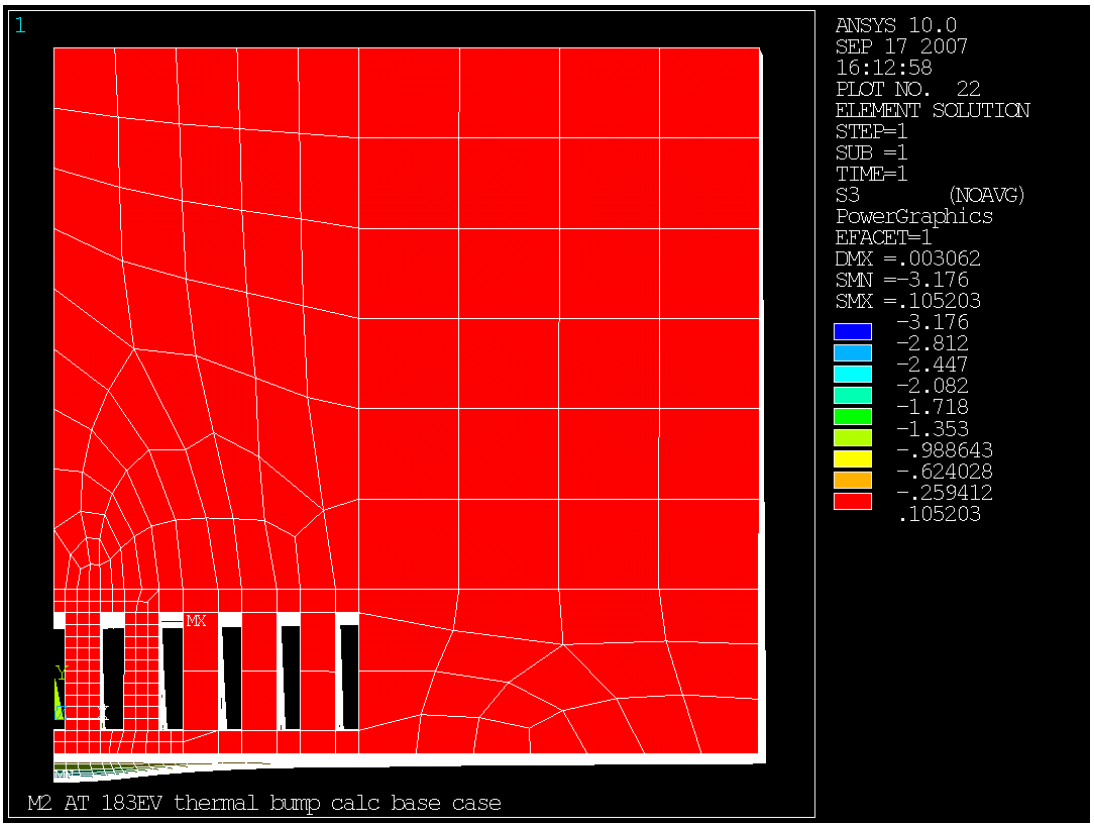

Figure 44. Third principal stress.

ANSYS path plots were generated for meridional and sagittal displacement and slope, with 380 points per meridional and 300 per sagittal plot. Small point counts (even considerably above the ANSYS default) result in the peak value of slope being understated in the path plots. The high count needed to represent the peak seems to introduce artifacts elsewhere in the sagittal slope plots.

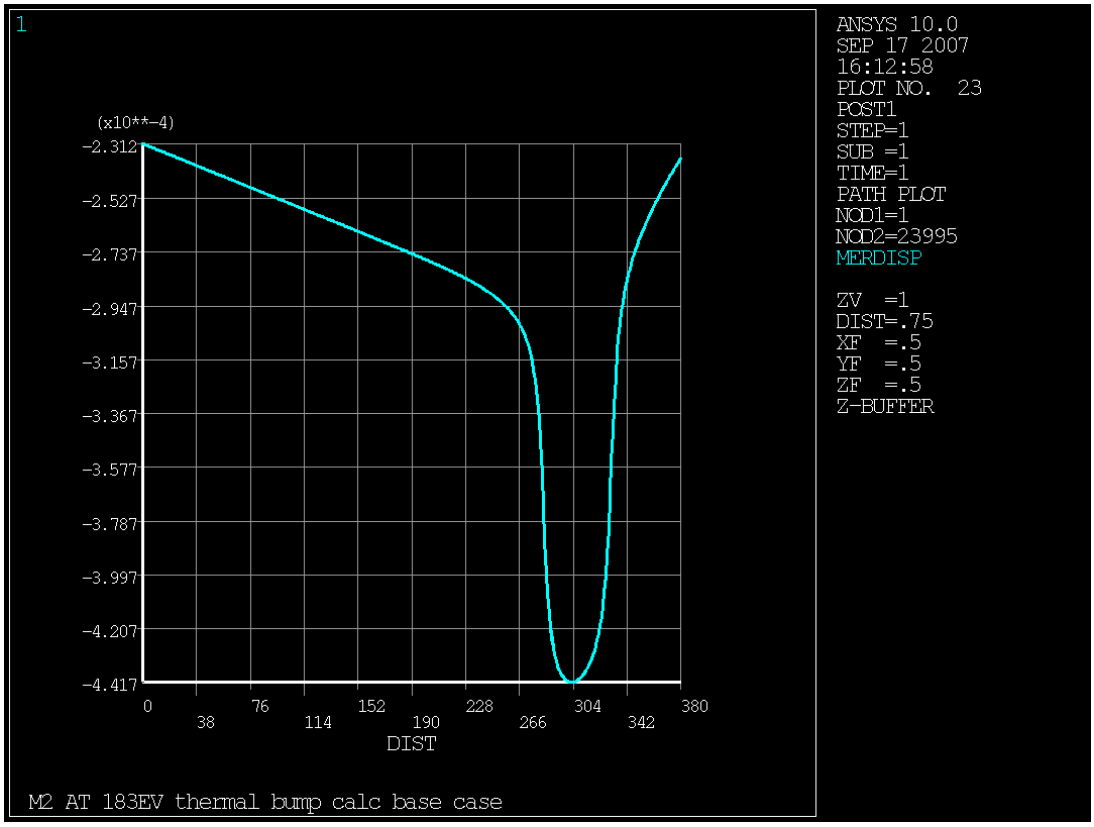

Figure 45. Meridional displacement plot, mm. Displacement is unequal at the two ends because the Z=380mm end is warmer than the z=0mm end. Peak displacement occurs shifted upstream from heat center for geometrical reasons.

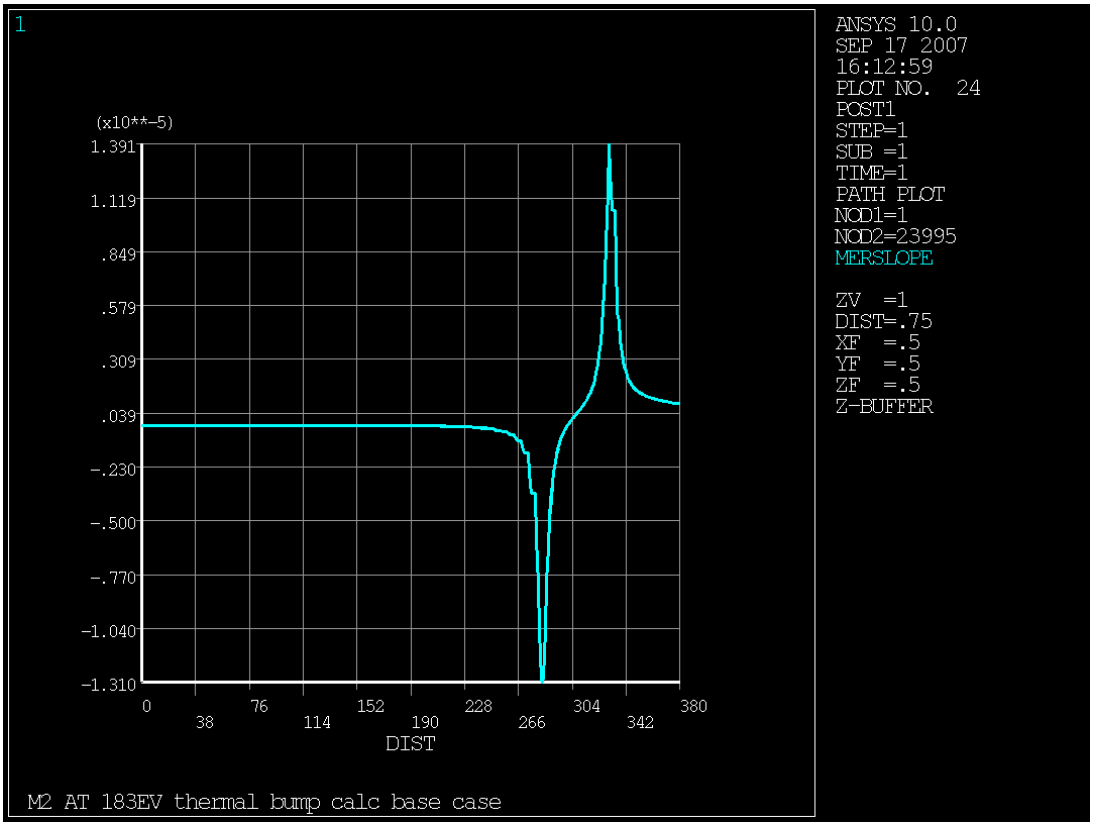

Figure 46. Meridional slope plot, radians. High curvature peaks occur at the front and back edges of the heat input area. The central slope is correctable but the end peaks are problematic.

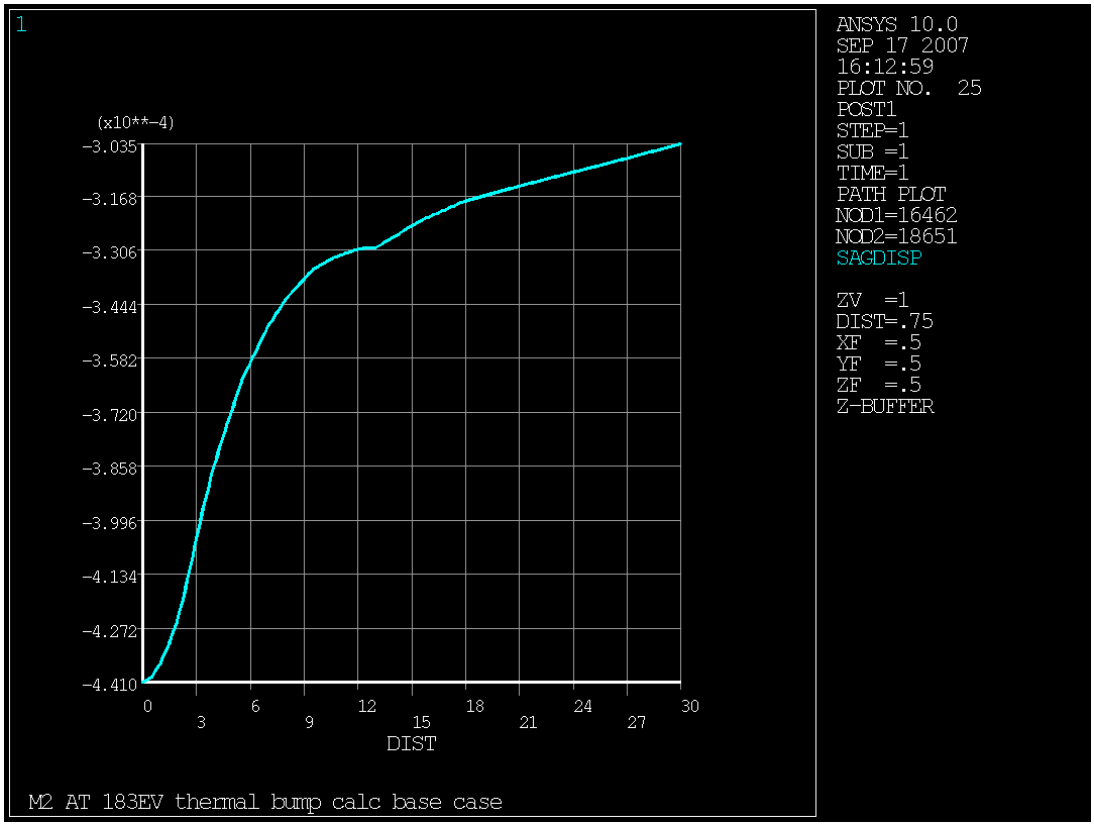

Figure 47. Sagittal displacement (mm) plot on path across midpoint of heat spot (Z=307mm). The range from 0 to 2.7mm is of interest for correction and appears highly correctable.

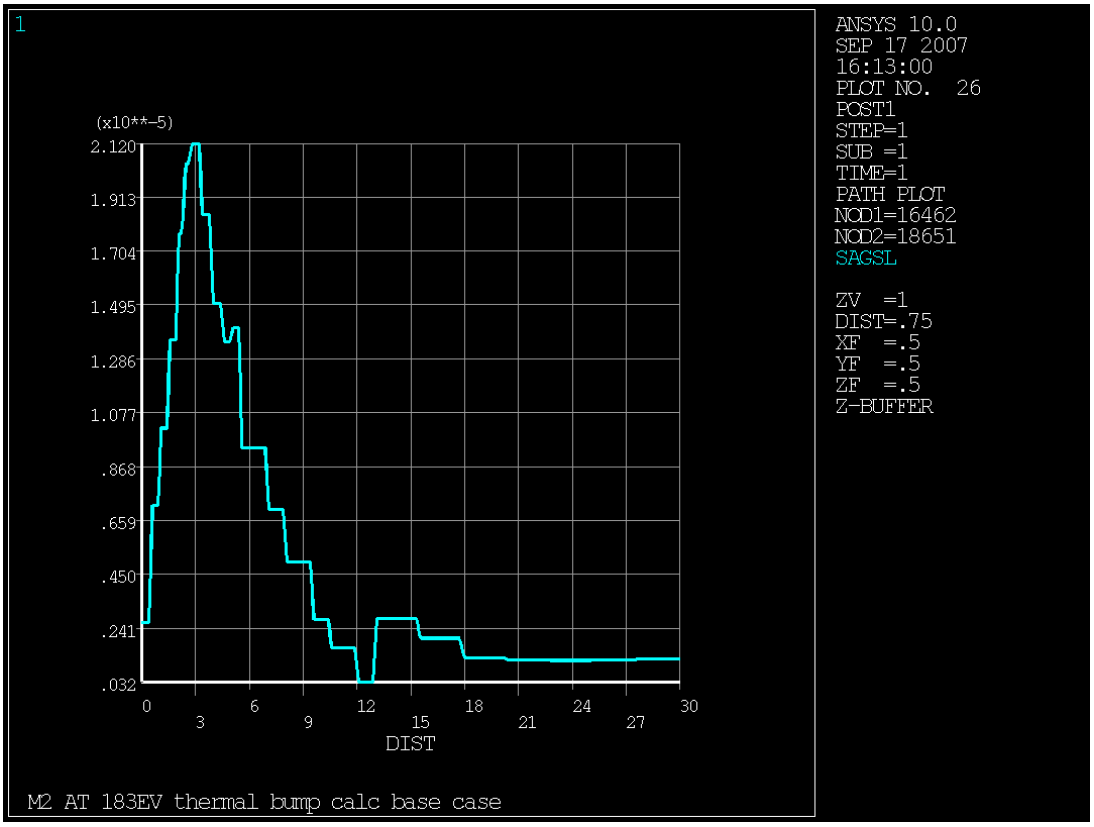

Figure 48. Sagittal slope (radians) on path through midpoint of heat spot (Z=307mm).

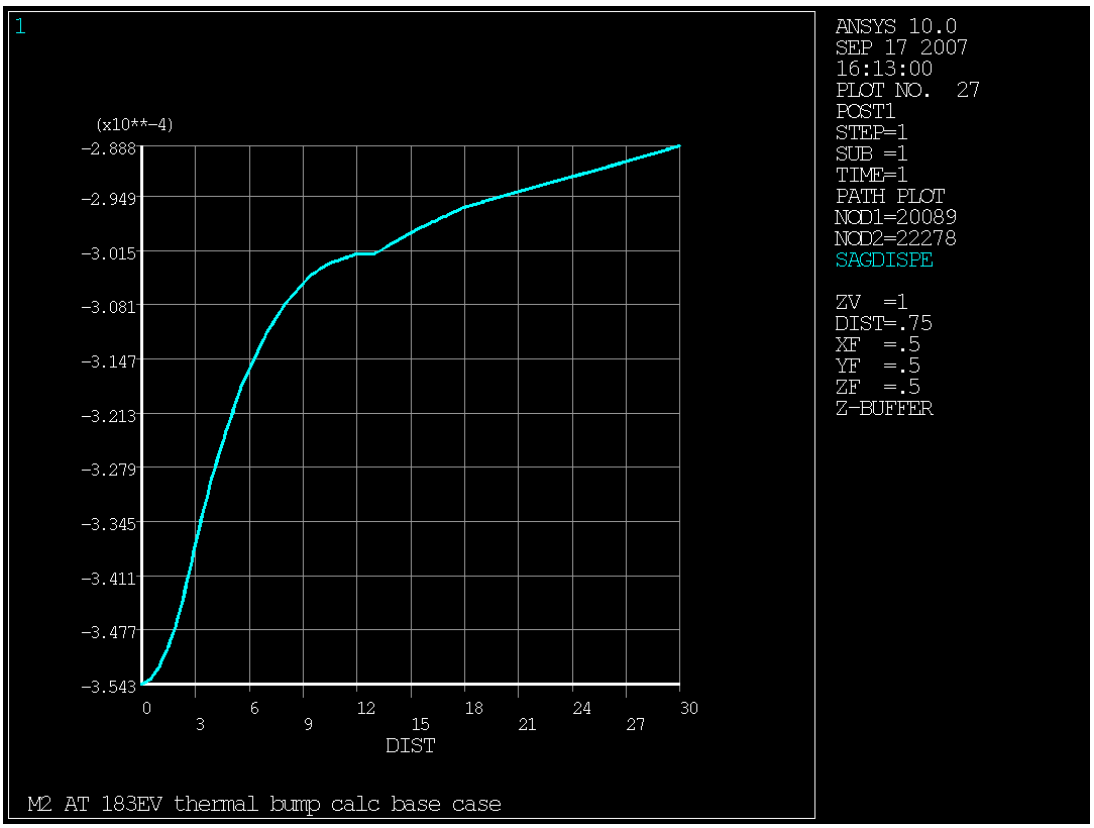

Figure 49. Sagittal displacement on path at downstream edge of heat spot (Z=331mm).

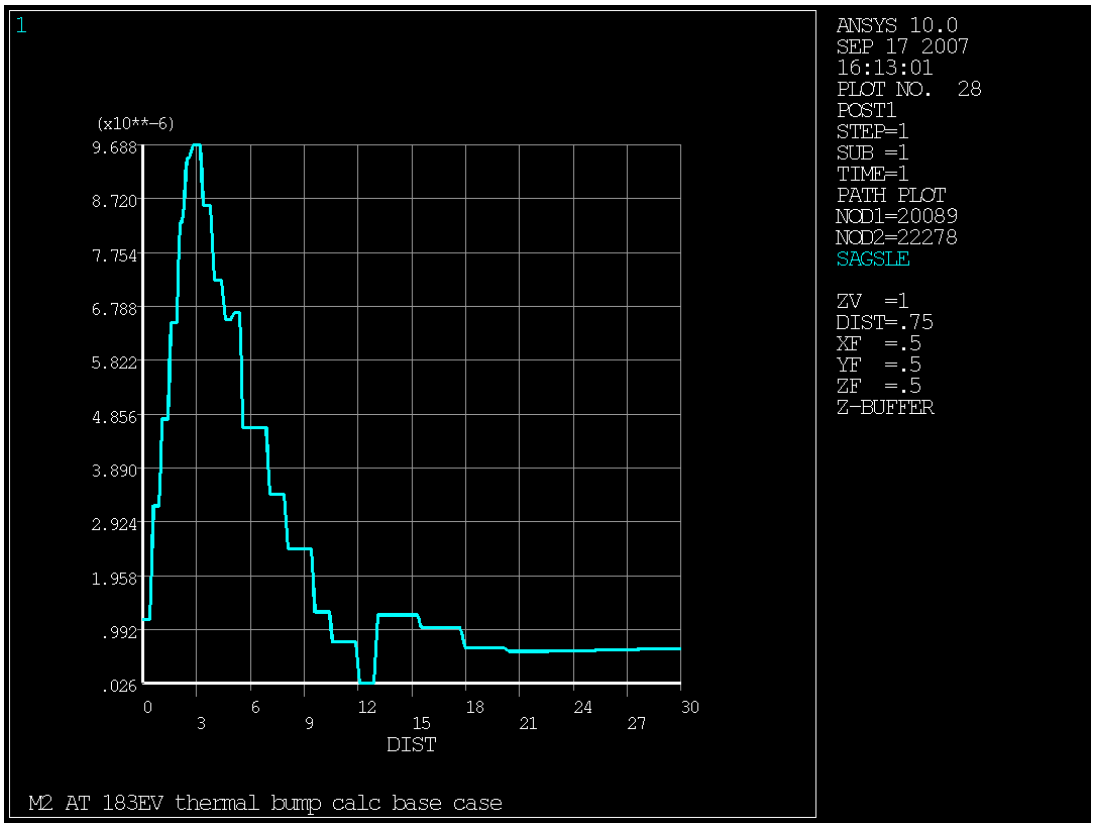

Figure 50. Sagittal slope on path at downstream edge of heat spot (Z=331mm). Note the peak slope is less than half the midpoint peak.

The resulting meridional and sagittal displacements were incorporated into a spreadsheet for analysis of slope and possibilities of compensation. It was determined the standard deviation of meridional slope after second order compensation was still several times too high, but central sagittal slope could be adequately compensated. Runs with a much thicker substrate (100 rather than 30mm) and with 3 fins rather than 5 were made. The 3-fin case showed minor changes in slope variation, with almost all parameters favoring the 5-fin case.

Subsequently a mesh refinement run was made on the base 5-fin case, and the resulting illuminated-surface displacements provided for ray tracing the deformed optic. Displacement and slope values matched within 11 percent between the base and refined runs, while temperature rise matched within one percent, giving confidence in the mesh quality. The ray tracing results predicted adverse effects on beam spot size downstream, confirming the conclusion from the spreadsheet based slope evaluation, and generating additional requests for ANSYS runs.

Some concern was expressed over the asymmetric meridional slopes and displacements such as shown in Figure 16. A model qualification run was made with the heat spot moved to centered axially at z=190mm. The resulting midpoint meridional slope was about -0.504×10^{-17} radians, 10^{-10} times lower than the absolute magnitudes of slope at z=189 and z=191mm, an excellent degree of symmetry. Some very small asymmetry is present since the difference between bulk coolant temperature and material reference temperature leads to axial expansion overall, and the structural constraint applied axially is at the Z=0mm (upstream) end. This would displace the midpoint about 0.5 micron downstream. At a rate of change of slope of 0.50295×10^{-7} radians/mm that is a tiny effect but still a much larger effect than the calculated asymmetry referenced to the midpoint. The asymmetry in slopes and displacements relative to heat spot midpoint is actually expected and necessary, as shown in the following figure.

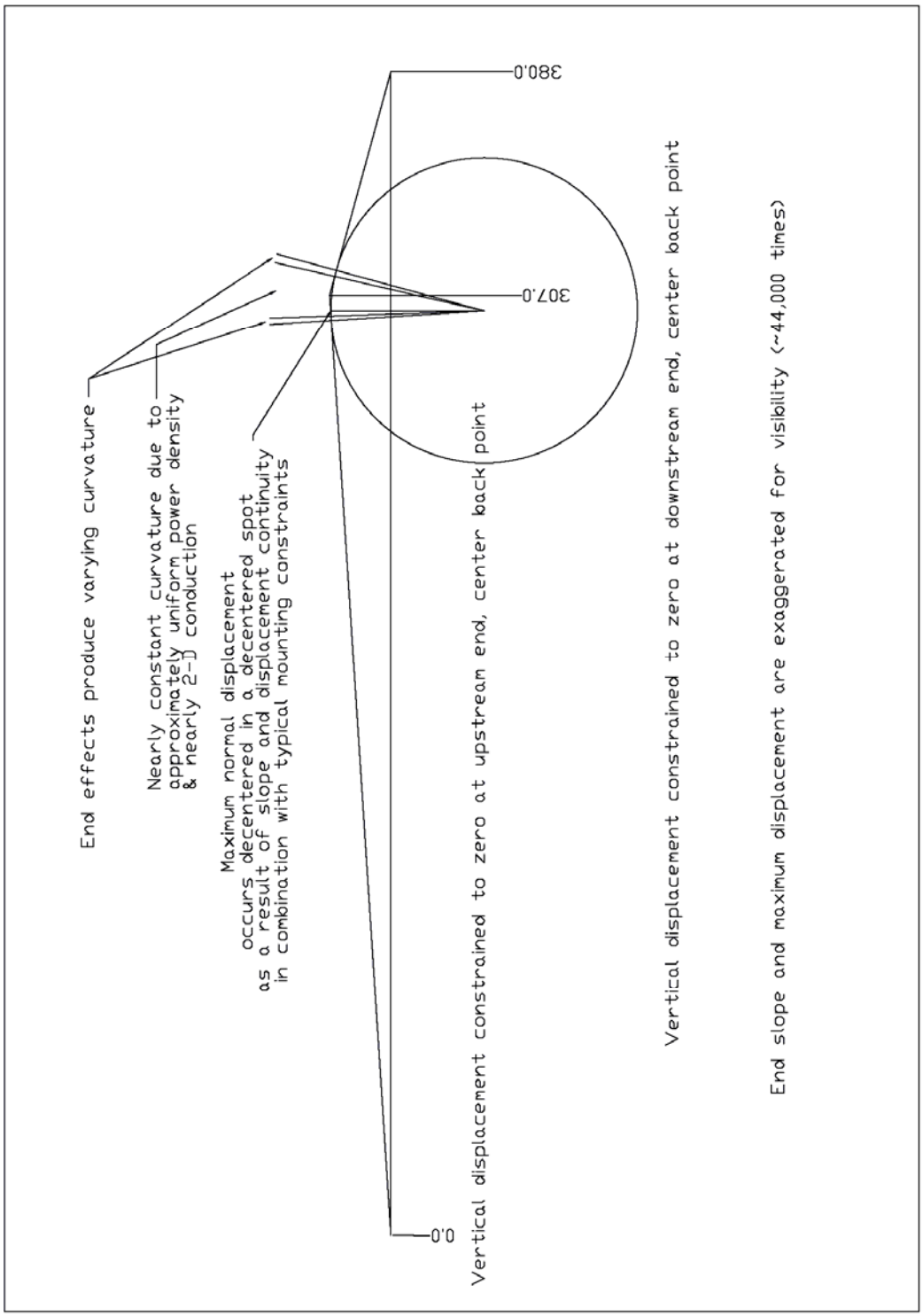

Figure 51. Asymmetric thermal load location generates asymmetric slopes and end displacements. Here the M2 optic is idealized as a slender bar with thermal bending over a segment.

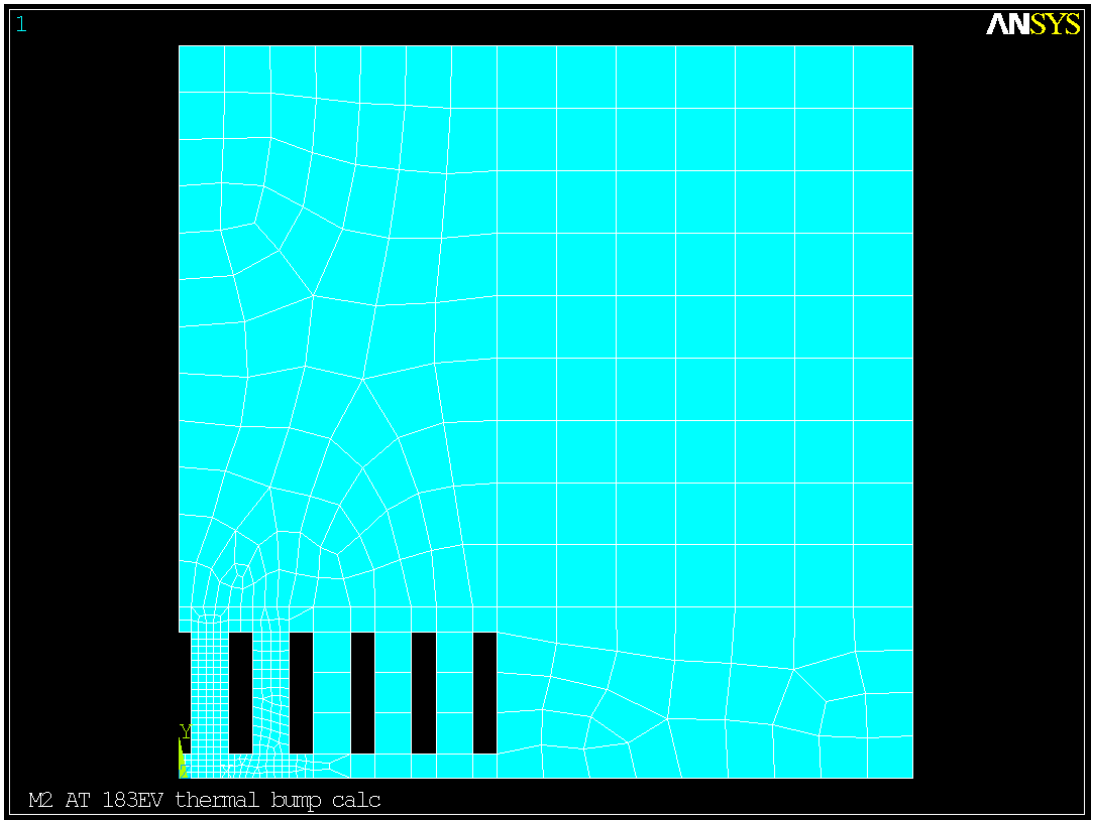

Figure 52. Refined mesh end view. The axial mesh spacing was also refined.

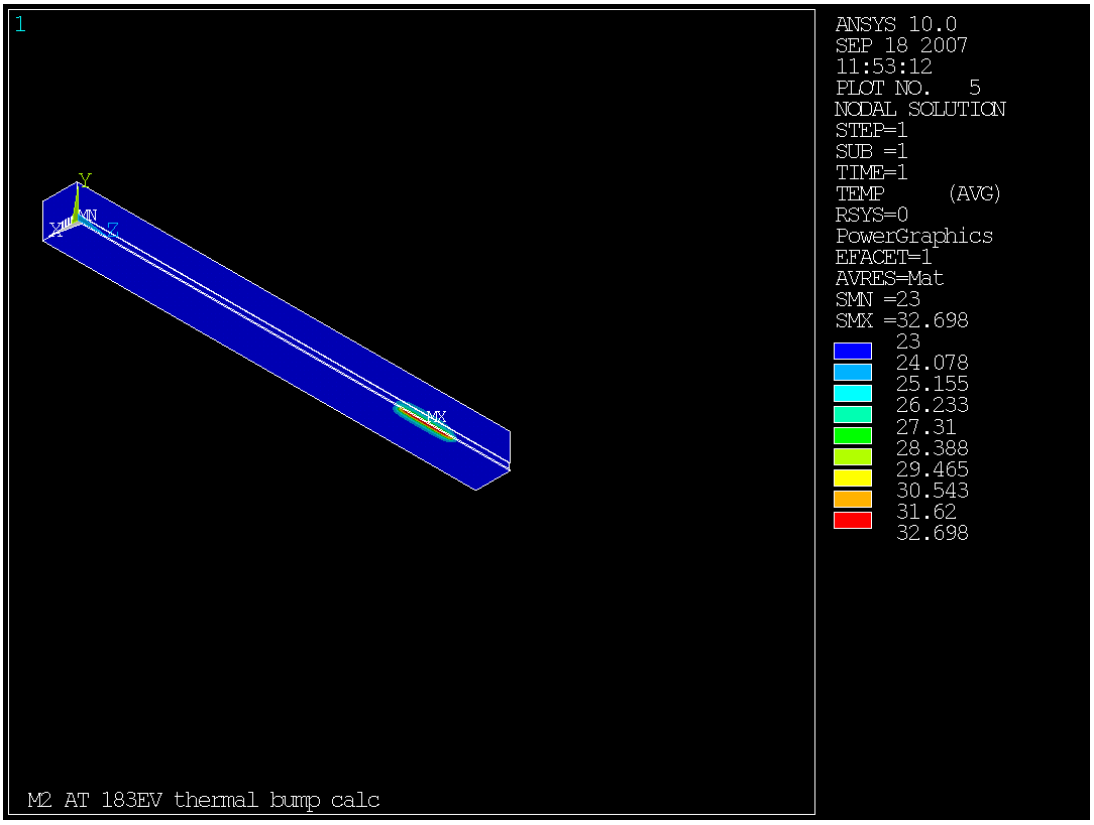

Figure 53. Maximum temperature rise above coolant bulk temperature with the refined mesh is 0.9% higher than coarse mesh run for same geometry & load case.

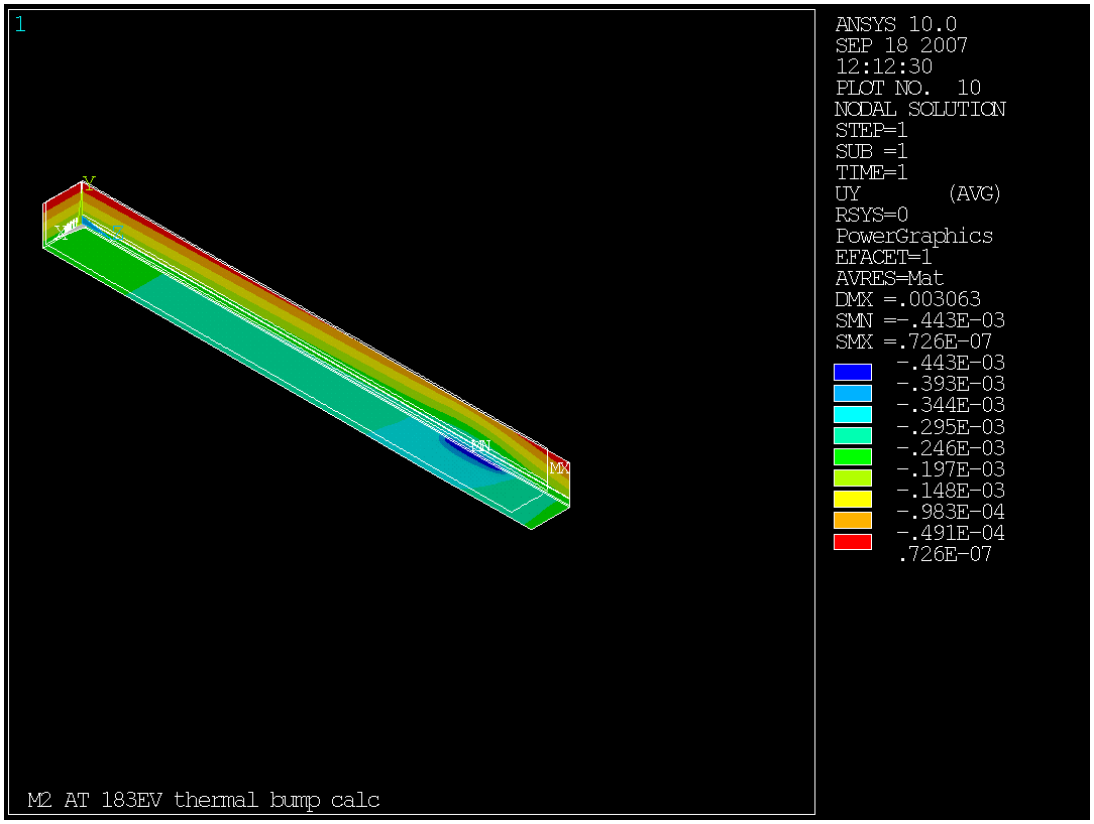

Figure 54. Refined mesh displacement in direction normal to the optical surface.

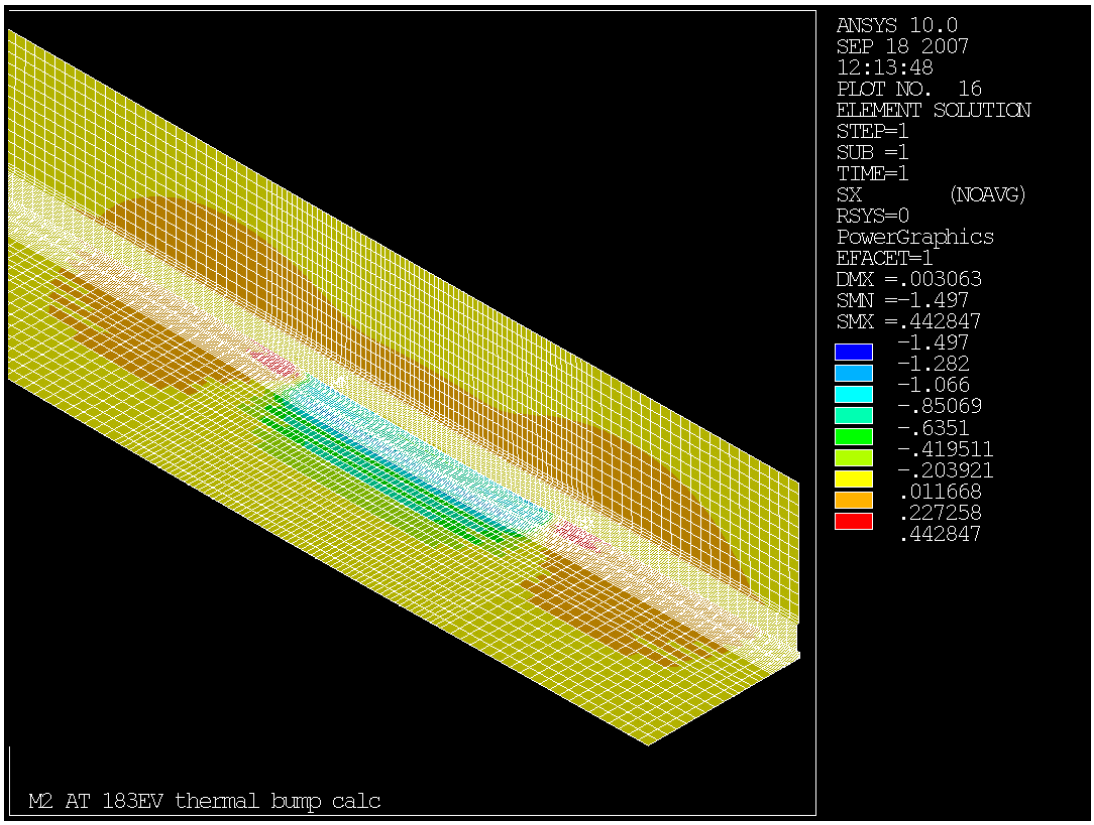

Figure 55. Refined mesh X axis stress.

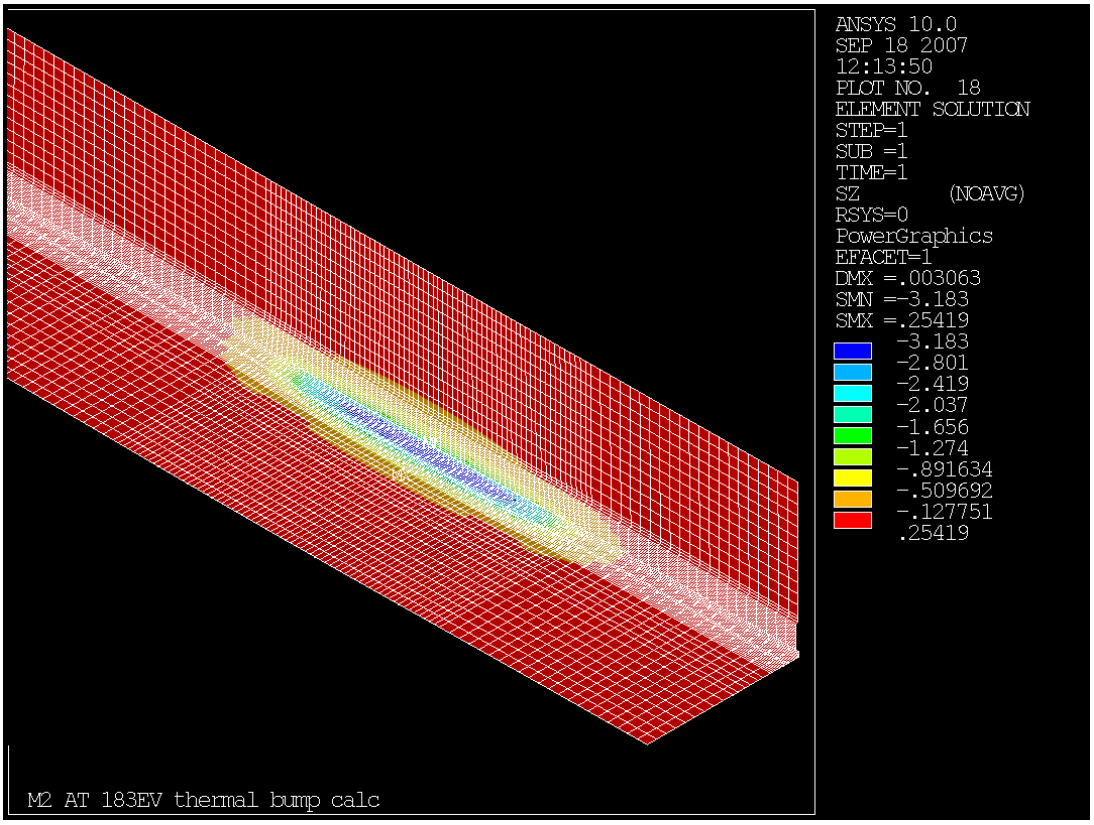

Figure 56. Refined mesh Z axis stress.

Table 2. Comparison of coarse and refined mesh 5-fin runs. The difference in slopes is largest at the edge sagittal value, at 11%.

Parameter	Coarse run	Refined run
Peak temperature, °C	32.612	32.698
Maximum displacement (which is axial), microns	3.062	3.063
Maximum normal displacement, microns	0.44175	0.44266
Maximum SDSG	0.48957	0.46697
Maximum SERR	0.124E-05	0.406E-06
SX extremes, N/mm^2	-1.403, 0.506	-1.497, 0.4428
SY extremes, N/mm^2	-0.2897, 0.4051	-0.3808, 0.3995
SZ extremes, N/mm^2	-3.176, 0.2272	-3.183, 0.2542
S3 extremes, N/mm^2	-3.176, 0.1052	-3.183, 0.0971
Meridional displ & slope, mm & microradians max	0.0004417, 13.91	0.0004426, 15.333
Central sagittal displ & slope, mm & microradians max	0.0004410, 21.2	0.0004419, 22.0
Edge sagittal displ & slope, mm & microradians max	0.0003543, 9.688	0.0003569, 10.77

Table 3. Comparison of 5-fin and 3-fin coarse mesh runs.

Parameter	Coarse 5-fin run	Coarse 3-fin run
Peak temperature, °C	32.612	32.679
Maximum displacement (which is	3.062	3.14

axial), microns		
Maximum normal displacement, microns	0.44175	0.457
Maximum SDSG	0.48957	0.69396
Maximum SERR	0.124E-05	0.146E-05
SX extremes, N/mm^2	-1.403, 0.506	-1.559, 0.4377
SY extremes, N/mm^2	-0.2897, 0.4051	-0.2710, 0.4281
SZ extremes, N/mm^2	-3.176, 0.2272	-3.156, 0.1867
S3 extremes, N/mm^2	-3.176, 0.1052	-3.156, 0.1442
Meridional displ & slope, mm & microradians max	0.0004417, 13.91	0.0004564, 13.99
Central sagittal displ & slope, mm & microradians max	0.0004410, 21.2	0.0004558, 20.86
Edge sagittal displ & slope, mm & microradians max	0.0003543, 9.688	0.0003683, 9.992

A requested run was with the length of heat spot increased from 48.046mm overall to 68mm overall. This was performed with the refined mesh.

Table 4. Comparison of refined mesh 5-fin base and extended heat spot runs.

Parameter	Refined base run	Extended spot run
Peak temperature, °C	32.698	32.719
Maximum displacement (which is axial), microns	3.063	3.111
Maximum normal displacement, microns	0.44266	0.472
Maximum SDSG	0.46697	0.45927
Maximum SERR	0.406E-06	0.421E-06
SX extremes, N/mm^2	-1.497, 0.4428	-1.476, 0.4559
SY extremes, N/mm^2	-0.3808, 0.3995	-0.3747, 0.3985
SZ extremes, N/mm^2	-3.183, 0.2542	-3.233, 0.2575
S3 extremes, N/mm^2	-3.183, 0.0971	-3.233, 0.0980
Meridional displ & slope, mm & microradians max	0.0004426, 15.333	0.0004721, 15.82
Central sagittal displ & slope, mm & microradians max	0.0004419, 22.0	0.0004697, 21.94
Z=331 sagittal displ & slope, mm & microradians max	0.0003569, 10.77 (downstream edge)	0.0004384, 21.54 (at Z=331, 10mm inside downstream edge of extended spot)

Extension of the heat spot lengthens the roughly cylindrical central portion of the normal displacements, improving the correctability of the distortions as intended. Normal displacements were provided to ray tracing to verify that.

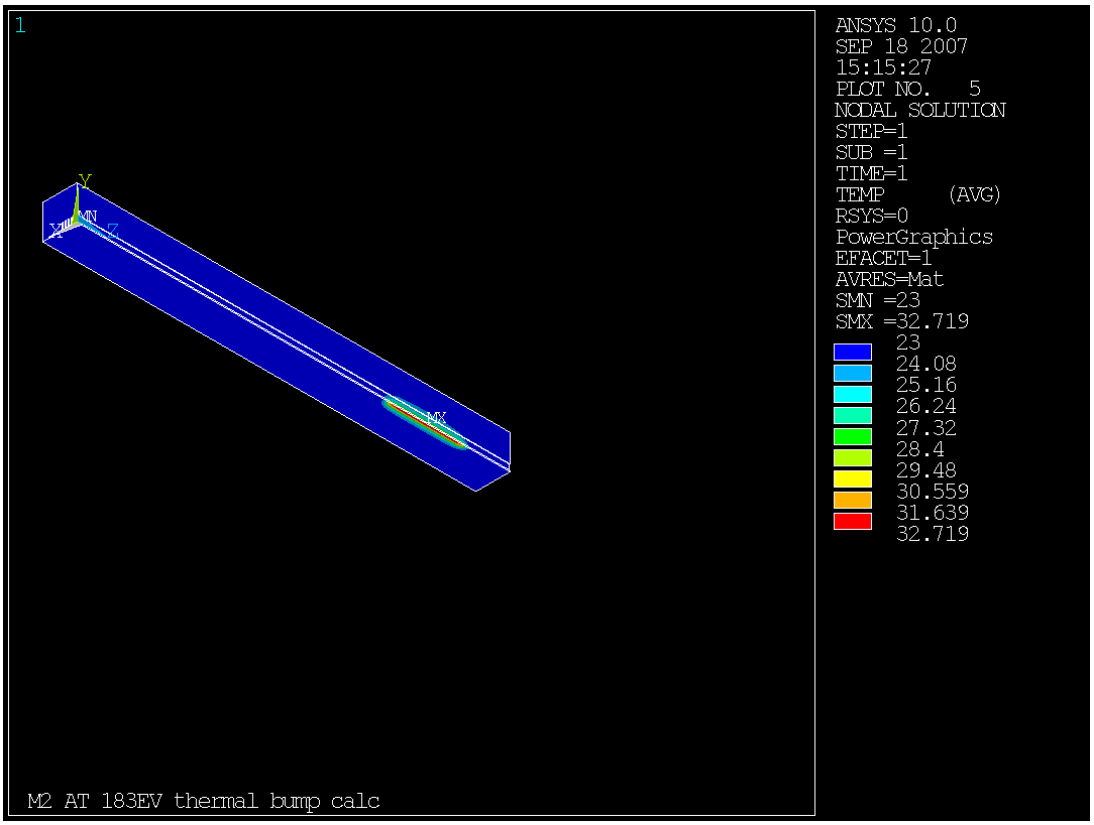

Figure 57. Temperature response of refined mesh 5-fin case with extended heat spot.

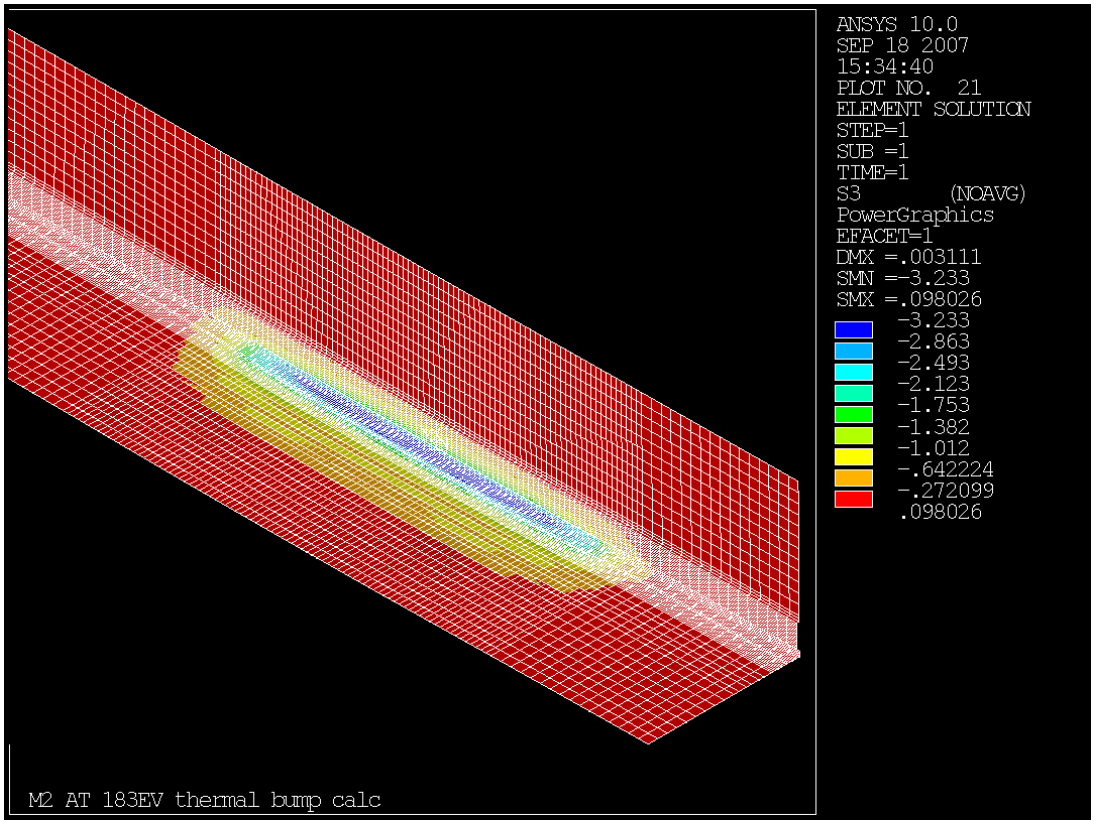

Figure 58. Refined mesh 5-fin case with extended heat load, showing third principal stress with mesh outline superimposed.

Stiffening the optic with a significantly thicker substrate appears to have only minor effects on slope, with 6% lower meridional slope and 6.3% higher edge sagittal slope.
Some results of the 100mm thick substrate case are shown below.

Table 5. Comparison of 100mm thick substrate to 30mm thick.

Parameter	30mm	100mm
Peak temperature, °C	32.612	32.604
Maximum displacement (which is axial), microns	3.062	3.149
Maximum normal displacement, microns	0.44175	0.962
Maximum SDSG	0.48957	0.5159
Maximum SERR	0.124E-05	0.109E-05
SX extremes, N/mm^2	-1.403, 0.506	-1.45,0.428
SY extremes, N/mm^2	-0.2897, 0.4051	-0.266, 0.4041
SZ extremes, N/mm^2	-3.176, 0.2272	-3.222,0.2055
S3 extremes, N/mm^2	-3.176, 0.1052	-3.222,0.0982
Meridional displ & slope, mm & microradians max	0.0004417, 13.91	0.000962, 13.08
Central sagittal displ & slope, mm & microradians max	0.0004410, 21.2	0.000962, 21.22
Edge sagittal displ & slope, mm & microradians max	0.0003543, 9.688	0.0008911, 10.30

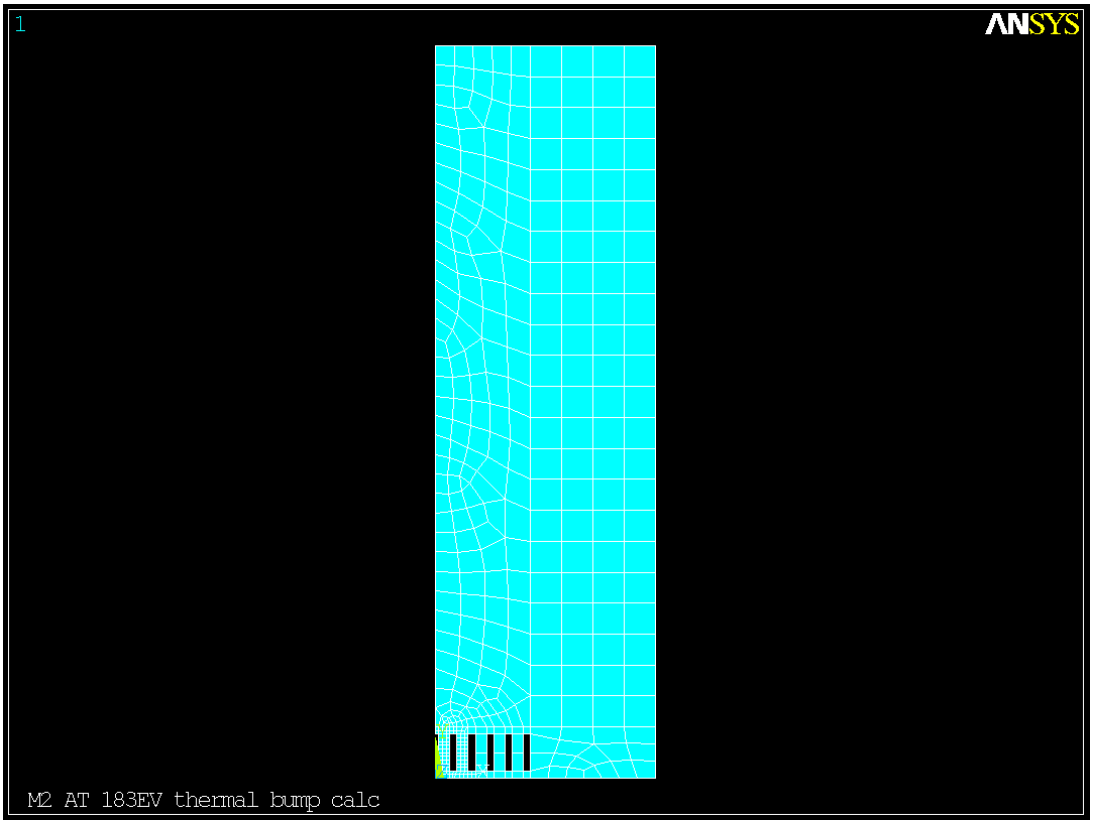

Figure 59. End view of mesh on 100mm thick case.

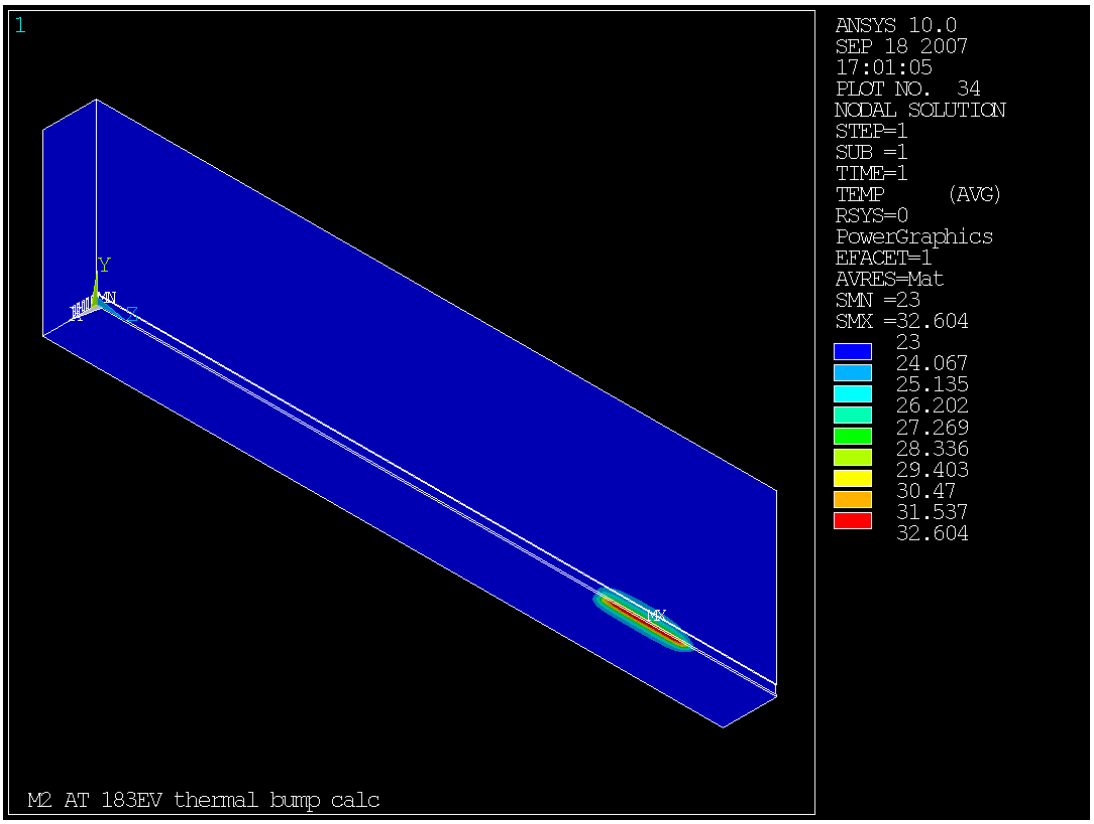

Figure 60. Resulting temperature solution.

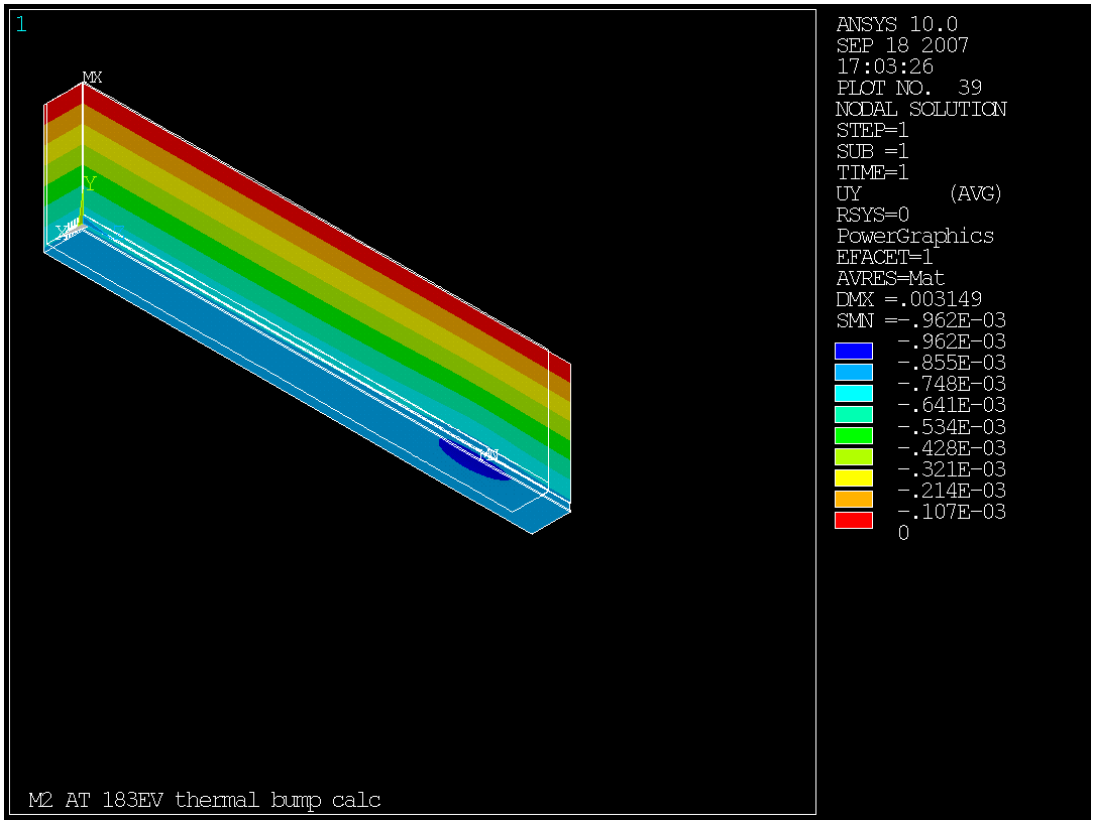

Figure 61. Displacement normal to the optical surface for 100mm thick substrate.

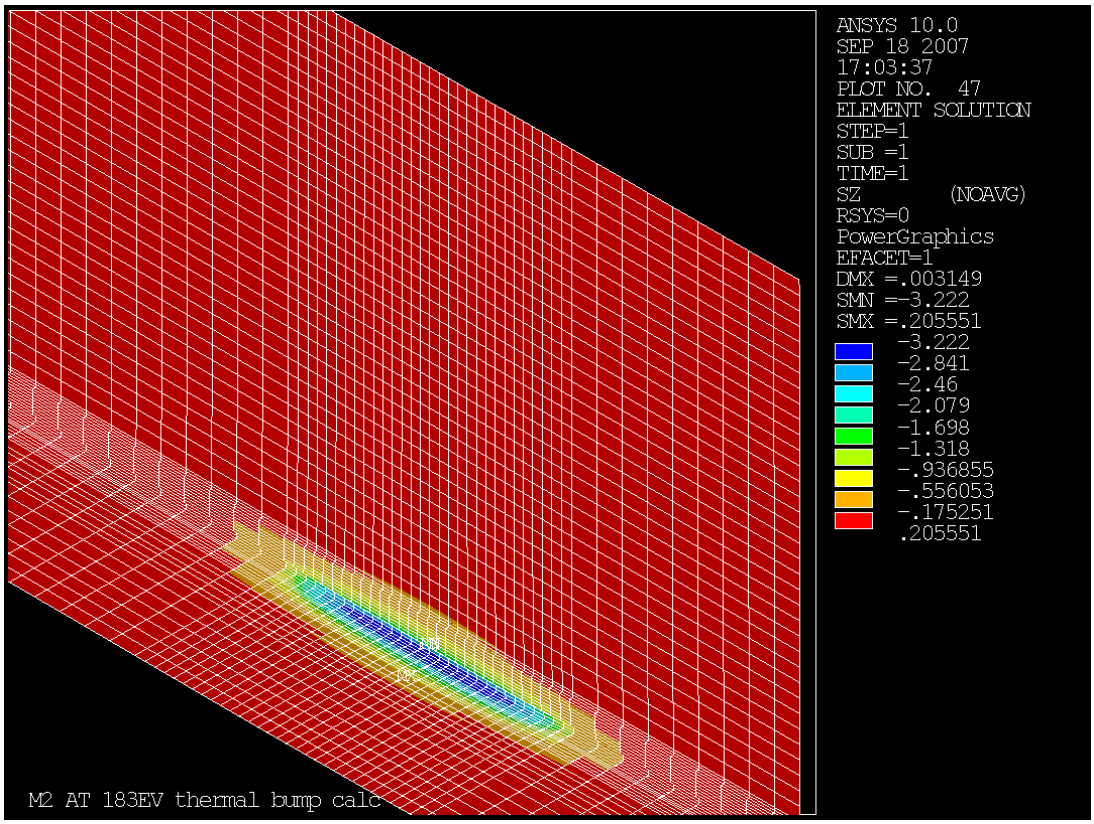

Figure 62. Z axis stress for 100mm thick substrate.

Summary

The M2 183eV operating case was selected for analysis as an expected worst case and determined to generate excessive distortion of the optical surface. A workaround was proposed, and simulated in ANSYS and in ray tracing, providing verification the workaround is sufficient to preserve optical figure at M2.

The 3-D parametric ANSYS model is adaptable to running many load and geometry cases. It still contains many approximations some of which should be removed in future design effort. With modification to handle generalized power density distributions, it will be applicable to additional optical elements in the beamline and additional beamline operating conditions. It is easily applicable to optimization studies. Variations in several variables were analyzed for effect on temperature and active optical surface shape. Evaluating surface slopes via path plots is an efficient way to forecast negative impact on ray tracing results & beamline performance.

The ANSYS outputs from differing meshes show that the temperatures and displacements reproduce well, and slopes to about 11% or better. Reproducibility of stresses is not as good; ANSYS measures of stress accuracy show that stress values from particular nodes & elements should not be relied on, as the values at a given node differ significantly among elements that have that node in common. However, the extreme values and the ranges of stress obtained reproduce reasonably well, and the extreme values are low in all cases. Peak thermal stresses obtained to date are low, below the level requiring acid etch. Stress concentrations and additional loads have not yet been examined. Uniform thermal expansion from reference temperature to (the slightly elevated) bulk coolant temperature is very significant in the overall displacement. These displacements were obtained with constraints applied at worst case locations (extreme ends of back surface) maximizing bulk expansion response and the effect of thermal bending on peak displacement. Real mirror mounting locations will straddle less than the optic's total length and so reduce the influence of thermal expansion on peak displacement. All simulation performed was steady state.

5 XAS: HARD X-RAY ABSORPTION SPECTROSCOPY

5.1 Executive Summary

This document describes the strategic need and preliminary technical design for a damping wiggler-based hard x-ray absorption spectroscopy beamline as an NSLS-II Project Beamline. It represents the synthesis of user and scientific community input, interactions with project and accelerator staff, contracted engineering reports from Accel Corporation, and technical reviews by the NSLS-II EFAC and others.

The technique of x-ray absorption spectroscopy uses each element's characteristic absorption edge(s) to obtain local (within ~10Å) information about that element. It is a non-destructive, element-specific probe of local physical and electronic structure, speciation, and chemical state. XAS measurements may be made by transmission, characteristic x-ray fluorescence, or photoelectron yield. Samples may be crystalline or amorphous, and in nearly any form (solid, liquid, gas, solution, mixture, etc.), and may be measured *in situ* under a variety of conditions.

5.2 Scientific Objectives

Mission and specifications: The mission of this beamline is twofold. One is to provide a versatile and highly productive facility for applications of hard X-ray Absorption Spectroscopy in a wide range of scientific disciplines including material science and catalysis, nanomaterials research, environmental science and geology, and life sciences and biology. This is necessary to address, from the outset of user operations, the significant demand for high-quality XAS at the NSLS. The second, and equally important, mission is to pursue cutting-edge capabilities and techniques in XAS, such as are appropriate to capitalize on the advanced qualities of the NSLS-II source. This beamline therefore is intended to outperform all currently available XAS facilities in the combined metrics of flux, versatility of spatial and energy resolution, and energy range.

Based on these objectives, beamline specifications are summarized as follows:

Source:	Damping Wiggler, length 7 m (or one of two canted 3.5-m segments)
Monochromator crystals:	LN2 cooled, flat crystals; 1st pair Si(111), 2nd pair Si(311) switchable by horizontal translation
Energy range:	~5 – 50 keV, with provisions for reaching 90 keV
Focusing:	macro: toroidal mirror, micro: K-B set
Spot size at sample:	operating values around 1mm macro- and 1 micron micro-focused, but up to 5x40 mm unfocused
Estimated photon flux at sample:	> 10^{13} – 10^{14} ph / s / 0.1% BW (10^{12} for microbeam)
Energy Resolution (standard):	dE/E 3 x 10^{-4} (Si(111))
High energy resolution mode:	1 x 10^{-5} or better, with energy-refining monochromator
Scan modes:	continuous-scan (slew) or step-and-count
Endstation 1:	microbeam XAS
Endstation 2:	bulk XAS, three sample positions: classic benchtop, controlled atmosphere, large apparatus

User need: Synchrotron XAS is a cornerstone of material and chemical analyses on the molecular scale. As such, its use has become routine and less "exciting," but not less important. A statistical analysis obtained from NSLS User Administration showed that, in FY06, 653 of 3295 on-site users at the NSLS (22.5%) were at the 8 beamlines devoted to hard XAS (and 2 beamlines performing microbeam XAS). To weigh possible overlap in these beamline-specific numbers, a manual count of unique individuals currently involved in XAS experiments yielded 505, a comparable percentage of the ~2250 current active NSLS users. These users

represent a wide range of scientific fields, are interested in nearly every element of the periodic table, and have samples ranging in size from nanometers to centimeters.

In order to benefit the greatest range of users, without compromising the more advanced capabilities and potential future directions, this beamline is equipped with versatile and adaptable endstation components founded on a solid infrastructure and beamline optics designed to deliver the highest quality (and quantity) of beam possible. These details are described more fully in the sections to follow. Efficiency is also an important aspect of productivity, so both the optical configuration and experimental setups are intended to minimize downtime. In addition, an available continuous-scan mode, rather than more typical step-and-count measurement, will significantly enhance throughput.

Scientific opportunities: Current challenges facing application of XAS in more difficult systems are signal strength, fluorescence detection, spatial and energy resolution, time, and energy range. The status of XAS as a more mature technique has left many with the impression that there is nothing new to develop. However, the unparalleled qualities of the NSLS-II open the door to considering new aspects of the technique (e.g. higher energy resolution) and new applications.

The very high flux available will make possible measurements at lower concentrations and using smaller sample mass. This is important in the study of catalysts, environmental contaminants, dispersed nanoparticles, and dilute biological systems. It will also enable “bulk” measurements of very small quantities of material, such as atmospheric particulates and marine colloids, extraterrestrial material, proteins and biological complexes, and sub-monolayer surface adsorbates.

Many problems in XAS analysis are the result of detector-limited fluorescence measurements. For example, an energy-dispersive solid state detector has intrinsic limits of energy resolution and total count rate. Samples with very low target signal and very high background will saturate the detector before enough useful signal is obtained. Interfering fluorescences can similarly overwhelm a weak signal. Increasing flux alone will exacerbate these problems. However, the considerably higher flux available here will enable the use of energy-selective detectors, such as wavelength-dispersive detectors or crystal analyzers. Historically these have not been widely used because they can only accept a very small fraction of the fluorescence emanating from the sample, and therefore required very high sample concentrations. The NSLS-II XAS beamline will provide sufficient flux to use energy-selective fluorescence detectors at trace concentrations. Recent advances in detector technology have made tremendous improvements and are expected to continue to do so. These further developments will be incorporated in the final design to add to the capabilities of this beamline.

Spatial resolution is the primary goal of the nanoprobe beamline. However, XAS experiments cover the whole range of spatial resolution from nm on up. Therefore this beamline is designed with an adaptability of spot size, from unfocused 5x40 mm down to as small as 200x200 microns in the “bulk” endstation, and down to ~1 micron in the microbeam endstation. Many XAS experiments involve processes occurring on a range of spatial scales, but have previously been relegated to separate bulk and micro facilities. Tunability of spot size at a single facility will allow users to better tailor measurements to their needs.

Energy resolution is most important for near-edge XAS structure (referred to as XANES or NEXAFS), where there may be sharp features that are highly sensitive to local electronic structure. These features, such as the pre-edge peak of hexavalent chromium (K edge 5.9 keV), the arsenate peak (As K edge at 12 keV), or pertechnetate (Tc K edge at 21 keV), are narrower than, or exhibit chemically-induced shifts of less than, the best resolution of a Si(311) monochromator. Yet methods of producing higher-resolution monochromatic beams are less efficient and naturally have lower bandpass, and thus have significantly decreased flux as compared with more typical energy resolution monochromators. The high flux and well-collimated beam available at NSLS-II afford the luxury of employing an energy-refining monochromator to accomplish these measurements even at trace concentrations.

Time-resolved experiments are naturally facilitated by high flux. While it will not be possible to move this high-heatload monochromator fast enough for true “quick” XAS (sub-second scan rate), the continuous-scan mode will collect scans on the order of one to three minutes, for time-resolved experiments on the appropriate scale.

Energy range has been a limiting factor in XAS applications. X-ray Absorption edges range from the soft x-ray regime to over 100 keV, while typical Synchrotron hard XAS facilities operate between 4.5 and 30 keV. The 5-90 keV range listed above encompasses the K edges of chromium to bismuth, and L edges of cesium through americium. There has recently been a dramatic increase in applications of "tender" (1-5 keV) XAS as facility development has made that range more accessible. Similar opportunities exist for higher energies (35-90 keV): using K edges as alternatives (or complements) to L edges, probing thick samples or buried regions, penetrating large-volume catalytic or high-pressure cells, avoiding interferences, and reducing radiation damage (e.g. in biological samples containing trace heavy elements such as mercury).

The rare-earth elements are of common interest to both materials research (optoelectronics) and geochemistry, at trace concentrations. Routine XAS work has been limited to the L edges (at 5.5 to 11.3 keV), but these often overlap and interfere (there being 48 L edges in that span). In contrast, the 16 K edges of these elements are nicely resolved over the span of 38 to 65 keV.

One other characteristic quality of NSLS-II that is of important consideration for these applications is its expected world-leading beam stability. While classic XAS experiments involved large uniform samples, most current and expected future samples are heterogeneous on varying spatial scales. These analyses require beam positional stability (e.g. better than 5 microns for a 1 mm spot) over a series of 1000-eV scans. Stable intensity (i.e. top-off injection) is critical to maintain stability of optics under high heat loads. And energy stability, the repeatability of energy calibration over a series of scans, is a prerequisite for useful high-energy-resolution measurements. The design of beamline components must then make a conscious effort to not degrade the inherent source stability.

Research programs: Specific research programs are being developed (or adapted) for this beamline by facility staff and leading user groups. Such programs will be the focus of a beamline workshop scheduled for January 16-17, 2008, following up on the NSLS-II User Workshop breakout session in July, 2007. Several of these will capitalize on the technical opportunities outlined above to address important DOE needs. The following two representative examples highlight research that will do so. In catalysis research, it is important to be able to measure the catalytic reaction *in situ* and/or in time-resolved fashion. However, in order to obtain sufficient signal quality in an appropriate time, this often requires preparation of samples with higher concentrations than are used in actual applications. These may not function the same as their dilute counterparts. The higher flux here will allow measurements at real-world application concentrations. This program will also require the capability of simultaneous XRD to more completely characterize sample systems in one run.

A similar example may be found in environmental stewardship and remediation. Of great concern to DOE is the subsurface contamination present at many of its sites, especially contamination by radionucludes and mercury. Typical concentrations in these environments, however, are below the current EXAFS sensitivity limits of most facilities. Moreover, wet sediment samples are heterogeneous, contain interfering elements, and produce high backgrounds due to fluorescence, scattering and diffraction. Yet detailed knowledge of chemical and physical speciation and processes is essential to determine appropriate courses of action for long-term stewardship and remediation of these DOE sites. The high flux, tunable spot size, energy resolution, and available energy-selective detection are all attributes which make the NSLS-II XAS beamline key in addressing this issue.

Future development and integrated facilities: The expected needs of the user community for XAS facilities at NSLS-II can not be met by a single beamline, however versatile and productive. Therefore, this beamline is part of a larger scope and long-term strategy that includes build-out of this beamline by canting the source, construction of additional non-Project beamlines, and migration of beamlines from NSLS.

The beamline design presented here explicitly includes accommodations for future canting. This is a highly desirable and cost-effective means of doubling capacity, as summarized here:

Sources:	Two canted damping wiggler segments (3.5 m each)
Separation between on-axis beams:	3.5 mrad

Inboard beamline:	microbeam, ~1 micron Acceptance up to 0.1 mrad x 0.1 mrad, on axis 1st experimental station additional optical components
Outboard beamline:	Bulk beam size Acceptance up to 1 mrad x 0.15 mrad max., on axis 2nd experimental station existing optical components

While the current project scope includes both endstations, it includes only one set of optical components for a single source. It is expected that canting of the source and addition of a second set of optics to make the two endstations independent will be undertaken at the earliest opportunity. There is very high demand, as well, for the lower energy range. This will likely be addressed by installing a complementary 1 to 5 keV bulk/micro XAS beamline at an adjacent dipole source as part of a core cluster. Additional non-Project XAS beamlines are expected to include “quick” XAS (sub-second scan time), perhaps on an undulator source, and specialized catalysis and biological XAS beamlines.

5.3 Insertion Device

XAS applications require a stable, broad energy range, non-coherent, high-flux source. The NSLS-II Damping Wiggler is an ideal source for XAS. These IDs are necessary for performance of the accelerator, and will be installed in high-beta straight sections. The standard geometry is a 7 m long device, but this can be effectively divided into two canted 3.5 m segments to provide additional capacity as described above. As shown in Figs. 5.3.1 and 5.3.2, the DW-100 source produces the highest total flux of all NSLS-II sources in the 5-35 keV energy range. Furthermore, it yields the highest brightness of the broad-spectrum sources over the same energy range. However, the spatial distribution of the generated radiation is energy-dependent. As shown in Fig. 5.3.3 and 5.3.4, the higher energy radiation is limited to the central portion of the fan. Since XAS applications require a uniform distribution as energy is scanned, this restricts use to the central on-axis portion of the fan. It also requires narrower acceptance when working at high energies, but that is naturally limited by the angular acceptance of the mirrors and monochromator. These factors make it undesirable to split a single source fan into the two experimental hutches; each application requires on-axis radiation by alternately sharing a single source (and eventually each having its own canted source).

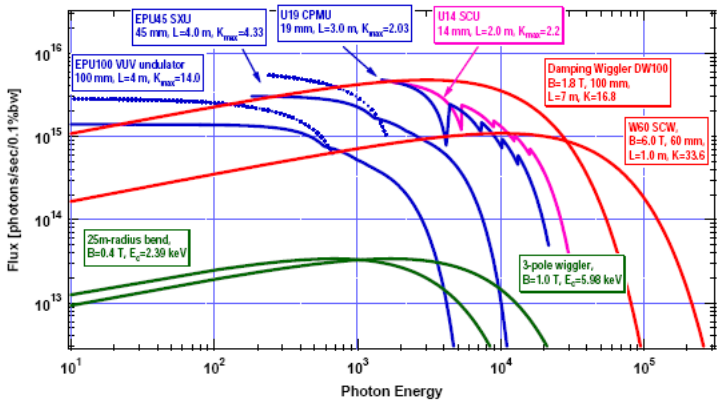

Figure 5.3.1. Flux of various NSLS-II sources.

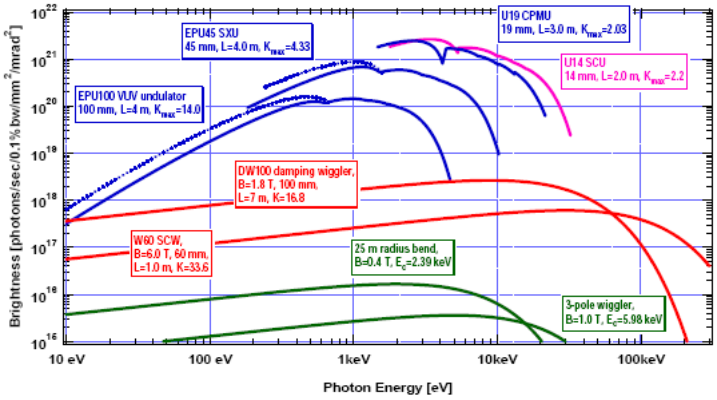

Figure 5.3.2. Brightness of various NSLS-II sources.

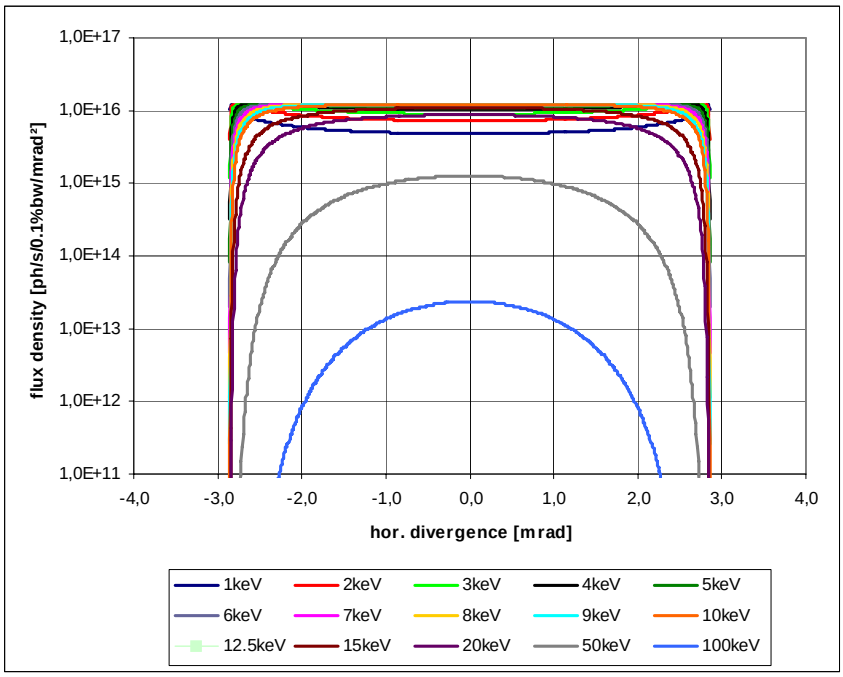

Figure 5.3.3. Horizontal distribution of flux density.

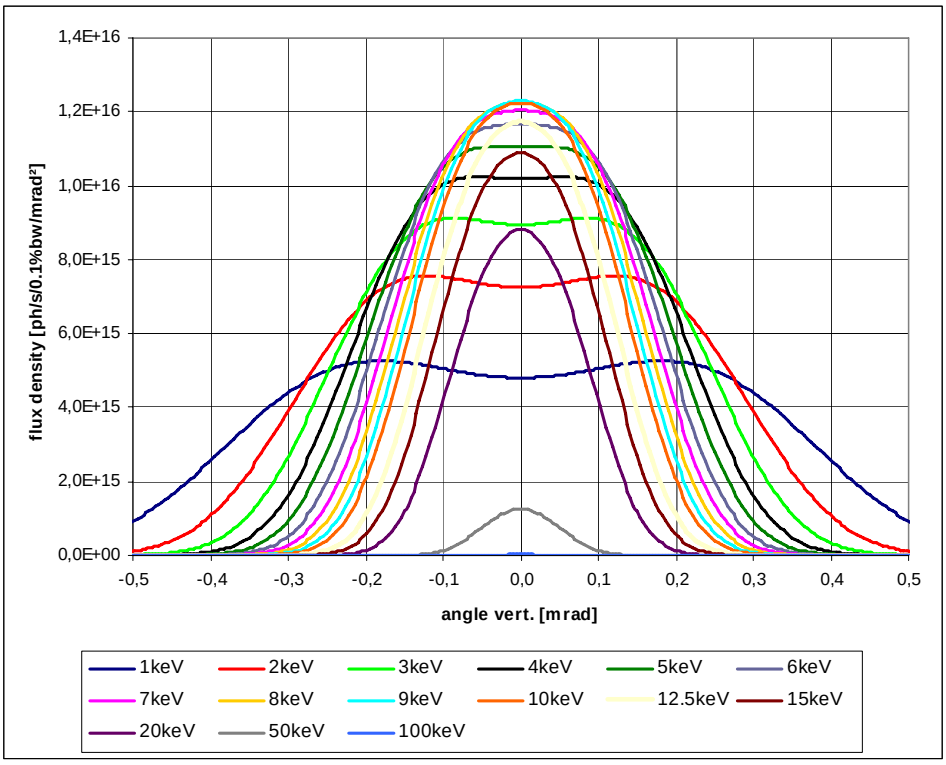

Figure 5.3.4. Vertical distribution of flux density.

The most challenging aspect of using the damping wiggler source is the unprecedented heat load. The full fan of a 7 m ID delivers approximately 65 kW of power, and even restricting acceptance to 1 mrad horizontal and 0.15 mrad vertical still delivers nearly 8 kW to the beamline optics. This maximum angular acceptance (in both dimensions) is defined by the optics (mirrors and monochromator), rather than by heatload limits. Heat load will be discussed further in the description of each component.

Current strategy for canting considers two possible paths. One is to begin operations with 7 m of wiggler in-line and introduce canting at a later stage. This has the advantage of extracting the highest possible flux during early operations when the ring current will not be at the full 500 mA, but has the disadvantage of requiring a repositioning and re-alignment of the ID, front end, and all optical components. The other path is to begin operations with two canted sections but only use one of them. This has the advantage of establishing the positions and alignments that will be used even when canting is fully implemented, and also provides the facility with an early test case for commissioning and refining canted wiggler sources. It has the disadvantage, however, of less flux initially. This second option is favored by beamline design personnel for the added reason that it reduces the heat load issue by an effective factor of two, and improves access to the lowest energy around 5 keV. In either case it is therefore unlikely that the beamline will experience full power from a 7 m wiggler at full ring current. However, component design is based on being able to handle this full heat load, so as to provide a margin of safety and to allow for potential future changes in beamline or project design.

Note that current ray-tracing, heatload and performance calculations are based on a damping wiggler with 100 mm period (DW-100). Current device design now calls for a period of 90 mm (DW-90); this will have a minor effect. Brightness and flux (within the used portion of the radiation fan) will increase slightly, as will heatload and power density. Ongoing thermal and performance modeling will take this into account as component design progresses.

5.4 Sector Layout

This sector begins with the insertion device as described above. Front End components are located within the ring tunnel, upstream of the shield (ratchet) wall. On the Experimental Floor, beamline layout consists of a first optic enclosure (FOE) containing all white-beam components and beamline optics through photon shutter, and two experimental endstations in series.

5.4.1 Front-End Layout

A standard front end layout is shown below, with specific items and their positions for this beamline in the table to follow. Note that accommodations are made now for future canting and upgrades.

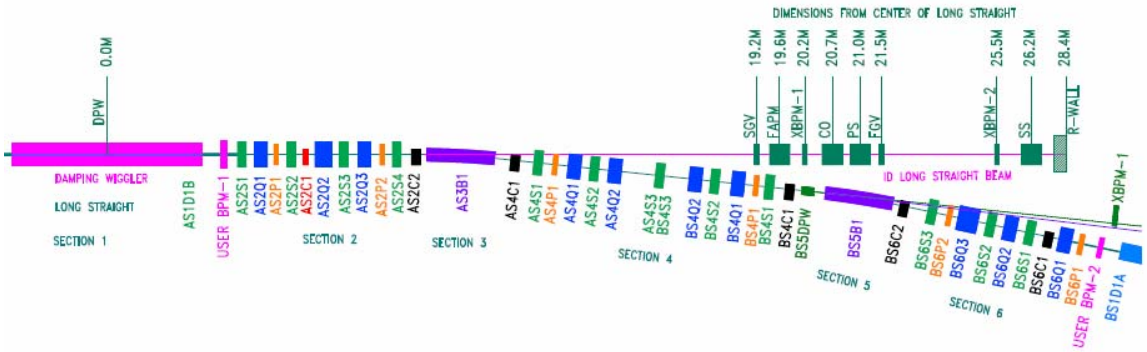

	Position (center) (m)	Acceptance (horiz x vert) (mrad)
Source	0.0	~5.5 x 0.8
Slow gate valve	19.2	
Fixed aperture mask	19.6	(-1.90/+2.35) x (+/- 0.25)
Beam position monitor	20.2	
Bremsstrahlung collimator	20.7	(-2.00/+2.45) x (+/- 0.30)
Photon shutter	21.0	
White beam slits (not shown)	22.5	(+/- 0.6) x (+/- 0.20) centered on outboard cant
room for white beam slits (second canted beam)	23.0	
room for possible future side-deflecting mirror	24.2	
Beam position monitor (removed from design)	25.5	
Safety shutter	26.2	
room for safety shutter (second canted beam)	26.7	
Bremsstrahlung collimator built into shield wall	28.2	(-2.00/+3.40) x (+/- 0.30)
Shield wall face	28.4	

A beamstop and gate valve will be initially installed at the shield wall for commissioning of the ID and front end components.

5.4.2 Beamline Layout

The following table provides a detailed layout of beamline components. Schematics and 3-D rendering of the XAS beamline follow the table. More detailed drawings can be found in Appendix 5B.

	Start	Center	Fixed Pos	Length
Shield Wall			28.4	
spool piece, gate valve, bellows	28.4			0.3
Pre-Filter, Attenuators (all water-cooled)	28.7			1.1
Bremsstrahlung collimator	29.8	30.1		0.6
gate valve, bellows	30.4			0.2
Mirror 1	30.6	31.5		1.8
gate valve, bellows	32.4			0.3
Monitoring	32.7			0.3
Steering mask and Be window	33.0			0.5
Double crystal monochromator (high heatload)	33.5	34.1		1.2
gate valve, bellows	34.7			0.2
space for monochromator, canted beam	34.9	35.5		1.2
Bremsstrahlung and white beam stop	36.1			0.5
Beam monitoring and Monochromatic slits	36.6			0.8
gate valve, bellows	37.4			0.2
High energy resolution monochromator	37.6	38.1		1.0
gate valve, bellows	38.6			0.2
Mirror 2	38.8	39.7		1.8
Gate valve, bellows	40.6			0.3
Space for Beam monitoring and Mono slits, canted beam	40.9			0.8
Space for optics, canted beam	41.7			1.6
Photon shutter	43.3	43.55		0.5
Space for Photon shutter, canted beam	43.8			1.0
FOE wall	44.8			0.4
flight tube, shielded	45.2			4.1
Experimental hutch wall	49.3			0.2
Monitoring	49.5			0.5
Exit window and slits	50.0			0.1
Sample location, Endstation 1 (incl. microfocusing optics)		51.5		2.7
Experimental hutch wall	52.8			0.2
Monitoring and slits	53.0			0.5
Sample location 1, Endstation 2		54.3		1.5
Sample location 2, Endstation 2		55.9		1.8
Sample location 3, Endstation 2		58.0		3.0
Hutch wall	59.8			0.2
End	60.0		60.0	

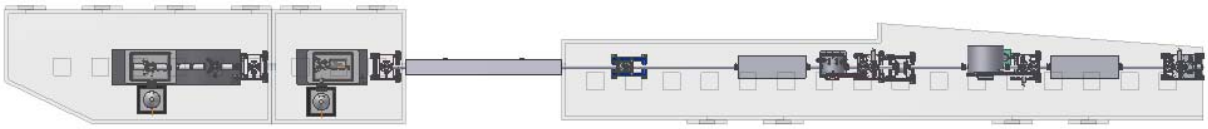

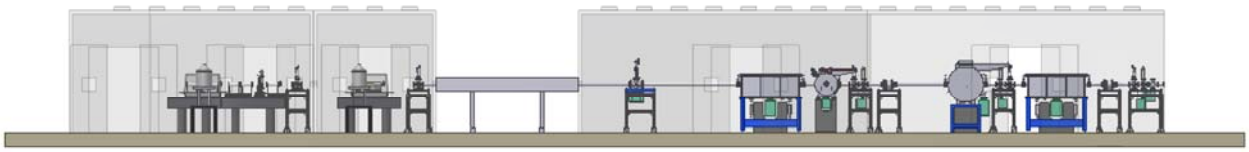

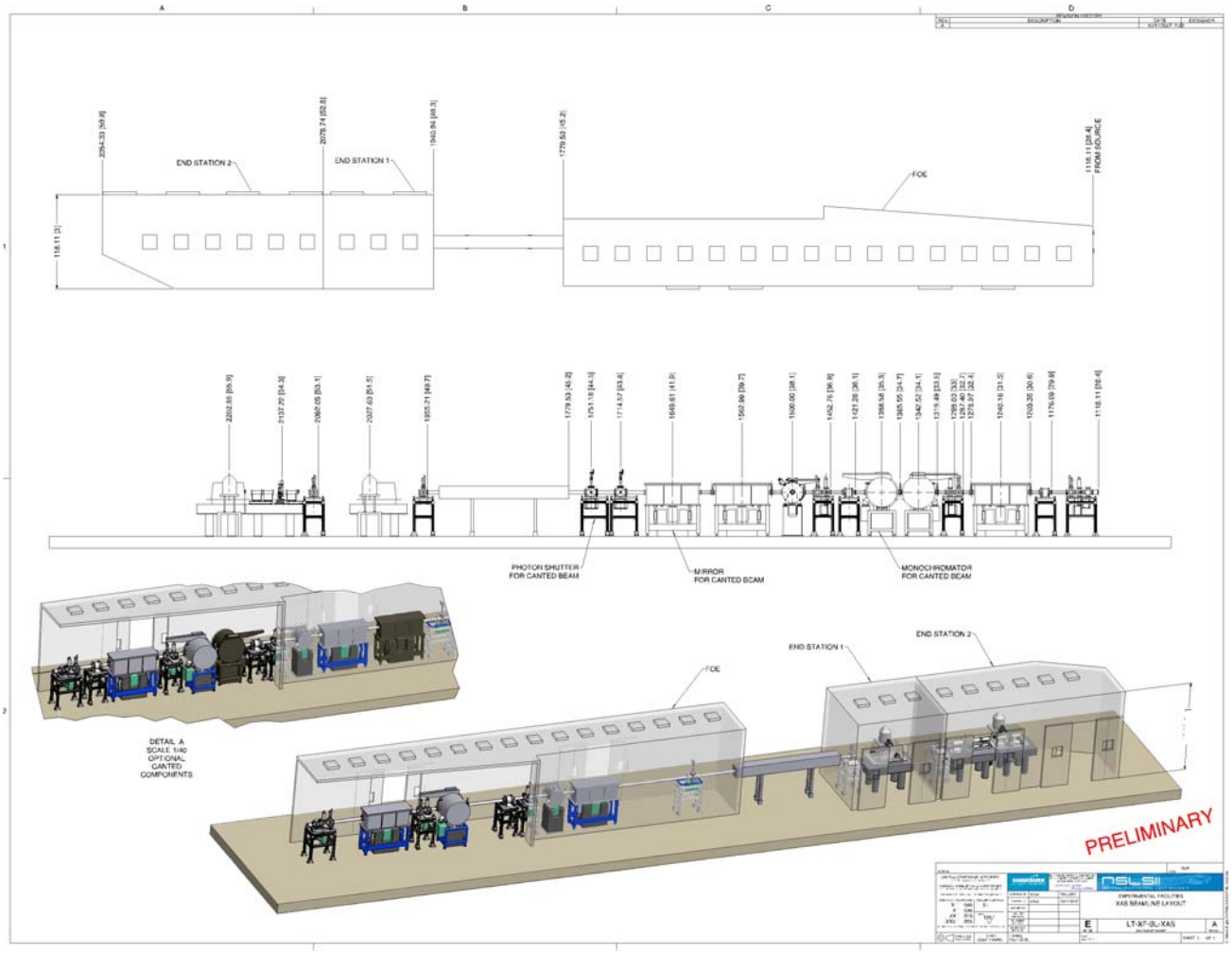

Initial ray-tracing and performance calculations are based on a beamline length of 64.3 m. Subsequent facility design refinements have decreased this to 60.0 m. Adjusting endstation positions required an increase in horizontal focusing to ~2.7:1, resulting in a marginally larger spot size and increase in vertical distortion of partly-focused beam. The ideal value is 2:1, and values of 3:1 or greater result in a decrease of horizontal acceptance of the focusing mirror to less than 1 mrad. Final design will consider this balance between layout and performance in consideration of planned optical elements. For example, it may be advantageous to place the future canted-beam monochromator downstream of this beamline's focusing mirror, thus resulting in more ideal 2.3:1 focusing with the added challenge of having adjacent white beam pass through the high energy resolution monochromator and mirror 2 chambers.

5.4.2.1 Survey and Alignment

All beamline components will be surveyed and aligned in place by the facility. In order to facilitate ease of alignment, all components will be fiducialized to external reference points on their table during assembly. These include horizontal and vertical position and angle, relative to the photon beam. All components are designed with a liberal tolerance allowance greater than 0.5 mm. Provisions will be made for laser pre-alignment of beamline optics.

5.4.2.2 Utility Layouts

This section describes the utility requirements assumed for the damping wiggler beamlines at NSLS-II. The numbers provided are estimations based on the current understanding of the beamline design; significant deviations may be possible depending on possible future evolution of the beamline layouts.

Cooling water. Cooling water is required for all high-heat-load components except the monochromator. Process water, the standard cooling water provided by the facility for this purpose, is clean de-ionized water at a temperature of approximately 20°C. Additional requirements are as follows: temperature stability within 0.1°C, pressure 60 to 100 psi, pressure stability within 5 psi, and free of pump vibrations.

The components and their requirements are listed in the following table.

Component	Number of Circuits	Consumption max.
Pre-Filter and Be-Window	2	4 l/min
Attenuator Units	4	8 l/min
Collimating Mirror and Mirror Protection Mask	1	12 l/min
Steering Mask and White Beam Monitor	2	6 l/min
Thermal Stabilization and Compton shielding of DCM	1	4 l/min
White Beam Stop	1	4 l/min
total:	11	38 l/min

If additional control is necessary, the DCMs temperature stabilization system will be separately supplied with temperature-controlled water by means of a dedicated chiller unit, thus allowing to set the flow to be set and the temperature precisely stabilized, independently from the main water supply in the hutch. This chiller will make it possible to set the water temperature in the range of 25 to 35°C and to keep it constant to ±0.1°C. It can either be equipped with its own electrical cooling system or be connected to the hutch cooling water.

Liquid nitrogen. The cryo cooler unit for the DCM requires connection to a liquid nitrogen (LN2) supply. It is recommended to have a LN2 supply tap within 2 to 3 m of the final cryo cooler position. LN2 is also needed within both experimental hutches for sample cooling and for auto-filling of detector dewars.

Compressed air. The following components must be connected to a dry, filtered compressed air supply having a pressure between 70 and 100 psi:

- the monochromatic beam shutter
- all gate valves
- attenuator units, if pneumatically driven

Electrical power. Three types of power are required: standard power for heating, pumps, etc.; low-noise power for measuring equipment; and UPS power for critical systems. Along the beamline a grounding bar is needed, to ground the beamline components. The grounding bar must be connected to the central power

distribution ground. A separate low-noise ground is also needed. Standard beamline service of 60 kW is expected to suffice. There are several distinct areas to which electrical power distribution is needed.

1. Beamline Control System Cabinets

A central 3-phase power distribution should be placed near the cabinets. In total, approx. 12 kW are needed.

2. Cryo Cooler Unit

This unit needs a single-phase power distribution of approximately 2.5 kW.

3. *FOE*

The required power in the FOE can be up to 30 kW to accommodate the extreme case where the full beamline might be pumped and baked at the same time.

4. Experimental Hutch

In the hutches, both low-noise and standard power outlets should be distributed along the length of the hutch. Total needs should not exceed 20 kW.

5. *Experimental Control Station*

The control station needs adequate power (of all three types) for computer controls, interfaces, and communications, estimated as 5 kW max.

Gases. Dry nitrogen is needed in the FOE, delivered to each vacuum pump-out port as described in 5.4.2.4. In addition, a distribution and control system is needed for local-source gases (helium, Argon, etc.) within the experimental hutches: for enclosures, ion chambers, detectors, sample cells and experimental apparatus.

5.4.2.3 Life Safety Code Compliance

Floor layout and access walkways will be arranged so as to comply with applicable emergency egress requirements. Figures 5.4.2.3a and b show initial access/egress walkways in red. Specific details will be developed in conjunction with layouts of neighboring beamlines, and in conjunction with ES&H personnel and NSLS-II policy. Exit routes will be posted and included in user training.

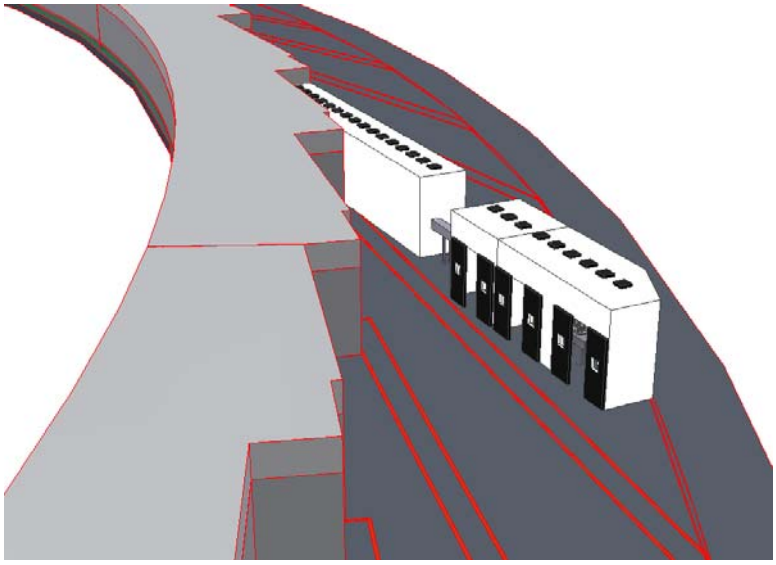

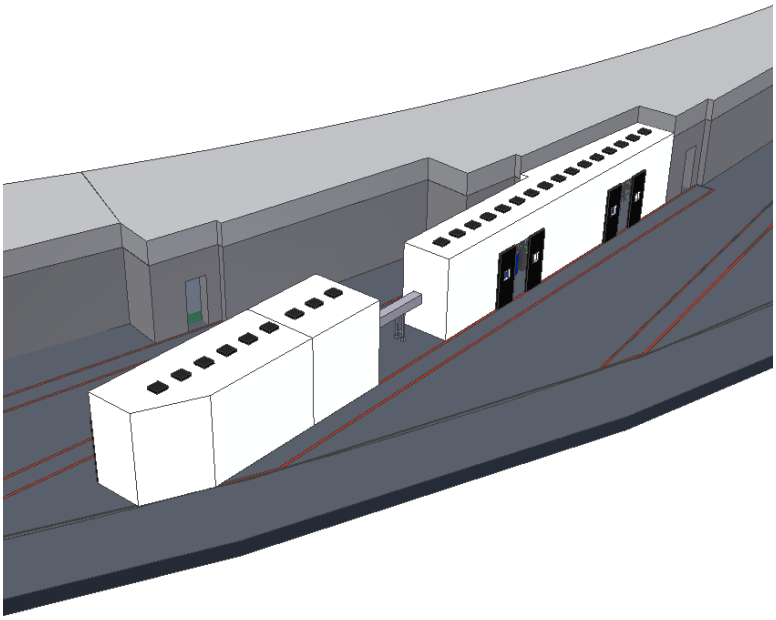

5.4.2.4 Beamline Vacuum System

There will be several vacuum sections, isolated from each other through gate valves. Each vacuum section will be equipped with an ion pump, full-range vacuum gauge, and pump-out port. Each pump-out port will consist of a rectangular, all-metal valve (CF40) to rough down the vacuum using a pump cart, and a valved connection to dry nitrogen supply to vent the section. The monochromator will also be equipped with a CF63 gate valve where an interlock-protected magnetic bearing (oil-free) turbo molecular pump will be permanently mounted.

The white beam section of the beamline will be bakeable in order to achieve a vacuum pressure below 10^{-9} torr. The monochromatic section is designed to achieve a base pressure in the 10^{-8} torr range or better.

Besides the large flanges of the monochromator doors (that are Viton sealed) and the flanges of the mirror vessels (metal-sealed for M1 and Viton-sealed for M2), all flanges will be bakeable metal-sealed Conflat standard. There will be no mechanical water-vacuum seals anywhere in this design.

The following diagram shows a general schematic overview of the vacuum and its protection system (note that the location of the water-cooled Be window has been changed from this layout):

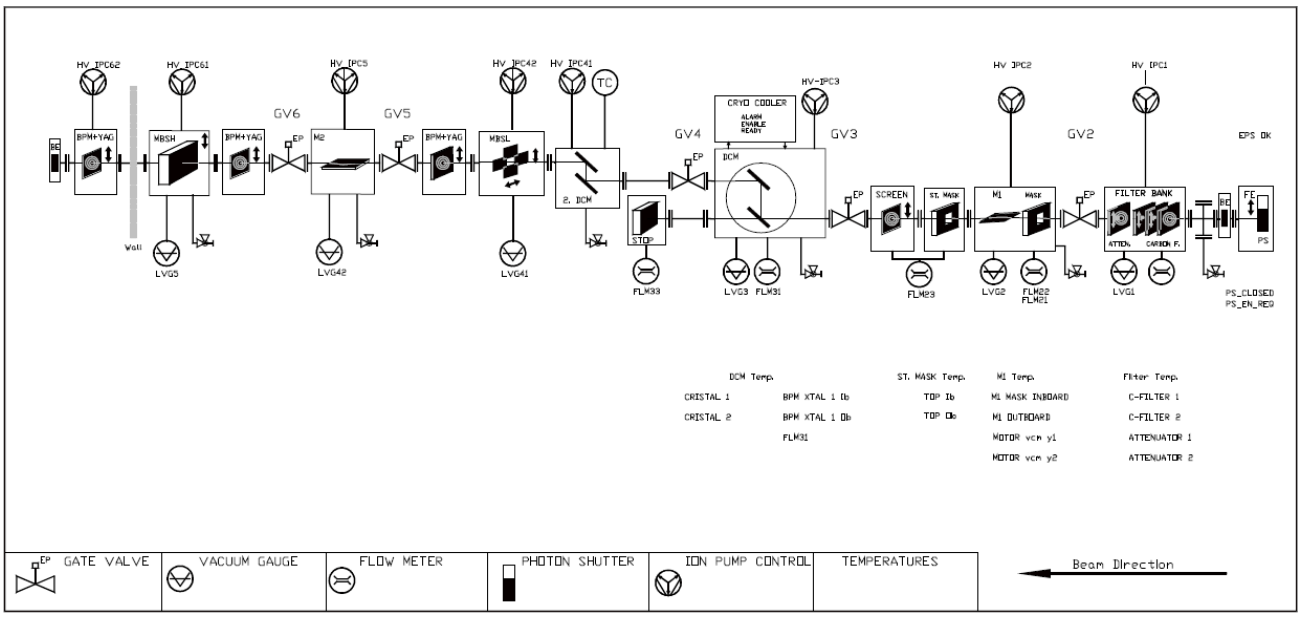

Figure 5.4.2.4

Vacuum control and Equipment Protection System sensors (pressure, temperature, water flow). All components (including valves, shutters and pumps) also have indicators of status or position.

5.4.2.5 Data Acquisition System and Motion Control

See Appendix G for general specifications of an example control system. This document was developed for several Accel components under consideration for this beamline.

5.4.3 Beamline Components

As tabulated in 5.4.2, the following items comprise the major beamline components necessary to deliver controlled monochromatic beam to the experimental hutches.

5.4.3.1 White Beam Slits

While these slits are located in the Front End, they will be under beamline control. Please refer to the appropriate chapter for detailed front-end specifications. In general, these slits will be water-cooled, accept up to 1.0 mrad horizontal by 0.15 mrad vertical, and have resolution and repeatability of better than 10 microns. The 4 independent blades will be tungsten-edged for the high energy range being used, and each capable of closing 2 mm past the centerline. Heat load modeling will need to be conducted in order to ensure that the blades can tolerate the required absorbed power. Accommodations will be made to include future blades to also define the second canted beam.

5.4.3.2 Pre Filter, Be window, Attenuators

Hard x-ray beamlines typically have a beryllium (Be) window to separate the beamline vacuum from the machine vacuum. A Be window also absorbs a significant fraction of the unused low-energy radiation, therefore reducing the overall power delivered to downstream components. However, in a wiggler beamline such as this, calculations of the absorbed power indicate that a Be window in the direct white beam would fail. Due to their high thermal conductivity and mechanical stability, carbon foils are typically used as a protective filter material in front of the Be window.

This beamline design incorporates three components, a set of graphite foil pre-filters to protect the Be window, a Be-window for vacuum isolation, and an additional attenuator package to further manage the power load on the optical components. The C pre-filter and Be window combine to absorb the lowest-energy radiation, and effectively establish the low-energy limit of the beamline's range.

The approach described here is to design a filter assembly that can be safely used whenever required in order to reduce the power levels on the optical components. Reduced power will improve the performance and stability of the white beam optical components such as collimating mirror and monochromator. Considering the high heat load which is produced by the wiggler the carbon filter unit is an essential component to maintain sustainable power levels down the beamline.

When considering the heat load absorbed by the most upstream filter, a standard water-cooled graphite filter is not able to cope with the high heat load. From experience at other facilities using similar powerful sources, there are two possible solutions:

A) Thin C foils which are only radiation cooled. In that case the foils become extremely hot (up to 1500°C or higher). This system is in place at NSLS X25, formerly a wiggler but now an undulator beamline. A stack of radiative cooled foils successfully withstand the power load (3.4 W/mm^2). They use seven foils from 5 µm up to 51 µm in thickness. After a few years operation, the foils do not show any visible damage. In addition it has been verified that the temperature of the foils is somewhat lower than calculated. This system has proven to work reliably up to temperatures over 1000°C.

B) High thermal conductivity Highly Oriented Pyrolytic Graphite (HOPG) foils, mounted in a water-cooled filter frame. This system is employed at ALS Beamline 5.0. HOPG is clamped between two water cooled copper frames and absorbs 10 W/mm^2 (250 µm). The contact pressure is finely adjusted by springs. Temperatures up to 1000 K are possible. After more than one year operation, there is no visible damage on the HOPG foil.

We have carefully evaluated the behaviour of specifically the first filter unit for the power load of the damping wiggler source; please refer to Appendix D. Both options, radiation cooled filter elements as well as contact cooled filter, are possible solutions for this beamline. A final careful FEA has to be done using the filter and source parameters for the configurations needed.

Be window and pre-filter

This component is very similar to the set-up used at different beamlines at BNL. It consists of a water cooled frame which holds the different filters. The radiation-cooled foil is hold in a Tantalum frame, since it must withstand the extremely high contact temperature, and will turn hot itself. The power then is dissipated into the surrounding environment and is absorbed by a water cooled copper surface positioned around the Tantalum frame. The Tantalum frames, together with the carbon foils, are placed in a water-cooled cartridge made of OFHC copper. The cartridge is held and mounted on a DN40CF flange. The assembly is mounted to a DN100CF base flange and fits in a DN100CF standard cross. PT100 temperature sensors (e.g. two sensors) will be installed in the copper cartridge and monitored by the control system. If any PT100 sensor exceeds a temperature limit the beam shutter will be closed. The PT100 sensors will be connected to an electrical feedthrough, the water pipe (SF-copper, Ø8x1) will be brazed on the cartridge and on a DN40CF flange avoiding water-to-vacuum joints.

A possible filter combination could be as shown:

Table 5.4.3.2 Possible pre-filter combination.

Filter no.	Filter thickness [μm]	Absorbed power [W]	Absorbed power density [W/mm²]
1	5	222	1.6
2	5	96	0.7
3	5	72	0.5
4	25	240	1.8
5	25	162	1.2
6	50	237	1.8
7	50	180	1.4
8	100	277	2.1
9	135	283	2.2
10	300	457	3.6
11	300	337	2.6

Attenuator Unit: This unit consists of a number of different filter setups, that allow tailoring the power load on the optical components to the right level of operation for each particular operational mode of the beamline. The design foreseen for your beamline is based on the one we have realized recently for other high heat load beamlines and is described in the following paragraphs. Currently, we assume that for the Damping wiggler beamlines it might be reasonable to work with two pneumatically driven attenuator units and two or even three motorized filter banks with different filters mounted.

The latest ACCEL design is based on a series of three water-cooled filters mounted on three pneumatic drives. These three carbon foils are of Annealed Pyrolytic Graphite (APG). These APG foils have a similar thermal behaviour than HOPG and are available down to thicknesses of 50μm. The foils are clamped to copper frames where the thermal contact is improved by (i) polishing the surface of the copper within the contact area and (ii) using springs that apply a well defined and well distributed contact pressure. The thermal conductivity of APG is similar to diamond. Due to its excellent mechanical properties and together with the advanced cooling each foil is designed to remove about 500 W. The power density on the first foil presents the most challenge and therefore limits the maximum thickness of the foil, while heat conduction as well as physical integrity under thermal stress define the minimum thickness of the first foil. The APG foil used in the existing system is 125 μm thick. This thickness presents a good balance between the transmission at lower energies and the still very good stability of the foil. The second foil can only be inserted in the beam when the first foil is already in.

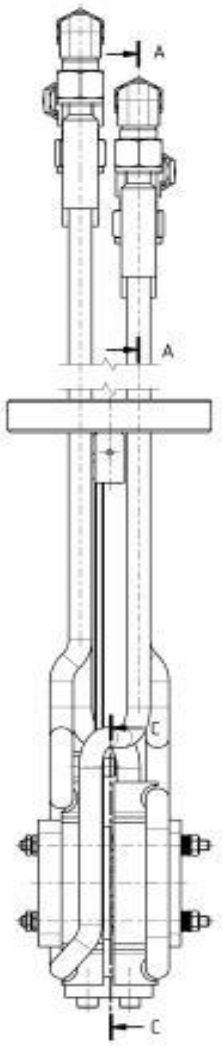

Figure 5.4.3.2a Directly cooled high power filter set-up, which can be pneumatically driven.

The fourth filter drive is motorized and consist of a cooled frame with five positions that can be used for graphite foils (Pyrolytic graphite) of different thickness to be used to further attenuate the beam. This filter design avoids water-to-vacuum joints. Water pipes are brazed to the each cooled copper frame and to the vacuum feedthrough, where edge-welded bellows permit the translation of the frames with the filters.

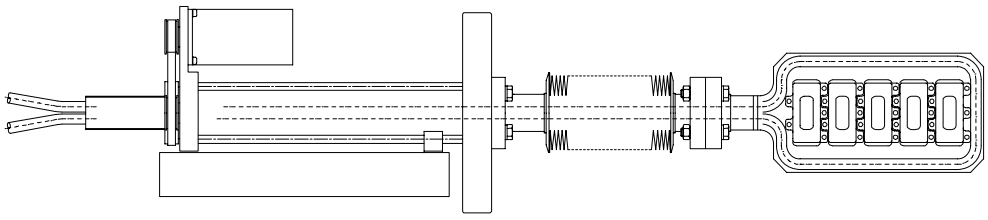

Figure 5.4.3.2b Example motorized water-cooled attenuator assembly

Please note that the filter bank must be equipped with a special protection, as the 2nd filter foil can only be introduced into the beam, when the 1st foil is already in the beam. Similarly the standard motorized filters units can only be put into the beam when both pneumatic filters are in the beam.

As an option the two first PG foils could be replaced by a 250 µm HOPG foil based on the above mentioned ALS design. Using such a design, the maximum temperature is reduced significantly and therefore we do not expect any influence by infrared radiation on the downstream optical components. On the other hand the use of HOPG will significantly reduce the flux at the sample at low energy.

The vessel of the filter assembly is equipped with view ports which permit visual inspection.

General*:*

UHV rated

Two pneumatic driven actuators:

- APG foils clamped on a double sided cooled copper frame
- 1000 W cooling capacity for each actuator
- position monitored by limit switches

Two motorized actuators:

- PG foils and metal foils clamped on a cooled copper frame
- 500 W cooling capacity
- position monitored by limit switches

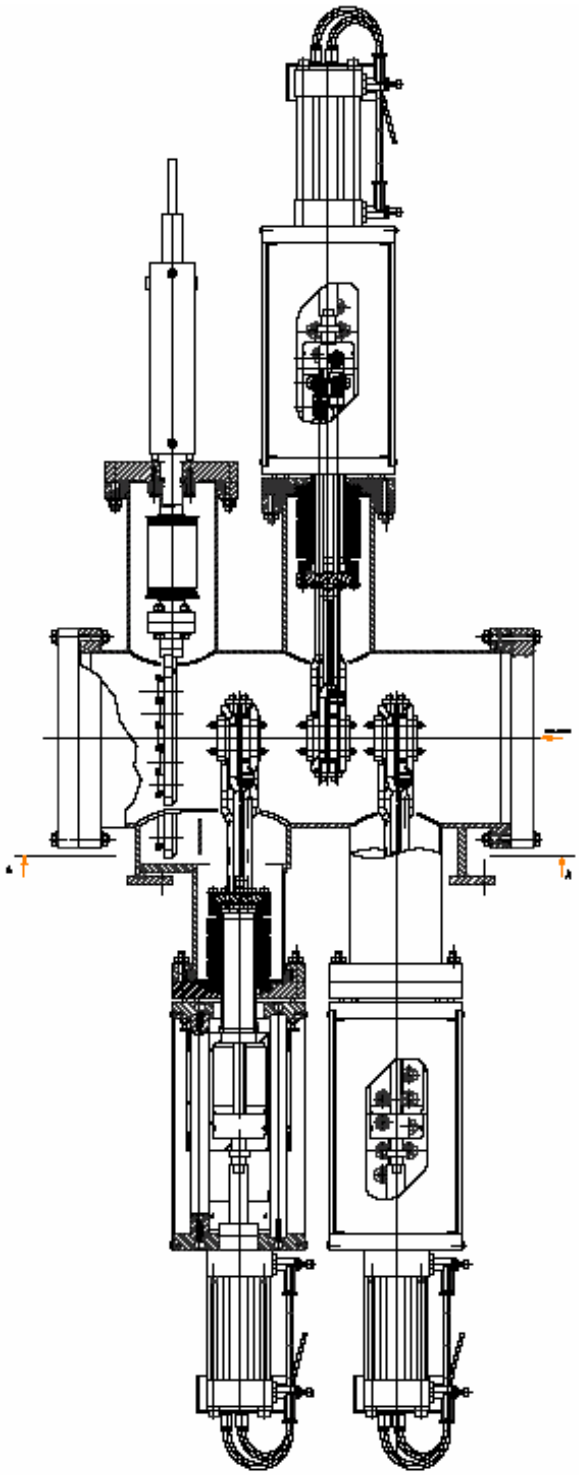

Figure 5.4.3.2c Example high heat load filter system as installed at the XAS beamline at ASP.

5.4.3.3 Bremsstrahlung Collimator

The collimator will absorb high-energy Bremsstrahlung radiation originating inside the ring and defines the extent of the remaining Bremsstrahlung extremal rays on which the dimensions of the downstream white-beam stop must be defined. The outer dimensions and dimensions of the aperture will be determined through

ray tracing. Appendix B shows the initial Bremsstrahlung ray-tracing, using two different types of collimators and stops. A lead Bremsstrahlung collimator basically consists of a rectangular vacuum pipe mounted inside a block of lead. Because of the vacuum pipe, some tolerances and the necessary clearance, the openings in such lead collimators are rather large. An in-vacuum tungsten collimator allows a much smaller beam opening and therefore much better collimation. This is the recommended option. In addition, the tungsten collimator is more compact; the absorption length for lead is determined to be 300 mm along the beam direction; for tungsten, 200 mm. The collimator assembly will sit on an adjustable support that will permit translation and tilting for precise alignment, then will subsequently be locked in place as part of the safety system.

5.4.3.4 White beam Mirror

A directly cooled Si mirror offers several advantages. This technology is in use at beamlines at NSLS and the ALS, and mirrors with the required quality characteristics can be procured. As long as the bond of such a mirror is not directly exposed to the x-ray beam, the stability of the frit-bonding seems not to be a problem, even after several years of use. This being the case, and to protect the end of the mirror from inadvertent exposure to direct beam, a water-cooled protection mask will be employed.

An additional feature required for such a high-intensity beam will be a shielding shroud over the sides and above the face of the mirror, to keep scattered radiation from heating the enclosure and positioning/bending mechanism components.

5.4.3.5 Steering Mask

A protective water-cooled steering mask just upstream of the monoichromator will serve to protect the DCM interior and any uncooled downstream surface from being hit by a miss-steered direct beam. Furthermore, a steering mask would serve as a conductance-limiting aperture for the vacuum performance between these two sections. To accommodate all operation modes of the beamline, this mask must sit on a vertical stage and will be equipped with edge-welded bellows to allow for the necessary translations.

The mask will have water channels, I.D. 8 mm, with copper tubes brazed to it (no water-to- vacuum joints are used in this design). The material will be Glidcop and the impinging area will have a suitable slope so it can withstand the high thermal stress that will be produced under worst-case conditions (i.e. full beam).

Specifications

Material	Glidcop
Total power capacity	≤ 6 kW
Maximum power density on surface	12 W/mm^2
Angle of cooled surface	Approx. 10°
Length of water cooled body	Approx 150 mm
Water flow maximum	6 l/min.
max. pressure	120 psi
Aperture size	1 mrad (h) x 0.15 mrad (v)

5.4.3.6 High-Heatload Monochromator

This component is the critical item of the wiggler-based XAS beamline. It must be able to handle the large heat load (perhaps as high as 2.5 kW) while still maintaining the requisite stability and optical quality.

Crystal design. As discussed in Appendix D, there are two ways to cool the crystals, either by direct or by indirect cooling. The monochromator designed by Accel is typically equipped with indirectly cooled crystals. This cooling method is certainly more robust and more reliable in terms of leak tightness, but is less

efficient for high heat loads. In such a case, the crystal set-up must be redesigned to accommodate direct-cooled crystals.

In-house monochromator development and design is based on the "hockey-puck" crystal geometry, and this will be pursued within the NSLS-II Project R&D program. This is the preferred option, as it is proven technology (on a smaller scale) and appears to be able to effect more efficient cooling.

Cryocooler. For cooling the crystals to LN_2-temperatures, a closed loop LN_2 cryo-system will be used. Originally developed for the ESRF, the Accel Cryotherm model is most highly regarded. Its control system is based on a PLC with an interface to a standard PC to manage the temperature controls system via EPICS.

5.4.3.7 High-Energy-Resolution Monitor

This device will be based on a high-precision version of a standard DCM. Choice of crystals, since cooling is not an issue, will be made on the basis of optimal energy range, bandpass, available crystal quality, and testing work to be performed at the NSLS.

5.4.3.8 Monochromatic Focusing Mirror

For the VFM, a configuration of two sagittal cylinders with different sagittal radii in the substrate is technically feasible; the polishing of such a mirror will be a very challenging process, but a vendor has accomplished several similar mirrors already.

The following table summarizes possible specifications for the two mirror substrates and benders, based on similar existing beamlines.

	M1	M2
Mirror Substrate	Monocrystalline Silicon	Fused Silica or ULE or Zerodur
Direction of Reflection	Downwards	Upwards
Shape	FLAT cylindrically bent to tangential cylinder	Double sagittal cylinder cylindrically bent to torus + central flat
Tangential Operational Bending Radius Range	5.0 km - flat (> 40 km)	3.5 km - flat (> 40 km)
Sagittal Bending Radius	flat (> 1 km)	(i) $R_{sag}1$= tbd mm (Pt coated) (ii) $R_{sag}2$= tbd mm (uncoated)
Substrate Length	approx. 1400 mm	
Substrate Width	~ 120 mm	~ 135 mm
Substrate Thickness	60 to 70 mm	60 to 70 mm
Optical Active Surface: Length	1200 mm	
Width	2 x 35 mm (Si & Pt)	2 x 35 mm (cylinders) polished width ~ 45 mm
Slope Error: Sagittal	< 15 µrad rms for M1 < 25 µrad rms for M2 (best effort < 15 µrad rms)	
Tangential	< 2.5 µrad rms on 1200 mm (Best effort: < 2 µrad rms)	
Micro Roughness	< 3 Å rms; best effort < 2 Å rms	
Coating	Pt> 600 Å; Cr underlayer	Pt> 600 Å; Cr underlayer Bare central flat

Cooling	YES, directly cooled	No

5.4.3.9 Beam Monitoring Elements

a) Water-cooled white beam CVD fluorescence screen: The device consists of a retractable water-cooled CVD diamond foil, acting as x-ray screen, mounted to a pneumatic drive; the fluorescent effect is based on the residual doping with nitrogen atoms. The diamond screen is transparent; i.e., beam detecting further downstream is possible. The assembly is mounted to a DN100 CF cross with one view port permitting a side view onto the screen. The pneumatic drive is equipped with limit switches. The vacuum feedthrough is made of edge-welded bellows. The water lines are brazed to the screen support to avoid vacuum-to-water joints. The foil is clamped to the cooled support.

The projection of the beam onto the 45° inclined foil will be monitored with a CCD camera. This system is capable of staying in the beam. However, because of the resulting absorption at photon energies below 10 keV, the screen should be withdrawn when not in use. Moreover, to increase the lifetime of the foil and prevent overexposure of the camera, this screen should only be used at reduced power levels—i.e., in combination with some of the carbon filters.

This screen has been installed at the high power wiggler beamline at the Australian Synchrotron Project.

General	
Screen material	CVD Diamond foil less than 0.125 mm thick
Screen slope	45°
Field of view	40 mm (h) x 20 mm (v)

These fluorescence screen monitors typically are mounted to a pneumatic drive via a vacuum feedthrough on a conflat flange. The water-cooled monitor is inserted in the beam by a stepper motor. Modeling of heat load and power absorption will be required. The flange is also equipped with a view port for the camera that provides side view of the screen. Examples can be seen below, for a water-cooled device and an uncooled device.

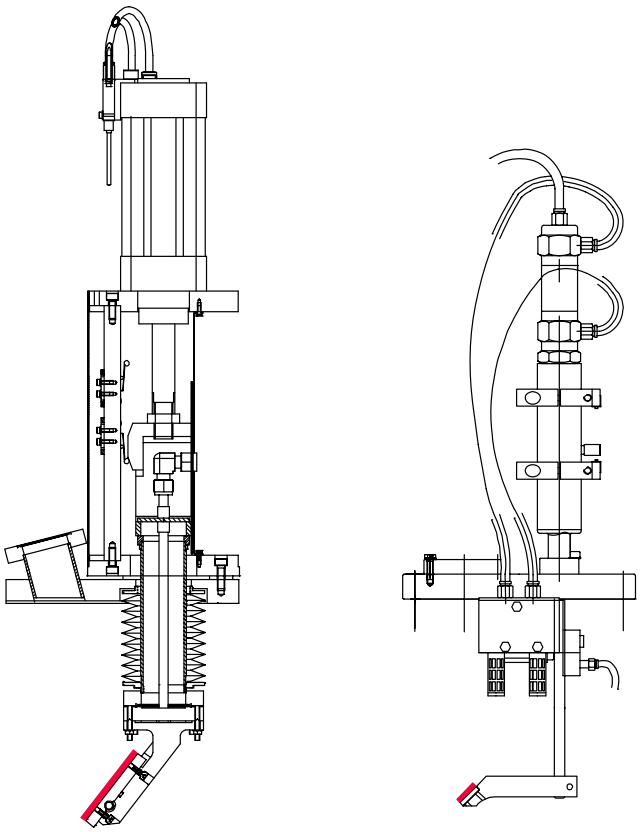

General:	Screen 1	Screen 2
Beam Size (hor. x vert.)	20mm x 15mm	≤ 40mm x ≤ 20mm
Screen Size (fluorescent region; hor. x vert.)	20mm x 20mm	50mm x 60mm
Water Cooling	yes	no

b) Quadrant diode beam position monitor (4-diode BPM): A standard monitoring device for monochromatic beams of large size is a quadrant type detector that monitors the fluorescence yield of a target foil. Beam position information is derived from the intensity ratio of one pair of diodes. The device is rated for UHV and consists of a diode holder (holding four diodes) and a fluorescence foil holder.

The four detecting silicon diodes are mounted to a vertical stage that permits a vertical positioning of the diodes which is needed to operate at different beam heights.

There are mounts for two foils, which can be of different kind, or be the same. Typically, thin chromium and copper foils are used, but silver foils might be used as well. Chromium and copper have been working up to photon energies of around 20 keV. There is an option to mount a YAG crystal underneath this foil holder. Than this YAG can be used to visualize the beam by means of a camera looking from the side onto a prism which is positioned behind the YAG.

The assembly is designed such that it mounts to a CF100 flange and fits a standard size DN100 CF cross.

The detection electronics for the diodes will consist of an integrated four-channel picoammeter.

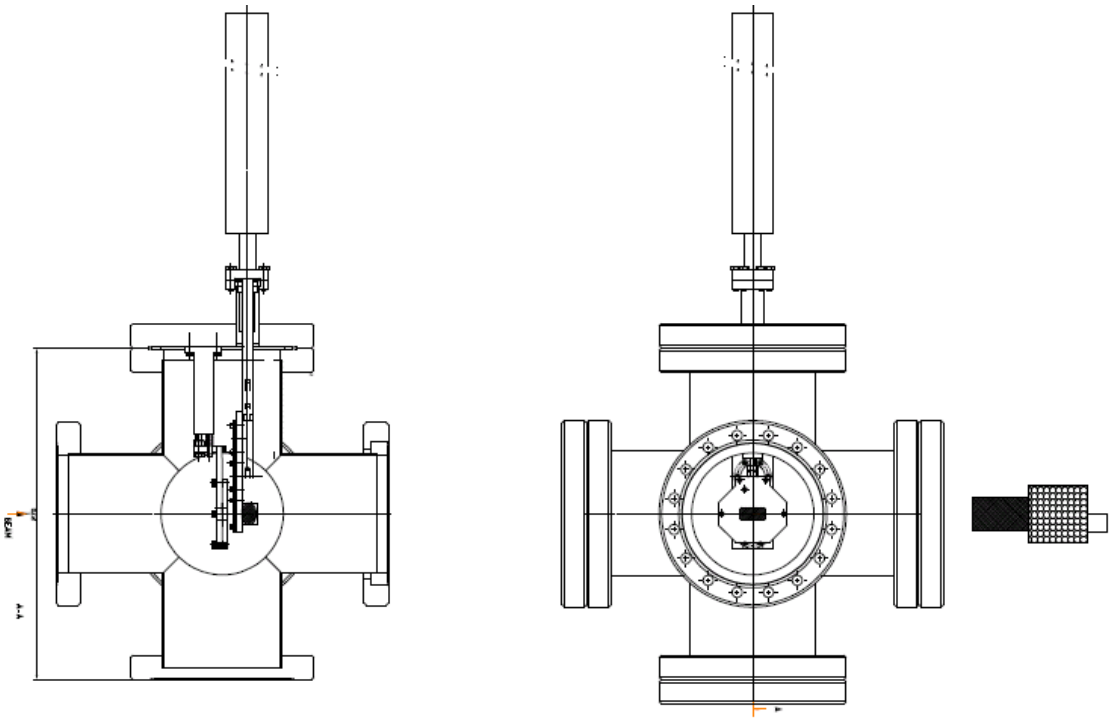

UHV rated BPM with diodes and fluorescent foil and screen

General:

Energy range	5 KeV to 25 KeV
Foils	0.5 micron Cr, Cu, or Ag
Photo current	~2 μA @ 10^{13} ph/s

Translation stages:

Stepper motor drives	linear actuator with 2-phase stepper motor and limits
Maximum stroke diodes	50 mm
Maximum stroke foils	100 mm

c) Endstation X-ray beam monitor and camera: This type of x-ray beam monitor is a commercially available visualization system for x-rays, or can be contrived with minimal effort. Such a system provides a field of view large enough to study the beam size, beam profile and the beam position stability of a focused beam in the endstation (at atmosphere), but must be removed from the beam path during data collection.

Feedback systems: electronic beam position monitors (type b above) will be strategically incorporated into at least two feedback systems.

The first of these will monitor beam position at the entrance slits for the high energy resolution monochromator. When this monochromator is in use, the BPM will be incorporated into a synchronization control loop that maintains tune between the two monochromators. While it is conservatively expected that the high-resolution mode of operation will preclude use of continuous-scan data collection (so as to allow for stabilization at each data point), this would be a desirable feature and is worth pursuing as part of final design.

The second feedback system will employ BPMs at the upstream end of each experimental hutch. These will be utilized (being highly sensitive due to the long lever arm) to control fine monochromator (and possibly mirror) adjustments to maintain beam position at the sample. This type of feedback is in place at a number of existing beamlines. While the NSLS-II source will have exemplary stability, feedback systems are likely to still be required to eliminate instabilities created by the beamline optics and their mechanisms.

5.4.3.10 Monochromatic slits and photon shutter

A standard design for in-vacuum monochromatic slits and for photon shutter will be developed for the NSLS-II experimental facilities. These designs will be used for all applicable beamlines.

5.4.4 Instruments

Instrumentation for the XAS beamline will consist of two endstations providing advanced capabilities to address cutting-edge challenges in local-scale physical, chemical, and electronic structures. The guiding philosophy for design of these endstations is to provide the widest range of high-quality XAS tools to fit current scientific needs. It is also intended to ensure a solid infrastructure that remains versatile and adaptable to both expected and unforeseen experimental needs of 2013 and forward.

A central aspect of this is detector selection. Preliminary design calls for a suite of detectors to answer the basic needs of various methods of measurement. It is expected that more detailed specifications for these detectors will be defined after further interactions with the community and through the Beamline Advisory Team process. Further technical developments are likely in the next few years; incorporation of these into final beamline design will enhance capabilities. Also, beamline design will explicitly include provisions to accommodate the subsequent addition of detectors beyond current project scope.

The following sections describe Endstation 2, the main experimental hutch for bulk XAS, and Endstation 1, the smaller upstream hutch for microbeam XAS. At initial operations, these endstations will operate from a single control station and share a single source and set of beamline optics. For efficient experimental setup, users will be able to access Endstation 2 while Endstation 1 is in use, but not vice versa. Eventually (but beyond Project scope), each endstation will operate independently, thus doubling capacity. In that arrangement, Endstation 2 will be served by the outboard of the two canted sources; Endstation 1 the inboard source.

This combination of endstations will provide a range of spot size from 5 x 40 mm to 1 x 1 micron, to cover the range of scale needed for the planned research programs. It will also complement efforts at the nanoprobe Project beamline which, combined with the planned soft x-ray spectromicroscopy facility, will pursue finer spatial resolutions.

Instrument control and data collection will include all motor drive channels, ion chamber and detector outputs, sample image capture, temperature, sample-cell and illumination control. Data collection software will include standard XAS scanning parameters, sample mapping functions (micro and macro beam), programmed sample locations and experimental control, and will also incorporate XRD data and image capture from sample cameras.

5.4.4.1 Endstation 2

This endstation will serve bulk applications at three sample positions. Each will have its own set of components to minimize downtime and effort for setting up or reconfiguring each experiment.

Sample position 1: The scientific mission of this classic benchtop style setup will be for *in-situ* analyses, grazing-incidence surface measurements, high concentration and fast-scanning applications, and use of high energy resolution fluorescence detection or simultaneous XRD.

Flow-through cells are important for *in-situ* measurement of catalysts at controlled temperature and gas flow, and for chemical (e.g. ion exchange), environmental (e.g. contaminant adsorption), and geochemical (mineral-water reactions) solution flow experiments. Flow-through cells are also important for some biological materials where a static solution may suffer radiation damage. Other *in-situ* sample cells include those for electrochemical and fuel-cell research, laser or small magnet units, or high pressure measurements.

Surface XAS is an important measurement technique that is ideally suited for the highly-collimated high-brightness beam provided by this source. Measurements are typically made in total reflection, using either the reflected beam (analogous to transmission through a thin sample) or fluorescence. The high flux at this

beamline will greatly improve the ability to measure very dilute (sub-monolayer) surface species, and the higher energy range will create additional opportunities to do so at buried interfaces or under solutions.

An important mode of data collection will be continuous-scan (slew) mode, where the monochromator is kept in continuous motion while measurements are made. Scans in this mode will take only one to three minutes each, resulting in very high throughput for more routine measurements. Time-resolved studies on this scale are thus possible.

Fluorescence detector-limited applications involve samples with low target signal but high background, or those with strong interference by overlapping fluorescence peaks (in a solid-state detector spectrum). These benefit from use of a high energy resolution or energy-selective detector, but such detectors typically accept only a very small solid angle of fluorescence from the sample. The very high flux and excellent macro focus of this beamline will make energy-selective detectors much more attractive. The wavelength-dispersive spectrometer included in this preliminary design will be useful on samples where conventional detection is unsuccessful.

Simultaneous XRD is of great interest to many of the catalysis and in-situ research programs, as well as for bulk characterization of samples in general.

Components at sample position 1 include the following (all within project scope):

- Optical table, fixed height
- Separate table for detector(s) at 90° to beam
- Beam-defining x-y slits
- Ionization chambers for I-zero, transmitted and reference measurements
- Optical rail
- Sample stage with x, y, z, rotation, and horizontal and vertical tilts
- LN2-cooled sample mount
- Stage adapter for flow-through cells
- sample temperature control
- Camera on sample position (45° to beam), with illuminator
- Compressed-helium cryostat
- Fluorescence detectors: Lytle, PIPS, and solid-state Si (e.g. the Vortex type)
- High energy resolution fluorescence detector, such as a wavelength-dispersive spectrometer
- Area detector for simultaneous XRD, to be placed downstream of sample stage
- Light-weight helium-filled flight tube to deliver beam to sample position 2 when needed

It is expected that each experiment will provide its own sample cells, but the support infrastructure (e.g. gas supply connections, flow control, temperature control and monitoring, etc.) is part of the beamline. The sample stage must have sufficient capacity to support the cryostat or other sample cell. Tilt geometries are needed for both horizontal and vertical polarization-dependent grazing-incidence measurements. Detectors will be positioned with appropriate stages. The area detector will be moved back, out of the beam path, when not in use, and may also be used in Endstation 1.

Sample position 2: The scientific mission of this station will be for low-concentration samples, hazardous radioactive or nanomaterials, and samples requiring clean environment or a controlled atmosphere. The "multi-use enclosure" employed here is designed to serve the needs of such samples. Based on designs in the planning stage at two NSLS beamlines, this enclosure would serve as a glove box, open up to operate as a fume hood, or simply be open to atmosphere. Sealed glove-box mode would be necessary for air-sensitive samples or those requiring a specific atmosphere. Examples include a variety of catalysts, redox-sensitive environmental samples, anaerobic biological samples, and atmospheric science applications. Radioactive samples, nanomaterials, and other hazardous materials require containment and often also need ventilation as in a fume hood. The enclosure would operate in that mode with the glove-bearing face opened for access. Policies and requirements as to HEPA filtration and monitoring for these materials will be more clearly defined in conjunction with ES&H personnel as the Project develops. The bottom of the enclosure will be lined with trays made of Teflon or similar materials for ease of cleaning and decontamination. Samples requiring no special care would simply be measured in air.

An important consideration for low-concentration measurements will be the requirement for a clean sample environment. Experience at NSLS X15B with ultra-low (sub-ppm) concentrations demonstrate the need to keep the sample free of dust during analysis, and to eliminate stray scatter from other parts of the hutch. This enclosure will be kept clean. Dust will not be a problem in glove-box mode; for open and fume-hood modes, an air-filtering curtain will be placed across the opening during analysis to reduce dust. As for contamination of the signal by scatter, that will be addressed by applying a collimating cone to the detector snout, and a scatter shield behind the sample.

Components at sample position 2 include the following:

- Support table, fixed height
- Separate table for detector at 90° to beam
- Multi-use enclosure (described above)
- Beam-defining x-y slits
- Ionization chambers for I-zero and transmitted beam measurements
- Sample stage with x, y, z, and rotation motion
- LN2-cooled sample mount
- Camera on sample position (45° to beam), with illuminator
- Multi-element Ge fluorescence detector, with a sealed feed-through into the enclosure
- Nose cone collimator and filter holder for detector
- Set of filters (shared)
- Light-weight helium-filled flight tube to deliver beam to sample position 3 when needed

The detector will be retractable and have height adjustment to center on beam. Experiments at this sample position can take advantage of components at position 1 for additional beam monitoring, analysis of reference samples, etc., or may employ a helium-filled flight tube to efficiently traverse position 1.

Sample position 3: The function of this position will be for any large apparatus that needs more room than is available at the benchtop position. Large magnets, catalytic cells, and large-volume high-pressure assemblies can be wheeled into the hutch in this position.

Components at sample position 2 include x-y slits, available channels for motor control, sample monitoring, and detectors, and approximately 2 x 2 m floor space.

Experiments at this sample position can take advantage of components at positions 1 and 2 for additional beam monitoring, analysis of reference samples, etc., or may employ a helium-filled flight tube as described above.

5.4.4.2 Endstation 1

As a complement to the bulk endstation (having a minimum spot size of about 0.2 x 0.2 mm), Endstation 1 will address microbeam applications for XAS, providing a very high flux (estimated 10^{12} ph/sec at 8 keV) in an approximately 1 x 1 micron spot size, and having the important ability to maintain focus and positional stability over a 1000-eV EXAFS scan. Its scientific mission will center on a) relating micron-scale elemental distribution to physical structure and chemical speciation in heterogeneous materials, and b) XAS measurements of small samples. Obtaining local information in heterogeneous samples is important for such examples as measuring micron-scale variations in catalyst systems, identifying reactive particles and local chemical transformations in environmental samples, exploring biogeochemical processes involving microbes, and relating structure and chemical processes in biological samples. This tool will also be useful for studying reaction and transport processes of nanoparticles in industrial, environmental, and biological systems.

The microbeam endstation also meets a critical need in the study of small samples, such as single crystals, small samples for grazing-incidence surface XAS, small-mass samples of atmospheric or marine particulates, and in nuclear forensics. Recent work at NSLS X27A employs orientation-dependent single-crystal XAS to examine site-dependent substitution chemistry. Atmospheric particulates, critical in cloud formation and global climate research, are naturally difficult to obtain in quantity. The field of nuclear forensics is a new application for microbeam XAS, as it becomes more important to be able to identify, on the basis of trace

particles, evidence of nuclear materials processing or weapons testing. And in high pressure research, microbeam XAS can be applied to diamond anvil cell experiments.

Simultaneous microbeam XRD and XAS is also an important aspect of this endstation, which will share an area detector with Endstation 1. Planned applications include identification of crystalline phases in heterogeneous samples to further characterize structure-function relationships, and to measure crystalline structural variations during local-scale reactions in, for example, catalytic or ion-exchange materials.

The primary mission of this microprobe will be XAS, as it is expected that other beamlines (at undulator sources) will specialize in x-ray fluorescence and XRD imaging at micron or submicron resolution. The optics and source described here are optimized for the stable energy scans required for XAS.

Components at Endstation 1 include the following:

- Support table, fixed height
- Multi-use enclosure (described above)
- Separate table for detector at 90° to beam
- Beam-defining x-y slits
- Miniature ionization chambers for unfocused and focused I-zero, and transmitted beam measurements
- Kirkpatrick-Baez microfocusing mirror set, within enclosure
- Sample stage with x, y, z, and rotation motions
- LN2-cooled sample mount
- Low- and high-resolution microscope cameras on sample position (45° to beam), with illumination
- UV illumination for sample imaging
- Light-weight helium-filled flight tube to deliver beam to Endstation 2 when needed

The sample stage will have sufficient precision for microbeam applications. Conventional K-B mirrors will be used to focus up to 0.1 x 0.1 mrad of on-axis wiggler beam to a ~1 micron spot. The detector will be retractable and have a positioning stage to center it on beam. The area detector for XRD listed in Endstation 2 may also be used in Endstation 1; in order to accommodate it outside the enclosure a large sealed x-ray transparent window will be installed on the downstream end of the enclosure.

This endstation is separated from the three sample positions in the “bulk” endstation for several practical reasons. First, it is a sufficiently different application of XAS that it will benefit from the distinction and the future opportunity to operate in an independent and optimized manner. Second, it improves efficiency to be able to take beam in the upstream hutch while setting up more elaborate experiments in the other. And third, its requirements for beamline optics (angular acceptance, heat load, and the like) differ from the bulk techniques.

5.5 Preliminary Safety Analysis

This section is concerned with Synchrotron and bremsstrahlung radiation protection.

5.5.1 Beamline Radiation Analysis

Geometrical Synchrotron and Bremsstrahlung Ray-Tracing

Please find the relevant synchrotron as well as bremsstrahlung ray tracing schemes in Appendix A. The results of these drawings were derived based on the following documents:

1. Technical Bulletin 20 of the Advanced Photon Source
2. NSLS II Technical Note no 020, Guidelines for NSLS II beamlines..
3. Document SR_lattice_frontend_longstraight_8_22_07.pdf
4. Comments in e-mail of Sushil Sharma about first aperture within the front end

For the creation of the initial ray-tracing files we used the following parameters:

Source point		center of long straight section
Fixed Aperture Mask (FAPM)	19.8 m	
First Pb collimator		20.7 m
Safety shutter position	26.2 m	
End of Front End		28.6 m
Bremsstrahlung source from center of straight section	4 m downstream	
Bremsstrahlung lateral source dimensions	+35 mm	outboard
		Inboard unknown
		Vertical ± 12.5 mm

In addition we defined the following parameters and used those in the evaluation:

Synchrotron radiation miss-steer	±2.0 mm	
Size of the First Aperture Mask:		2.5 mrad (h) x 0.5 mrad (v)

The horizontal size of the first front end aperture was assumed to be 2.5 mrad to take a practical start. We assume that the size of this aperture will be part of future discussions, since this challenging aperture has to be designed together with both ID beams and the goal is that the Front-End delivers only a fan of 1mrad (h) x 0.15 mrad (v). For our ray-tracings we have assumed that there is a further mask just outside the Shield Wall defining the beam to 1 mrad x 0.15 mrad,

Please see Appendix A for the ray-tracing files which were realized using the above input parameters. Those file can be used for detailed discussions and have to be updated when the detailed parameters of the Front-Ends are available.

Further thoughts are needed on the first collimator. Most likely concerning two ID lines (3.5 mrad apart) this collimator will be a combination of an in-vacuum tungsten together with an outside lead collimator.

As it can be seen in the horizontal schemes the size of the beamline collimator inside the FOE is still reasonable. Most interesting is the result on the vertical ray tracing. As it is typically (and practically) done at other beamlines we have placed the beam defining second aperture at the end of the front end assembly right after the ratchet wall. This allows a rather small vertical opening of the collimator in the FOE and therefore an efficient collimation of the Bremsstrahlung at the beginning of the FOE.

Our target is the smallest possible collimator aperture resulting in the smallest possible beam offset of the monochromator. The conflict arises from the requirement to provide enough absorbing material inside the Bremsstrahlung stop between the Bremsstrahlung extremal and the aperture for the monochromatic beam. In this evaluation we follow the assumption that 11 mm are necessary.

In the ray-tracings we have assumed a vertical opening of the first lead collimator in the FOE of 15mm. Under this assumption one needs at least a DCM offset of 30mm to fulfill the requirements at the beam stop. This should be possible and acceptable. By using an in-vacuum tungsten collimator and optimizing the positions one could probably reduce the vertical offset at the DCM to 25mm. But this needs further detailed evaluations based on the more detailed design of the Front-End.

Enclosures:

There will be three beamline radiation enclosures at the XAS beamline, one first optics enclosure (FOE) and two contiguous experimental hutches. The FOE contains all beamline optics, and will be shielded for white beam and Bremsstrahlung scatter. The FOE with its lead-shielded sides interfaces to the ratchet wall of the storage ring. Following the standard regulations for white beam hutches, the labyrinths to run electricity as well as media and power connections will be located on the roof. The hutch will be long enough (approx 17 m) to accommodate the optics for both the original beamline and the canted beamline to be built later. One

double door with sliding panels, large enough to accommodate larger components being moved via fork lift, will provide access to the hutch.

The beam transport between the FOE and the first EH will be a tunnel type (coffin style) transport. Such an enclosure design will provide enough flexibility to accommodate vacuum pipes for both canted beamlines. Shielding interfaces such as guillotines are included.

The FOE will be equipped with an overhead crane (1 metric ton). A summary of the specifications is as follows:

First Optics Enclosure, white beam hutch (FOE)

	Sides 17 m x 3.3 m	Downstream wall 3 m x 3.3 m	Roof 17 m x 2.5 m
Shielding requirements: Lead (mm)	23 mm	50 mm	14 mm

- one extra panel of size 1 m x 1 m x 50 mm at the downstream wall centred at 1400 mm above the floor
- one sliding double door (white beam hutch)
- 10 lockable, hinged chicanes on the roof
- one hutch crane (1 metric ton), on trolley above trace of beam
- one set of guillotine, adjustable shielding around beam pipe on downstream wall
- painted with primer

Shielded Beam Transport (coffin style, base with lid)

- lead shielding of 7 mm thickness
- dimensions: 8 m long, 0.4 m x 0.4 m cross section
- support stands every 2 m with gussets
- painted with primer

First Experimental Enclosure, monochromatic hutch (EH-1)

	Upstream wall 3 m x 3.3 m	Sides 3.5 m x 3.3 m	Downstream wall 3 m x 3.3 m	Roof 3.5 m x 3 m
Shielding requirements: Lead (mm)	6 mm	6 mm	6 mm	5 mm

- one sliding door
- three lockable, hinged chicanes on the roof, three on the sides
- one set of guillotine, adjustable shielding around beam pipe on upstream wall
- painted with primer

Second Experimental Enclosure, monochromatic hutch (EH-2)

	Upstream wall 3 m x 3.3 m	Sides 7 m x 3.3 m	Downstream wall 3 m x 3.3 m	Roof 7 m x 3 m

Shielding requirements: Lead (mm)	6 mm	6 mm	6 mm	5 mm

- one sliding double door
- one sliding single door
- seven lockable, hinged chicanes on the roof, four on the sides
- one set of guillotine, adjustable shielding around beam pipe on upstream wall
- painted with primer

Provision will be made to run cable trays and utilities inside and outside the hutches.

5.5.2 Personnel Safety System

This will be a beamline-specific application of the NSLS-II standard PSS, and will encompass hutch door interlocks, beam-stops, photon and safety beam shutters. Specific components are described elsewhere, and this beamline will utilize one touch-screen panel, one shutter control, emergency-stop and personnel-check provision for all three enclosures, and door interlocks for 1 door on FOE, two on EH1 and two on EH2.

5.5.3 Equipment Protection System

This will be a beamline-specific application of the NSLS-II standard EPS, and will include vacuum, temperature, water flow, beam status, and cryo-cooler status. Specific components are described elsewhere.

5.6 Additional Requirements Imposed on the Conventional Facilities

Endstation multi-use enclosures will need to interface with common exhaust system planned as part of facility.

6 XPD: POWDER DIFFRACTION X-RAY BEAMLINE

6.1 Executive Summary

This chapter describes the design for a damping wiggler based high-energy high-resolution powder diffraction beamline at NSLS-II. This beamline is optimized for high-energy high-resolution x-ray powder diffraction, operating in the energy range from around 20 keV and extending well above 50 keV. This facility will be the only high-resolution instrument in the United States capable of collecting data at high energies and will make it ideal for *in situ* and time resolved studies of samples held in environmental cells. The following sections give a description of the scientific objective of the powder diffraction facility and a conceptual design of the beamline and end-station layout. In proposing a beamline design which could operate effectively, considering the very high power loads that are delivered from the NSLS-II damping wiggler source, the ACCEL x-ray synchrotron beamline design company were hired to arrive at a suitable set of beamline components that would be able to manage these high heat-loads and provide the required optical functions. In this process, a range of scenarios were considered in the design. In this chapter, we highlight our current thinking for such a design, taking some of the concepts and suggestions provided by ACCEL. The scope of this NSLS-II powder diffraction beamline is to provide one high-energy high-resolution x-ray powder diffraction end-station and an additional enclosure for "routine" powder diffraction. This additional enclosure could be equipped with existing NSLS-I equipment and provide an additional facility that could ultimately be served by a canted wiggler source.

6.2 Scientific Objective

The proposed powder diffraction beamline at NSLS-II will be a tunable high-resolution facility with the ability to collect data at high energies (20 keV to 100 keV), offering exceptional capabilities such as fast (milli-second) readout rates and high angular resolution on the same instrument. This will be an outstanding research facility for studying the structure and kinetics of materials under real conditions, and will meet the needs of the powder diffraction user community. For example, there are dedicated powder diffraction facilities at ESRF (BM16, ID31), DIAMOND (I11, I15), APS (sector 16, 5-BM-C, 6ID-B,C,D, 12-BM-B, 33BM-C), SOLEIL (CRISTAL, HighPressure, MARS, SIXS), the Swiss Light Source (MS), and the Australian Synchrotrone. Powder diffraction has widespread scientific interest, such as in the fields of metallurgy, solid-state chemistry, nanomaterials, microelectronics, mineralogy, and the biological and pharmaceutical sciences. In addition, the study of condensed matter at extreme conditions is developing into a very rich field of research. In situ elastic scattering provides the data required to derive structure models, which is essential to systematic searches for new classes of materials and to rationalizing their desirable properties.

The proposed NSLS-II powder diffraction beamline will be the only high-resolution instrument in the U.S. that is capable of collecting data at high energies, which will make it ideal for in situ and time-resolved studies of samples held in environmental cells in which the pressure, temperature, and chemistry can be varied. The high-energy x-rays will be able to propagate through environmental cells, allowing for the investigation of materials made up of high-Z components, and enabling high-q accessibility, which is crucial for atomic pair distribution function analysis and high-pressure cell research. By employing a high-resolution crystal analyzer array, this new instrument will allow enhancement, through suppression of the fluorescence and Compton components (including diffuse scattering), required to evaluate technologically important disordered materials. Due to the inherent small instrumental (and source) broadening, the high resolution of

the crystal array will enable the measurement of accurate peak-profiles, thus allowing the investigation of strain, lattice defects, and micro-structure. The implementation of a fast position-sensitive strip-array detector will also allow the real-time , microsecond timescale study of phase transitions, transformations, and catalytic reactions as a function of temperature, chemical gradients, and pressure. For combinatorial science and screening, robotic sample changers will facilitate rapid sample change and high-throughput data collection.

The great interest and excitement in the proposed NSLS-II powder diffraction beamline was evidenced at the NSLS-II user workshop held on July 17 – 18, 2007, where a breakout session on powder diffraction (http://www.bnl.gov/nsls2/workshops/UserWorkshop_BOS1.asp) was attended by more than 50 people. During this workshop, ideas on the capabilities of the beamline and research areas were discussed. In these early stages of the project, a beamline access team (BAT) is beginning to form and a further workshop is to be held on November 30, 2007.

6.3 Insertion Device

The powder diffraction beamline will be located on a damping wiggler source, which is located in a high-β straight-section of the NSLS-II ring. Unlike the NSLS-II undulator, bending-magnet and 3-pole wiggler sources, the NSLS-II damping wiggler extends the range of high energy x-ray access well beyond the 50 keV region, thus allowing the study of samples under real conditions, i.e. in environmental chambers. The basic parameters for the damping wiggler source used in this design are shown in the tables below Tables 6.1

Table 6.1 NSLS-II Machine and Damping Wiggler Parameters.

NSLS-II Machine & Damping Wiggler Parameters	
Electron energy, Eo	3 GeV
Electron current, Io	500 mA
Number of periods	70
Period length, λu	10 cm
Magnetic field	1.8 Tesla
Deflection parameter, k	16.81
Critical energy	10.8 keV

Table 6.2 RMS Electron Beam Values at the Center of the High-β Straight Section.

Root-Mean-Square electron beam values at the center of high-β straight-section	
Horizontal electron beam size, σ_x	99.0 μm
Vertical electron beam size, σ_z	5.5 μm
Horizontal electron beam divergence, σ_x'	5.5 μrad
Vertical eectron beam divergence, σ_z'	1.8 μrad

We note that as a result of optimization of the damping wiggler design, the period of this device has subsequently been refined to 90 mm. This has the advantage of reducing the angular fan of the radiation, making canting two devices more practical. While this is not expected to have a large impact on the design considerations presented here, it will be necessary to reevaluate any of these issues in light of the new source design.

Figures 6.1 and 6.2 show the flux (integrated over 3 mrad horizontally) and brightness values for the various NSLS-II sources. With a critical energy of 10.8 keV, the NSLS-II damping wiggler has flux values of 1.7 x 10^{15} (at 20 keV), 3.3 x10^{14} (at 40 keV), 5.6x10^{13} (at 60 keV),1.0x10^{13} (at 80 keV) and 1.4x10^{12} (at 100 keV) ph/sec/0.1% BW/mrad. The corresponding brightness values are 2.2x10^{18} (at 20 keV), 1.0x10^{18} (at 40 keV), 5.7x10^{17} (at 60keV), 2.6x10^{17} (at 80keV) and 1.2x10^{17} (at 100 keV) ph/sec/0.1%BW/mrad2/mm^2.

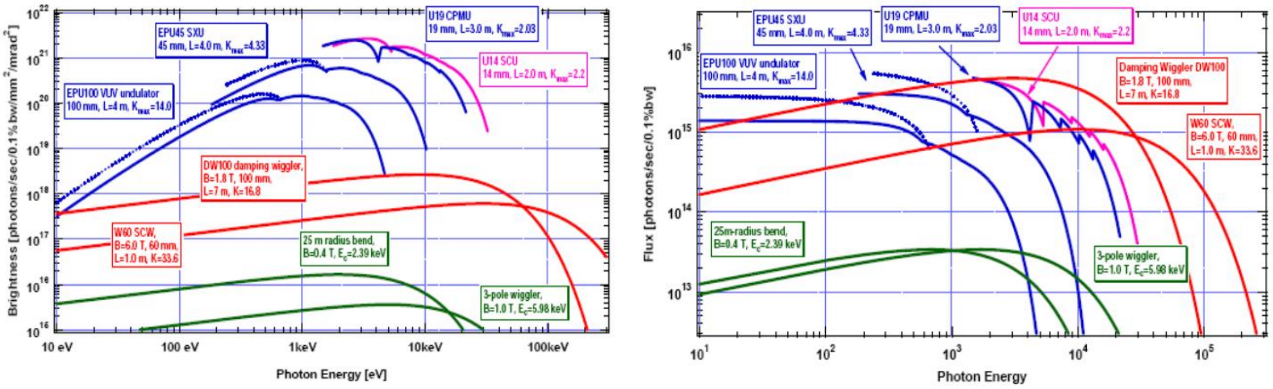

Figure 6.1 Flux and brightness curves for the various NSLS-II sources, including the 7.0m-long damping wiggler source.

Figure 6.2 shows the flux and brightness comparisons between the NSLS-II damping wiggler source and the existing NSLS X17 super-conducting wiggler (a high-pressure diffraction beamline). As is evidenced by these plots, the NSLS-II damping wiggler source exceeds the X17 source output and will make the proposed high-energy high-resolution powder diffraction beamline at the NSLS-II machine a very powerful facility.

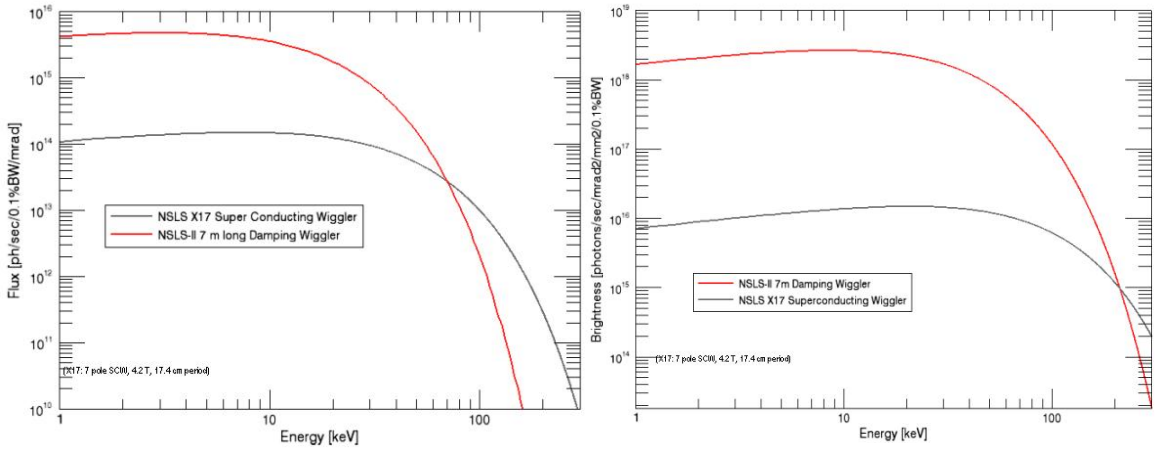

Figure 6.2 Flux and brightness comparisons between the NSLS-II 7m long damping wiggler source and the NSLS-I super-conducting wiggler.

6.4 Sector Layout

The following sections describe the conceptual configuration of the NSLS-II powder diffraction facility.

6.4.1 Front-End Layout

A layout of a typical front-end is shown below (SGV: slow gate valve; FAPM: fixed aperture mask, XBPM: photon BPM; CO: lead collimator; FGV: fast gate valve; SS: safety shutter). The components that are not shown are: 1) ratchet wall collimator (a beam pipe going through the ratchet wall and surrounded by lead), and 2) a gate valve downstream of the ratchet wall collimator (this gate valve can be removed after commissioning).

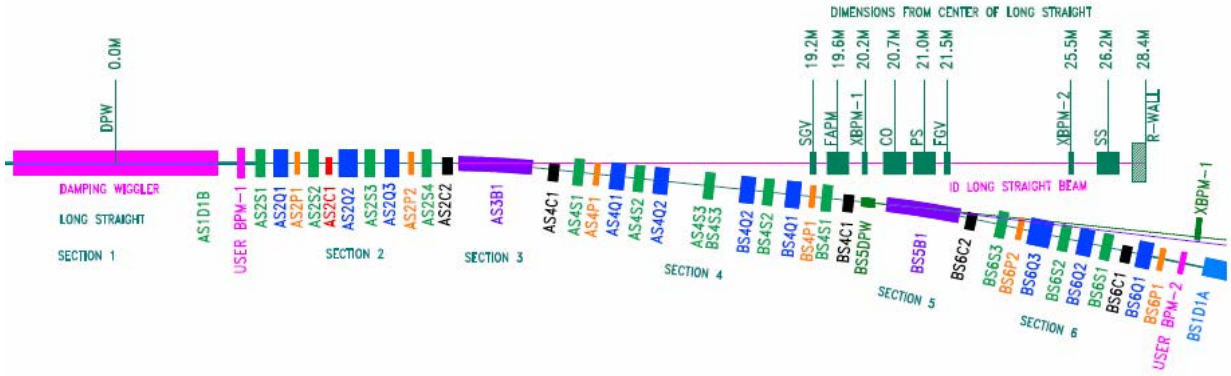

Figure 6.3 Front-end layout plan of NSLS-II.

For the NSLS-II powder diffraction beamline, the fixed aperture mask (FAPM) will limit the angular acceptance to 1 mrad (H) x 0.15 mrad (V) and reduce the power load on the downstream optical components (see Section 6.4.3). In addition, white-beam X-Y slits will be situated between the second x-ray beam position monitor (XBPM-2) and the fast gate valve (FGV), to further reduce power loads and reduce the angular acceptance, if required.

6.4.2 Beamline Layout

From discussions with the user community, potential BATs, and vendors, a conceptual design of the NSLS-II powder diffraction has been devised that would meet the requirements for a high-energy high-resolution facility. Furthermore, the beamline will be designed in way that it allows the addition of a second beamline, which could be served using a second canted wiggler in the same straight section.

Outlined in the tables below are the beamline performance, as described by the various operational modes. All flux values assume a 1mrad (H) x 0.1 mrad (V) acceptance.

Table 6.4 lists the photon flux, in units of ph/sec/0.1%BW, before and after the 1.5m-long Pt-coated vertically focusing/collimating mirror, which operates at a fixed grazing incidence angle of 2 mrad. For operations above 40 keV, where the mirror reflectivity falls considerably, it is withdrawn from the optical path. Reflected in these values are 5 mm of carbon pre-filters.

Table 6.4 Flux at and after the vertical focusing mirror, which is located in the front optical enclosure.

Energy [keV]	Flux at Mirror (with 5 mm carbon) ph/sec/0.1%BW	Flux after mirror (withdrawn for > 40 keV) ph/sec/0.1%BW
20	$4.6x10^{14}$	$3.7x10^{14}$
40	$1.7x10^{14}$	$1.2x10^{14}$
60	$3.7x10^{13}$	
80	$7.2x10^{12}$	
100	$1.3x10^{12}$	

Tables 6.5 and 6.6 detail the x-ray flux, in units of ph/sec, at the sample position (location H in the high-resolution enclosure – Figure 6.4, 57.7 m from the damping wiggler source), using both sagitally-focusing silicon-111 and -311 double-crystal Laue monochromators. The bandpass of these crystal orientations are noted in the table captions. The horizontal focused beam size (FWHM) are estimated from the ~2:1 focusing of this device and current NSLS measurements (see section 6.4.3.3). In the vertical direction, the 1.5 m long mirror in the FOE can deliver a focused 400 μm (FWHM) beam and a 3 of mm beam in the high-resolution/collimating mode, below 40 keV.

Table 6.5 Bent Laue Mode (2:1 focusing): dE/E ~$1x10^{-3}$ – Si(111). 0.5mm-thick Laue crystals and 2mm silicon pre-filter. 5 mm carbon.

Energy [keV]	Flux at sample [ph/sec]	Beam dimensions at sample
20	1.8x1013	300 μm (H) x 400 μm (V) / 3mm – mirror in
40	1.1x1014	300 μm (H) x 400 μm (V) / 3mm – mirror in
60	3.0x1013	300 μm (H) x 5 mm (V)
80	6.2x1012	300 μm (H) x 5 mm (V)
100	1.1x1012	300 μm (H) x 5 mm (V)

Table 6.6 Bent Laue Mode (2:1 focusing): dE/E ~$1x10^{-4}$ –Si(311). 0.5mm-thick Laue crystals and 2mm silicon pre-filter. 5 mm carbon.

Energy [keV]	Flux at sample [ph/sec]	Beam dimensions at sample
20	7.2x1012	300 μm (H) x 400 μm (V) / 3mm – mirror in
40	4.4x1013	300 μm (H) x 400 μm (V) / 3mm – mirror in
60	1.2x1013	300 μm (H) x 5 mm (V)
80	2.5x1012	300 μm (H) x 5 mm (V)
100	4.4x1011	300 μm (H) x 5 mm (V)

For very high-resolution powder diffraction work, the Laue crystals can be unbent to eliminate contributions to the vertical beam divergence that can be induced by the sagittal bending. In this mode, the flux and beam size values are shown in Table 6.7. To reduce the horizontal beam size, we propose to use a graded multiplayer focusing optic within the experimental enclosure. Table 6.8 shows both the x-ray flux and beam dimensions for this mode of operation.

Table 6-7 Unbent Laue – for high resolution. dE/E ~1x10^{-4} – Si(111)

Energy [keV]	**Flux at sample** [ph/sec]	**Beam dimensions at sample**
20	1.8x1012	5.8 cm (H) x 400 μm (V) / 3mm – mirror in
40	1.1x1013	5.8 cm (H) x 400 μm (V) / 3mm – mirror in
60	3.0x1012	5.8 cm (H) x 5 mm (V)
80	6.2x1011	5.8 cm (H) x 5 mm (V)
100	1.1x1011	5.8 cm (H) x 5 mm (V)

Table 6.8 Unbent Laue – for high resolution. dE/E ~ 1x10^{-4} – Si(111) + 0.5mm-long graded multiplayer optic.

Energy [keV]	**Inc. Angle** [mrad]	**Hor. Accep.** [mm]	**Flux at sample** [ph/sec]	**Beam dimensions at sample**
20	7.7	3.15	9.8x1010	14 μm (H) x 400 μm (V) / 3mm – mirror in
40	3.9	1.95	3.7x1011	14 μm (H) x 400 μm (V) / 3mm – mirror in
60	2.6	1.3	6.7x1010	14 μm (H) x 5 mm (V)
80	1.9	0.95	1.0x1010	14 μm (H) x 5 mm (V)
100	1.5	0.75	1.3x109	14 μm (H) x 5 mm (V)

The conceptual layout for the NSLS-II powder diffraction beamline is shown in Figure 6.4. The beamline consists of the following optical components:

A. a pre-filter and beryllium window – to isolate the beamline from the machine vacuum, and a filter unit to limit the power load on the downstream optical components

B. a 1.5 meter long bendable focusing/collimating mirror operating at a fixed grazing incidence angle of ~ 2mrad, which will be coated with platinum and be able to function up to 40 keV. Above this energy, this mirror will be withdrawn from the optical path

C. a sagitally focusing double-crystal Laue monochromator to provide focusing and wavelength selection, with the required band-pass

D. beam monitoring unit

E. a monochromatic photon beam shutter

F. sample position in the upstream experimental hutch (endstation equipment not in the scope of this project)

G. a horizontal focusing graded multiplayer for focusing the beam onto small samples at H

H. a sample position in the downstream experimental enclosure

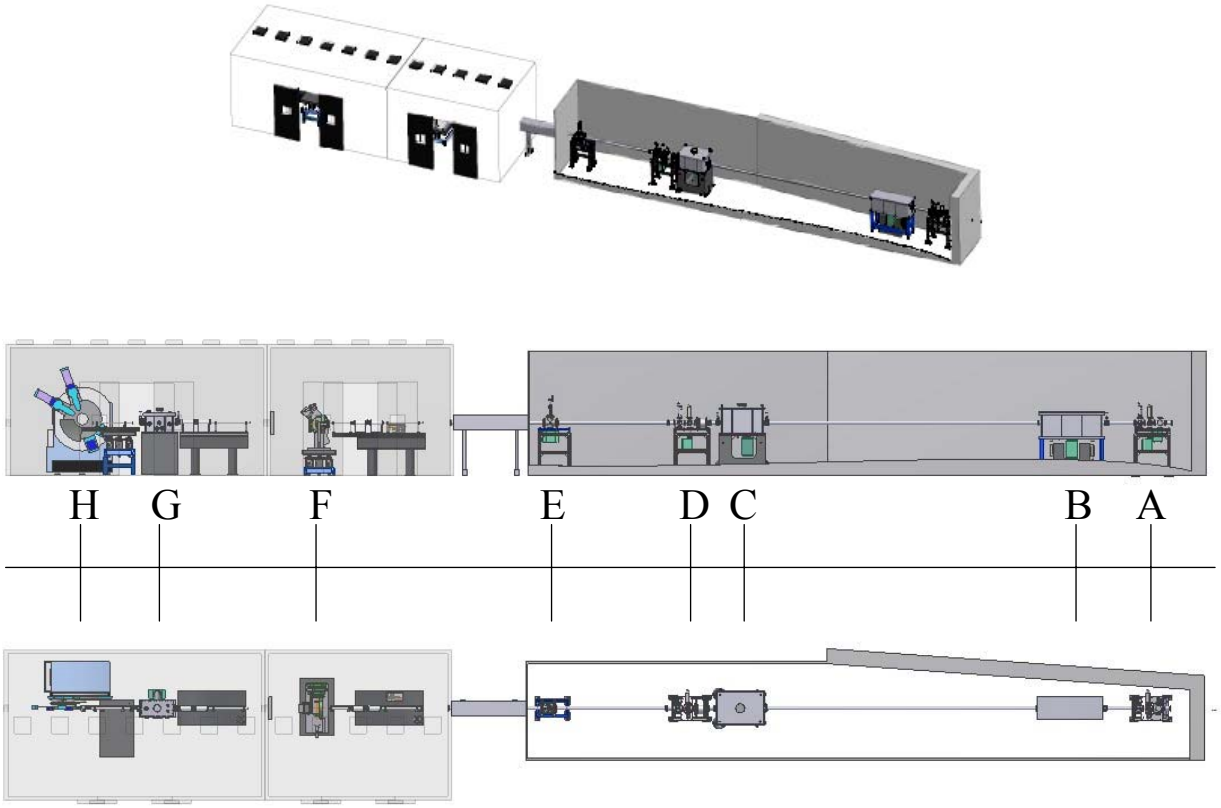

Figure 6.4 Conceptual layout for the powder diffraction beamline.

Table 6.9 Distances of the various components from the conceptual layout of the powder diffraction beamline.

Component	Distance from Source
A. Be window and Filter Unit	29.0 m
B. 1.5m-long focusing/collimating mirror	31.1 m
C. Sagitally Focusing Double-Crystal Laue Monochromator	40.0 m
D. Beam Monitoring Unit	41.36 m
E. Monochromatic Photon Shutter	45.1 m
F. Upstream Sample Position	51.3 m
G. Horizontally Focusing Graded 0.5 m long Multilayer	55.6 m
H. Downstream Sample Position	57.7 m

6.4.2.1 Survey and Alignment Plans

All beamline components will be surveyed and aligned in place by the facility. To facilitate ease of alignment, all components will be fiducialized to external reference points on their table during assembly. All components are designed with a liberal tolerance allowance greater than 0.5 mm.

6.4.2.2 Utility Layouts

Cooling water is required for all high-heat components. Requirements for the standard cooling water supply and the components and flow rates that are needed are shown in the tables below.

Table 6.10 Cooling water requirements for the XPD.

Approximate Temperature	20°C to 30°C
Temperature Stability	± 1°C
Maximum Pressure	6 bar
Pressure Stability	± 0.1 bar
Quality	de-ionized but not ultra-pure

Table 6.11 Flow requirements for the various XPD optical components.

Component	# of Circuits	Max. Consumption
Pre-Filter and Be window	1	4 l/min
Attenuator Units	4	8 l/min
Vertical Collimating/Focusing mirror and mirror protection mask	1	12 l/min
Thermal Stabilization and Cooling of Laue mono	1	Local Chiller
White Beam Stop	1	4 l/min

The cryo-cooler unit for the double-crystal Laue monochromator requires connection to a liquid nitrogen supply. It is recommended to have a liquid nitrogen supply within 2 to 3 meters of the final cryo-cooler position. The following components must be connected to a dry, filtered compressed air supply having a pressure of between 70 psi and 100 psi: the monochromatic photon beam shutter, all gate valces and the pneumatically driven attenuator filter units. There are three main areas where electrical power is required:

- Control system cabinets: A central 3-phase power distribution should be placed near the cabinets. In total, approximately 12 kW are required,
- Cryo-cooler unit: This unit needs a 1-phase power distribution of approximately 2.5 kW,
- Enclosures:

Within the hutches, two types of power outlets should be provided for each section: a low-noise outlet for measuring equipment and a standard outlet for mobile pumps and heaters. The outlets should be distributed along the length of each enclosure. The required power in the front optical enclosure could be up to 30 kW to accommodate the extreme case where the full beamline may be pumped and baked at the same time. Along the beamline a grounding bar is needed, to ground the beamline components. The grounding bar must be connected to the central power distribution ground.

6.4.2.3 Beamline Vacuum System

We have assumed that there will be several vacuum sections, isolated from each other through gate valves. Each vacuum section will be equipped with one ion pump and has one rectangular all-metal valve, CF40, to rough down the vacuum using a pump cart and to vent the section. The monochromator is equipped with one all-metal valve CF16 for venting and, in addition, with a CF63 gate valve where a turbo molecular pump will be permanently mounted. Each section is also equipped with a full-range vacuum gauge. The white

beam part of the beamline will be realized to be bakeable in order to achieve a vacuum pressure below 10^{-9} mbar. The monochromatic part is designed to achieve a base pressure in the 10^{-8} mbar range. Besides the large flanges of the monochromator doors (that are Viton sealed) and of the mirror vessels (metal sealed for the VCM and Viton sealed for the VFM) all flanges will be realized according to the Conflat standard.

The layout of a typical vacuum system for one beamline section, and a general overview of the entire vacuum and EPS systems are shown in Figure 6.6.

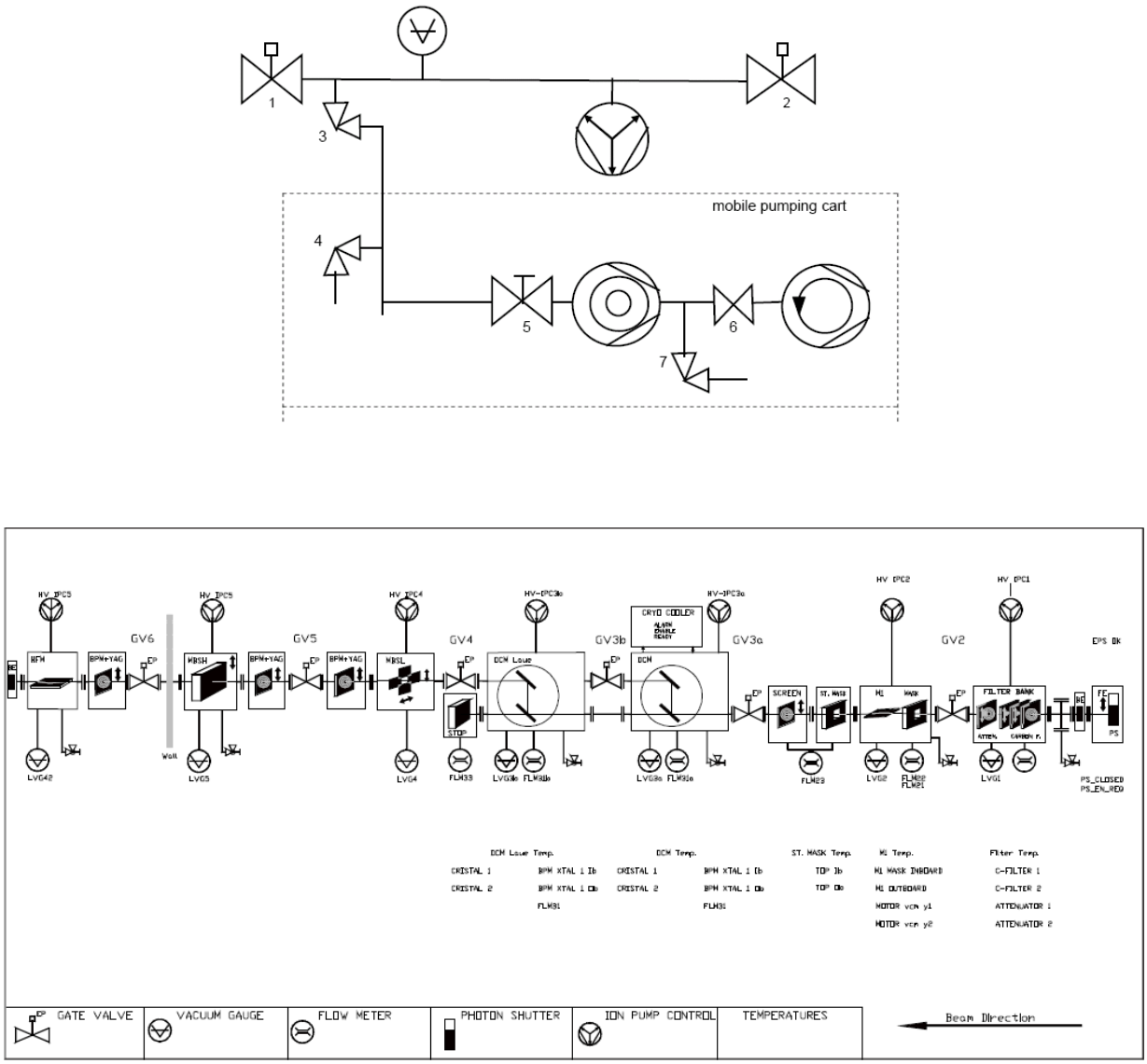

Figure 6.6 **Top**: 1,2 : Sub-section isolation valves. 3: full metal right-angled valve attached to the BL-section. 4: Right-angled valve to vent either the sub-section or the pumping station. 5: hand actuated gate valve CF63. 6: valve to separate the pre-pump from the leak detector. 7: valve to connect the leak detector. **Bottom**: General schematic overview of the entire vacuum and EPS system. The DCM indicated in the drawing is from earlier design considerations, and does not exist in the current configuration.

6.4.2.4 Beamline Control, Motion Control, and EPS

This section covers a general specification for a beamline control system, including the Equipment Protection System (EPS) and the vacuum controls as it could be realized for a NSLS-II beamline. The particular control system chosen here is based on Delta-Tau hardware and Experimental Physics and

Industrial Control System (EPICS) software. The EPS is based on a PLC unit and covers the vacuum monitoring and control as well. This document provides the specifications for the design of a typical beamline control system (BLCS). The beamline control system is the electronic hardware and software interface between the beamline operator and the beamline components. It must be versatile and robust to allow the operator reliable remote control of the beamline components and endstation hardware for the purpose of aligning the beamline and conducting experiments in a precise and yet safe and protective way. It should also have the capability of easily implementing high-end automation. The complete BLCS for the beamline consists of the software and hardware for the following subcomponents:

- control of the full beamline (through EPICS IOCs)
- motion control
- beamline diagnostics
- vacuum control
- beamline equipment protection system (BLEPS)
- control of the closed-loop cryo-cooler

The overall hardware and software architecture is determined by the use of EPICS for beamline control. Within this architecture, field I/Os (i.e., signals from beamline components, experimental stations, etc.) are concentrated in controllers called EPICS IOCs. There can be several EPICS IOCs per beamline. These IOCs communicate to EPICS channel access clients (operator workstations), other EPICS IOCs and embedded EPICS IOCs using TCP/IP. Through these IOCs, the control of the motion of the component axes, detectors, feedback, interfacing to the BLEPS, etc. is established. From an EPICS client, a user can remotely operate the beamline through operator interfaces. Previous releases of EPICS Base required that EPICS IOCs use a vxWorks operating system. However, EPICS Base Release 3.14 has allowed the configuration of operating systems such as Unix, Linux, and Windows as EPICS Soft IOCs. With this configuration, use of non-VME hardware is now possible, lending greater flexibility in the choice of control hardware.

6.2.4.5.1 Overall Beamline Control

The BLCS uses many hardware and software interfaces to establish communication between the various devices that constitute the beamline. The design of the BLCS aims to combine the advantages of having centralized control for convenience of software maintenance and upgrade and yet distributed intelligence for more flexibility, better cable management and housekeeping. All cabling from the beamline components can be routed to control cabinets located near the optics and hutch. Figure 6.7 shows a possible layout of the beamline control devices and the communication interfaces.

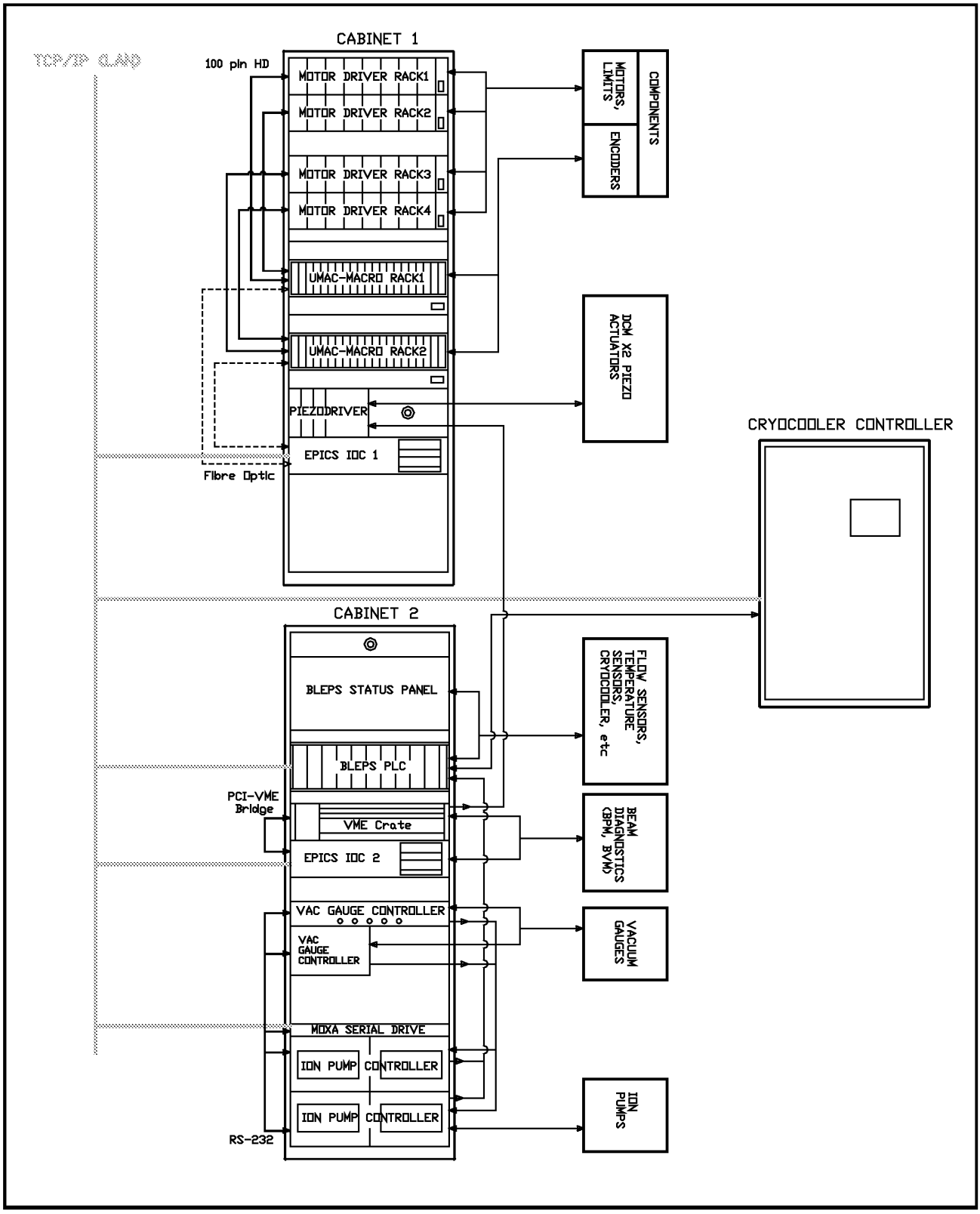

Figure 6.6 Possible layout of the powder diffraction beamline control system.

The beamline control hardware will be housed in two 19-in. control cabinets or racks. The cabinets will consist of several control crates where a crate is a 19-in., variable-height enclosure. The crate types are listed in Table 6.11.

Table 6.11 Possible Crate Control Configurations for the Powder Diffraction Beamline.

Crate	Function
EPICS IOC	A workstation PC running a Linux O/S and configured as an EPICS SoftIOC. It will have PCI slots populated with the motion controller and signal processing cards.
UMAC MACRO Crate	The distributed interface to the stepper motor drivers, encoders, motion control related DIO and AIO
Stepper driver crates	8-axes stepper driver crates
Piezo controller	Control for the piezo actuators
BLEPS	The BLEPS PLC, I/O modules and Status Display Panel
Vacuum gauge control	For readout of the vacuum gauges installed on the beamline
Ion pump controllers	Each controller serves two ion pumps. Two controllers occupy 19-in. x 3HU.
MOXA Serial Drive	Provides serial ports for communication of serial devices with the EPICS IOC. It communicates with the EPICS IOC through TCP/IP.

Each cabinet has an input power requirement of 3-phase/400VAC, 20A. The 3-phase supply is broken out into three single-phase 230VAC supplies within the cabinet which powers the instrumentation crates.

The cryo-cooler control unit will be a stand-alone unit comprising all the control electronics for controlling and monitoring the liquid nitrogen cryo-cooler. It will contain its own PLC for signal processing and alarm handling and will communicate with the beamline EPS through TCP/IP (and hardware connections, if required) to perform specific safety interlock tasks. It will also have a local control/status panel for constant monitoring independent of the network.

These are local electronics that need to be located close to components and are mounted onto the support structures of the components. Local electronics include interpolators for electronics and LVDT readouts. The LVDT readouts output 0-10 V analog signals which will be routed to an ADC readout in the control cabinet.

The beamline will be controlled through EPICS. The EPICS environment will consist of: 1) IOCs running Linux, 2) EPICS Base 3.14.7 or higher, and 3) State Notation Language/Sequencer sequence programs: MEDM and EDM, other EPICS extensions as required, and SynApps.

The control hardware used in the powder diffraction beamline should be supported through EPICS device driver and device support modules. Purely soft support modules are also required to provide useful functions such as data acquisition, scanning, save/restore, user calculations, etc. Through these modules a user, sitting at an EPICS client, can communicate with the EPICS IOCs, the EPICS IOCs can communicate with the control hardware, and the hardware components communicate with each other. The operator interfaces will be the GUIs through which a user operates the beamline. GUIs will be developed with MEDM or EDM.

Beamline motion control refers to the control of all the movable axes of the beamline, the readback of the encoding elements, and the activation of protective switches that limit over-travel. Furthermore, when incremental encoders are used, homing mechanisms should be incorporated for calibration of the absolute position of the axis. Motion control hardware includes the following: 1) motion controller system, 2) motor amplifiers/drivers, 3) connection hardware (interface panels, connectors, cable), 4) Limit/Home switch hardware, and 5) encoder hardware.

For motion control hardware, we are considering the intelligent motion controllers from Delta Tau due to their excellent performance for synchronized correlated motions and for their flexibility. The MACRO[1] distributed system consists of two 32-axis motion controllers residing in PCI slots of the EPICS IOC1, connected through fiber optics to UMAC-MACRO crates. These UMAC-MACRO crates can be customized to output signals supporting several types of motors, digital and analog I/Os, and encoder inputs.

Each 19-in. UMAC-MACRO crate can support up to 32 motorized axes. Each set of eight axes in the UMAC-MACRO connects to one eight-axis motor driver crate. The Turbo PMAC2 PCI Ultralite is a member of the Turbo PMAC family of boards optimized for interface to the system through the MACRO ring. It can command up to 32 axes through the MACRO ring. The Turbo PMAC2 PCI Ultralite is a full-sized PCI-bus expansion card. This card is capable of PCI bus communications, with or without the optional dual-ported RAM (DPRAM).

For this beamline control, the card will be delivered with the DPRAM option. Standalone operation is also possible, and communications can occur through an RS-232 port. Through the rest of this chapter, the 32 axis PMAC2 motion controller will be referred to as the PMAC. MACRO is an acronym for Motion and Control Ring Optical and is a non-proprietary digital interface developed by Delta Tau for a single-wire connection between the multi-axis motion controllers, amplifiers, and I/O through a fiber optic ring. The MACRO minimizes wiring complexity, reduces hardware, and eliminates noise in large systems. The high-speed 125 Mbits/sec transfer rate is capable of closing the servo loops across the MACRO ring, allowing the flexibility to choose distributed intelligence or centralized control. The 16-axis UMAC MACRO CPU provides a remote interface for encoders, flags, direct-PWM digital drives, analog drives, and/or digital I/O for a Turbo PMAC2 with MACRO interface. It communicates with the Turbo PMAC2 solely through the MACRO ring, but interfaces to standard drives, encoders, flags, and Opto-22 style I/O through on-board connectors. It is designed to run up to 16 motors. Through the rest of this chapter, the 16-axis UMAC MACRO CPU will be referred to as the UMAC.

An interface board between the UMAC-MACRO Crate and the Stepper Driver Crate forwards the step/direction signals and returns the limit/flag signals. Each board provides signals for eight axes and connects to the stepper-driver crate through a standard 100-pin, high-density connector. This interface board will be mounted on the rear of the UMAC-MACRO crate.

Bipolar stepper drivers will be provided to match the requirements for the specific axis in terms of torque requirements, drive currents, and micro-stepping. All motorized axes on optical components (monochromator and mirrors) and slit systems will be encoded with incremental encoders (quadrature or analog). All motorized axes will be fitted with limit switches to determine the travel range and to protect against mechanical damage caused by over-travel. These switches are externally mounted and can be adjusted to set a required travel range. The limit switch contacts are configured to be “normally closed.” Homing of the component axes, to zero the counter, is performed using the precision end switches. Table 6.12 lists typical types of cables and connectors.

Table 6.13 List of possible cables and connectors for the powder diffraction beamline.

Function	Cable Type	#CondPairsxCross-section	Connector
Motor	Facility standard	4x2x0.75mm^2 + 6x0.25mm^2 (separately shielded)	Trim-Trio Souriau e.g. UTO014-12ST
EPS SIGNALS	Unitronic LiHCH (TP)	4x2x0.25 12x2x0.25	SubD-9 (valves, flow, pressure) SubD-25 (temperatures)
Quadrature ENCODER	Unitronic LiHCH (TP)	8x2x0.25	SubD-15
Analog Encoder	Belden 8164	4x2x0.23	SubD-15
D/A/Video SIGNALS	Coxial	RG58U, RG174	BNC, Lemo

[1] Motion and Control Ring Optical

The motion control software is determined by the use of the Delta Tau motion controller and the EPICS control software. PMAC Executive Pro Suite is a Windows-based suite of programs, running on Windows XP and 2000, that communicates to the PMAC through its serial port. It allows standalone operation of the motion controller for initial configuration of the hardware and for testing of connections to the stepper drivers. It also contains tuning and plotting programs useful for performance demonstration and debugging at a lower level. Uploading and downloading of files and variable settings is possible for quick configuration and saving/restoring of settings.

The EPICS support for the PMAC2 controller will also contain a set of setup files that must be downloaded to the PMAC. These files are not EPICS specific but are required to set up the communication of the EPICS IOC to the controller. They will be preloaded to the PMAC/UMAC prior to establishing EPICS communication. As mentioned before, our design is based on control of the motion of the component motors though EPICS through the support developed for the Turbo PMAC2 PCI Ultralite motion controller currently in use at the XAS beamline at the Australian Synchrotron.

Beam position monitors will be installed along the beamline as diagnostic elements. To read out the current signals from these monitors, use of compact quad-electrometer electronics are considered. These devices are supported in EPICS and can be used to feed back the BPM signal to a piezoelectric actuator via a 16-bit DAC. They can also be used for ion chambers.

There will be beamline vacuum control and monitoring instrumentation, consisting of a vacuum gauge controller, the Pfeiffer Maxiguage TPG256A, and the ion pump controllers. The vacuum gauge controller and the ion pumps will interface to the EPICS IOC via their RS232 ports. RS232 ports are provided by the MOXA Nport5610-8 serial device server which communicates to the EPICS IOC via TCP/IP. Vacuum level readouts from the vacuum gauges will be input into the vacuum controller which will compare the readings against preset trip points. Status of these trip points are directly wired to the BLEPS as digital inputs. The status of the HV of the ion pumps is directly monitored by the BLEPS. Through EPICS, the pressures read by the vacuum gauges will be remotely available.

The primary purpose of the beamline EPS is to protect the individual beamline components against x-ray damage, loss of vacuum, loss of coolant flow (water and liquid nitrogen), and elevated temperatures. The beamline EPS communicates with the Beamline Personal Safety System (BLPSS) PLC and with the Front End EPS and Front End PSS (FEEPS, FEPSS) through specified interface signals. Communication to the EPICS IOCs is via modbusIP. The EPS hardware will be based on the Programmable Logic Controller (PLC) technique (e.g., Schneider Electric TSX Premium), including a CPU (TSXP572634M) with an Ethernet interface. The BLEPS hardware will consist of an approximately 4HU 19-in. crate (CPU and I/O modules) and a 6HU local display panel. The display panel will be an etched aluminum plate with green/red LEDs to indicate satisfactory/unsatisfactory conditions of the relevant component signal. The BLEPS PLC will be programmed to take protective actions in the case of detection of unfavorable conditions in the beamline.

Control and monitoring of the PLC will be available through GUIs and will offer the following functions: 1) Monitoring: EPS alarm status, beamline gate valve status, temperature values, flow trip points status, pressure trip point status, ion pump HV status, cryo-cooler ready/alarm/enable status, pneumatic actuator position status, and conductivity meter readings; and 2) Control: beamline gate valves and pneumatic actuator insertion/retraction.

For ease of configuration of the BLEPS, the beamline will be divided into EPS vacuum sections. The vacuum sections are defined based on the specific beamline component configuration and the need to isolate the components. Vacuum sections are bounded by gate valves. Based on information on the beamline design and requirements for communication with other sections of the beamline control system, interface signals will be determined. All relay contacts are “normally open” (N/O), 24 VDC Flag return signals. In general, the following type of beamline signals will be monitored by the BLEPS: process cooling water (PCW) flow, conductivity, critical device temperatures (filters), fixed and “disaster” masks,, monochromator crystals, vacuum, cryo-cooler status, gate valves position, pneumatic-driven filters, and beam position monitors.

The cryo-cooler controller is a stand-alone control cabinet which controls the closed-loop liquid nitrogen circuit used to cool the monochromator Laue crystals. It interfaces to the EPICS IOC for remote monitoring and control and to the BLEPS for communication of ready status and alarm signals.

6.4.3 Beamline Components

The following items describe the various beamline components for the high-energy, high-resolution powder diffraction beamline.

6.4.3.1 White Beam Slits

These components are included in the front end (Section 6.4.1), thus they do not belong to the scope of supply for the beamline.

6.4.3.2 Pre-Filter, Beryllium Window, and Attenuators

In hard x-ray beamlines, one typically uses a beryllium (Be) window to separate the beamline vacuum from the machine vacuum. Such a window has also the advantage that it absorbs a good fraction of the unused low energy x-ray spectrum, therefore reducing the overall power dumped on downstream components. However, in a wiggler beamline such as the NSLS-II DW 100 described here, calculation of the absorbed power indicates that a Be window in the direct of white beam from the wiggler simply would fail. Due to carbon's high thermal conductivity and mechanical stability, carbon foil(s) is (are) typically used as a protective filter material in front of or instead of a Be window. The combination of carbon filters and Be windows must be carefully tailored, taking into account both the absorbed heat load and the requirement for the highest possible flux transmission at lower energies. Our approach is to design a filter assembly that can be safely used whenever required, to reduce the power levels on the optical components.

Reduced power always will improve the performance of white beam optical components such as the focusing/collimating mirror and the sagitally-focusing double-crystal Laue monochromator. Considering the high heat load that is produced by the wiggler, the carbon filter unit is an essential component for maintaining sustainable power levels along the powder diffraction beamline. With respect to the heat load absorbed by the most upstream filter, a standard water-cooled graphite filter cannot cope with the high heat load. From experience at other facilities using similar powerful sources, we considered two possible solutions: 1) Using thin C foils which are only radiation cooled. In that case the foils become extremely hot – up to 1500°C and higher. 2) Using high-thermal-conductivity highly oriented pyrolytic graphite (HOPG) foils to form a filter frame, which can be safely water cooled.

In the following paragraphs some proven designs are summarized:

ALS, Beamline 5.0[2]

HOPG is clamped between two water cooled copper frames and absorbs 10 W/mm^2 (250 μm). The contact pressure is finely adjusted by springs. Temperatures up to 1000K are possible. After more than one year operation, there is no visible damage on the HOPG foil.

NSLS, MGU-undulator-beamline[3]

A stack of radiative cooled foils successfully withstand the power load from a wiggler (3.4 W/mm^2). They use seven foils, starting from 5 μm up to 51 μm. After a few years of operation, no visible damage can be observed on the foils. In addition it has been verified that the temperature of the foils is somewhat lower

[2] Private communication with D.Cambie; "Annealed Pyrolytic Graphite filter for beamline 5.0 at the ALS" - D.Cambie, C.Cork – MEDSI proceedings 2004

[3] private communication with P. Montanez and L. Bermann

than the calculated value. This system has proven to work reliably up to temperatures of 1000°C and slightly higher.

CHESS, wiggler-beamlines[4]

A HOPG foil was brazed directly to a copper block (12 W/mm^2 on 250 µm). Some cracks observed in the foil most likely were caused by the cooldown process during brazing. The system worked for some time, but failed with doubled power load. The replacement design has operated without failure for several months. The HOPG is clamped on two sites in a copper frame with improved water-cooling performance (jet-stream-cooling, very closed to the edge of the HOPG).

The consultant evaluated the behavior of the first filter unit for the power load of the damping wiggler source (please refer to Appendix D), demonstrating that both options, radiation-cooled filter elements as well as contact-cooled filters, are possible solutions for this beamline. A final careful FEA must be carried out using the final source parameters. In the beamline design they incorporated two components, a Be-window with sufficient pre-filters and an attenuator set up to manage the power load on the optical components:

6.4.3.2.1 Pre-Filter

This component is very similar to the setup already in use at several beamlines at BNL. It consists of a water-cooled frame that holds the different filters. The radiation-cooled foil is held in a tantalum frame, since it must withstand the extremely high contact temperature, and will become hot itself. The power then is dissipated into the surrounding environment and is absorbed by a water-cooled copper surface positioned around the tantalum frame. The tantalum frames, together with the carbon foils, are placed in a water-cooled cartridge made of OFHC copper. The cartridge is held and mounted on a DN40CF flange. The assembly is mounted to a DN100CF base flange and fits in a DN100CF standard cross. PT100 temperature sensors (e.g., two sensors) will be installed in the copper cartridge and monitored by the control system. If any PT100 sensor exceeds a temperature limit, the beam shutter will be closed. The PT100 sensors will be connected to an electrical feed-through. The water pipe (SF-copper, Ø8x1) will be brazed on the cartridge and on a DN40CF flange, avoiding water-to-vacuum joints. Possible carbon filter combinations are shown in Table 6.14.

Table 6.14 Possible Carbon Pre-Filter Combinations for the Be Window.

Filter no.	Filter thickness [µm]	absorbed power [W]	absorbed power density [W/mm²]
1	5	222	1.6
2	5	96	0.7
3	5	72	0.5
4	25	240	1.8
5	25	162	1.2
6	50	237	1.8
7	50	180	1.4
8	100	277	2.1
9	135	283	2.2
10	300	457	3.6
11	300	337	2.6

[4] private communication with J.Savino; "Improved high heat load graphite filter design at CHESS wiggler beamlines" – J.J.Savino, Q.Shen – SRI 2003 Proceedings

6.4.3.2.2 Attenuator Unit

This unit consists of a number of different filter setups that allow tailoring the power load on the optical components to the right level of operation for each particular operational mode of the beamline. The design being considered is based on one built recently by ACCEL for other high heat load beamlines and is described in the following paragraphs. Currently, we assume that for the DW beamlines it might be reasonable to work with two pneumatically driven attenuator units and two, or even three, motorized filter banks with different filters mounted. The latest design is based on a series of three water-cooled filters mounted on three pneumatic drives. These three carbon foils are of annealed pyrolytic graphite (APG). The foils have a thermal behavior similar to that of HOPG and are available down to thicknesses of 50 μm. The foils are clamped to copper frames where the thermal contact is improved by 1) polishing the surface of the copper within the contact area and 2) using springs that apply a wel-defined and well-distributed contact pressure. The thermal conductivity of APG is similar to diamond. Due to its excellent mechanical properties, and together with the advanced cooling, each foil is designed to remove about 500 W. The power density on the first foil constitutes the biggest challenge and therefore limits the maximum thickness of the foil, while heat conduction as well as physical integrity under thermal stress define its minimum thickness. The APG foil used in the existing system is 125 μm thick. The second foil can only be inserted in the beam when the first foil is already in place.

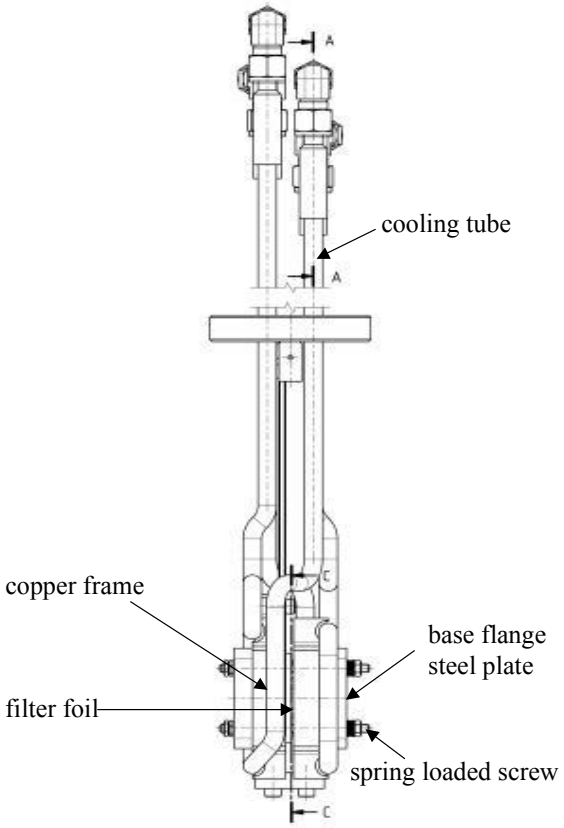

Figure 6.xx Directly-cooled high-power filter set-up, pneumatically driven.

The fourth filter drive is motorized and consist of a cooled frame with five positions that can be used for graphite foils (pyrolytic graphite) of different thickness to be used to further attenuate the beam. This filter design avoids water-to-vacuum joints. Water pipes are brazed to each cooled copper frame and to the vacuum feed-through, where edge-welded bellows allow the translation of the frames with the filters.

6.4.3.3 Sagitally-Focusing Double-Crystal Laue Monochromator

Sagittal focusing using Laue crystals was pioneered at the NSLS (Zhong et al., 2001; Zhong et al., 2002; Zhong et al, 2003). The concept is shown in Figure 1a. This new x-ray optics concept makes it possible to focus a large divergence of high-energy x-rays produced by the NSLS-II damping wiggler. The extent of such focusing is similar to that of sagittal focusing by a Bragg crystal, except for a factor related to the asymmetry angle. The anticlastic bending facilitates the use of inverse-Cauchois geometry in the meridional plane to provide better energy-resolution and to increase the photon flux by an order-of-magnitude compared to traditional sagittal focusing with Bragg crystals. Furthermore, sagittal focusing by a Laue crystal is preferred over a Bragg crystal at x-ray energies above 30 keV because, unlike Bragg crystals, the length of the beam's footprint on a Laue crystal is small and insensitive to energy. For many experiments, beam divergences of order 1 milli-radian at the sample will be tolerable. In diffraction experiments with a vertical scattering plane geometry, a larger divergence in the horizontal plane can also be tolerated.

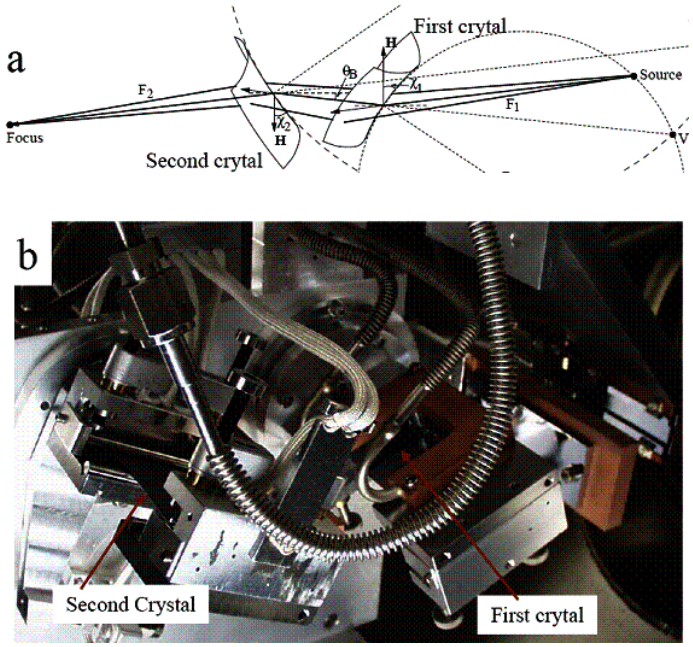

Figure 1: The mechanism of the sagittal focusing with asymmetric Laue crystals, bending of the crystals causes precession of the diffraction vector (H) around the axis of sagittal bending, and the resulting focusing of the diffracted beams. b) Photograph of a monochromator installed at the NSLS X17B1 beamline.

A double-crystal sagittally focusing monochromator, based on this concept, has been constructed and tested, and has been in use at the X17B1 beamline for two years, providing 67 keV x-rays (Figure 1b). It focuses a horizontal divergence of 3 milli-radians to a brightness-limited horizontal dimension of 0.2 mm. The x-ray flux-density at the focus was a few hundred times larger than that of unfocused x rays. Currently, using this device, flux on a small sample in a diamond-anvil cell is limited by the brightness of NSLS storage ring.

1. Z. Zhong, C. Kao, D.P. Siddons, H. Zhong, and J.B. Hastings, "X-ray reflectivity of sagittally bent Laue crystals", *Acta. Cryst. A* **59** (2003) 1-6.
2. Z. Zhong, C. Kao, D.P. Siddons and J.B. Hastings, "Rocking-curve width of sagittally bent Laue crystals", *Acta Cryst, A* **58** (2002) 487-493.

3. Z. Zhong, C.C. Kao, D.P. Siddons and J. B. Hastings, "Sagittal focussing of high-energy synchrotron x-rays with asymmetric Laue crystals, II: experimental studies", *J. Appl. Cryst.*, **34** (2001) 646-653.
4. Z. Zhong, C.C. Kao, D.P. Siddons and J. B. Hastings, "Sagittal focussing of high-energy synchrotron x-rays with asymmetric Laue crystals, I: theoretical considerations", *J. Appl. Cryst.* **34** (2001) 504-509.

After reviewing the current status of the sagitally-focusing double-crystal Laue monochromator, we do not expect any major technical difficulties to realize a final version of the device that could be integrated in the powder diffraction beamline, apart from the management of the rather large heat load expected on the set of necessary C and Si pre-filters, and also on the first crystal itself, and on the white beam stop that has to be positioned in between the two diffracting elements. In order to get a quantitative feeling of the challenges related to the large heat load inherent to the damping wiggler source, we have carried out a preliminary study focused on what could be reasonably thought to be the worst-case scenario: a full 7 m long damping wiggler and the maximum acceptance of the beamline of 1 (hor) x 0.15 (ver) mrad^2. Results are detailed in **Table 6.14 Power load on filters and crystals, on the powder diffraction beamline, for a fixed acceptance of 1 (hor) x 0.15 (ver) mrad^2.**

C Pre-filter thickness [mm]	Si Filter thickness [mm]	Power absorbed in C Pre-filter [W]	Power absorbed in Si Filter [W]	Power absorbed in first Laue Xtal [W]	Power dump in beam stop [W]
2	0	3331	0	1642	2435
2	1	3331	2246	354	1477
2	2	3331	2840	177	1060
3.5	0	4057	0	1182	2169
3.5	1	4057	1691	310	1350
3.5	2	4057	2215	159	977
5	0	4560	0	907	1941
5	1	4560	1341	271	1236
5	2	4560	1803	143	902
10	0	5578	0	457	1373
10	1	5578	724	180	926
10	2	5578	1037	102	691

and **Error! Reference source not found.** below.

Power load on filters and crystals for a fixed acceptance of 1x0.15 mrad^2 :

Table 6.14 Power load on filters and crystals, on the powder diffraction beamline, for a fixed acceptance of 1 (hor) x 0.15 (ver) mrad^2.

C Pre-filter thickness [mm]	Si Filter thickness [mm]	Power absorbed in C Pre-filter [W]	Power absorbed in Si Filter [W]	Power absorbed in first Laue Xtal [W]	Power dump in beam stop [W]
2	0	3331	0	1642	2435
2	1	3331	2246	354	1477
2	2	3331	2840	177	1060
3.5	0	4057	0	1182	2169
3.5	1	4057	1691	310	1350

3.5	2	4057	2215	159	977
5	0	4560	0	907	1941
5	1	4560	1341	271	1236
5	2	4560	1803	143	902
10	0	5578	0	457	1373
10	1	5578	724	180	926
10	2	5578	1037	102	691

As can be seen from the results, even with the thickest C shielding, it would be rather difficult to work with a single 2 mm Si filter in front of the Laue monochromator, because of the very high heat load that would not be sustainable by a single Si blade. It would then be necessary to split the overall 2 mm Si over several thinner blades, similarly to what is done with the C pre-filters. Moreover, the white beam stop after the first crystal should probably be a sloped block made of GlidCop as the total power and, mostly, the power density is still high and because of space constraints it may not be possible to design the stop with a very shallow slope to the incident beam. Finally, even with the max. shielding (10 mm C + 2 mm Si), there are still ~ 100 W dump in the first crystal and the large amount of shielding material would make the device transmission not very efficient below 30 keV. Careful attention should then be dedicated to the matching of protective material thickness vs. overall transmission and vs. power loading of all elements (filters, crystal and beam stop), unless the beamline acceptance is significantly reduced. The envisaged system design will result in an extreme stable, massive and compact system. The vacuum chamber will directly sit onto a solid U-shaped granite block avoiding efficiently amplifications from floor vibrations. Based on our approach of in-vacuum solutions the monochromator mechanics will be placed inside the vacuum vessel. As a result the design will be very compact avoiding vacuum feed-throughs for any movements and the mechanics of all movements will be placed to the crystals as close as possible. Therefore, the system will prove to be very stable and precise and will yield the following advantages: The intended design for the monochromator will permit operation in the energy range of 20-100keV with a constant beam offset of 15 mm upwards. The following adjustment units are shown in Table .

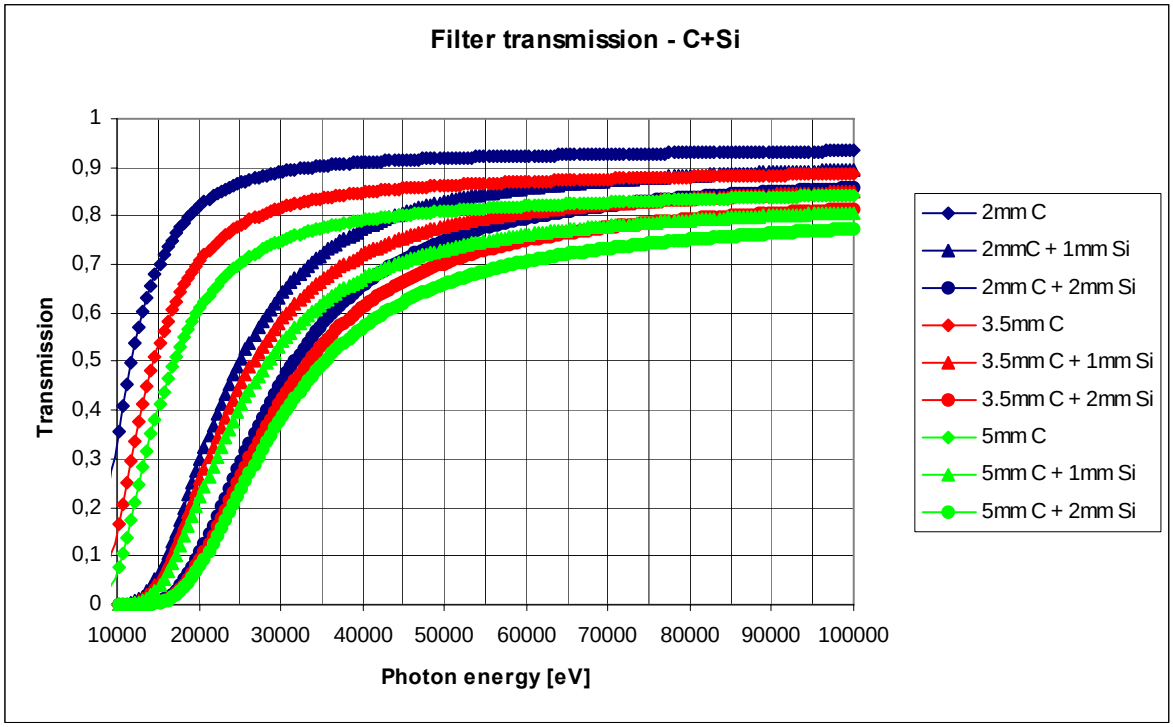

Figure 2: Transmission of various filter combinations on the powder diffraction beamline.

Table 6.15 Possible Adjustments for the Sagitally-Focusing Double-Crystal Laue Monochromator.
Bending adjustments are not shown in this table.

Movement	Range	Resolution	Repeatability
Whole optic assembly:			
Transversal (Y)	150 mm	≤ 5 µm	≤ 20 µm
1st and 2nd crystal units:			
Longitudinal (X)	500 mm	≤ 0.5 µm	≤ 20 µm
Yaw rotation (ϕ_1)	360°	≤ 10 µrad	≤ 10 µrad
Vertical (Z1)	40 mm	≤ 0.1 µm	≤ 5 µm
Roll rotation (χ_1)	-20 – 20°	≤ 10 µrad	≤ 20 µrad
Bragg rotation ($\theta 1_{coarse}$)	-5 – 35°	≤ 10 µrad	≤ 20 µrad
Bragg rotation ($\theta 1_{fine}$)	± 50 µrad	≈ 0.01µrad	≈ 0.06" (uni-directional)

6.4.3.4 White Beam Shutter

The white beam shutter is included in the front-end section (Section 6.4.1), and thus does not belong to the scope of supply for the beamline.

6.4.3.5 Vertically Focusing/Collimating Mirror

The basic design of the damping wiggler powder diffraction beamline foresees a single vertically collimating/focusing mirror placed in the front optical enclosure (white beam section), upstream of the sagitally-focusing double-crystal Laue monochromator. Nevertheless it has been decided to make provisions

for a possible upgrade of the beamline optics, leaving enough space in the beamline layout for the installation of a further horizontally/vertically focusing mirror (double toroid) downstream of this monochromator. Special attention has been paid to the cooling of the mirror, which is exposed to a significant level of absorbed power load and whose performance is rather critical in determining the ultimate energy resolution of the monochromator. An established technical solution for the mirror cooling, similar to the one that is implemented at the 7 Tesla superconducting wiggler HMI beamline at BESSY and at the Australian Synchrotron XAS beamline relies on indirectly cooling the mirror substrate with three Cu cooling blades immersed in a Ga-In eutecticum bath filling grooves machined in the optical surface of the mirror. This technical solution has already demonstrated to be able to cope with a total absorbed power load of the order of 2 kW but may fail for the even higher loads that the mirror may face at NSLS-II (Appendix D).

We have then explored two additional options that offer a better chance to withstand extreme heat loads: (i) Directly cooled Glidcop Mirror or (ii) Directly cooled Si Mirror. There is a possibility to use Glidcop as a mirror substrate material. This solution allows a direct cooling schema, which certainly has some advantages for higher power loads of a few kW (Appendix D). It should be noted that some doubts exist on the long term stability of Glidcop when exposed to the white beam and furthermore it is a more challenging material to polish than Si. A more favored direction is to use a directly cooled Si mirror. This technology is in use at beamlines at NSLS and the ALS and such mirrors can be realized with the requested quality. Provided that it is not directly exposed to the X-ray beam, the stability of the frit-bonding seems not to be a problem even after several years of use. Mirror specifications are shown in the table below.

Table 1 Specifications for the ACCEL vertically focusing/collimating mirror, for the powder diffraction beamline.

Mirror Substrate	Mono-crystalline Silicon (or Glidcop)
Direction of Reflection	Upwards
Shape	FLAT /cylindrically bent to tangential cylinder
Tangential Bending Radius	5.0 km - flat (> 40 km)
Sagittal Bending Radius	flat (> 1 km)
Substrate Length	approx. 1400 mm
Substrate Width	~ 120 mm
Substrate Thickness	60 to 70 mm**
Optical Active Surface: Length	1200 mm
Optical Active Surface: Width	2 x 35 mm (Si & Pt)
Sagittal Slope Error:	< 15 µrad rms
Tangential Slope Error:	< 2.5 µrad rms on 1200 mm (Best effort: < 2 µrad rms)
Micro Roughness	< 3 Å rms; best effort < 2 Å rms
Coating	Pt> 600 Å; Cr underlayer/ Bare central Si stripe
Cooling	Directly cooled

The ACCEL high stability mirror system mechanics is designed to be very robust, reliable and to allow easy access for maintenance and installation. A key design feature is that the mirror positioning mechanics is directly supported by a massive granite block that is mechanically decoupled from the vacuum chamber. This design allows to realize a very stable system and to greatly reduce the influence of vibrations propagating along the beamline. In order to get an as easy as possible access to the mirror, rectangular vacuum chambers are used. The chamber lid can be removed and then the entire mirror with its positioning mechanics is easily accessible.

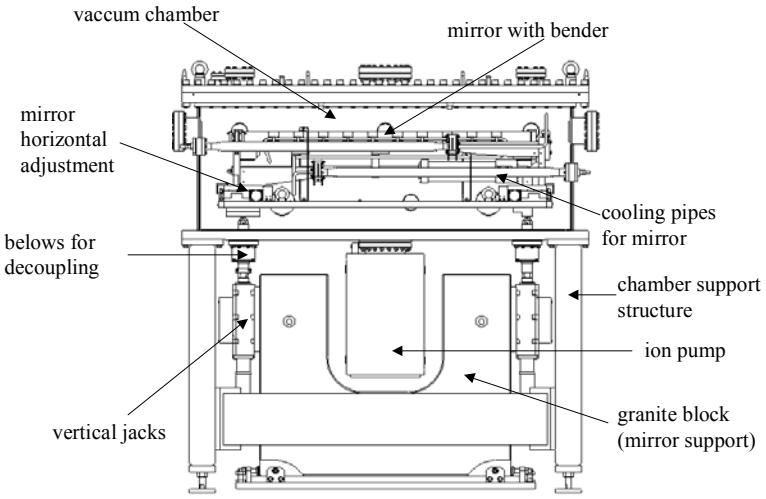

Figure 6.xx Side view of a high stability mirror system with a water-cooled bender.

Overall Technical Description. A very important design aspect of the high stability mirror systems is the complete mechanical separation between the optics and the vacuum chamber. This aims to avoid as much as possible vibration propagation to the mirrors. A massive granite block directly supports the mirrors holders/benders that are mechanically isolated from the vacuum chamber by means of edge-welded bellows. Another design guideline is to use in-vacuum actuators for the horizontal translation and its associated rotation (yaw), in order to (i) preserve the decoupling between the vacuum chamber with its support structure and the mirror with its positioner and (ii) to realize a system as compact as possible. Thus, two UHV compatible horizontal translation stages will be installed in the vacuum chamber (one at each extremity of the mirror), with one independent UHV compatible stepper motor each. Vertical translations will be performed by means of vertical jacks that also perform the two remaining rotations (pitch and roll). The mirror can thus be remotely adjusted in five independent degrees of freedom. All rotations (pitch, roll and yaw) will be realized by means of software pseudo-motors. Translations in/out of the beam will be realized by moving at the same time, of the same amount and in the same direction the three motors that act on the vertical jacks. Pitch and roll rotations will also be realized by the same three jacks. Horizontal translation (strip change) and yaw rotations will be realized by means of the two in-vacuum motors that act on the horizontal linear translation We suggest using a protective water-cooled steering mask between the mirror and the monochromator. It serves to better protect the monochromator interior or any un-cooled surface downstream from being hit by a mis-steered hot beam coming off the 1st mirror and further serves as a conductance limiting aperture for the vacuum performance between these two sections. To accommodate all operation modes of the beamline this mask has to sit on a vertical stage and will be equipped with edge welded bellows to allow for the necessary translations.

The mask will have water channels, I.D. 8 mm, with copper tubes brazed to it (no water-to- vacuum joints are used in our design). The material will be Glidcop and the impinging area will have a suitable slope so that it can withstand the high thermal stress that will be produced under worst conditions.

6.4.3.5 Beam monitoring elements

Beam monitoring elements are extremely important for beamline alignment. In this section, three such systems (as provided by ACCEL), are described: (a)Water-cooled White Beam CVD fluorescence screen The device consists of a retractable water-cooled CVD diamond foil, acting as x-ray screen, mounted to a pneumatic drive; the fluorescent effect is based on the residual doping with nitrogen atoms. The diamond screen is transparent, i.e. beam detecting further downstream is possible. The assembly is mounted to a

DN100 CF cross with one view port permitting a side view onto the screen. The pneumatic drive is equipped with limit switches. The vacuum feed-through is made of edge-welded bellows. The water lines are brazed to the screen support to avoid vacuum-to-water joints. The foil is clamped to the cooled support. The projection of the beam onto the 45° inclined foil will be monitored with a CCD camera. This system is capable of staying in the beam. However, because of the resulting absorption at photon energies below 10 keV, we advise to withdraw the screen when not in use. Moreover, to increase the lifetime of the foil and prevent overexposure of the camera, this screen should only be used at reduced power levels, i.e. in combination with some of the carbon filters. This screen has been installed at the high power wiggler beamline at the Australian Synchrotron Project.

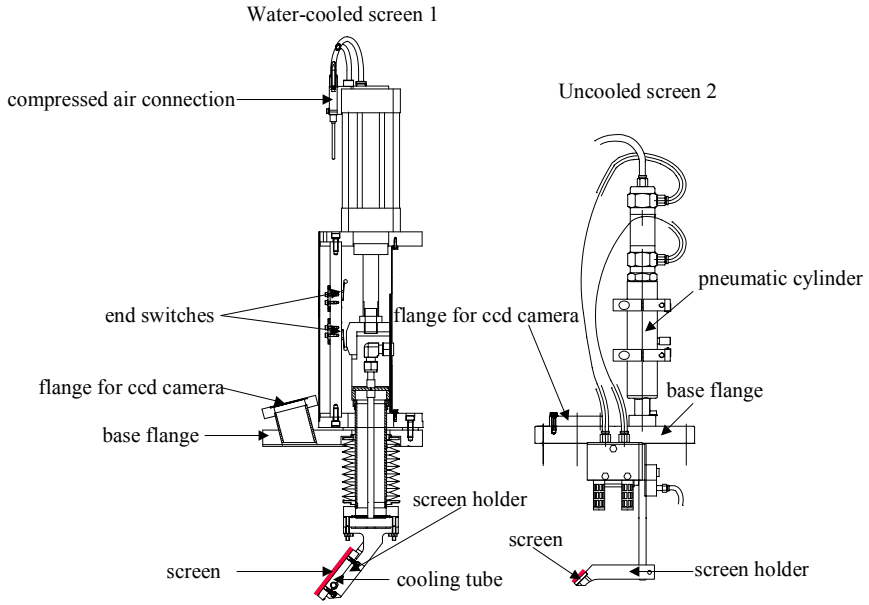

Figure6.xx Examples of ACCEL fluorescence screen beam monitors.

b) The fluorescence screen monitors typically are mounted to a pneumatic drive via a vacuum feed-through on a conflat flange. The water-cooled monitor is inserted in the beam by a stepper motor. The flange is also equipped with a view port for the camera that provides side view of the screen. Examples can be seen in Figure, for a water-cooled device and an un-cooled device.

c) Quadrant diode beam position monitor (4-diode BPM). ACCEL standard monitoring device for monochromatic beams of large size is a quadrant type detector that monitors the fluorescence yield of a target foil. Beam position information is derived from the intensity ratio of one pair of diodes. The device is rated for UHV and consists of a diode holder (holding four diodes) and a fluorescence foil holder. The four detecting silicon diodes are mounted to a vertical stage that permits the vertical positioning of the diodes which is necessary to operate the BPM at different beam heights.There are mounts for two foils, which can be of different kinds, or be the same. Typically, thin chromium and copper foils are used, but silver foils might be used as well. Chromium and copper have been working up to photon energies of around 20 keV. There is an option to mount a YAG crystal underneath this foil holder. Then, this YAG can be used to visualize the beam by means of a camera looking from the side onto a prism which is positioned behind the YAG. The assembly is designed such that it mounts to a CF100 flange and fits a standard size DN100 CF cross. The detection electronic for the diodes will be consisting of an integrated four-channel pico-ammeter with direct digital output.

d) The x-ray beam monitor is a commercially available visualization system for x-rays. Such a system provides a field of view large enough to study the beam size, beam profile and the beam position stability of a focused beam in the end-station (at atmosphere).

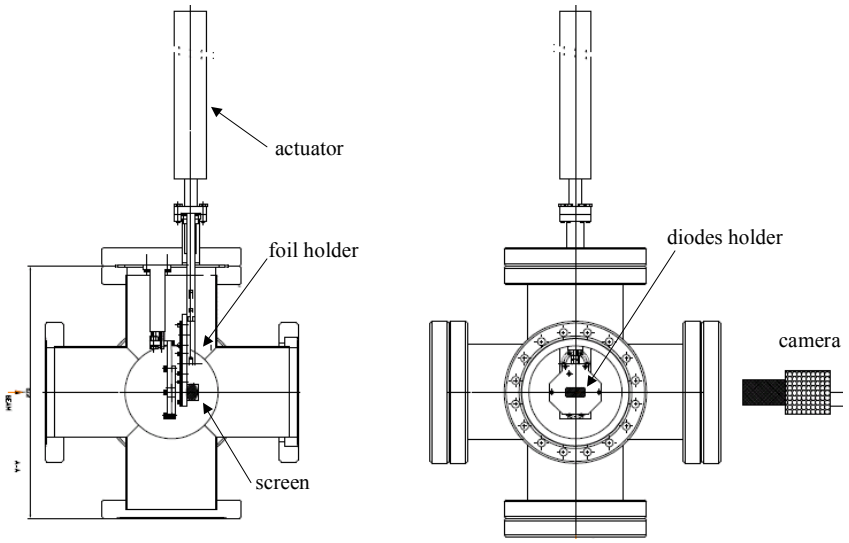

Figure 6.xx BPM (UHV rated) with diodes and fluorescent foil and screen.

6.4.3.6 Monochromatic Shutter

Although the powder-diffraction beamline anticipates using in-house fabricated monochromatic beam shutters, we include a description of the ACCEL photon shutter for completeness. These shutters consist of a high-density material absorber block, which is moved by means of a pneumatic actuator. The feed-through is mounted to a DN100CF flange. The motion of the pneumatic actuator is transferred to the absorber block through an edge-welded bellow, which has a guaranteed life time of 10^5 cycles. The absorber block is made of a Tungsten alloy having a Tungsten content of > 95% and a density of 17.5 g/cm³. The pneumatically driven actuator has a stroke of 60 mm. The pneumatic drive can be operated within a pressure range between 4 to 8 bar. The necessary magnetic valve is switched with a voltage of 24 V. The speed is adjustable by means of one-way restrictors. Each limit (upper and lower) of the stroke is indicated by two independent electromechanical switches. In case of failure (i.e. no power supply at the magnetic valve and no pressure at the pneumatic actuator), the shutter will close due to gravity. In Figure, we present a shutter that was recently designed for GM/CA-CAT (APS) and CMCF (CLS) where redundancy in form of double actuators was required.

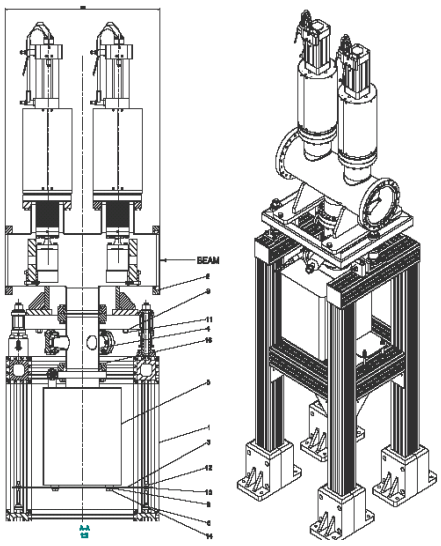

Figure 6.xx Sketch of one of ACCEL's monochromatic photon shutters.

6.4.3.7 Vacuum windows

A typical solution for the final widow in the powder diffraction beamline is to use a Be foil of appropriate aperture, diffusion bonded to a stainless steel double sided flange. The exit Be window will be carbon coated to protect the beryllium surface against oxidation in air.

Table 6.xx Specifications for the final Be window in the powder-diffraction beamline.

General:	
Material	stainless steel flange
	CF100
Foil material	Be-foil, PF-60, both sides polished
Foil thickness	0.250 mm
Aperture size of Exit window	tailored

6.4.3.8 Enclosures

There will be three beamline radiation enclosures at the damping wiggler powder diffraction beamline; one first optics enclosure (FOE) and two experimental hutches. The FOE contains all beamline optics (filter units, mirror, monochromator, beam monitoring assembly and photon shutter), and will be a white beam hutch. The FOE with its lead shielded sides interfaces to the ratchet wall of the storage ring. Following the standard regulations for white beam hutches, the labyrinths to run electricity as well as media and power connections will be located on the roof. The hutch will be very long (approx 17 m) to accommodate the optics for both the original beamline and possible optics for a canted beamline. One double door with sliding panels, large enough to move in larger components using a fork lift, will provide access to the hutch. Based on our experience with regulations at national US laboratories and following the ALARA practice we have based our evaluation for the FOE on the more conservative numbers for lead shielding that are presented in the document, NSLS-II Technical Note 014, Table 6, i.e. following the thickest lead shielding requirements for the FOE (see details below). The beam transport between the FOE and the first experimental hutch will be a tunnel type (coffin style) transport. Such an enclosure design will provide enough flexibility to accommodate vacuum pipes for beamlines. The shielding of interfaces such as guillotines etc. is included. All three

enclosures will be equipped with an overhead crane (one metric ton), several labyrinths and sliding doors. A summary of the specifications is as follows:

First Optics Enclosure, white beam hutch (FOE):

	Upstream wall 2 m x 3.3 m	Sides 17.5 m x 3.3 m	Downstream wall 3 m x 3.3 m	Roof 17.5 m x 2.5 m
Shielding requirements Lead [mm]	16 mm	23 mm	50 mm	14 mm

- one extra panel of size 1 m x 1 m x 50 mm at downstream wall centred at 1400 mm above floor
- one sliding double door (white beam hutch)
- 10 times chicane on the roof, all chicane with hinges
- one hutch crane, 1 metric ton
- one set of guillotine, adjustable shielding around beam pipe on downstream wall
- painted with primer

Shielded Beam Transport (coffin style, base with lid):

Lead shielding of 7 mm thickness.
Dimensions: 2 m long, 0.4 m x 0.4 m cross section
Support stands every 2 m with gussets.
Painted with primer

Upstream Experimental Enclosure, monochromatic hutch (EH-1):

	Upstream wall 4 m x 3.3 m	Sides 7 m x 3.3 m	Downstream wall 4 m x 3.3 m	Roof 7 m x 4 m
Shielding requirements Lead [mm]	6 mm	6 mm	6 mm	5 mm

- One sliding door
- 5 times chicane on the roof, 3 times chicane on the sides, all chicane with hinges
- one hutch crane, 1 metric ton
- one set of guillotine, adjustable shielding around beam pipe on upstream wall
- painted with primer

Downstream Experimental Enclosure, monochromatic hutch (EH-2)

	Upstream wall 4 m x 3.3 m	Sides 7 m x 3.3 m	Downstream wall 4 m x 3.3 m	Roof 7 m x 4 m
Shielding requirements Lead [mm]	6 mm	6 mm	6 mm	5 mm

- One sliding double door
- One sliding single door
- 5 times chicane on the roof, 3 times chicane on the sides, all chicane with hinges
- one hutch crane, 1 metric ton
- one set of guillotine, adjustable shielding around beam pipe on upstream wall
- painted with primer

Provision will be made to run cable trays and utilities inside and outside the hutches.

6.4.4 Instruments

This section describes the end-station instrumentation necessary to perform high-energy high-resolution powder diffraction. The scope of the powder diffraction beamline allows for one end-station (Endstation 1), that will allow high-energy high-resolution powder diffraction, with the other optical enclosure (most upstream enclosure) to be populated in the future – possibly by existing NSLS-I equipment and served by a canting wiggler source in the high-β straight-section.

6.4.4.1 Endstation 1

This section describes the high-energy high-resolution powder diffraction end-station. Our current thinking in designing this facility is to use equivalent set-ups employed at various high-energy high-resolution powder diffraction stations at other synchrotron radiation facilities. In general, the end-station consists of a highly accurate 3-axis diffractometer: One axis is used for sample orientation (or spinning), the second axis holds a fast read-put position sensitive silicon strip detector for in-situ time-resolved studies and remains essentially fixed, and the third axis is used to hold a multi-crystal silicon array analyzer system that can be rotated in the vertical diffraction plane. The scientific drivers for this particular instrument has been outlined in the first two sections of this chapter. Two high-resolution diffractometers, whichexist at various high-resolution powder diffraction beamlines, could be employed at this beamline.. We show two multi-channel crystal arrays on the drawing (Figure 14, taken from the SLS design), but a different design and large array could be easily envisaged. The resolution of the rotary stages need to be highly accurate to obtain accurate peak positions and reliable data. The Newport and RPI systems have the necessary resolution to enable the operation of this facility. The other all resolution of the system should provide peak shape resolution of < 5 milli-degrees, thus allowing accurate peak profile measurements essential in the study of strain, microstructure and lattice defects. Mython strip array detectors (PSI design) are to be installed at the DIAMOND, SLS and Australian synchrotron facilities and our design will incorporate similar technology; a 7000-element silicon strip detector array currently being fabricated at the NSLS for in-situ real time material studies. A variety of sample environments (not shown) has been included in our budget, consisting of cryostats, furnaces, laser heating and diamond-anvil cells for high-pressure research. In addition, a robotic sample chamber has been included (not shown) for high-throughput measurements for combinatorial investigation and screening purposes. The overall design is relatively standard, except for the inclusion of a graded bendable multiplayer system that will be used to focus the beam to ~ 14 microns in the horizontal for studying small samples (e.g. for high-pressure diamond-anvil cell research). This mirror is located relatively close to the sample position to minimize beam motion as the multiplayer is rotated to match the incoming x-ray wavelength.

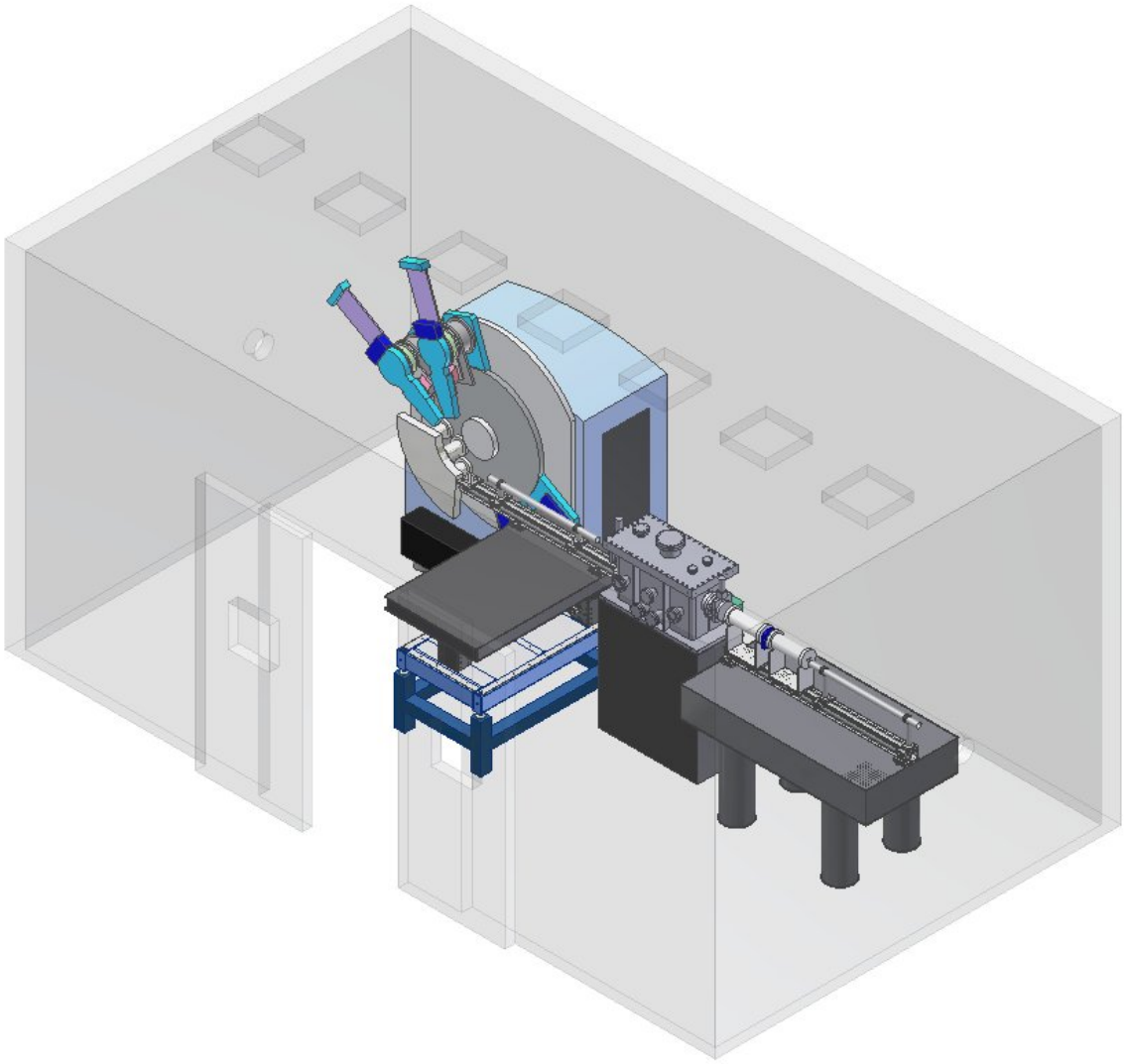

Figure 3: Conceptual design of the NSLS-II high-energy high-resolution powder diffraction beamline. For clarity, sample environments (such as crysostats, furnaces and diamond-anvil cells) and a robotic sample changer for high-through-put applications are not included in the figure.

6.4.4.2 Endstation 2

Although not in the scope of the present NSLS-II project, the most upstream optical enclosure is included to serve as a possible second powder diffraction beamline. This second beamline, which could be served by a canted wiggler source in the high-β straight section, could be populated by existing NSLS-I equipment. For example, there are many Huber diffractometers, several CCD cameras and robotic sample changers operational at NSLS beamlines at this current period of time.For example, we show in Fig XXX, a routine powder diffraction setup, with a huber diffractomer, with a ccd camera on a 2-theta arm. We anticipate such a facility would also be in high demand at the NSLS-II machine.

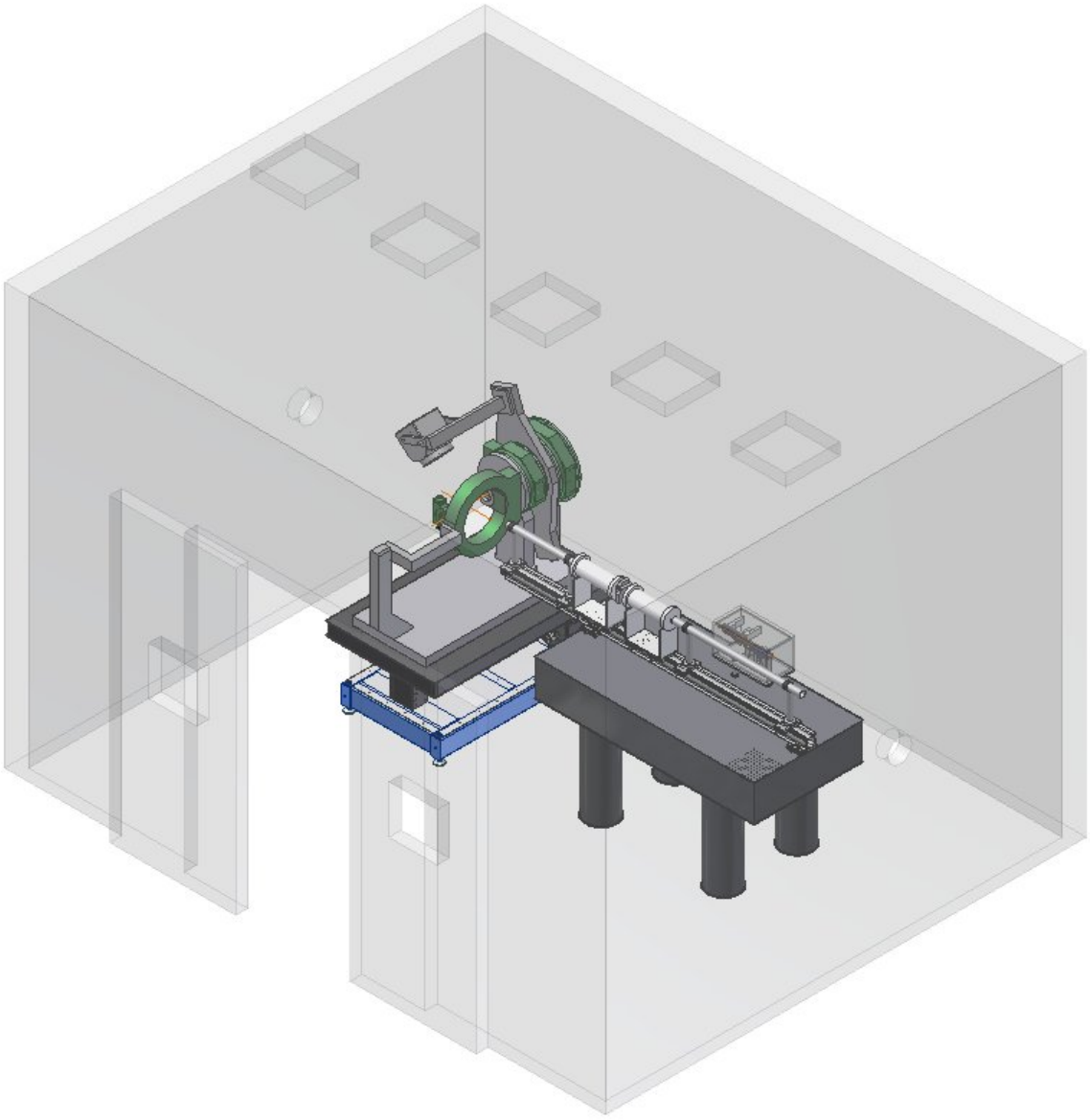

Figure 4 Conceptual layout for a second powder diffraction beamline, upstream of the high-energy high resolution NSLS-II powder diffraction beamline. Note that this end-station is not in the current scope of the NSLS-II project.

6.5 Additional Requirements Imposed on the Conventional Facilities

Powder diffraction experiments will be performed in both the high-resolution (crystal array) and area detector modes. The crystal analyzer is the most demanding in terms of angular stability, since it aims to provide high d-spacing resolution and precision. The area detector mode is primarily affected by position stability. Both modes are sensitive to beam energy changes.

In the crystal analyzer mode, the critical requirement is angular stability. A typical powder peak width using an analyzer crystal is in the range of 0.001^{o} to 0.01^{o} at 17 keV, depending on the sample quality. 0.001^{o} is unusually good. Let us consider 0.005^{o} as typical. Then, the photon beam stability should be 10% of this value i.e. 0.0005^{o}, or 8 μrad.

A related concern is the energy stability, since energy maps directly to d-spacing in a diffraction experiment. Using Si(111), it's intrinsic energy resolution, $dE/E \sim 10^{-4}$, which sets a limit on what we can achieve with a sample. If we assume we can find centroids to a few percent of this, we end up with an energy stability requirement of at least 10^{-5}. This maps to an angular stability of 1 or 2 μrad [Si(111) at 17 keV has a Darwin width of 15 μrad], and a monochromator temperature stability of 10 Kelvin.

All of the above arguments are directed in the vertical plane of diffraction.

Area detector measurements are typically 10 times or more lower resolution than using a crystal analyzer, so angular stability is not the limiting case. In contrast to the crystal analyzer mode, position stability is important, since position is used as an angle analogue. If we assume a focused beamline with a focal spot of 100 μm and a detector with similar spatial resolution, then using the '10% rule', beam stability should be on the 10 μm level. Similar arguments apply to energy stability. In this case, the spatial stability requirements are in both the horizontal and vertical directions.